The University Of Sheffield.

Zeolites as sensitizers in water-gated thin film transistors sensors

By:

Nawal Hassan Alghamdi

A thesis submitted in partial fulfilment of the requirements for the degree of Doctor of Philosophy in Physics.

Department of Physics and Astronomy

The University of Sheffield

February 2021

Dedication

I dedicate this thesis to the memory of my father, who would have been so proud of me.

Acknowledgment

First and foremost, I express my gratitude and praises to the almighty god **Allah** for blessing me and for giving me the strength, the patience and guidance to accomplish my PhD.

I would like to express my sincere thankfulness to my previous first supervisor Dr. Martin Gerll for his support, advise and motivation during the first two years and a half of my PhD. Appreciations extended to my current supervisor Dr. Andrew Parnell for his support and advice especially in writing my thesis. Also, I would like to thank my second supervisors Prof. Merlyne De Souza and Prof. Richard Jones, special thanks go to my personal tutor Prof. Simon Goodwin for his kind advice and support and to Dr. Marco Conte for his help and cooperation in the work on catalytic zeolites sensitizers.

Immeasurable gratitude goes to my family members for their love and support, my dearest mother, my beloved husband, and all my sisters and brothers especially my little gorgeous sister Manal. Also, I would like to thank my close friends for their support and the time we enjoyed together during my study time in the U.K.

I would like to thank my lab group members; Dr. Talal Althagafi, Dr. Abraham Kirwa, Dr. Abbad Al Baroot, Dr. Alhulw Alshammari and Zahrah Alqahtani for their help, ideas and discussion during our work.

Special thanks to the Saudi Cultural Attaché in London and the University of Tabuk in Saudi Arabia for the financial support of my PhD study.

Abstract

Thin film transistor TFT technology has emerged in several applications including in sensing applications. The discovery of water gated thin film transistors (WGTFTs) in 2010 made possible a new technique of sensing waterborne analytes, where the test solution is the gating water and the sensitizer is integrated into the WGTFT architecture. The work presented in this thesis is toward improving the performance of WGTFTs sensors.

The solution processing of semiconductors offers a simple manufacturing method to produce good performance in TFTs using metal oxide semiconductors in particular. In this work, aiming to improve the stability of the WGTFTs sensors, solution processed SnO_2 thin films prepared by spray pyrolysis were used as the semiconductor in WGTFTs. SnO_2 transistors show good stability under water gating, especially when compared to other metal oxide semiconductors (here compared to ZnO). Another favorable property of SnO_2 WGTFTs is the very low threshold voltage V_{th}. Therefore, the SnO_2 WGTFT is adopted for the sensing experiments in this thesis.

Also, very sensitive WGTFTs sensors were achieved here by incorporating zeolites as sensitizers in the WGTFT architecture. Zeolites are porous aluminumsilicate minerals with different sizes of cages and channels that analytes are trapped in. As a first attempt, a PVC (Polyvinylchloride) membrane was sensitized with mordenite zeolite to detect the radioactive isotope of cesium $^{137}Cs^{+}$ in the drinking water where this sensitized membrane is included in the WGTFT sensor. Such a sensor for Cs^{+} shows very good performance with a very low limit of detection of sub-nanomolar and also a very high binding constant K of 10^9 L/mole. In a similar way and to investigate further this finding with zeolites sensitizers, a different zeolite 'clinoptilolite' was used to sense the existence of heavy metals in water, in particular here lead Pb^{2+} and copper Cu^{2+} cations. Very similar behavior was obtained confirming the success of such a new family of sensitizers in the WGTFTs sensors field.

Another type of zeolite is the catalytic zeolites where these zeolites are modified to be catalysts. As the first step in the catalytic reaction is the adhesion of the analyte onto the surface of the catalyst, so we used this fact to build a sensor from catalytic zeolites as sensitizers to the analyte that is meant to be catalyzed in water, where hydrocarbons are usually the analytes. The finding that a good catalyst is also a good sensitizer is approved here with benzyl alcohol as an analyte.

Also, this work shows that a specific type of analyte can be detected by our sensors which is hydrocarbons with a free dipole.

Declarations

1. The work presented in chapters 6,7,8 is based on published work.

Chapter 6: [N. Alghamdi, Z. Alqahtani, and M. Grell, J. Appl. Phys. **126**, 064502 (2019)]

Chapter 7: [Z. Alqahtani, N. Alghamdi, and M. Grell, J. Water Health **18**, 159 (2020)]

Chapter 8: [N. Alghamdi, Z. Alqahtani, C. Zhou, N. Sano, M. Conte, and M. Grell, Chem. Pap. 74, 4169 (2020)]

2. Some sections in chapter 8 (8.2.1, 8.2.3, and 8.3.1) were performed with my collaborators in the chemistry department (Sheffield University), these are important parts to link the catalyst activity of zeolites to our sensing application.

Table of Contents

List of publications and conferences

Publications:

1. Alghamdi, N., Alqahtani, Z. and Grell, M., 2019. Sub-nanomolar detection of cesium with water-gated transistor. *Journal of Applied Physics*, *126*(6), pp.064502.

2. Alqahtani, Z., Alghamdi, N. and Grell, M., 2020. Monitoring the lead-and-copper rule with a water-gated field effect transistor. *Journal of Water and Health*, *18*(2), pp.159-171.

3. Alghamdi, N., Alqahtani, Z., Zhou, C., Sano, N., Conte, M. and Grell, M., 2020. Sensing aromatic pollutants in water with catalyst-sensitized water-gated transistor. *Chemical Papers*, 74, pp.4169–4180.

4. Alqahtani, Z., Alghamdi, N., Robshaw, T. J., Dawson, R., Ogden, M. D., Buckely, A., Grell, M. 2020. "Water-Gated Transistor Using Ion Exchange Resin for Potentiometric Fluoride Sensing." *Micromachines* 11(10), pp. 923.

Presentations at conferences:

1. Alghamdi, N., Alqahtani, Z. and Grell, M., "Sub nano-molar detection of Caesium by water gated SnO_2 Thin film transistor", (oral presentation), IOP PGS Conference: Printing for the future 2019, Hemel Hempstead, United Kingdom, April 2019

2. Alghamdi, N., Alqahtani, Z. and Grell, M., "Sub nano-molar detection of Caesium by water gated SnO_2 Thin film transistor", (oral presentation), UK Semiconductors 2019 Conference, Sheffield, United Kingdom, July 2019

Departmental Presentations:

1. Alghamdi, N., Algarni, S., Althagafi, T., Albaroot A., Alqahtani Z., Grell, M., "Water gated thin film transistors as ion sensors" (oral presentation), the Materials-seminars Group in the physics department, Sheffield University, April 2019

2. Alghamdi, N., Alqahtani, Z. and Grell, M., “Sub nano-molar detection of Caesium by water gated SnO_2 Thin film transistor”, (oral presentation), PhD Presentations- Departmental Research Day, Sheffield, United Kingdom, April 2019

List of figures

List of tables

Acronyms and abbreviations

AC	Alternating current
AAS	Atomic adsorption spectroscopy
E_g	Band gap
CB	Conduction band
I_{on}/I_{off}	Current on/off ratio
DI water	Deionised water
DP	Deposition precipitation
DC	Direct current
I_D	Drain current
V_D	Drain voltage
EDL	Electric double layer
eV	Electron volt
EPA	Environmental Protection Agency
FET	Field effect transistor
V_{fb}	Flatband voltage
V_G	Gate voltage
IE	Ion exchange
ISE	Ion Selective Electrodes
ISFET	Ion selective field-effect transistor
ISM	Ion selective membrane
LoD	Limit of detection
μ_{lin}	Linear mobility
V_M	Membrane potential
µm	Micrometre
µM	Micromolar
mV	Millivolt
MCM-41	Mobil Composition of Matter
μ	Mobility of charge carriers
MOSFET	Metal Oxide Semiconductor Field Effect Transistor

nm	Nano meter
nM	Nano molar
PC	Personal computer
PTM	Phase transfer membrane
PBS	Phosphate buffered saline
pM	Pico molar
PVC	Poly(vinylchloride)
SBA-15	Santa Barbara Amorphous-15
μ_{sat}	Saturated mobility
SEM	Scanning Electron Microscopy
C_i	Specific capacitance
SS	Subthreshold swing
THF	Tetrahydrofuran
TFT	Thin film transistor
ΔV_{th}	Threshold voltage shift
V_{th}	Threshold voltage
SnO_2	Tin oxide
VB	Valence band
WGTFT	Water gated thin film transistor
WI	Wet impregnation
XPS	X-ray photoelectron spectroscopy
ZSM-5	Zeolite Socony Mobil 5
13X	Zeolite type 13X
Y	Zeolite type Y
ZnO	Zinc oxide

Chapter 1: Introduction and Motivation

1.1 water

Water is essential for the existence of life. It accounts for 75% of the earth's surface and about 70% of the human body. Some unusual properties of water give it such importance. The water molecule (H_2O) is formed of two hydrogen (H) atoms and one oxygen atom (O). Due to the uneven distribution of electrons in both O and H, the water molecules have polar covalent bonds. Thus, water is a polar molecule with a negative charged part and positive charged part (figure 1.1). Water molecules are linked to each other by a hydrogen bond (H-bond), where H is always involved in such a bond. In this case the positive part H^+ of a water molecule attracts the negative part O^- of another molecule. A H-bond is a strong bond that holds water molecules together and is responsible for many of waters properties. For example the high boiling point and its surface tension[1,2].

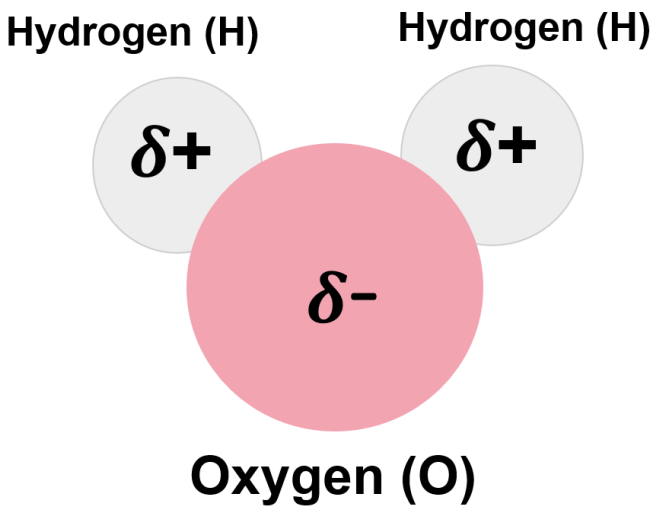

Figure 1.1: Diagram of a water molecule with positive and negative parts.

Water is considered a good solvent for polar molecules. For each solute that is dissolved in water, a spherical shell of the water molecules or 'hydration shell' surrounds the solute molecules (or ions). Molecules with a tendency to dissolve in water are called hydrophilic, whereas the non-polar molecules (e.g. some hydrocarbons) are insoluble in water and called hydrophobic[1]. Generally, the hydration shells increase with small radius solutes.

Another property of water due to the strongly polarized O-H bonding[1] is the spontaneous dissociation or autoproteolysis of water molecules as presented in equations 1.1 and 1.2 below:

$$H_2O \rightarrow H^+ + OH^- \qquad 1.1$$

or

$$2\,H_2O \rightarrow H_3O^+ + OH^- \qquad 1.2$$

In pure water the concentration of both H^+ and OH^- is equal, $[H^+] = [OH^-] = 10^{-7}$ M.

The acidity or alkalinity of water is quantified by the pH measure as in equation 1.3 below:

$$pH = -\log [H_3O^+] \qquad 1.3$$

So if the negative logarithm of hydronium H_3O^+ (or H^+) ions concentration is less than 7 the water considered acidic whereas in the case of pH is above 7 the water is basic or alkaline[2].

In nature, water is rarely found as pure water but mostly contains a mixture of dissolved salts. The aqueous solution is widely used to describe such solution where the water is the solvent. For example sea water, where the dominant salt is sodium chloride (NaCl), also in ground water where sodium Na^+, calcium Ca^{2+}, bicarbonate CHO_3^- and sulfate SO_4^{2-} are the major ions. To clarify here, generally the positively charged ions (such Na^+, Ca^{2+}) are called cations, where anions are the negatively charged ions (such Cl^- and F^-). The existence of some of these ions in water is beneficial at certain levels, but beyond certain concentrations such water can be unsafe to use. Also, some

harmful ions can be found in water such as heavy metals, for example from industrial waste, in this case water is very harmful for humans and other living creatures. In addition, the water pH differs mainly due to chemical impurities. For example, when some of the transition metals dissolve in neutral water it acidifies it (pH < 6.5)[3]. The safe and permitted pH level for human drinking water is in the range 6.5 - 9.5, according to European Union regulation[4].

An additional example of aqueous media are biofluids. Body fluids vary in pH, for example blood and spinal fluid have a pH of 7.4 and the stomach fluid is highly acidic with a pH range of (1.5 – 3.5). The ion concentration and pH in the body fluids are homeostatic which means the ability to maintain the same environment inside the body including ion concentration, pH, temperature and sugars (e.g. glucose) and hormone concentration[5]. Similarly, the pH buffered solutions keep the pH value as constant as possible and only changing in a narrow range. Therefore, such a solution is used to simulate biofluids in biosensing applications.

1.2 Sensors for waterborne analytes

Different waterborne analytes are found in water, some of these analytes are essential for life such as Calcium (Ca^{2+}) and iron ($Fe^{2+, 3+}$), if not exceeding certain levels. For example, Calcium (Ca^{2+}) and fluoride (F^-) are some of the dissolved ions in drinking water, both are very beneficial for human health especially for bones and teeth, but elevated concentration of such ions in the human body causes serious health problems. The safe allowable level of an analyte in water is commonly expressed as the potability limit. Another type of analytes are non-essential and toxic such as heavy metals and radionuclides. In the case when such solutes exceed the water potability, they act as water pollutants (table 1.1).

Also, the presence of heavy metals ions such as Mercury (Hg^{2+}), Lead (Pb^{2+}) and Cadmium (Cd^{2+}) in water is very dangerous for the environment. The toxicity of heavy metals are caused by the correlated malfunction and damage in important organs such as the brain, kidneys and lungs[6,7]. Figure 1.2 shows the most common contaminations in the ground water of Europe, where heavy metals accounted for about the third of the total pollutants. Among heavy metals Hg^{2+} is considered the most poisonous and affects seriously the brain and kidney. According to the World Health Organization (WHO) the standard level of mercury in drinking water is 2 µg/l[8]. Additionally, lead

Pb^{2+} is classified as a carcinogen by the Environmental Protection Agency (EPA) and can cause chronic poisoning inside human bodies. Some water pipes are made of or contain lead Pb^{2+} which pollutes the drinking water which travels through these pipes. The potability of lead in drinking water is limited to 15 µg/l (72 nM), more than that is considered harmful[9]. Cadmium Cd^{2+} and its compounds are also very toxic, the International Agency for Research on Cancer has categorized Cadmium Cd^{2+} as a group (1) carcinogen for humans. Cadmium and its compounds have a high tendency to bio-accumulate due to their high water solubility compared to other metals. Humans are exposed to Cd^{2+} from different sources including batteries, paints, plastic and steel industries[6,8]. The long time exposure to Cd^{2+} even at low concentration (above 3 µg/l) can lead to serious health problems such as iron deficiency, kidney disease and lung damage[8,10].

Table 1.2: The potability limit of common ions contaminations mentioned here (according to the world health organization WHO).

Element	**Potability limits (µg/L)**	**Potability limits (nM)**
As	50	675.6
Cd	5	44.4
Pb	15	72
Hg	2	10
Cs	1	7.5
Al	200	7434

Pollutant	Potability limit
Cyanide	0.5 mg/l
Ethylbenzene (BTEX)	0.3 mg/l
Toluene (BTEX)	0.7 mg/l
Benzene (BTEX)	0.01 mg/l
Xylenes (BTEX)	0.5 mg/l
Chloroform (CHC)	0.3 mg/l
1,1-Dichloroethene (CHC)	140 µg/l
Benzo[a]pyrene (PAH)	0.7 µg/l

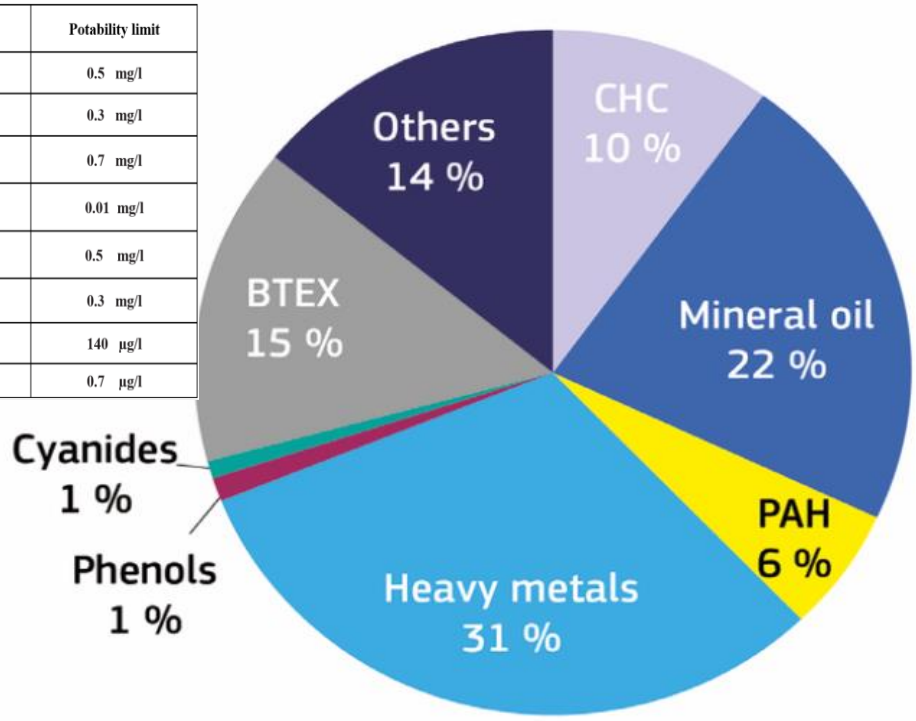

Figure 1.2: The most common contaminants in groundwater across Europe[11]. Where BTEX stand for Aromatic Hydrocarbons (benzene, toluene, ethylbenzene, and xylenes); CHC for Chlorinated Hydrocarbons such as chloroform; and PAH for Polycyclic Aromatic Hydrocarbons. Inset: Table of potability limits of the pollutants in figure 1.2 according to WHO.

In some areas the geological nature of the aquifers causes leakage of some toxic elements such as heavy metals. For example, in Bangladesh groundwater is contaminated with Arsenic (As) exceeding the allowable limit by the World Health Organization. Consuming such water with such high toxicity leads to an increase in the likelihood of arsenic-induced cancers[7]. Furthermore, in March 2011 after the earthquake in Japan, Fukushima Nuclear Power Plant was damaged resulting in releasing of huge number of radionuclides (e.g.^{137}Cs and ^{90}Sr) to the environment. When such pollutants enter the human body, they accumulate especially in the soft tissues and can cause serious health risks such as thyroid cancer. The danger of radioactive isotopes will continue for long period because of their long half-lives, for instance the half-life of ^{137}Cs is about 30 years[12,13].

In 1988 a contamination incident happened in Cameford south west of England when 20 tonnes of aluminum sulphate $Al_2(SO_4)_3$ were unintentionally placed in the drinking water supply[14]. As a result the acidity of the water rose, which lead to dissolution of other harmful metals from the piping network. This accident caused number of harmful health effects, both short and long term[14].

In addition to ions contamination, some molecules are considered very poisonous if present in the environment including in water. Fertilizers and fuels industries are some sources of organic pollutants. Benzene for example is a group 1 carcinogenic to humans, if spilt in water it can cause serious diseases such as leukemia. There are known incidents where this level has been exceeded in drinking water[15, 16], for example in the vicinity of oil fracking sites or accidental petrol spillages.

From what has been discussed above, it is clear that water can potentially contain some harmful analytes. These contaminants need to be monitored in water for everyone's safety. Providing safe water to drink, within the potability limit, is essential. Generally, sensors are used to detect the presence of various waterborne analytes and the concentration of them. Different types of sensor are used for monitoring water safety. Therefore, it is required to develop a sensors technology to have enhanced sensitivity and selectivity, and this will be demonstrated in this thesis.

1.3 Overview of sensor technology

Sensors are in great importance for our daily life as they are utilized in various areas. Sensors play a significant role in many fields such as monitoring pollution and human health. Generally, a sensor can be defined as a device that responds to a change in a certain property and converts that to a readable signal. Sensors can be classified into three main groups, physical, chemical sensors and biosensors. In physical sensors physical properties of the system are provided, such as temperature and mechanical sensors[17]. Where chemical sensors respond to specific chemical substances (analytes) in the environment, that response can also be from the chemical reactions that such analytes undergo. Biosensors are devices that detect physiological or biochemical changes. Normally, a sensor consists of a transducer and receptor (or sensitizer) where the receptor binds to the target analyte and the transducer transforms the result of this binding to a measurable

signal. For example, chemical sensors transform chemical information of the analytes and receptor interaction in the system into a signal.

Chemical sensors are relatively inexpensive and not bulky compared to other analytical techniques such as atomic adsorption spectroscopy (AAS). Chemical sensors can be divided according to the nature of the transducer and the receptor to different categories[18], some examples are the electrochemical and optical sensors and are explained below.

Electrochemical sensors: in electrochemical sensing, the effect of the electrochemical interaction between the analyte and the sensitizers is transformed to an electrical signal. The most common types of electrochemical sensors are potentiometric and amperometric. Typically, potentiometric sensors are presented by sensing electrode, where sensitizers are included, and a reference electrode such as in Ion Selective Electrodes (ISE). The potential difference between these two electrodes is measured by a high impedance velometer at zero (or near zero) current flow between them, where the developed potential is proportional to the analyte concentration. In amperometric sensors the electrochemical reaction between analytes and sensitizers produces a current where the sensor potential is set at a constant value. An applied voltage is used as a force to drive the current.

Optical sensors: in these devices the interaction between analytes and receptors result in changes in the optical properties that transform and act as useful signals. There are different optical sensor types that are divided according to the nature of the changed optical properties. Generally, optical sensors can be either colorimetric or fluorometric. In colorimetric sensors the sensitizers used are called chromophores, which change their optical properties (absorption band) when they bind to the analytes in the sample. On the other hand, the fluorometric sensors measure the fluorescence of the sample by a fluorometric sensitizer namely a “fluorophore” which change its optical properties, for example, either fluorescence enhancement or fluorescence quenching when it binds to the analyte. Therefore, the presence of analyte can be determined based on the change in fluorescence[19].

Additionally, electrical sensors such the metal oxide gas sensors. In this case the interaction between the analyte and the sensor material causes a change in the electrical properties of the sensor which translate as electrical signal[20].

Another type of sensors mentioned above are Biosensors. In this type of sensor; biological responses (e.g. physiological or biochemical) are converted into readable signals. A special family of receptors are involved in biosensors which are bio-receptors where different transducers can be used in biosensors, these include electrochemical and optical transducers[21]. Bio-receptors are biomolecules that are immobilized on a transducer surface and work via the recognition and binding of target analytes by a biochemical mechanism. Antibody antigen and enzymatic bio-receptors are some examples of biomolecules used in biosensors. These sensors help widely in diagnosing and monitoring human health, such as glucose and cholesterol biosensors[18]. Very recently a biosensor based on a potentiometric transducer, which is the field effect transistor (FET), has been used successfully to detect the recently emerged COVID-19 virus in clinical samples[22].

Generally, sensor performance is evaluated by a number of parameters such as the limit of detection the LoD, sensitivity, selectivity, response time and dynamic range[20]. Initially, each sensor needs to be calibrated before the extracting of such parameters. In calibration, a sensor is exposed to different analytes concentrations and responses are recorded for each concentration with the assumption that at zero analyte concentration the response is zero. Therefore, graphically the response curve, the relation between analytes concentrations and the response, is termed as the calibration curve. Responses differ according to the sensor type, for example voltage, current or fluorescence, and sensors can display linear or non-linear characteristics with concentration.

From the calibration curve, three important characterizing sensor technology parameters can be extracted, these are; the sensitivity, selectivity and the limit of detection (LoD)[23]. Sensor sensitivity can be defined as the smallest change that can be detected by the sensor; it can be measured graphically as the slope of the calibration curve. Selectivity refers to the ability of a sensor to discriminate between the main analyte and interfering analytes present in the same test sample. Generally, the sensor selectivity is dependent on the sensitizer (not the transducer) which mean a sensitizer binding with one analyte (meant to be detected) is stronger than others in the sample. Quantitatively, this is expressed by a selectivity coefficient, which compares the interaction of a sensor with the target and the interfering analytes. Also, it is calculated from the ratio of the binding constant of the sensitizer with the analytes, where higher selectivity coefficient means highly selective sensor[24]. Moreover, the limit of detection (LoD) is the lowest concentration of the analyte

that can be sensed. So, for an analyte concentration below the LoD no valid response can be detected by the sensor[25]. In a sensor, the limit of detection LoD depends on both the sensitizer and the transducer. Quantitively and for instance[26] in a linear relation with analyte concentration, the LoD is given via dividing 3 times the standard error Δb of the calibration curve by its slope m as in equation 1.4 :

$$\mathrm{LoD} = \frac{3\Delta b}{m} \qquad 1.4$$

An ideal sensor should have a low limit of detection LoD and a rapid response time, and also high sensitivity and selectivity. Similarly, stability of the senor is of high importance which is defined as the ability of a sensor to replicate the same response for a period of time. For example, some organic based sensors tend to be quite unstable due to polymer degradation[27].

Most of the sensor families mentioned above are employed in waterborne analytes detection. For example, the use of optic fibers to detect Al^{3+} and F^- ions in water[28]. The most important and relevant to this work is the use of potentiometric sensors for waterborne analyte detection. Potentiometric sensors have been reported widely in ion sensing [e.g.[29],[30]], however they are also used in sensing non-ionic analytes in water [e.g.[31,32]].

Generally, in potentiometric sensors, sensitizers are embedded in a matrix (e.g. a PVC membrane) to form a sensing element towards a certain analyte, where in the case of sensing ions it is called an ion selective membrane ISM. The sensitized membrane is then incorporated in the potentiometric transducers and it is the origin of the potential difference in this family of sensors. The classic and very common potentiometric sensor is the ion selective electrode (ISE). Subsequently, a simplified development in potentiometric ion sensing was the ion selective field-effect transistor (ISFET). Firstly, the ISFET was used only as pH sensor then it was improved to cover the sensing of different ions. The interfacial potential in an ISFETs is analyte concentration dependent and causes the threshold voltage variation. Recently, a new family of potentiometric sensors have emerged these are water gated thin film transistor (WGTFT). In the case where the analytes in the gating water of such a transistor interact with sensitizers in the membrane, an

interfacial potential is developed and subsequently changes the threshold voltage (V_{th}) of the transistor[33,34].

Generally, the commonly used conventional techniques in waterborne analytes detection are the spectroscopic techniques such as atomic absorption spectroscopy (AAS) and inductively coupled plasma mass spectrometry (ICP-MS), these methods are very sensitive, selective and have very low limits of detection in the femtomolar levels[35]. However, such techniques include very expensive instrumentation with high power consumption. Also, the sample preparation contains a number of stages, which is time-consuming, and complex analytical procedures are involved as well. Due to the complex equipment used in these techniques, they are not suitable for on-site applications and they cannot be used as portable devices[36]. In contrast, and by comparing to our sensors in this project, WGTFTs sensors are simple, low cost and rapid technique as a simpler analytical method and short time analysis are involved. In addition, WGTFTs are portable devices and they can be suitable for in-field-applications. The relatively lower sensitivity of our sensor compared to other spectroscopic sensors can be improved by further modification of the sensor, for example here by the use of new sensitizers.

1.4 Scope of this thesis

The work in this thesis focuses on the recent innovation in waterborne analyte sensors, that is the water gated thin film transistors or 'WGTFT' (figure 1.3). Firstly, a new inorganic semiconductor was introduced into a WGTFT, which is the sprayed pyrolyzed tin oxide SnO_2. WGTFTs with SnO_2 display a number of advantages compared with other WGTFTs semiconductors. In an aqueous media SnO_2 shows super long-term stability when compared to ZnO, the most used solution-processed inorganic semiconductor in WGTFTs[37]. Also, SnO_2 transistors have low threshold voltage and that is favorable in a WGTFT sensor. So, a stable sensors platform was accomplished by applying sprayed SnO_2 semiconductor in WGTFTs. Secondly, a new family of sensitizers namely "zeolites" were introduced in WGTFTs sensors. Zeolites are commonly used in cleaning water from harmful ions such as radioactive isotopes and heavy metals by extraction. Here, the zeolite mordenite which is known as a good adsorbent for radioactive cesium $^{137}Cs^{+}$, was used in the sensitized membrane of a WGTFT for $^{137}Cs^{+}$ detection. Also, clinoptilolite zeolite is used for the removal of heavy metals from water. Similarly, clinoptilolite was also used as a lead

Pb^{2+} and copper Cu^{2+} sensitizer in the same way. The performance of these sensors was promising and a low limit of detection (LoD) was achieved in both cases. These LoDs were below the potability of such pollutants in water and follow the global guidelines of drinking water. Also, such low LoDs have not been achieved previously using organic sensitizers. The overall response characteristic of zeolite-sensitized WGTFTs is different to that of conventional organic sensitizers, and such characteristics are probably responsible for the low LoD. Also, in this thesis zeolites are used as sensitizers for some non-ionic aromatic organic pollutants. As some zeolites act as catalysts for aromatic pollutants, we find that these zeolites succeed as sensitizers for the same pollutants with WGTFTs sensors.

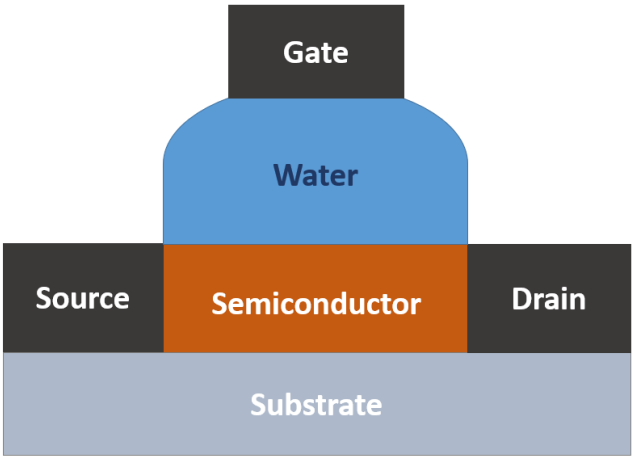

Figure 2.3: The architecture of the water gated thin film transistor WGTFT

The organization of this thesis is as shown below, where chapters 1, 2, 3 describe the background and theories, chapter 4 shows the devices fabrication and characterization and chapters 5, 6, 7, and 8 illustrate the main results:

Chapter 1 presents some basic information about water as essential for life and contaminants that can get into the water and the need for sensors for safe health and the environment. Also, sensors technology is briefly explained including potentiometric and specifically the water gated thin film transistor WGTFTs.

in **chapter 2** the background of thin film transistor (TFT) as the base of our sensor (WGTFT) is covered, including their history, structure and operation. In addition, the TFT semiconductors is shown, including the solution-processed SnO_2 used in this project. Then, the electrolyte gating of TFT and the electric double layers formed EDLs is explained.

Chapter 3 introduces potentiometric sensors and the sensitized membrane used in these sensors with some examples of sensitizers. Also, different types of potentiometric sensors are presented, including WGTFT and the common response characteristics of such sensors.

Chapter 4 explains in detail all the processes to fabricate WGTFT sensor and all the characterization techniques used.

Chapter 5 shows the preparation and the characterization of the sprayed pyrolysis of SnO_2 as a semiconductor film in a WGTFT and its sensing capability.

Chapter 6 shows the result of the first attempt of the implantation of zeolites as sensitizers in the membrane of WGTFT. Mordenite was used here to detect ($^{137}Cs^{+}$) in tap water**.**

Chapter 7 demonstrates another zeolite namely clinoptilolite when similarly set in WGTFT for sensing lead (Pb^{2+}) and copper (Cu^{2+}) ions in tap water.

Chapter 8 illustrates how catalytic zeolites can be used as sensitizers in a WGTFT to sense the associated unsaturated hydrocarbon pollutants specifically benzyl alcohol.

In chapter 9 an overall conclusion of this thesis and some viewpoints for future work related to this project are given.

Chapter 2: Devices and materials for transistor- based sensors

2.1 Thin Film Transistor (TFT) History

The transistor is a semiconductor device which is used for regulating (to amplify, switch) the electric signals (voltage, current). Transistors have been extensively utilized in the industry of modern electronic devices such as computers and mobile phones. Furthermore, as this thesis will show transistors demonstrate excellent properties as sensors. Initially, the concept of the field effect transistor was proposed by Julius Edgar Lilienfeld in 1925[38]. At Bell laboratories in 1959, Kahng and Atalla fabricated the first working field effect transistor called a MOSFET (Metal Oxide Semiconductor Field Effect Transistor)[39]. In this type of transistor, the semiconductor is highly doped and crystalline, commonly using doped-Silicon. The advent of the thin film transistor or TFT as a special type of MOSFET was in 1962. Paul Weimer demonstrated the first TFT using polycrystalline Cadmium Sulfide as a semiconductor film, this was deposited on an insulating substrate[40]. Importantly the TFT is relatively cheaper and easier to fabricate compared to a MOSFET. The discovery of TFT technology has emerged in various applications. For example in liquid crystal displays (LCD's), where they act as pixel switches, and in the bio-sensing field for the detection of biomolecules[41].

2.1.1 Structure of Thin Film Transistor (TFT)

Thin film transistors TFTs are field effect transistors as described above in 2.1. In a TFT the (un-doped) amorphous or polycrystalline semiconductor layer and contacts are deposited on an insulating substrate. These transistors have some differences from MOSFETs. In the latter a highly doped crystalline semiconductor layer forms the substrate as well. (See figure 2.1).

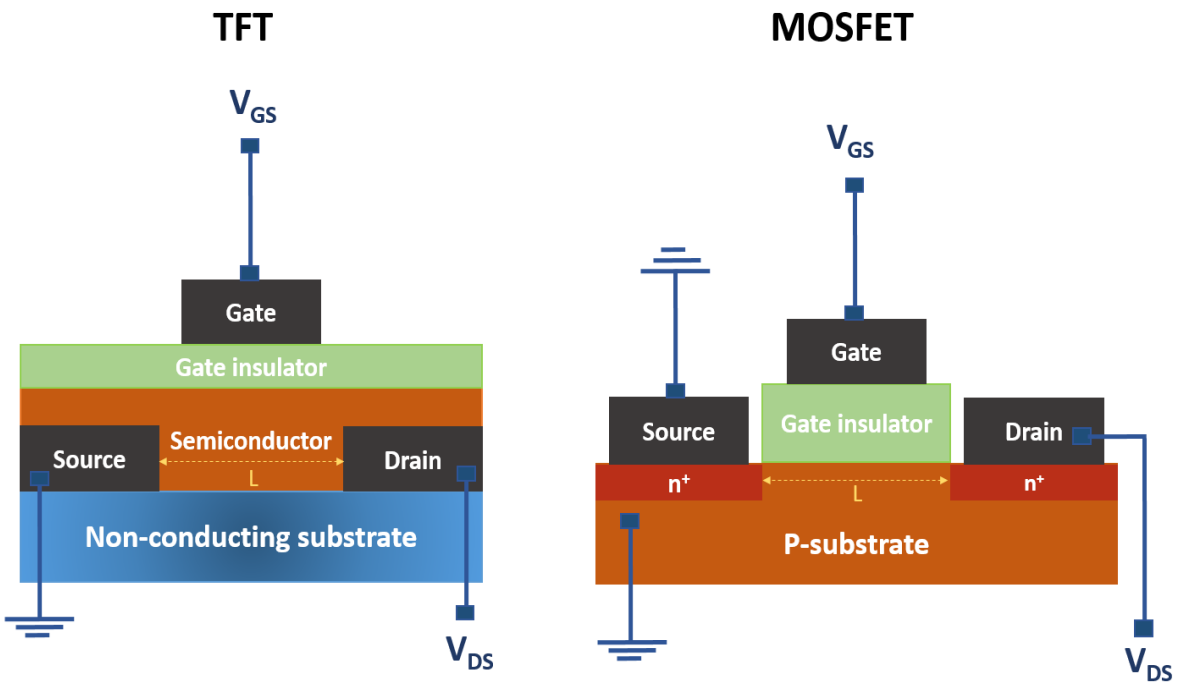

Figure 2.1: The structure of a thin film transistor (left) compared to the structure of a p-type MOSFET (right).

A TFT basically consists of three terminals (a source, drain, and gate), a thin semiconducting film, the dielectric layer and the non-conducting substrate where all the TFT components are deposited on top of it (figure 2.1(left)). Commonly both source and drain contacts are deposited on the surface of the substrate and divided by a distance L which is the semiconductor channel length, where W is the width of the channel. On top of the semiconductor film is a dielectric layer, which is sandwiched between the gate contact and the semiconductor, this layer is the gate insulator. The configuration of these layers results in different TFT architectures. By considering the position of the source/drain contacts in respect to the gate contact (top/bottom gated, top/bottom contact) and also to the gate insulator (staggered, coplanar), four different basics TFT constructions are identified[42]. Figure 2.2 below illustrates these designs.

Each architecture has its own advantages and disadvantages and could suit a certain application but not others. For example, in designs (B) and (D), where the semiconductor layer is covered by a gate insulator and metal, these are appropriate for light sensitive semiconductors such as a-Si: H (Hydrogenated amorphous silicon) and for TFTs application in LCDs. Also, in the process of

semiconductor crystallization, where very high temperatures are applied, the structure (D) is ideal for thermally delicate materials. As the semiconductor layer is the first layer to be deposited, so all other subsequent layers in the TFT will not be damaged by heat[43]. Architectures (A) and (B) offer an easier path for charge carriers to cross from source to the channel area as indicated by the yellow dashed arrows in figure 2.2. In this thesis a TFT structure similar to design (B) is used, where the contact is first deposited on the substrate then the semiconductor.

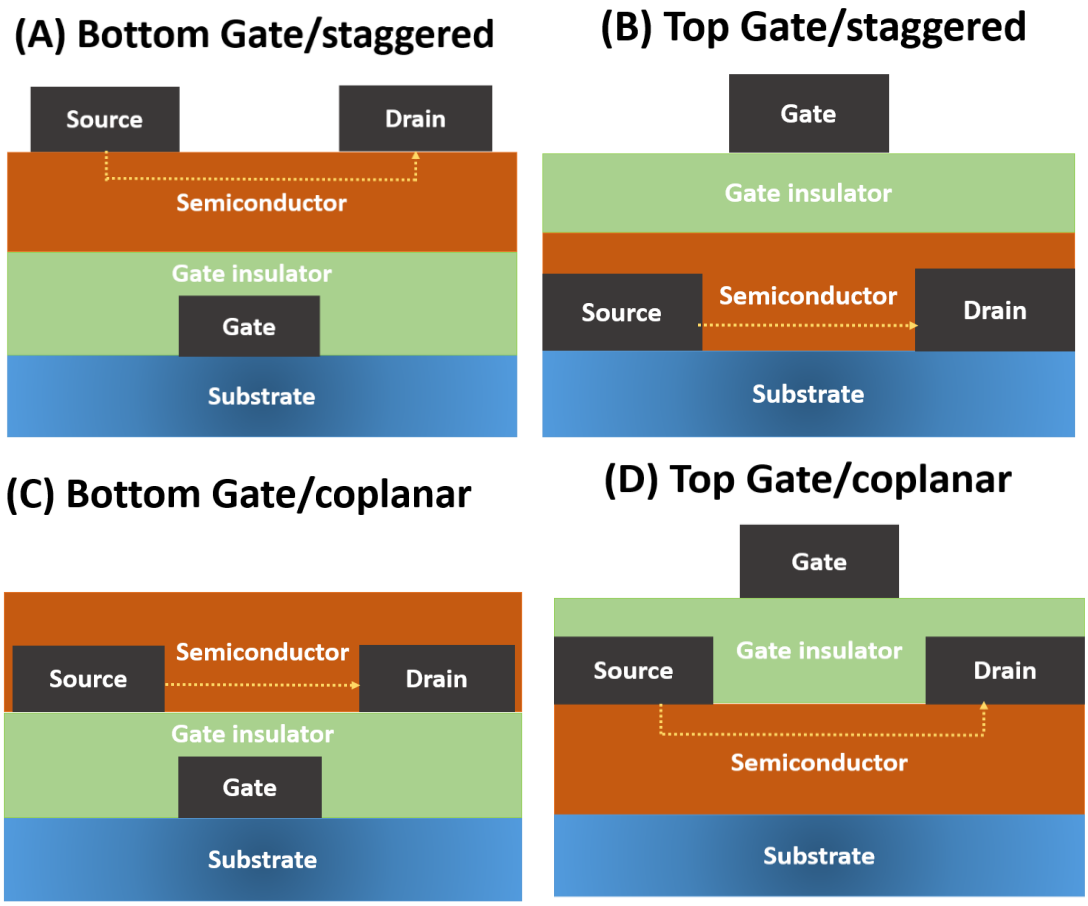

Figure 2.2: The four different architecture of TFT A, B, C, D. The dashed yellow line is the path of charge carrier flow in the channel.

2.2 Operation Principle of a TFT

The TFT as a field effect transistor is a voltage operated device, wherein an applied voltage controls the flow of current in the conducting channel of the device. The operation principle of a

TFT differs from that of a MOSFET. Basically, a MOSFET works in an inversion mode due to the doped semiconductor. In contrast a TFT operates in accumulation mode as an intrinsic semiconductor is used.

When a sufficient positive gate voltage V_G is applied at the gate contact of the TFT (illustrated in figure 2.3 and figure 2.4), electrons in the semiconductor film are pulled toward the insulator/semiconductor interface allowing the formation of an accumulation layer of electrons. The thickness of this accumulation layer is normally 1-2 nm, as reported by Tanase et al.[44].

By applying a voltage between the source and drain terminals V_D, electric current flows through the channel I_D. The illustration in figures 2.3 and 2.4 describes a n-type TFT whereas in p-type TFT's a negative gate voltage is applied, and an accumulation layer of holes is formed. The applied gate voltage V_G to turn a TFT on, by forming a conductive channel area, has to exceed a certain voltage point called the threshold voltage V_{th}. In section 2.3 below V_{th} and other key parameters are quantitatively explained during the process of TFT operation.

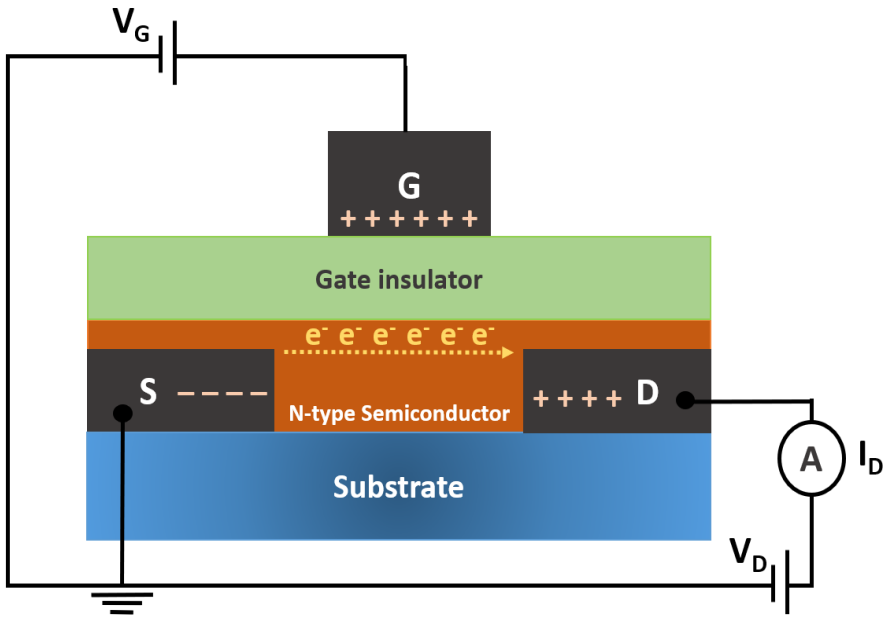

Figure 2.3: Illustration of the connections and the operation of a n-type TFT, S, D, G are source, drain and gate.

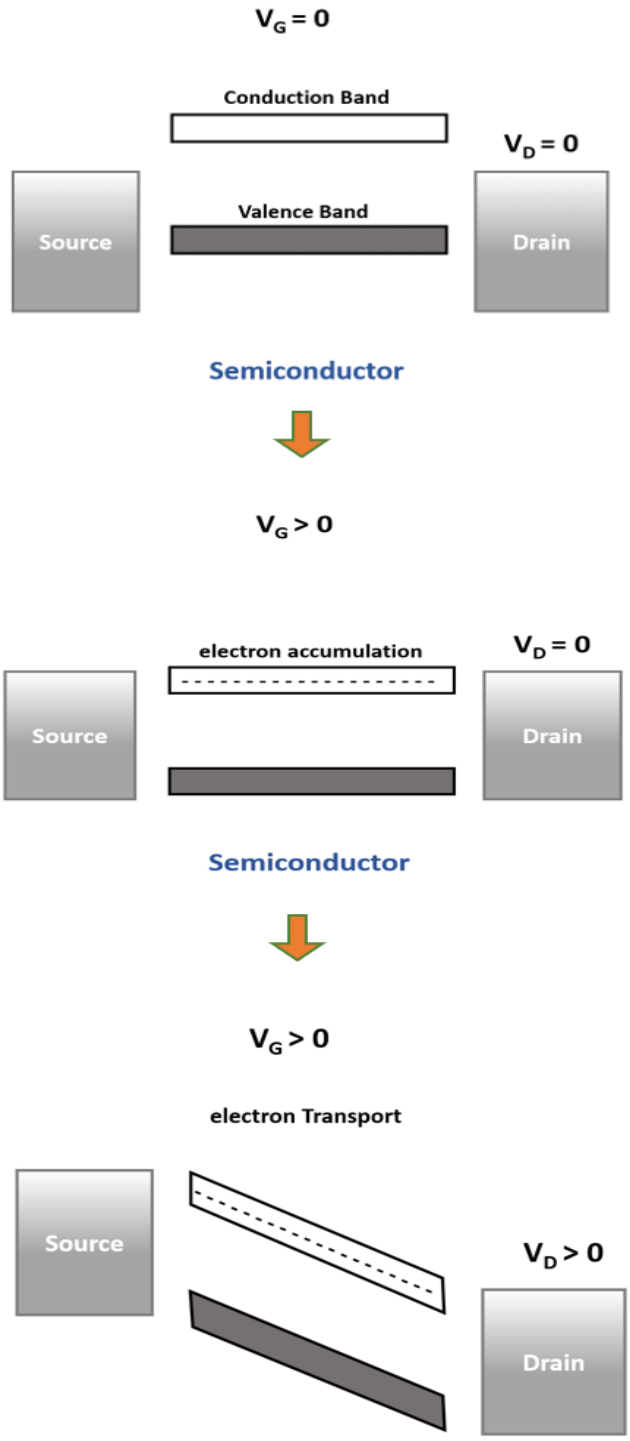

Figure 2.4: Energy diagram explaining the operation of TFT

2.3 Quantitative Description of TFT Operation

To describe TFT operation three main regimes are presented, these regimes are mainly controlled by the relation between the values of V_G, V_D and V_{th}. First and as mentioned in 2.2 V_{th} is a key parameter in TFT work, therefore it will be explained in more detail[45].

The threshold voltage V_{th} is defined as the gate voltage required to form an accumulation layer in the transistor channel and this leads to a conduction path between source and drain, V_{th} relies on a number of factors as shown in equation 2.1 below:

$$V_{\mathrm{th}} = V_{\mathrm{fb}} + \frac{qp_0 d_s}{\mathrm{C_i}} \qquad 2.1$$

Where V_{fb} is the flatband voltage, q one carrier charge ((+) for hole / (-) for electron), p_0 denote the trap density in the semiconductor film and the semiconductor/insulator interface, d_s indicates the thickness of the semiconductor film, C_i is the specific capacitance (capacitance per unit area) of the gate insulator.

The flatband voltage V_{fb} depends on the material properties of the gate metal and the semiconductor. Especially, the value of the metal work function and the semiconductor electron affinity for n-type semiconductor or the ionisation potential for p-type. Initially at 0 V of the V_G, the energy bands bend at the metal/semiconductor contact (see figure 2.4 and figure 2.5), to get rid of this bending and allow electrons (or holes) to pass to the semiconductor the gate voltage should be increased. The point of gate voltage when energy bands flatten and charge carriers start to appear in the channel area is the faltband voltage V_{fb}[45].

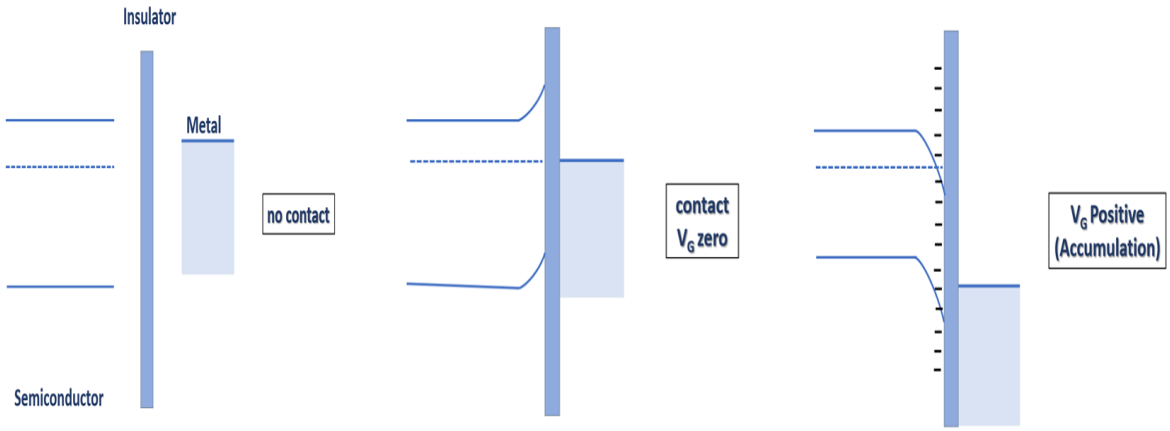

Figure 2.5: Schematic of the band bending with and without an applied gate voltage.

Another significant parameter that influences the V_{th} is C_i, the capacitance per unit area of the gate insulator, which is given by equation 2.2:

$$C_i = \frac{k\varepsilon_0}{d} \qquad 2.2$$

Wherein, k is the relative permittivity of gate insulator ε_0 is the vacuum permittivity and finally, d denotes the gate insulator thickness.

The use of electrolyte gating media offers a relatively high specific capacitance which is desirable and results in a low V_{th}[46]. Also, the high value of C_i can help moderate the effect of traps. In this case equation 2.1 can be expressed as $V_{th} \approx V_{fb}$

The first region of TFT operation is called the subthreshold regime:

The applied V_G in this region is lower than V_{th} ($V_G < V_{th}$), the drain current I_D is very low, and the accumulation layer is not yet formed. Although, the drain current I_D in the subthreshold region increases exponentially with the gate voltage V_G until the V_{th} point is accomplished[47]. Equation 2.3 below defines the subthreshold drain current:

$$I_D = K\mu C_i \frac{W}{L}\left(1 - e^{\frac{-qV_D}{K_B T}}\right) e^{\frac{qV_G}{nK_B T}} \qquad 2.3$$

where K is a constant linked to TFT device structure and the materials used, μ denotes the charge carrier mobility, C_i is the gate insulator specific capacitance, W and L are the channel width and length, q represents the elementary charge, k_B is Boltzmann's constant, T is the absolute temperature, n represents the ideality factor and is given by [$n = (1+ C_s/C_i)$] where C_s is the specific capacitance of the traps in both the semiconductor bulk and the semiconductor-insulator interface.

From the subthreshold region an important parameter can be extracted which is the subthreshold slope (S) or as generally expressed the inverse of this slope "subthreshold swing" (SS). Equation 2.4 indicates how to calculate SS:

$$SS = S^{-1} = \left(\frac{\partial \log_{10}(I_D)}{\partial V_G}\right)^{-1} \qquad 2.4$$

Subthreshold swing is expressed by the unit mV/decade, which means how much mV of the gate voltage V_G is needed to increase the drain current I_D by an order of magnitude. So lower values of SS are more desirable, especially in TFT switching applications as the TFT turns from off to on state faster and by applying a low V_G. Another way to represent SS is by using the ideality factor n in (equation 2.5):

$$SS = \ln(10)\frac{nK_B T}{q} \qquad 2.5$$

At a room temperature of 300 K° and by subtract $n = (1+ C_s/C_i)$ in equation 2.5 we get:

$$SS = 60\frac{mV}{dec}\left(1 + \frac{C_s}{C_i}\right) \qquad 2.6$$

Equation 2.6 illustrates that both C_s and C_i play a role in minimizing the value of SS.

In general, the values of SS in organic thin film transistors OTFTs are reported to be in the range of 500-5000 mV/dec[47]. Recently lower values were reported, especially by incorporating a high capacitance gate dielectric[48,49]. Metal oxide thin film transistors have shown more desirable SS below 100 mV/dec[50] and down to 68 mV/dec with a high dielectric constant gate insulator (of $In_{0.0025}Nb_{0.0025}Ti_{0.995}O_2$)[51]. Solution processed SnO_2 TFTs have relatively high SS values ranging from 800-5000 mV/dec[52,53,54], where smaller SS values have been achieved for nanowire SnO_2 transistors with solid electrolyte gating (85 mV/dec)[55]. Also, ultra-thin SnO_2, deposited by physical vapor deposition, give a small SS value of 110 mV/dec[56]. The electrolyte gating of TFT provides a high specific capacitance due to the formation of electric double layers EDLs (this will be discussed in 2.5), consequently electrolyte gated TFTs have shown pleasing results for SS of 94 mV/dec[57].

The second region is when the V_G reaches V_{th} ($V_G > V_{th}$) and a conducting accumulation layer is formed, this region is called the linear region as I_D increases linearly with V_D and the whole device works as an ohmic resistor (illustrated in figure 2.6 a). The drain current in the linear regime is given by equation 2.7 below[58,59]:

$$I_{D,lin} = \mu C_i \frac{W}{L}\left((V_G - V_{th})V_D - \frac{V_D^2}{2}\right) \qquad 2.7$$

In the case of $V_D << V_G - V_{th}$, the quadratic term $\frac{V_D^2}{2}$ can be neglected and equation 2.7 becomes:

$$I_{D,lin} = \mu C_i \frac{W}{L} V_D(V_G - V_{th}) \qquad 2.8$$

Thirdly the saturation region when V_D exceeds the difference between $V_G - V_{th}$ ($V_D > V_G - V_{th}$). In this condition the channel near the drain contact is pinched off and the drain current I_D becomes independent of the drain voltage V_D (can only be modulated by V_G)[58]. Figure 2.6 b and c describes the formation of the saturation regime and the pinch off. The saturated drain current in this region is given by equation 2.9[59]:

$$I_{D,sat} = \mu C_i \frac{W}{2L} (V_G - V_{th})^2 \qquad 2.9$$

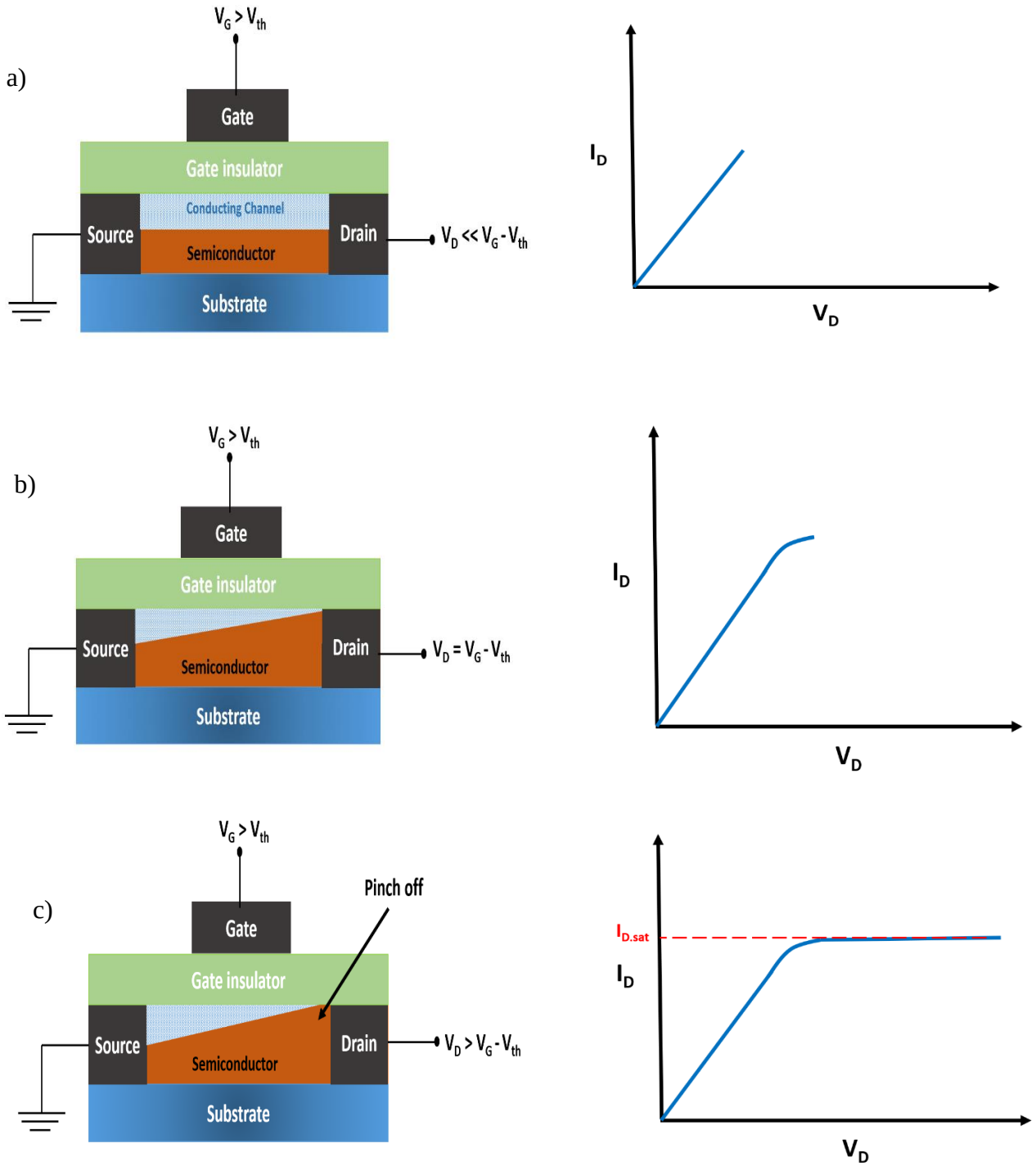

Figure 2.6: Operation regions of field effect thin film transistors demonstrated by the output characterisation of the transistor, a) Linear region, b) Start of the saturation region, c) Saturation region.

The TFT electrical measurements can be illustrated in two different characteristics forms, output and transfer. The output characteristics show the relation between the V_D and I_D at constant values of V_G. Usually this type of measurement is used to assess the quality of the device. Secondly, transfer characteristics which study the relation between V_G and I_D with constant values of V_D. These characteristics can be exhibited in both linear and saturation regimes. Figures 2.7 a and b show diagrams of the ideal output and linear transfer characteristics.

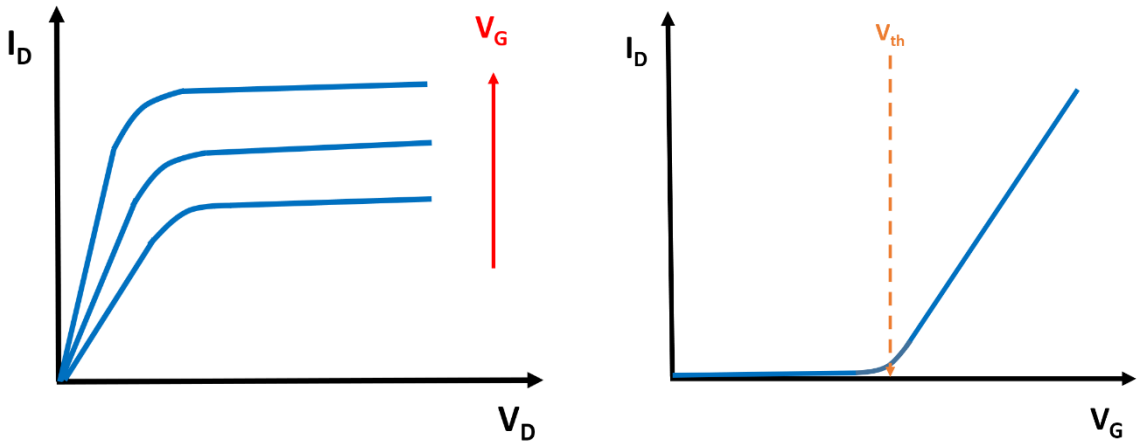

Figure 2.7: Illustration of TFT ideal output (left) and transfer (right) characteristics.

2.4 Semiconductor material fundamentals:

In the following section I will explain some important and fundamental concepts of semiconductor material before moving to TFT semiconductors.

Semiconductors are very important materials that we could not envisage life without them nowadays. Many essential technologies rely on semiconductor materials, these include everyday electronic devices (phones, computers). The key property of semiconductors is the ability to modulate the electrical conductivity in the region between conductors and insulators[60].

Energy bands:

On the atomic level of the semiconductor, every two neighboring atoms are joined by a covalent bond by sharing a valence electron. In reality, there are a huge number of atoms bonded together

to build the material (not a single pair of atoms). Therefore, with the huge number of atoms electrons can be instead visualised by forming energy bands. The main two bands in materials are a valance band, conduction band and a band gap between these two bands. Material types are categorized according to the alignment of these bands to conductors, semiconductors and insulators as the illustrations in figure 2.8. In the conductor case, there is no gap between the conduction and the valence bands so electrons can freely move between the two overlapping bands. In the case of insulators there is a large gap between the valence and conduction band (more than 5 eV) which electrons cannot overcome to move from valence to conduction band. In semiconductors the band gap is relatively small (typically less than 2 eV). As a result electrons in the valence band can move to the conduction band if they get sufficient energy to free them. Energy can be obtained in the form of heat, light, or via an electric field[45].

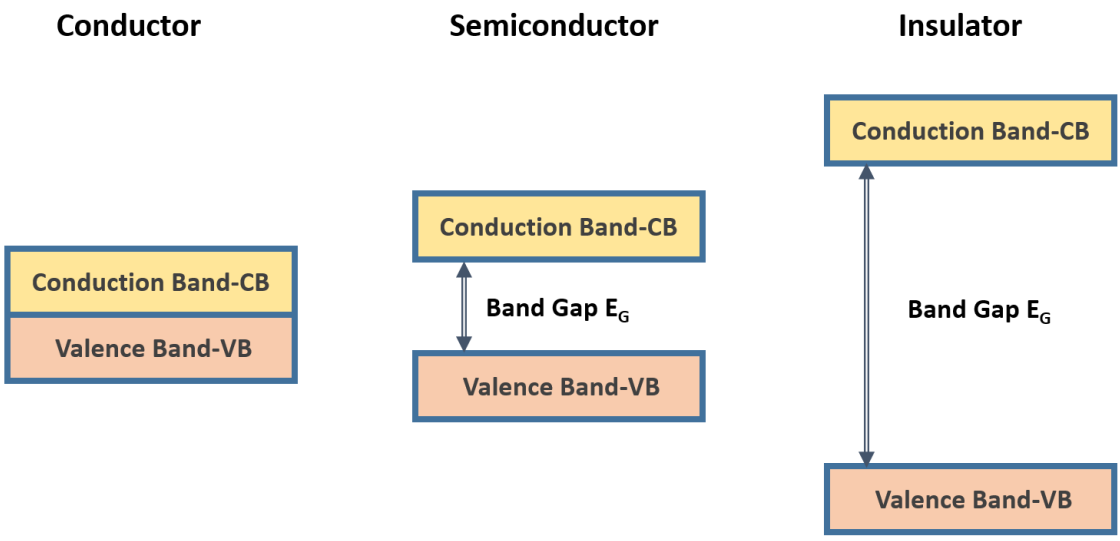

Figure 2.8: Illustration of the energy band alignment in a conductor, a semiconductor and an insulator.

In general, semiconductors can be classified into different categories according to the composition, presence of impurities and crystallinity. In terms of the composition, it can be an elemental or a compound semiconductor where 2 or more elements are involved. Elemental semiconductors are inorganic such as Si and Ge, whereas compound semiconductors can be both organic, for instance

the organic semiconducting polymer pentacene, and inorganic semiconductors such as GaAs and ZnO[60]. Moreover, semiconductor materials can be classified into pure intrinsic where no impurities (dopants) involve, and extrinsic semiconductors where dopants are intentionally introduced into the material. Extrinsic doping is divided into two classes, n-type and p-type doping. In the n-type semiconductor, elements with an extra valence electron are introduced into the semiconductor material. The generated electrons from such doping contribute to the conduction band and increase conductivity. As an example, the implementation of Arsine (As) in Germanium (Ge). In contrast, p-type doping works by adding impurities with a lower electron valence. In this case the absence of an electron, called a hole is generated. Holes contribute as charge carriers in the semiconductor by understanding that electrons fill the holes and holes move along in the opposite direction to electron. For example, doping Sillicon (Si) by Aluminium (Al)[60,45]. In addition, a semiconductor can be formed to have a certain degree of crystallinity, crystalline, poly-crystalline and amorphous. In crystalline semiconductors atoms (or molecules) are arranged in repetitive order, while in the amorphous phase atoms (or molecules) are randomly arranged (with no long range order). A poly-crystalline semiconductor is a phase in between crystalline and amorphous when there are many crystals but these vary in size and orientation. The variation in the degree of crystallinity in a semiconductor leads to a variation in important parameters such as the electrical mobility [60,61].

Charge carrier injection, transport and mobility:

Suitable carrier injection from the metal electrodes to the semiconductors is a significant factor for optimal devices performance. The match between the energy bands and levels of metal and semiconductor when the two come into contact, controls the carrier injection quality. As illustration (figure 2.9), for charge carriers (here for example electrons) the work function of the metal electrode used should be close to the energy bands of the semiconductor, for electron injection electron affinity and the bottom of the conduction band, and for hole injection ionisation potential and the top of the valance band. The difference between the work function and the related energy level represents the potential barrier[62]. For instance, different metals (Cr, Pt) are shown in figure 2.9 with the SnO_2 electron affinity of 4.5 eV. In the case of Pt (work function of 5.7 eV) as metal contact to SnO_2 the barrier height is 1.2 eV, where in Cr there is no barrier, thus electrons inject easily into SnO_2. Carrier injection from metal to semiconductor mainly follows two

mechanisms, thermionic emission and field emission. The former mechanism suggest that electrons gain enough thermal energy to overcome the barrier, whereas the latter follow quantum mechanics by suggesting the tunneling of electrons through the barrier[62].

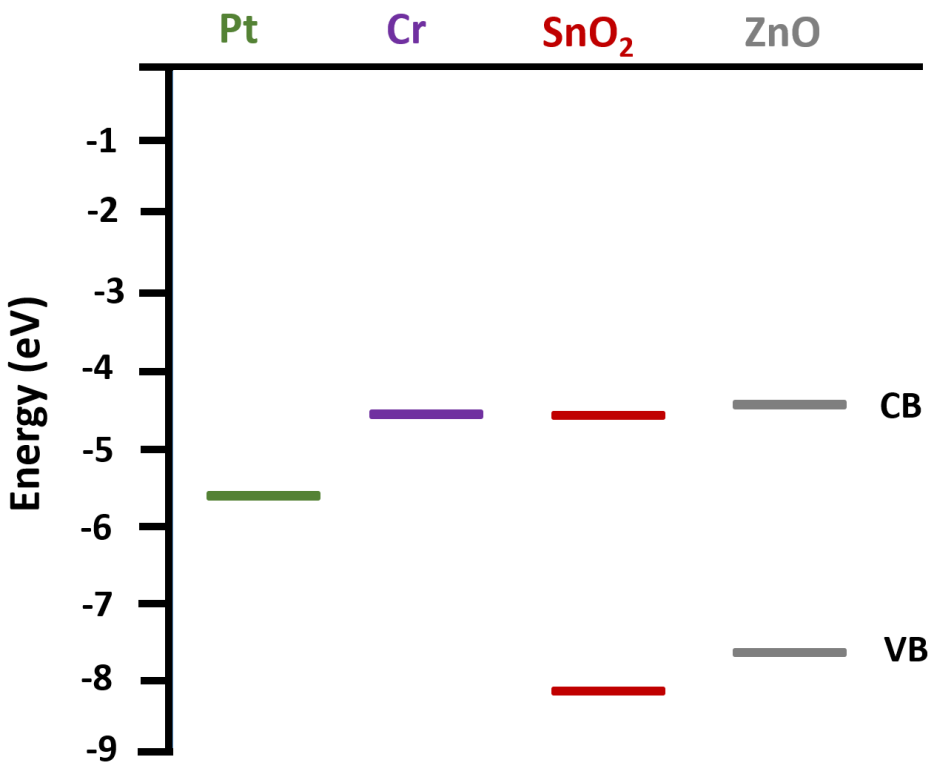

Figure 2.9: The electronic levels of ZnO, SnO_2 semiconductors and contact metal examples of Pt and Cr.

After the injection of charge carriers into the semiconductor, these carriers should travel from the source to the drain electrode of the TFT as the drain current I_D. The transport of charge carriers in the semiconductor film is controlled by a few factors including the mobility of these carriers and the charge traps. The level of purity and crystallinity of the semiconductor influences the carrier mobility (μ). A highly ordered crystalline semiconductor results in high carrier mobility whereas in poly-crystalline semiconductors the grain boundaries act as trap sites and result in a reduction in mobility[63].

When an electric field is applied across the semiconductor, charge carriers will move in the direction of the applied field 'drift'. The average drift velocity of carriers per unit of electric field gives the mobility of charge carriers (μ)[63] as shown in equation 2.10

$$v = \mu E \qquad 2.10$$

Where v is the drift velocity, E the applied field.

The units of electric field mobility of charge carriers μ, is quoted in $cm^2/V.sec$.

2.5 TFT Semiconductors

Over the years several semiconductors have been used in thin film transistor technology. The first TFT was Cadmium Sulfide CdS TFT, then followed by Cadmium selenide CdSe TFT in the early 1970s. Utilizing both films gave a high electric mobility (above 40 $cm^2/V.s$). However, these TFTs were not applicable for large scale processing[64]. The advent of Si based semiconductor films in TFTs in the period 1980s-1990s assisted the development of TFT technology and also commercializing them in the technology of flat panel active matrix liquid crystal displays (AMLCDs). Both amorphous and polycrystalline silicon were engaged, as they are suitable for large scale processing. Poly-Si requires a very high growth temperature of up to 1000 ℃ and results in high charge carrier mobility (above 100 $cm^2/V.s$) whereas amorphous silicon requires a lower process temperature and has very low mobility (less than 1 cm/V.s)[42]. Nevertheless, the above mentioned TFT materials require expensive fabrication techniques including a very high vacuum deposition environment such as Plasma-enhanced Chemical Vapor Deposition (PECVD) and Low Pressure Chemical Vapor Deposition (LPCVD).

In recent years, organic films have drawn more attention as TFTs for their unique properties. Organic thin film transistors OTFT have a simpler fabrication process than other semiconductors principally due to solution processing, as there is no demand for high temperature (normally all done below 200℃). Also, organic films can be fabricated on a range of flexible substrates, including plastics and even paper substrates[41]. OTFTs are involved in multiple applications such as flexible displays and sensors. Generally, the charge-carrier mobility in OTFTs is higher than

that for a-Si (around 10 $cm^2/V.s$)[42,65]. However, the poor stability of OTFTs in air remains a considerable challenge[42].

Other semiconductors in the TFT field are oxide semiconductors which are considered an important step forward in TFT developments due to their improved performance in several aspects in both amorphous and crystalline phases[64]. Common metal oxide semiconductors that have been utilized in TFTs are indium–gallium–zinc– oxide (IGZO), znic oxide (ZnO), indium oxide In_2O_3 and tin oxide SnO_2 for a range of application include in CMOS technology, displays and sensors[43,66,67]. These semiconductors provide high carrier mobility, are transparent and make more stable TFTs devices. High mobility can be reached even in the amorphous phase[66]. For instance at the same level of crystallinity of both materials, ZnO TFT's give a higher mobility than Si based TFTs[42,68]. The process of fabricating oxide semiconductors is very different to the expensive instrumentation that used to produce highly crystalline films as often cheap solution process methods are used to achieve polycrystalline films[66].

In this work, the solution processed metal oxide semiconductors of SnO_2 and ZnO were used in WGTFTs. Both semiconductors will be described in detail in (2.4.1).

2.5.1 Solution processed inorganic Semiconductor

Generally, there are two types of solution processing used for semiconductors. Firstly, the semiconductor is fully formed by previous chemical synthesis and is then molecularly dissolved in an organic solvent to be processed as semiconducting films without any chemical reaction. This processing is widely used for semiconducting (conjugated) organic polymers and nanoparticle semiconductor inks. Secondly, precursor route inorganic semiconductors that are processed from appropriate dissolved salts. This precursor undergoes a chemical reaction during the deposition to result in a semiconducting film.

Different solution precursor techniques used to deposit inorganic semiconductors rely on different procedures to produce the semiconductor film. For example spray pyrolysis[69,70,71] (more details in 4.3.1), sol-gel[72,73], spin-coating[74,75] are solution processing methods that have been reported for processing metal oxide semiconductors.

In this project, we work with solution processed metal oxide semiconductors SnO_2 and ZnO, prepared by chemical spray pyrolysis. More details about the structure and properties of both will be discussed in 2.4.1.1 and 2.4.1.2 below:

2.5.1.1 ZnO

Zinc Oxide (ZnO) is a binary II-VI semiconductor compound that has been utilized in many electronics and optoelectronics applications due to its advantageous properties. For instance, ZnO holds a direct and wide band gap (3.37 eV, figure 2.9) with a large exciton binding energy of 60 meV [76,77]. Also it has a high electron density[78] of 10^{21} cm^{-3} and is resistant to light and other radiation[79]. ZnO is also non-toxic and can be inexpensively processed from solution[80].

The most common and stable ZnO at ambient atmosphere is a hexagonal form with a wurtzite crystal structure, as illustrated in figure 2.10. In such a ZnO structure each Zinc ion (Zn^{2+}) is surrounded by four Oxygen ions (O^{2-}) and similarly each oxygen ion is surrounded by four Zinc ions[76].

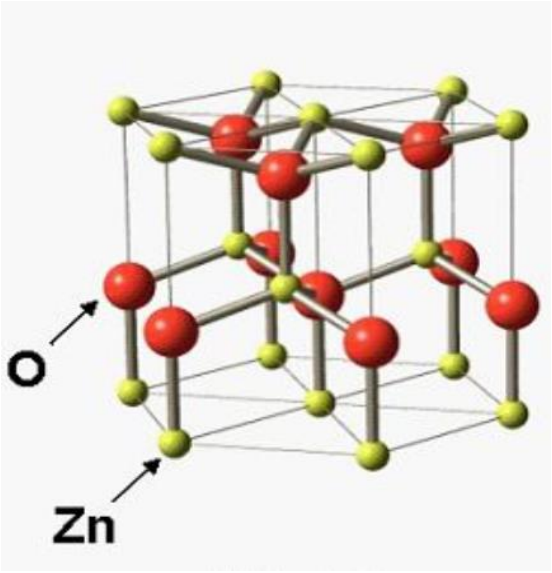

Figure 2.10 : The wurtzite crystal structure of ZnO [81].

Albeit stoichiometric, ZnO should be an intrinsic (undoped) semiconductor, practically prepared ZnO is usually found to be unintentionally n- doped. The probable reason for this is due to intrinsic defects in ZnO. These defects such as oxygen vacancies and zinc interstitials, cause a variation in stoichiometry[82]. Another reason could be the diffusion of Hydrogen during the ZnO growth, as H exists in almost all the growth methods. Also, H has the ability to perform as a shallow donor[80]. Conversely, p-type doping of ZnO can be achieved by deliberately adding related dopants for example[83].

In 1968 the first attempts to prepare ZnO TFTs were reported, however they exhibited poor performance[84]. Decades later, in 2003 a transparent ZnO TFT was achieved by Hoffman et al[85] . In the same year Nomura et al. reported a transparent ZnO TFTs with a high mobility of 80 $cm^2/V.s$ which was deposited by pulsed laser deposition technique (PLD) [86].

In 2007 a solution processed ZnO TFT was achieved with good stability and a high mobility of 5.25 $cm^2/V.s$[87] compared to organic solution processed semiconductors but still lower than crystalline ZnO films prepared by vacuum deposition processes. Zinc acetate ($Zn(CH_3CO_2)_2$) was dissolved in an organic solvent and then underwent a thermal conversion reaction to form a ZnO film[87]. Different precursors were reported in the preparation of ZnO films by spray pyrolysis including Zinc chloride ($ZnCl_2$), Zinc acetate (ZnAc) and Zinc nitrate ($Zn(NO_3)_2$) and each precursor related to specific properties of the film produced [88]. Comparison of ZnO films from different precursors dissolved in DI water as a solvent, a clear variation was found in the crystallinity and transparency level, $ZnCl_2$ shows better crystallinity while a ZnAc prepared film is more transparent[88].

Generally spray pyrolysis ZnO films have a poly-crystalline nature, consequently the electron mobility is lower compared to crystalline films produced for example by pulsed laser deposition 110 $cm^2/V.s$ [89]. Nevertheless, sprayed ZnO with (Li) doping show a high mobility of 85 $cm^2/V.s$ as reported by Adamopoulos *et al* [90,91].

A precursor-route water gated ZnO TFT was first reported in 2012 by Al Naim [92]. The water gating of ZnO TFTs permits them in the platform of sensing analytes in water as in [93,94].

2.5.1.2 SnO_2

Tin Oxide SnO_2 is a wide band gap (3.6 eV) semiconductor from group IV. SnO_2 has been exploited in a number of important applications including gas sensors, catalysis, and transparent conductors due to its good qualities of high transparency, electric conductivity and electrochemical properties [95,96] . Other advantages of SnO_2 are that it can be easily processed from solution and at relatively low temperature < 200 ºC, displays superb chemical stability and UV radiation resistance[97]. SnO_2 is an intrinsically n-type semiconductor as a result of the presence of defects. These defects perform as donors and are generally oxygen vacancies or interstitial tin atoms [43,95]. Unlike some other metal oxides, stable and high quality p-type doping has been achieved for SnO (another tin oxide but less stable than SnO_2) this mainly develops from Sn vacancies[43]. SnO_2 has rutile-type tetragonal structure with a unit cell that consists of two tin and four oxygen atoms[95,98] as shown in figure 2.11.

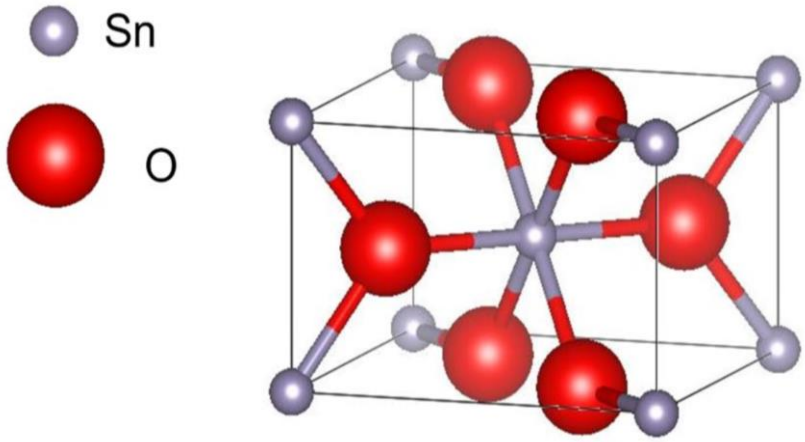

Figure 2.11: The crystal structure of SnO_2 [98].

Although ZnO is now more commonly used in TFTs, SnO_2 was first proposed for TFTs in 1964 even before ZnO[99,100] where Klasens and Koelmans proposed the use of evaporated SnO_2 on the glass substrate with Aluminium as a gate, source, drain electrodes and Aluminium oxide (Al_2O_3) as gate insulator[43,99]. Following that in 1969 a SnO_2 TFT was fabricated by Aoki and Sasakura, but this TFT suffered from some drawbacks. It worked in depletion mode and could not turn off, and saturation of the drain current could not be reached[101]. In 1996, improved performance of SnO_2 TFTs (depletion mode) was reported, the SnO_2 film was prepared by pulsed laser deposition, with

an electric mobility of 5 cm^2/V.s and on/off current ratio of 2 [102]. SnO_2 TFTs in enhancement mode was achieved in 2004 [103] with a good on /off ratio of 10^5. More recently, an increasing number of SnO_2 TFTs were investigated with different preparation methods of the SnO_2 films, including high electric mobility TFTs [104,105,106]. Improvements in the electric performance of SnO_2 TFTs especially helped to achieve lower threshold voltage and higher electron mobility, electrolyte gating boosted the performance of these TFTs as reported in[107,108,109].

Of particular relevance to this thesis, are SnO_2 TFTs prepared by spray pyrolysis which have been reported and exhibited good electrical performance[110,111]. In addition, as the water gating of SnO_2 has not been reported before in literature, it will be investigated in this project.

2.6 Electrolytes as Gate Media in TFTs

High specific capacitance insulators are very desirable in field effect transistors as this is linked to the beneficial properties of low threshold voltage V_{th} and high electric mobility μ, as shown from equations 2.8,2.9 and from equation 2.2. The specific capacitance depends on insulator thickness and the dielectric constant. An electrolyte is a liquid (or solid) material with free mobile ions[46]. For example, by dissolving salt (e.g. NaCl) in a polar solvent (e.g. water), the salt undergoes dissociation by forming positive and negative ions. The specific capacitance of electrolytes is found to be in the range of 1-10 μF/cm^2, which is larger for those of conventional dielectrics in TFTs, such as SiO_2 and polymeric insulators[112]. So, the use of electrolytes as gate insulating layer in TFTs enhances their performance.

An electrolyte's huge capacitance is caused by the formation of an electric double layer (EDL). This concept of EDL is discussed in 2.5.1 below.

2.6. 1 Electric Double Layers (EDLs)

When two electrodes with an applied voltage across them are introduced into the electrolyte, the ions in the electrolyte move to the surface of the electrode of opposite charge polarity. Thus, two layers of electrolyte ions are formed close to electrodes surfaces, these layers are known as electric double layers EDLs [46]. The EDLs always come in pairs where EDL of positively charged ions

(cations), that is formed near the negatively charged electrode called cationic EDL, and the EDL of negatively charged ions (anions) is formed near the positively charged electrode called anionic EDL (figure 2.12). EDLs have the advantage of high capacitance in the range of 1-10 μF [113] due to the EDL being ultra thin (thickness ≈ 1 nm) and a high electrolyte large charge density.

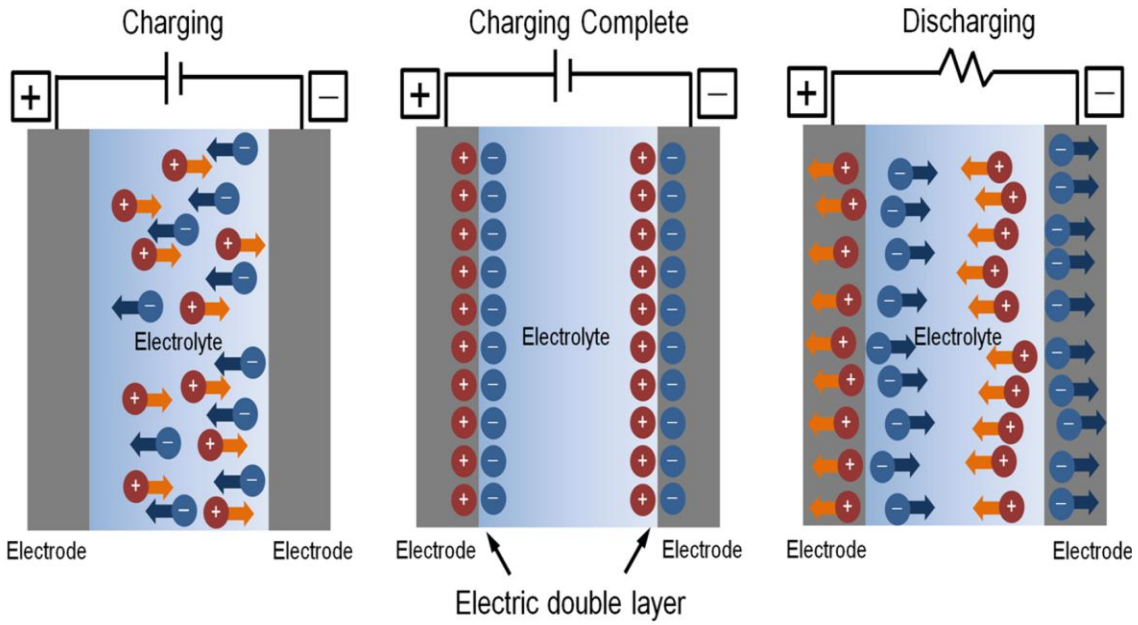

Figure 2.12: The charging and discharging of an EDL capacitor. [46] Charging when a voltage is applied, cations and anions move to the electrode surface until a balanced EDL is formed. Discharging when the applied voltage is removed.

To explain the EDL layer at the surface of the electrode in electrolyte solution three models have been proposed. An initial model was proposed by Von Helmholtz and called the Helmholtz model (figure 2.13 a). In this model a layer of counter ions forms near the electrode surface. Solvent molecules surround these ions and prevent them reaching the surface of the electrode. The small distance (on the order of nm) that isolates ions from the electrode surface is called the Helmholtz plane. Balancing of charge on the electrodes takes place by counter ions, and the electrical potential builds across this layer only, whereas the bulk electrolyte has zero potential. Nevertheless, this model fails to explain the capacitance of EDL, due to some limitations, such as disregarding the reliance of EDL capacitance on the electrolyte ion concentration and the electrode potential. Accordingly, modification of the Helmholtz model was proposed by Gouy and Chapman. This

model includes the effect of thermal motion of ions' distribution and electrostatic attraction. The Gouy and Chapman model suggests an exponential drop in the electrical potential from the electrode toward the bulk. As a result, two layers were formed; the Helmholtz layer and the diffuse layer (figure 2.13.b). However, the calculated capacitances from this model do not match with the experimental values, which is still a weakness of this model. Consequently, Stern developed the Stern model, which is a combination of the two previous models (figure 2.13.c). This model suggested that the balancing of the ions at the electrode-electrolyte interface is influenced by both the Helmholtz layer and the diffuse layer (not only Helmholtz layer). Therefore, the electric potential firstly drops at the outer Helmholtz plane and afterward drops exponentially in the diffuse layer on the way to the electrolyte bulk, whereas the diffusion layer width increases with decreasing ion concertation[46].

From Stern's model and to find the total capacitance of EDL, which mathematically is two capacitors in series[114] as shown in equation 2.11 below:

$$\frac{1}{C_S} = \frac{1}{C_{HZ}} + \frac{1}{C_{GC}} \qquad 2.11$$

Where C_S is the total capacitance of a single EDL, C_{HZ} is the capacitance of Helmholtz's layer and C_{GC} is the capacitance of the diffuse layer (Gouy-Chapman layer).

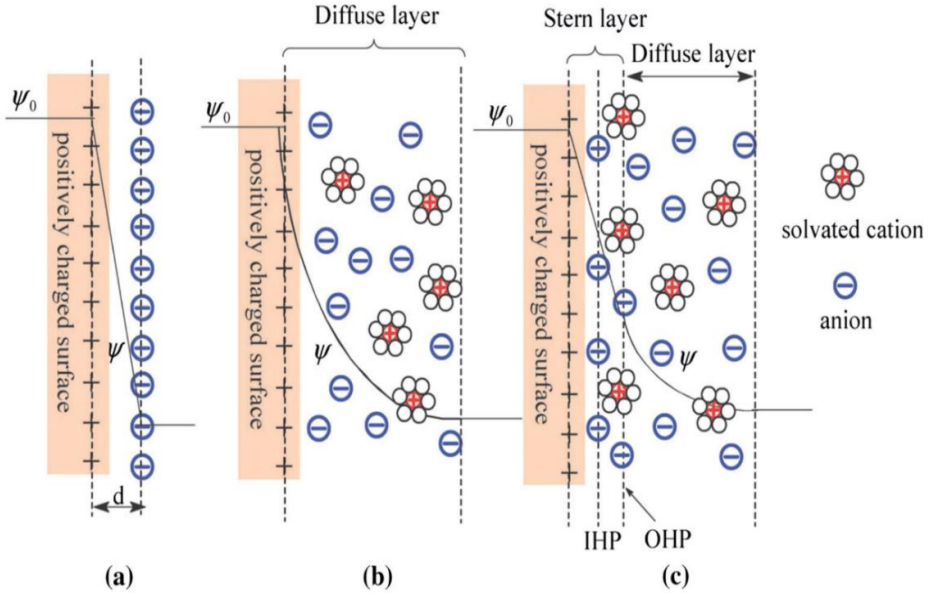

Figure 2.13: The three models used to describe the electrical double layer EDL: (a) the Helmholtz model, (b) the Gouy–Chapman model, and (c) the Stern model[46].

Electrolytes are considered DC insulators as the build up of EDL shields the bulk electrolyte from the applied voltage, so no current flows. Thus to measure the conductivity of an elelctrolyte AC current should be used to avoid the formation of an EDL. The applied DC voltage on any electrolyte is limited by the electrochemical window of this elelctrolyte, as beyond a certain voltage point, the electrolyte will decompose electrochemically, for example electrolysis of water occurs at 1.23 Volts.

2.7 Electrolyte- gated TFTs

This section displays examples of common electrolytes that are used in gating thin film transistors including aqueous electrolyte, as in this thesis, and other electrolytes reported in literature.

2.7.1 Examples of Electrolytes used as TFT Gate Media

Water:

Deionised DI water is considered a poor electrolyte in comparison with tap water, as the latter contains some dissolved salts. In DI water a small portion of ions are present due the auto-protolysis (auto-dissociation) of water molecules H_2O, by deprotonating to OH^- and then protonating by another H_2O molecule to H_3O, as in the following equation 2.12:

$$2\,H_2O \rightarrow H_3O^+ + OH^- \qquad 2.12$$

DI water builds EDL of sufficient capacitance to operate a thin film transistor, as reported by Kergoat *et al* in 2010 and the capacitance of such an EDL is about 3 µF/(cm^2)[34].

When salts, bases or acids solution are added to DI, the conductivity increases. For instance, the conductivity of DI water is 5×10^{-6} S/m or less, whereas in tap water it is 5×10^{-2} S/m[115]. If DI water is left in the atmosphere, some carbon dioxide (CO_2) will become dissolved and produce carbonic acid and that will increase the conductivity of the water[116].

In this work, we mostly used tap water as well as DI water, as tap water contains many ions at various concentration (appendix A6.1 and [117]), this leads to a higher capacitance of the related EDL in TFTs. For example, a 5wt% NaCl aqueous solution was compared to DI water, the EDL capacitance increased to10.6 μF/cm^2 at 0.5 volt[118].

Buffer Solution:

Buffer is an aqueous solution that contains both acids and bases. The buffer pH value is unaffected by adding a small amount of base or acid. One of the most common buffer solutions is phosphate buffered saline (PBS), which is used in many biosensing applications as it simulates the body fluids, its pH is 7.4. For example, standard PBS ions concentrations are very similar to those found in living organisms.

Since PBS comprises higher ion concentrations than that in DI water, higher EDL capacitance is achieved in electrolyte gated TFT. Accordingly, it results in a low threshold voltage and higher drain current [119].

Ionic liquid:

An ionic liquid (IL) is an organic salt which consists of mobile ions of both cations and anions with low melting point, below room temperature. Besides the high EDL capacitance, IL's possess some other advantages such as thermal and chemical stability, zero volatility, a wide electrochemical window (about 4.5 volt), and conductivity of 0.43 S/m[120]. As an example of an IL gating an organic TFT, a high capacitance of 30 μF/cm^2 (at 10 Hz) was achieved[57,121].

Other electrolytes were reported to gate thin film transistors including organic polar solvents (ethanol, acetone, methanol) [122] and polymer electrolytes as in[109,123]

2.7.2 Operation Principle of electrolyte- gated TFTs

From the electrolytes' discussion above, they show good performance to be utilized in gating TFT's, instead of conventional insulators, as they have low operating voltage due to the high

capacitance (EDL capacitance). Figure 2.14 shows the formation of a conducting channel in both dielectric and electrolyte TFT (n-type).

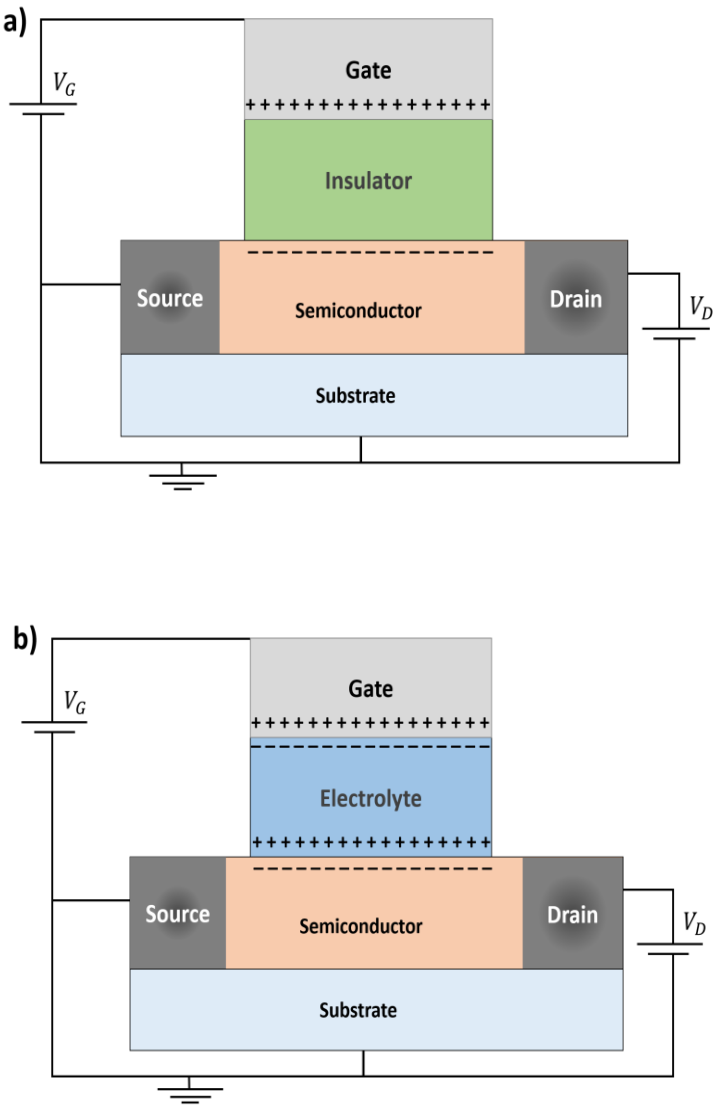

Figure 2.14: Construction of conduction channel in both a) Dielectric gated TFTs and b) Electrolyte gated TFTs.

In principle, the operation of Electrolyte Gated TFTs is the same as a dielectric gated TFT, whereas in the former an electric double layer is formed when a gate voltage is applied in electrolyte/gate contact and electrolyte/semiconductor interfaces[124] figure 2.14.

There is another operation mode of Electrolyte Gated TFTs and this mainly depends on the nature of the semiconductor being permeable or impermeable, and is called electrochemical transistors. In a permeable semiconductor, electrolyte ions under applied voltage could pass to the semiconductor bulk and dope it (figure 2.15). For example, some organic semiconductors show electrochemical doping when gated with electrolytes, which is called organic electrochemical transistors (OECTs) as in [124,125]. In this work we deal with transistors in field effect operation mode and not the electrochemical mode.

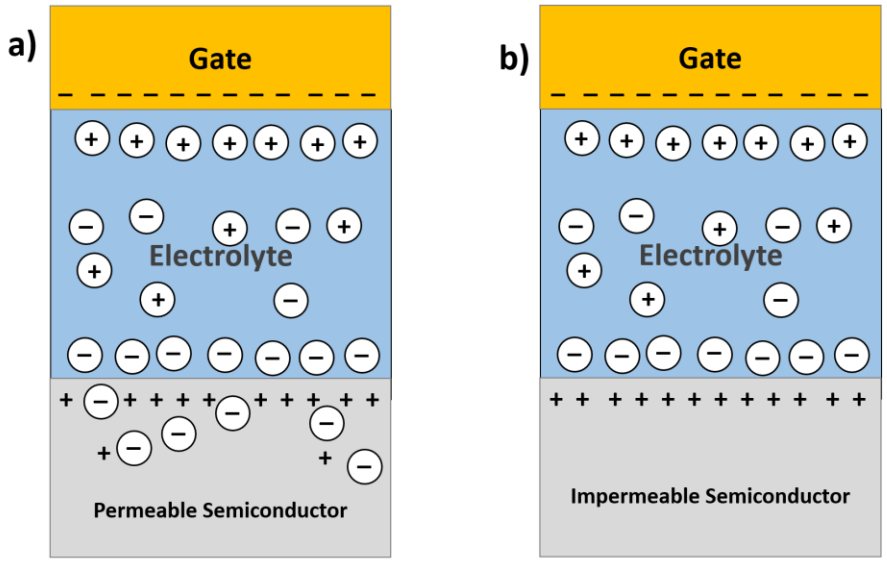

Figure 2.15 Diagram of electrolyte gated organic a) permeable b) impermeable TFTs.

Electrolyte gating of TFTs paves the way for these devices to contribute in sensing applications. In section (3.3), the use of water gated TFTs as sensors will be explained.

Chapter 3: Basic principles of potentiometric sensors for waterborne analytes

3.1 Introduction to potentiometric sensors

Sensors are devices used to investigate the presence and measure the concentration of specific analytes in different media. Sensing is controlled by a change in a specific property of the sensor. Generally, a sensor contains two main parts: a sensitizer (or receptor) and a transducer. In potentiometric sensors, a change in the electric potential is induced by the interaction between the analyte and the sensitizer [126,127]. Practically sensitizers are embedded in a phase transfer membrane, when sensitizers in such membranes bind with the analytes (e.g. ions) a membrane potential will be built up. The membrane potential is transduced via electric measurement by the transducer, where this potential is proportional to the analyte concentration. Potentiometric sensors have a number of advantages, these include low cost and energy consumption, portability, and simplicity[126,33]. The main two classes of potentiometric sensors are ion-selective electrodes ISEs and field effect transistors FETs. The phase transfer membrane will be discussed in (3.2) and examples of different potentiometric transducers will then be discussed in (3.3).

3.2. Phase transfer membranes

In potentiometric sensing the sensitizers are widely embedded in a medium, very commonly a plasticized PVC membrane, and the analytes are dissolved in a liquid phase medium. The interaction between the analyte and the sensitizer occurs when the analyte migrates from one phase to another, so such a membrane is called a phase transfer membrane. The term ion selective membrane is commonly used in the literature and refers to the same membrane, specifically when sensing ions, and to describe ion selective sensitizers the term ionophores is commonly used.

Practically, when a phase transfer membrane is placed in between two solutions of different concentrations of a specific analyte, analytes in both interfaces of the membrane/solution bind to the sensitizers and a potential difference is built up across the membrane. This potential is measured electrically as a variation in the voltage. One of these solutions has a known concentration (the reference solution) and the second one with an unknown concentration, the one to be measured.

3.2.1 Phase transfer membrane matrix

Various selective membranes matrixes have been reported, including glass membrane, crystalline materials and polymeric [128]. Polymeric based membranes are considered very practical and fit in different potentiometric transducers[127]. Membranes in this matrix are very flexible and a different class of sensitizers can be incorporated. The most common practical polymeric based membrane is PVC poly(vinylchloride), this membrane was adopted for this project.

PVC membranes typically consist of a high molecular mass polyvinyl chloride (PVC), sensitizer, and plasticizer, in some cases an ion exchanger is used. All of these components are dissolved in an appropriate solvent, very commonly tetrahydrofuran, a viscous solution is formed from this mixture that can be poured on a planar surface. This is left to dry and results in a thin film of PVC membrane that can be implanted in potentiometric transducers. Typically, plasticizer accounts for a relatively large proportion of the volume, about 66% whereas the PVC is nearly 33% of the whole content. The plasticizer added here is to improve the membrane mechanical properties and elasticity. In general, the plasticizer should be compatible with the PVC polymer, insoluble in aqueous solution, and non-toxic[129]. The commonly used plasticizers in the preparation of PVC membranes are ortho-nitrophenyloctyl ether (NPOE) which is used in this work, dibutyl phthalate (DBP), bis (2-ethylhexyl) sebacate (DOS), dioctylphthalate (DOP), and tris(2-ethylhexyl) phosphate (TEHP)[129].

The exploitation of selective PVC membranes in potentiometric sensors has been used for a long time and have shown good results. For example, PVC membranes have been used for ion sensing for various ions such, as Al^{3+}, Cu^{2+}, Pb^{2+} as reported in [130,131,132]. In addition to ions other molecules have been detected by such membranes, examples are ascorbic acid[133], and Trimipramine[134].

3.2.2 Common Sensitizers: Organic macrocycles

Sensitizers are very important as they are key components that control the sensitivity and the selectivity of the sensors. Organic macrocycle compounds are very common as classic sensitizers especially for ion sensing. These sensitizer ‘ionophores’ function by catching the target ions inside

their cavities, where they have different sizes of holes to match large variety of ions. Examples of these ionophores are calix[n]arenes and crown ethers, these will be discussed below in more detail.

Calix[n]arenes:

Calix[n]arenes are considered one of the most prominent groups of water insoluble ionophores. These macrocycles are easily synthesized from the reaction between formaldehyde and phenol derivatives[135]. The word calixarene was derived from the molecules shape where 'calix' (in Greek) refers to vase shape and the term 'arene' denotes the aromatic hydrocarbons in the molecules.

In Calix[n]arenes the [n] subscript denotes the number of ring units, for illustration see figure 3.1, this shows an example of calix[4]arenes, which has the smallest cavity size, and calix[6]arenes. As shown in figure 3.1 there are lower rim (phenolic) and upper rim (aromatic), both of these rims can be functionalized to be receptors[136].

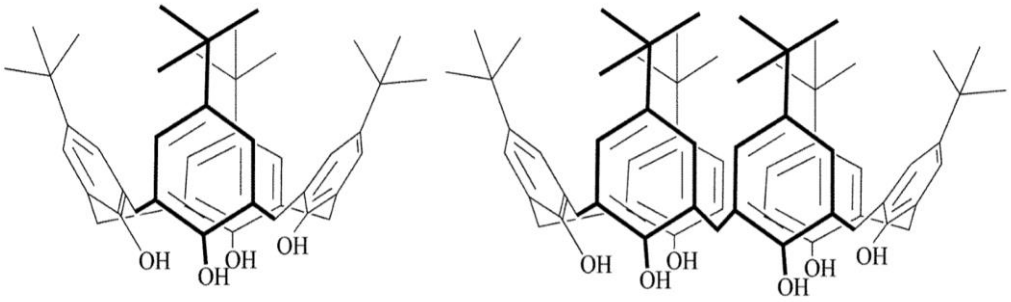

Figure 3.1: Structures of Calix[4]arenes(left) and Calix[6]arenes (right)[135].

Calix[n]arenes have been utilized in potentiometric sensors to detect different ions. Calix[4]arene shows good selectivity towards the small calcium cations, it has been applied in an ion selective electrode and water gated TFT[137,138]. In addition, calix[6]arene has been used in caesium sensing[139].

Crown Ethers:

A crown ether is a cyclic organic molecule that consists of a ring containing several ether groups. The central cavity in such a molecule acts as a binding site to analytes of matching size. Due to the presence of oxygen atoms on the crown ether cavity, a complex is formed with the target ions[140].

Figure 3.2 shows an example of the crown ether (18-crown-6), where 18 is the number of atoms in the ring and 6 is the numbers of O atoms. The ibenzo-30-Crown-10 has shown good selectivity toward potassium cations, as reported in [141,93,] whereas a 15-crown-5 cavity is suitable for sodium ions[142].

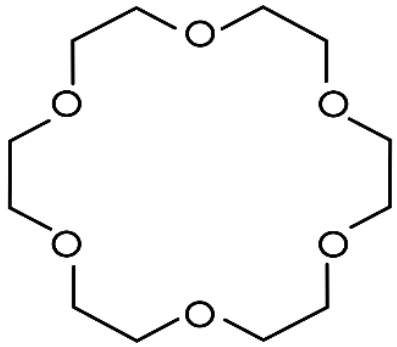

Figure 3.2: the chemical structure of 18-crown-6

It is worth to mention inorganic zeolites here, these are another type of receptor and have been used as ion and molecule adsorbents in different electrochemical sensors, including amperometric and potentiometric sensors[133] (e.g. ISE- ion selective electrodes). The novelty of zeolites incorporation in water gated TFT transducers will be discussed later on this thesis, in chapter 6.

3.3 Examples of potentiometric transducers

3.3.1 Electrochemical cells

An electrochemical cell or electrochemical transducer comprises two electrodes; a reference electrode and a sensing electrode (figure 3.3) both electrodes are inserted in two solution

compartments, the reference solution (with fixed analyte concentration) and the sample solution (a solution with an unknown analyte concentration to be identified). A sensitised membrane is normally attached to a sensing electrode and separated between the reference solution and the sample solution. As the sensing electrode in the electrochemical cell is responsible for the sensing process, this electrode is generally called the ion selective electrode or ISE. Because of the difference in analyte concentration in both sides of the selective membrane, a membrane potential is built up and as a result both electrodes give different potentials. This potential difference is proportional to the analyte concentration in the sample solution[127]. To measure the potential difference between the two electrodes the reference and the ISE, a voltmeter with high impedance is used, this should prevent the flow of current between these electrodes, but in reality a very small current near zero does pass through.

ISEs represent a large group of potentiometric sensors. In the early of 20th century the first ISE developed was a glass pH electrode[143], the field of ion selective electrodes advanced during the 1960's[144]. ISEs have been broadly reported for sensing[143] different ions.

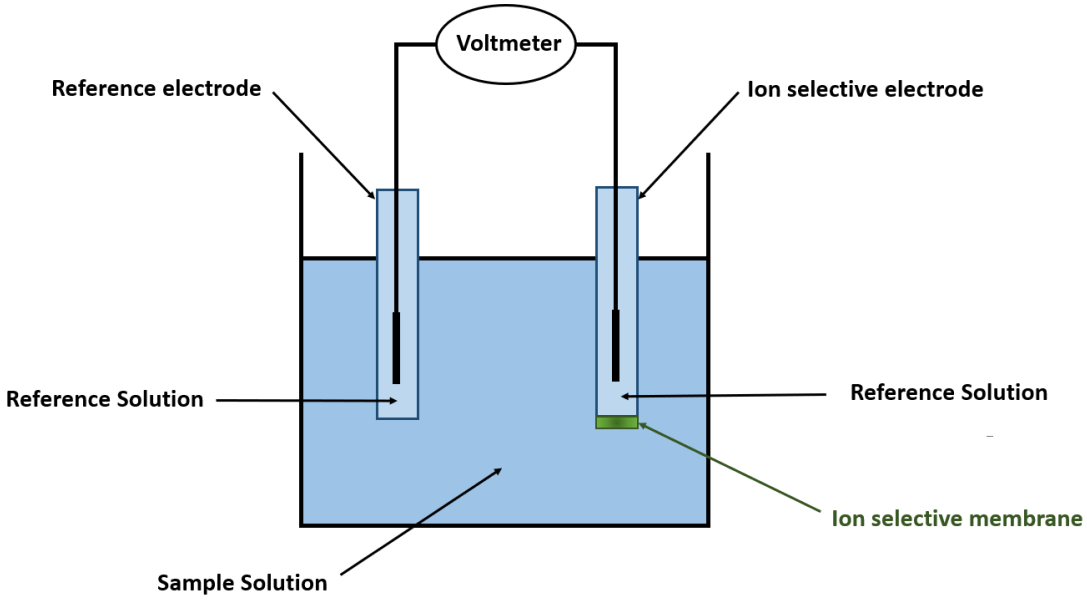

Figure 3.3: Schematic diagram of the electrochemical transducer.

3.3.2 Ions selective field effect transistor ISFET

The concept of an ion selective field effect transistor ISFET was introduced first by Bergveld in 1970[145,146]. The construction of the ISFET is very similar to the MOSFET (see 2.1.1) but with the gate electrode replacing by a solution connected to a reference electrode (figure3.4), this reference electrode can be considered as the gate electrode in the MOSFET[147].

The ISFET was initially used as a pH sensor, where the gate oxide SiO_2 surface potential changed from the interaction (protonation and deprotonation) between the oxide group on the surface and the ions in the solution (H^+, OH^-). Later on and to sense other ions in the same way, the gate material was modified, or a selective membrane was deposited on to the gate to allow the communication with the target ions in the solution, which results in a surface potential. Alteration of the surface potential caused by this mechanism will produce a change in the drain current (the threshold voltage), this variation in current is related to the number of ions in solution. In other words, the membrane potential is transduced by the ISFET to a current signal in a fully potentiometric mechanism, where no current is needed.

The advent of ISFETs brought attention to the potentiometric field as it offered great advantages compared to conventional ISEs, for example they can be smaller in size as no reference solution is needed, have shorter response time and a low output impedance[147].

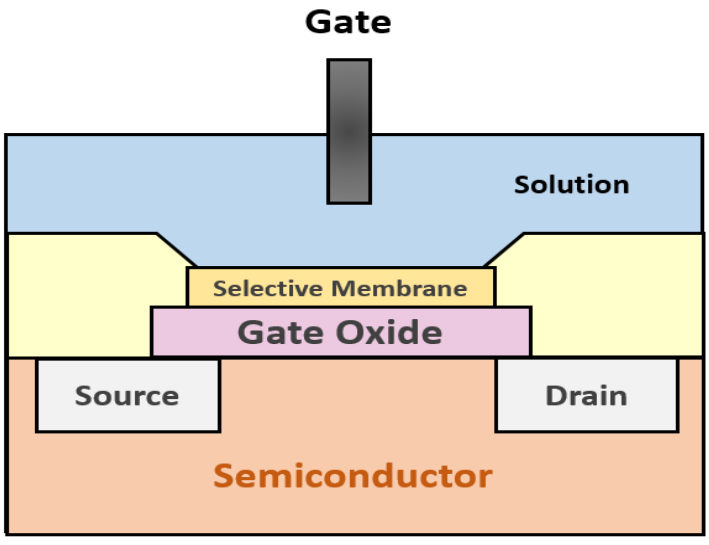

Figure 3.4: The structure of an ISFET transducer.

3.3.3 WGTFT

The Kergoat et al paper in 2010 demonstrating a water gated TFT, brought new sensing technology in the field of water sensors[34]. For a typical WGTFT (discussed in 2.6) to be a sensor, sensitizers are required to implant in its design. WGTFTs sensors do transduce the existence and concentration of analytes in the gating water to an electric signal that can be translated to changes in the electrical performance of the WGTFT. For illustration, when the analytes in the gating water bind to the sensitizers, which are incorporated in the construction of the WGTFT, the interfacial surface potential (where this binding occurs) will change; this results in a change in the threshold voltage of the WGTFT. The surface potential adds to the externally applied gate voltage, resulting in a shift of the threshold voltage. In general this interfacial potential is caused by ions binding or surface dipoles[138,32,148]. WGTFTS have been used to sense different analytes, this includes ions[93,148,149] and molecules such as dopamine and amine[32,150].

In WGTFTs, sensitizers are usually embedded in a plasticised membrane as explained in (3.2) and merged in different parts of the WGTFT architecture. In 2013 List-Kratochvil et al. successfully demonstrated a water gated TFT to detect Na^+ in water[148]. They used an organic semiconductor film and a design similar to the conventional electrochemical cell where an ion selective membrane is separated between the two reference and test solutions (figure 3.5). A benefit of this design is that the semiconductor film is not in contact with the analyte, which helps prevent any sensing interfering from the interaction between the semiconductor and the analytes. A simpler and more portable design of a WGTFT was done by Melzer et al in 2014[149] , in this work no reference electrode or solution were used. The ion selective membrane was coated on the metal gate electrode, and carbon nanotubes were used as the semiconducting film to sense the presence of K^+, Ca^{2+} and Cl^- (figure 3.6). This design demonstrated promising performance for a simple ion selective WGTFT. Earlier work was performed in 2013 using the same method of functionalizing the gate electrode to detect dopamine. In this case an electrolyte of PBS buffer as the gating media and an organic semiconductor film were used[32]. The analysis method for measuring the response of the WGTFT sensor used in this work, is adopted for the work in this thesis (see more about this method in (4.6)).

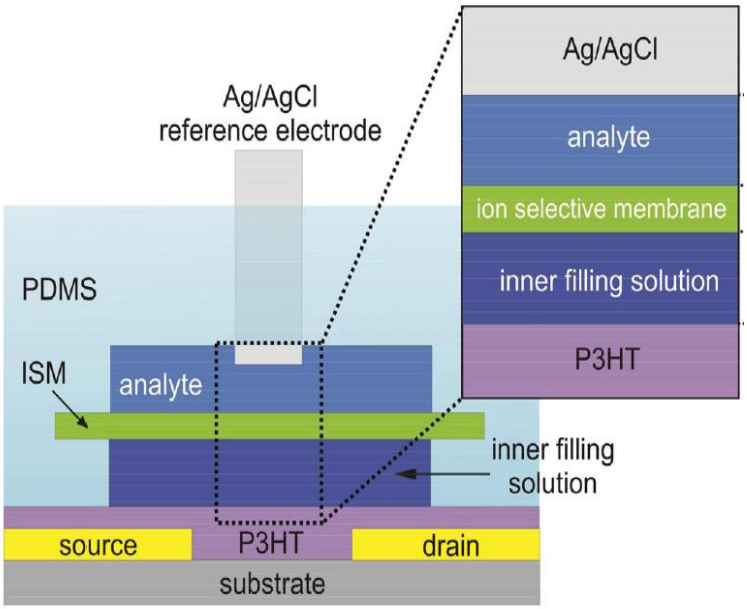

Figure 3.5: structure of an ion selective WGTFT designed by List-Kratochvil et al.[148].

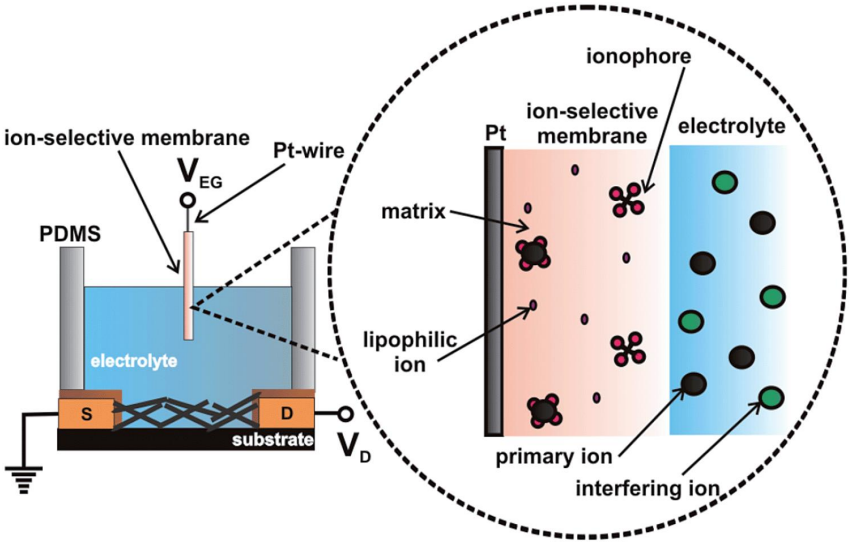

Figure 3.6 The construction of an ion selective WGTFT with ion selective membrane on the gate electrode designed by Melzer et al.[149].

Furthermore the semiconductor surface of ZnO in a WGTFT has been functionalized with molecular recognition elements and shows versatility in sensing analytes of different types

including ions (K^+) and molecules (glucose)[94]. In 2016 Althaqafi et al reported that sensitizers could be included during the processing of the semiconductor film without need for a sensitised membrane. In this work a calix[4]arene macrocycle as ionophore of Ca^{2+} cation was dispersed in the processing solution of P3HT and a good response was obtained in comparison to WGTFTs with an implanted ion selective membrane[148,149].

3.4 Sensor Response Characteristics

Regarding the response characteristics, potentiometric sensors usually follow the Nikolsky Eisenman law which is a modification of the Nernst law by introducing the limit of detection LoD. Whereas for optical sensors the response characteristics are controlled quantitively by a law derived from the Langmuir adsorption isotherm. Nevertheless, a Langmuir potentiometric sensor has already been reported[31] and also a Nernstian optical sensor[151]

3.4.1 Nernst Characteristics

The most reported response characteristics in the potentiometric sensors are Nernstian (they obey the Nernst equation) which is discussed below:

When a phase transfer membrane (PTM) for example an ion selective membrane (ISM) is inserted in between two solutions; the inner/reference solution with known analyte concentration and outer/test solution with an unknown concentration. When analytes in both compartments bind to sensitizers in an ISM, a potential is developed on both sides of the membrane, which leads to, a potential difference across the membrane. This potential difference is linked to the ionic activities of the both inner and outer solutions. The relation between ionic activity and the potential difference (voltage) is given by the Nernst equation[152] (equation 3.1):

$$E_m = \Delta V = 2.3 \frac{RT}{zF} log \frac{a_{analyte}}{a_{inner}} \qquad 3.1$$

where $E_m = \Delta V$ is the membrane potential, R *is* the ideal gas constant (8.314 J/Kmol), T is the temperature in Kelvin, *z* is the valency of the ion (e.g. z = 1 for

Li^+, 2 for Mg^{2+}), F is the Faraday constant (9.643×10^4 C/mol) and *a* donates the activity of the target ion in the analyte and the inner solution.

The term 2.3 $\frac{RT}{zF}$ is the Nernst slope and at room temperature of 25℃ (298 K) gives $\frac{59\ mV}{z}$, for z=1 Nernst slope is equal to 59 mV and for z=2 it gives 29.5 mV.

The membrane potential relies on the ion activity, which is actually a measure of the effective concentration of ions. Equation 3.2 below relates the ions activity to ion concentration by an activity coefficient γ[152]:

$$a = \gamma c \qquad 3.2$$

At dilute aqueous solutions the activity coefficient $\gamma = 1$, so $\frac{a_{analyte}}{a_{inner}} = \frac{c_{analyte}}{c_{inner}}$ and as the inner/reference solution is fixed in the structure of a sensor, equation 3.1 can be written as 3.3 or 3.4:

$$E_m = \Delta V = 2.3\ \frac{RT}{zF} \log\left(a_{analyte}\right) \qquad 3.3$$

$$E_m = \Delta V = 2.3\ \frac{RT}{zF} \log\left(c_{analyte}\right) \qquad 3.4$$

In the real world there is no ionophore that is selective for just one specific ion. Each ionophore prefers to interact with one ion more than other ions (interfering), and that can be described by the selectivity coefficient $K_{i,j}$ which is given by the following equation 3.5:

$$K_{i,j} = \frac{a_i}{(a_j)^{\frac{z_i}{z_j}}} \qquad 3.5$$

Where a_i and a_j is the activity of the target and interfering ions respectively, and z_i , z_j is the charge of the target and the interfering ions respectively.

For a selective ionophore, $K_{i,j}$ should be larger than 1, a value $K_{i,j}$ =1 means that such an ionophore responds equally well to both target and interfering ions.

When considering the interaction of interfering ions as well as the target ions a modification of the Nernst equation is applied to form a new equation called the Nikolsky-Eisenman equation[153] as shown in equation 3.6:

$$E_m = \Delta V = 2.3 \frac{RT}{zF} \log (a_i + K_{i,j}.(a_j)^{\frac{z_i}{z_j}}) \qquad 3.6$$

$$E_m = \Delta V = 2.3 \frac{RT}{zF} \log (a_i + a_{st})$$

$$\text{Where } a_{st} = K_{i,j}.(a_j)^{\frac{z_i}{z_j}} ,$$

$as\ a_{st} = c_{st}$ from equation 3.2, The concentration value of c_{st} represents the limit of detection (LoD) of such analyte sensors.

Figure 3.7 shows a diagram of the relationship between the membrane potential and the logarithm of ion concentration based on the Nikolsky-Eisenman equation. Generally, the Nikolsky-Eisenman equation is more realistic than the Nernst equation. In reality every electrolyte has interfering ions even DI water (due to DI water autoprotolysis). Also, at zero ion concentration the Nernst equation assumes an infinite potential (valid at high concentration only) where in the Nikolsky-Eisenman curve the potential flatlines at low ion concentration and the LoD can be extracted.

The utilisation of organic macrocycle sensitizers as an ISM in this family of sensors follows the Nernstian characteristics with LoDs in range of 100 nM-1µM [138,93,148].

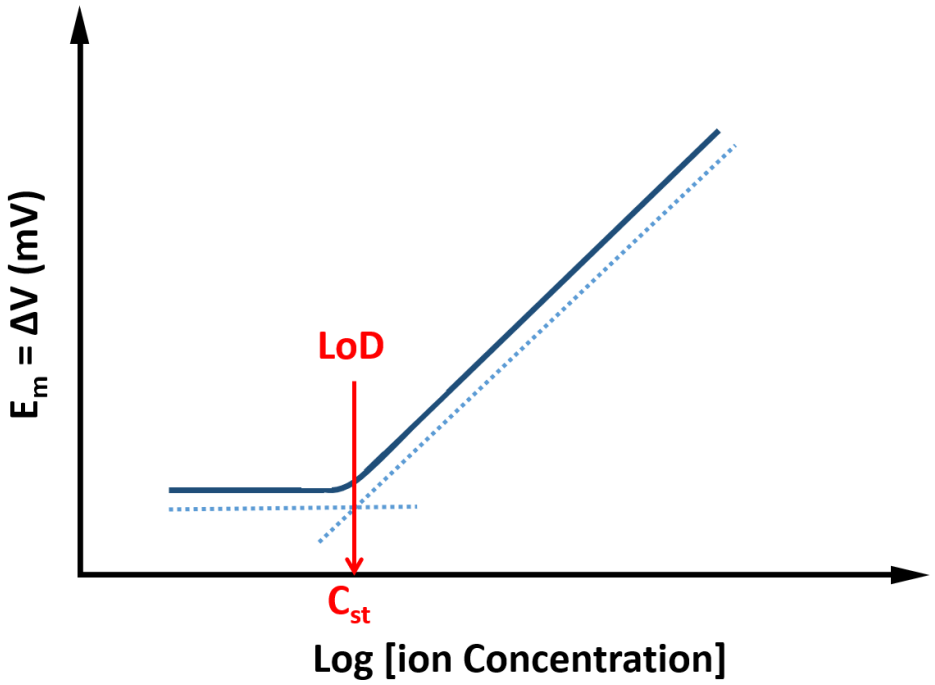

Figure 3.7: A diagram of the relationship between the membrane potential and logarithm of ion concentration based on the Nikolsky-Eisenman equation

3.4.2 Langmuir isotherm

Langmuir characteristics have been reported widely for the adsorption of different analytes using a number of sorbents such as zeolites and activated carbon[154,155]. In 1916 a theoretical equilibrium isotherm 'Langmuir Isotherm' was established by Irving Langmuir which related the number of molecules (in a gas or a liquid phase) adsorbed on a surface with the concentration of these molecules[156]. The adsorbing surfaces are homogenous with a finite number of equivalent binding sites for analytes to occupy whereas each binding site occupy one molecule only, leading to the formation of a monolayer of adsorbed species on the external surface of the adsorbent (figure 3.8).

Assuming that adsorbate molecules (A) and vacant sites on the surface (S), as in figure 3.8, when adsorption between A and S occurs the occupied site is called (SA) equation 3.7:

$$S + A \Rightarrow SA \qquad 3.7$$

Where the interaction between S and A can be reversable and irreversible depending on the nature of the bonding, and both of S, A have the units of concentration for example mol/ L or mg/g.

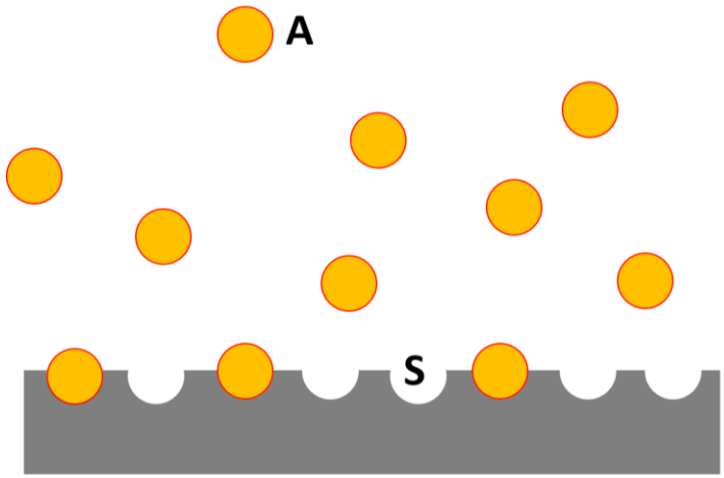

Figure 3.8: The formation of a monolayer when molecules A occupy the binding sites S on the surface.

The adsorption equilibrium constant of analytes/sensitizers can be written as:

$$K = \frac{[SA]}{[S][A]} \qquad 3.8$$

If θ is the fraction of the occupied surface sites where $0 < \theta < 1$, so $[SA]$ is proportional to θ and $[S]$ is proportional to $(1-\theta)$ where $[A]$ can be expressed as the solute's concentration c [157]. Therefore, the Langmuir equilibrium constant K can be written as in equation 3.9:

$$K = \frac{\theta}{(1-\theta)c} \qquad 3.9$$

By rearranging equation 3.9 we get the Langmuir isotherm equation 3.10:

$$\theta = \frac{Kc}{1+Kc} \qquad 3.10$$

A plot of Langmuir isotherm characteristics based on equation 3.10 is illustrated in figure 3.9.

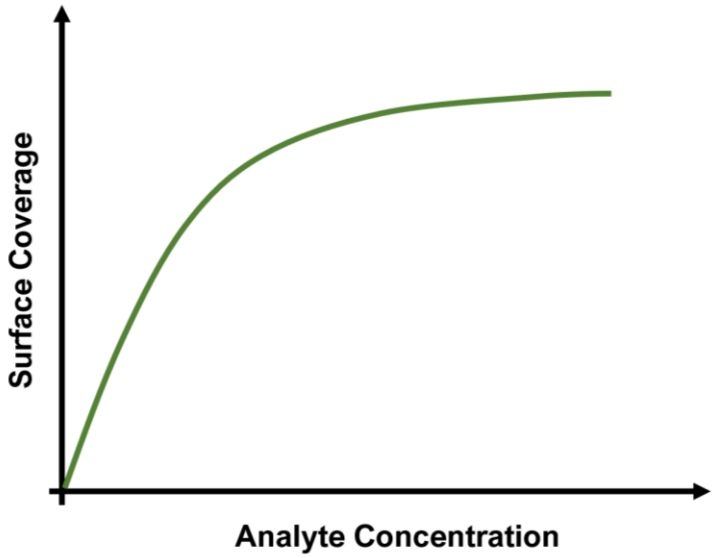

Figure 3.9: Schematic diagram of Langmuir isotherm characteristics.

At low molecule concentration c, a linear relation between θ and c is obtained where K is the slope of this line:

$$\theta = Kc \qquad 3.11$$

Whilst at high concentration, Langmuir equation converts to:

$$\theta = \frac{Kc}{Kc} = 1 \qquad 3.12$$

If the Langmuir isotherm characteristics are considered in a sensor where analytes bind to the sensitizers. At high analyte concentration when all sites on the surface are occupied, the Langmuir isotherm equation can be written by considering the maximum adsorption capacity X_{max} as in equation 3.13 where X_{max} is related to (S), the number of binding sites, which is fixed for each sensor[158].

$$\theta = \frac{X(c)}{X_{max}(c)} = \frac{Kc}{1+Kc} \qquad 3.13$$

$X(c)$ is the adsorption at a concentration c of the analyte.

An important parameter is the concentration $c_{1/2}$ where half of the sites are occupied by molecules, $\theta = 1/2$. The value of $c_{1/2}$ = 1/K where K can be extracted from the linearized form of the Langmuir equation which is Benesi-Hildebrand plot [159,160] by plotting 1/ $X(c)$ and 1/c. The equilibrium constant K is calculated from equation 3.14 below, where y is the intercept of the straight line with the y axis and m is the slope of this line.

$$K = y/m \qquad 3.14$$

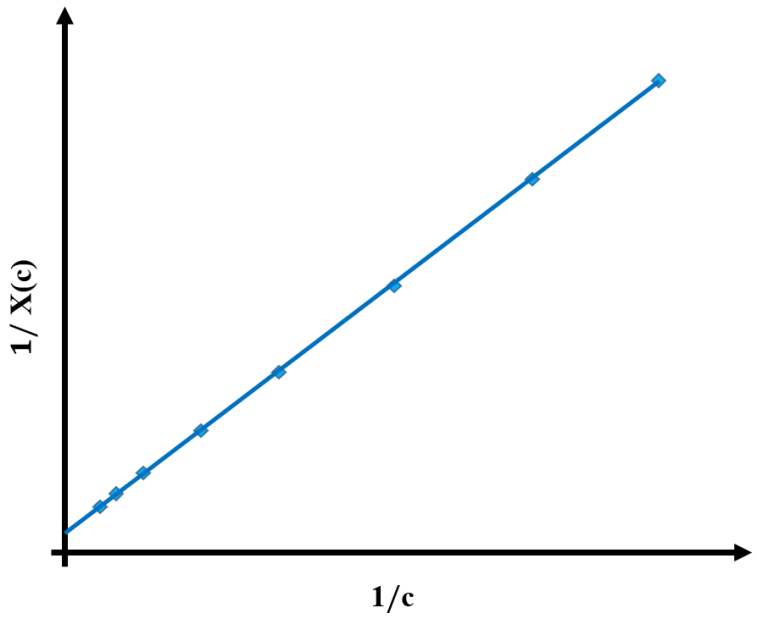

Figure 3.10: Diagram of a Benesi-Hildebrand plot

The limit of detection LoD in a Langmuir like characteristics sensor can be obtained by linearizing the response plot (similar to figure 3.9) where c on x-axis and $(1 + Kc).\ X(c)$ on the y- axis, and applying the three criterion method equation 3.15:

$$LoD = \frac{3\Delta b}{m} \qquad 3.15$$

Where Δb is the error in the intercept and m is the slope of the straight line.

3.4.3 Langmuir-Freundlich isotherm

Langmuir-Freundlich isotherm adsorption is also very common, it combines the characteristics of the Langmuir isotherm and the Freundlich isotherm[161,162] behaviour. Therefore the Langmuir-Freundlich isotherm is analytically very flexible and can cover various possible cases of adsorption[155,163]. This model is expressed using the following equation 3.16:

$$Q = Q_m \frac{(Kc)^\beta}{1+(Kc)^\beta} \qquad 3.16$$

Where Q is the amount of adsorbed analyte, Q_m donates the maximum adsorption capacity of the system, c is the analyte concentration, K is the adsorption constant and β is the homogeneity index.

For a homogenous material β is equal to 1, when heterogeneity of the material increases β decreases (β <1)[163]. So, at β =1 equation 3.16 becomes:

$$Q = Q_m \frac{Kc}{1+Kc} \qquad 3.17$$

Equation 3.17 at a homogenous surface is the same as the Langmuir equation.

In general, Langmuir isotherm and Langmuir-Freundlich isotherm models have been reported for a number of potentiometric sensing of molecules as in [150,31,164] not yet for ions, but an electrochemical transistor gave Langmuir like response with ions, as reported in [165]. In this work the sensing characteristics follow these two models for different analytes including ions, as will be shown in chapter 6,7,8.

Chapter 4: Thin Film Transistor (TFT) Fabrication and Characterization

This chapter is divided into two parts. The first part describes the fabrication of WGTFTs, including the preparation of the contact substrates (4.1, 4.2), thin film deposition (4.3) and design of the two chamber module for the WGTFT, which is our sensing unit (4.4). The second part describes the different techniques we used to characterize WGTFTs, morphological (4.5) and electrical (4.6) characterization. Figure 4.1 below illustrates the fabrication steps of WGTFTs used in this work.

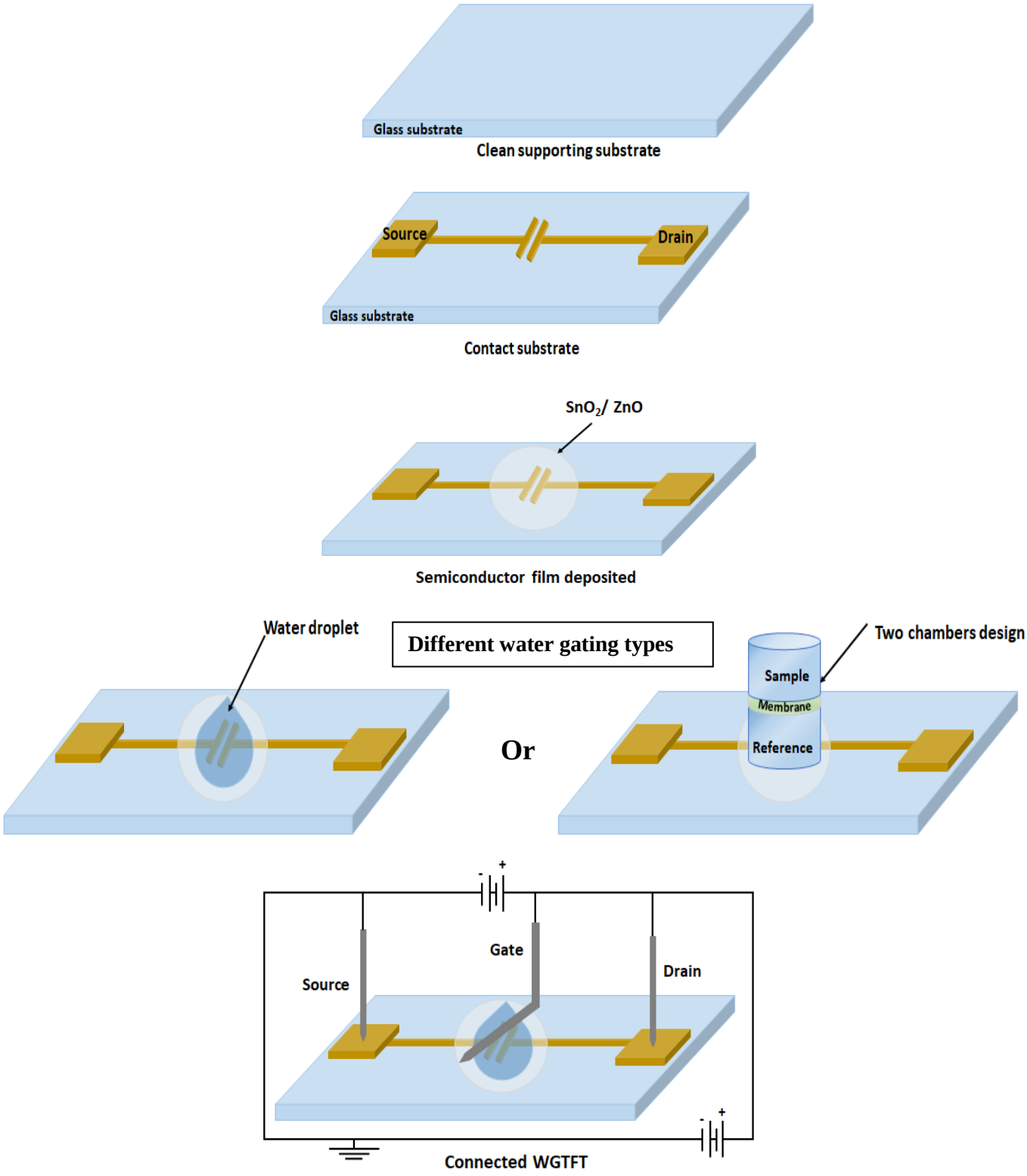

Figure 4.1: WGTFTs fabrication stages. (Starting from the top down).

4.1 Supporting Substrates

The base substrate for the WGTFTs used in this work were sourced from Ossila Ltd (order code S151). These substrates are ultra-flat glass slides with a size of 20 mm x 15 mm and have a thickness of 1.1 mm covered by a thin layer (20 nm) of SiO_2. Such substrates allow perfectly for the required transistor configuration of Top-Gate Bottom-Contacts Transistor.

4.1.1 Substrate Cleaning

Cleaning substrates before deposition of further layers is vital to avoid any defects in the TFTs. Poorly cleaned substrates could result in inappropriate or poorly performing devices. For example, poor adhesion of the contact metal leads to non-functional transistors.

In this work, the first processing step is to chemically clean the substrates prior to contact deposition. All the cleaning steps were carried out in a cleanroom whilst wearing clean gloves and handling the substrates using clean tweezers (cleaned by acetone). Substrates were arranged in a Teflon holder, they were visually inspected and sprayed with dry nitrogen gas. The Teflon holder has slots with the precise dimensions to hold substrates individually, allowing cleaning for both sides of the substrate (fig 4.2). Substrates were first cleaned by immersing the Teflon holder in a beaker filled with DI water with stirring. Afterward, the substrates were dried using dry N_2 gas. Organic solvents with sonication were used next to get rid of any organic residuals. The substrates were immersed in a beaker filled by acetone and then they were placed in a sonic bath for 5 min at a temperature of 55℃. After that, the substrates were removed and dried again using dry N_2 gas. Subsequently, the substrates were immersed in alcohol (isopropanol) and again placed in a sonic bath for 5 min at 55℃, then removed and dried using dry N_2 gas.

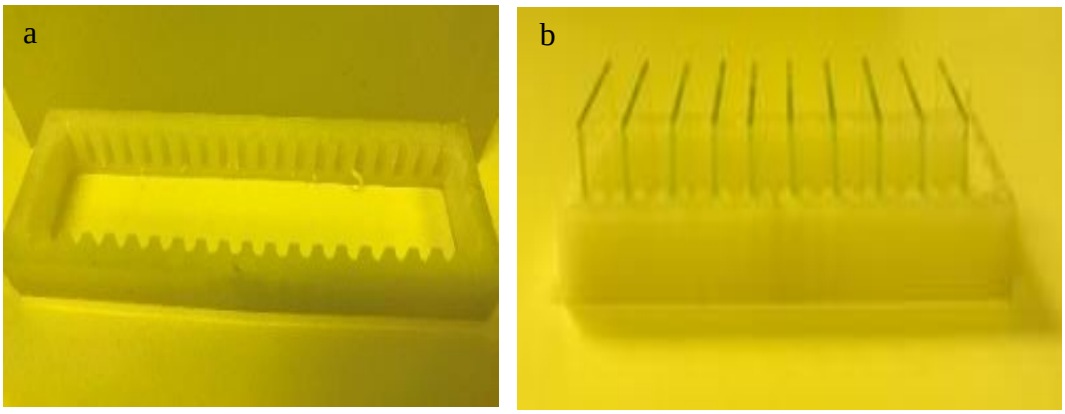

Figure 4.2: (a) The Teflon holder used for substrates cleaning. (b) Substrates loaded into the holder.

4.1.2 Ultraviolet Light Ozone Cleaning

After the cleaning process in 4.1.1, the supporting substrates were cleaned by ultraviolet light induced Ozone (instrument: Bioforce nanosciences), this was conducted to remove any remaining organic impurities. Ozone is considered a strong oxidizing agent, which can decompose any remaining organic residue. Practically, the clean substrates from 4.1.1 were placed in a clean Petri dish and inserted in the instrument chamber for approximately 4.5 min. This chamber is illuminated with intensive UV radiation in the wavelength range 185nm-254nm, to generate ozone from atmospheric oxygen.

After the process in 4.1.1 and 4.1.2, each substrate was kept in a small clean box ready for contact deposition.

4.2 Deposition Technique for TFT Contacts

To produce TFTs with source and drain metal contacts the technique of thermal evaporation was used. In section (4.2.1) the thermal evaporation technique will be described and in (4.2.2) the process we used to deposit the metals contacts will be explained.

4.2.1 Thermal Evaporation Technique

Thermal evaporation is a fabrication technique used to deposit thin layers of metal and low molecular weight materials under high vacuum by evaporating from solid state material (the source material) to a vapour, which is then deposited by condensation on the surface of the target substrate. The evaporation of the solid source material is achieved by passage of sufficient DC current to produce a very high temperature above the melting point of the material to be deposited using "resistive-Joule heating" (see fig 4.3). The high vacuum is generated by using a sequence of rotary and very high pumps, which results in a chamber pressure in the ranges of 10^{-5}- 10^{-8} Torr. Such a high vacuum deposition environment is important as it helps to eliminate any type of reactions between the evaporated atoms (or molecules) and the atmospheric gas molecules such an oxidation or collision and which would reduce the long mean free path for the travelling atoms. To determine the mean free path at a certain vapour pressure equation 4.1 is used:

$$\lambda = \frac{k_B T}{P\pi d^2\sqrt{2}} \qquad 4.1$$

Where λ is the mean free bath of atoms (or molecules), k_B is Boltzmann constant, T is the absolute temperature, P the vapor pressure and d is the diameter of the atoms (or the molecules)[166].

If we assume the diameter of the evaporating atom is about 0.4 nm and pressure is as low as 10^{-6} Torr, we get a mean free path of 44 m that means atoms can travel without collision for about 44 m. As the distance between the metal source and the substrates in the used thermal evaporator here is about 15 cm, this is ideal.

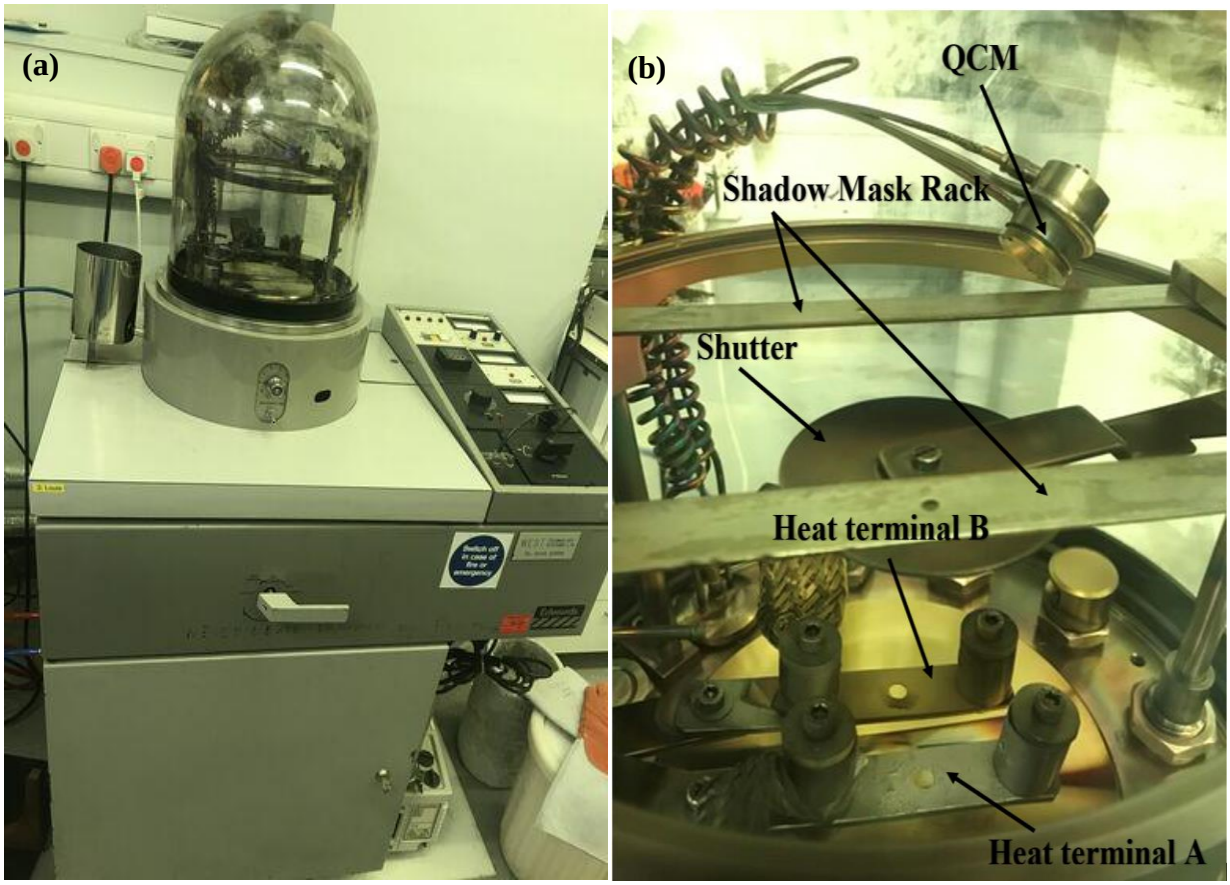

Figure 4.3: (a) The thermal evaporator photo (Edwards E306 Bell-jar). (b) The main components inside the evaporator.

There are other important parts of the thermal evaporator as shown in fig 4.3, for example the holder of the material to be evaporated. These holders come in different shapes (coils, boats and baskets) to best hold the source material and they are usually made from Tungsten (W) a metal with a very high melting point. In our work we used tungsten boats to carry the gold wire and for Chromium evaporation we used tungsten rods plated with chromium. These holders are connected to the heating source to pass high current to the metals[167].

The quartz crystal microbalance (QCM) was used to measure the thickness and deposition rate of the evaporated metal on the substrates' surface. Therefore, it is needed to be placed on the same level as the substrates holder. Fundamentally, a QCM is composed of a thin plate of quartz with metallic electrodes. When a mass is deposited on the surface of the QCM, this results in a shift in

the resonant frequency of the QCM, the change in resonant frequency can be related to the change in mass thickness. This relation is illustrated by Sauerbrey equation as below (equation 4.2)[168]:

$$\Delta f = -\frac{2 f_0^2}{A\sqrt{\rho_q \mu_q}} \Delta m \qquad 4.2$$

Δf, Δm are the changes in the frequency and the mass respectively. Where f_0 is the resonant frequency, A is the exposed area of the quartz crystal. ρ_q and μ_q are the quartz density and shear modulus and their values are ρ_q = 2.648 g/cm^3 and μ_q=2.947x10^{11} g/cm·s^2.

4.2.2 TFT Contacts Substrate Fabrication by Thermal Evaporation

An Edwards E306 Bell jar thermal evaporator was used for the fabrication of our TFT contact substrates. Before starting the process of deposition source and drain contacts we first prepare the substrates and the metals source and upload them to their holders in the thermal evaporator. We used a shadow mask (sourced from Ossila, order Code S151) that produces 5 pairs of source and drain contacts (this shadow mask is shown in figure 4.4). The cleaned substrates (from 4.1.4) were placed in the substrate holder, this holder is covered by a magnetic sheet and a metallic lid to firmly hold substrates. The shadow mask was then placed onto the other side of the substrates, which should be the SiO_2 coated side, followed by the shadow mask support piece for mechanical support of the thin shadow mask (appendix fig A4.1). Afterwards, all stacks of the shadow mask and the substrates were loaded into the thermal evaporator with the substrates and mask facing toward the metals to be evaporated. The metal sources used in the evaporation of the source/drain contacts were gold Au and chromium Cr. Because of the poor adhesion of Au on the glass substrates, we used Cr to solve the issue, as Cr has good adhesion for both Au and glass. As in figure 4.3, there are two terminals connected to the heating source in the evaporator A and B. A wire of Au of about 4 cm length was placed into a tungsten boat which was connected to terminal B, and a rod of tungsten coated with Cr was connected to terminal A.

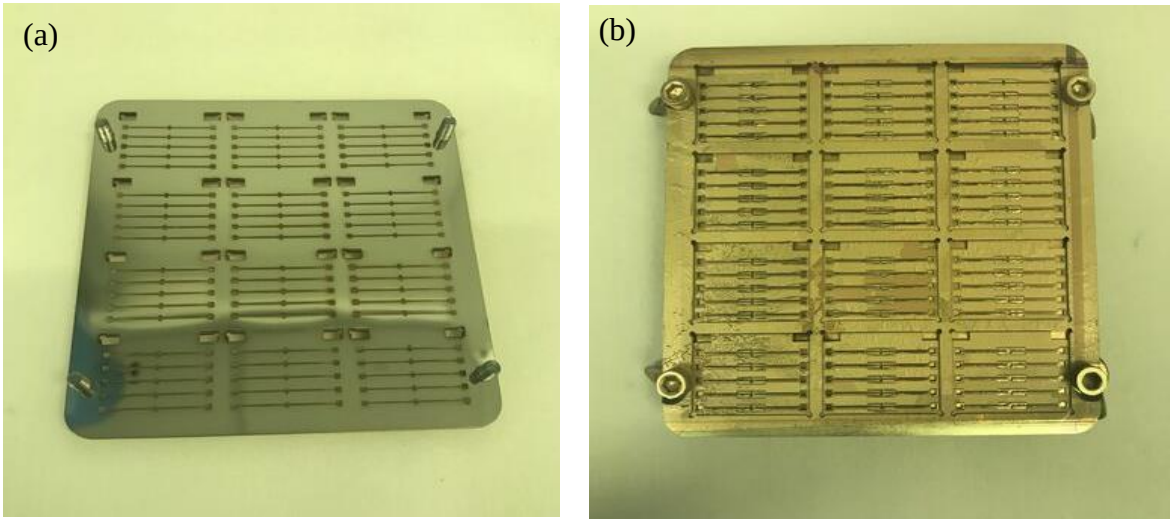

Figure 4.4: Photos of (a) The shadow mask. (b) The shadow mask stack

After that, the thermal evaporator jar was closed, the pumps then evacuated the jar and the pressure inside dropped, until it hit a base pressure of ~ 10^{-7} Torr. The current passing through terminal A was increased until there was sufficient current to heat Cr until it began evaporating (2.6 Amps for Cr and 2.1 Amps for Au). Before recording the thickness of the evaporated Cr, a steady evaporation rate needed to be reached, so a mechanical shutter was used to cover the substrates. A deposition rate of 0.2 A/s for Cr and 1 A/s for Au was used to deposit the metal layers. The film thickness was recorded using the QCM, a Cr thickness of 5-10 nm was enough to act as an adhesion layer. For the deposition of Au, the same process as in Cr deposition was followed whereas the desired Au film thickness was about 100 nm.

A TFT substrate after contact deposition is shown in fig 4.5 (a) along with a clear diagram of its geometry, with the actual dimension shown in fig 4.5 (b). The active area in the WGTFTs is the gap between the two horizontal lines referred to as “channels”. The width of channel W is equal to 1000 µm and its length L=30 µm and that gives a geometry factor W/L of 33.

(a)

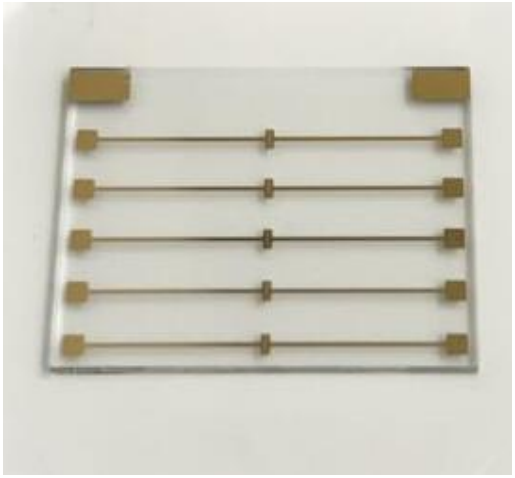

(b)

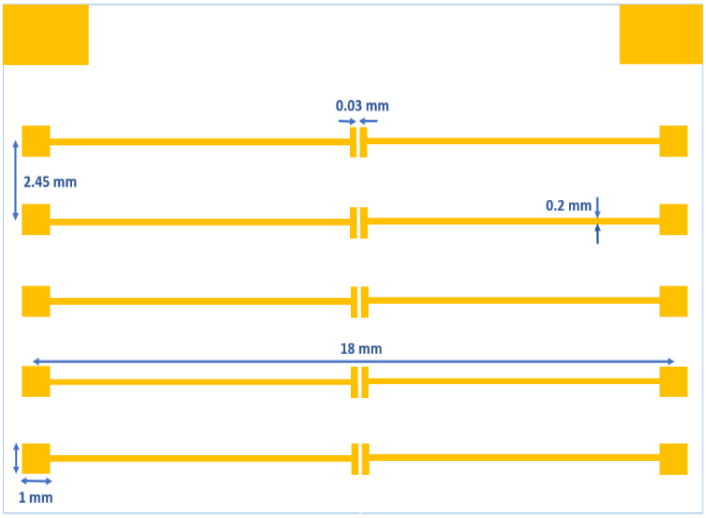

Figure 4.5: (a) Photo of the TFT substrate after the source/drain contact deposition. (b) The TFT geometry of the source/drain contacts.

Note that here we used Au as metal contacts due its resistance to corrosion and oxidation. As we prepare our semiconducting films by spray pyrolysis (next section), there are many advantages of Au over other metals such as Al and Cr that would form oxide layers under high temperature[169].

4.3 Deposition Techniques for Thin Film Semiconductors

Various deposition techniques are used to produce thin films of semiconductors based on the nature of the deposition process, which are mainly physical or chemical processes. Here we adopted a chemical deposition process that uses a solution, namely spray pyrolysis. In the next section 4.3.1, we will describe the spray pyrolysis technique in more details.

4.3.1 Spray Pyrolysis Method

Spray pyrolysis is a chemical process where a thin film of selected material is deposited by spraying a suitable precursor solution (the precursor is dissolved in a suitable solvent) onto a heated surface. The desired film is obtained after solvent evaporation and a subsequent pyrolysis reaction takes place[170].The spray pyrolysis approach can be applied to produce films of various materials

types to be utilized in several applications such as solar cells. For example, metals (e.g. Pd and Cu)[171,172], and metal oxides (SnO_2, In_2O_3 and ZnO) [173,96,174] have been prepared by spray pyrolysis. This method possesses numerous advantages in terms of devices fabrication. Mainly the cost of deposition due to the capability of depositing films using inexpensive equipment (figure 4.6) onto different types of substrates, no high quality substrates are needed nor a high vacuum atmosphere. Also, it makes possible mass production, as spraying can cover a large surface area. One advantage of spray pyrolysis over other methods is the ability to deposit films with specific properties by the optimization of the spraying conditions[175].

In principle the spray pyrolysis equipment involves a solution atomizer and a substrate heater with a temperature controller (fig 4.6). The atomizers can be ultrasonic waves, a high electric field or (as used in this work) compressed gas; in which the precursor solution is exposed to a stream of air to release droplets from the nozzle. The process begins with the formation of precursor droplets from the atomizer through the spray nozzle, which then fall onto a heated substrate. At this point these droplets coalesce and decompose to form a thin film on the hot substrate[176,177] Figure 4.6 shows the component parts used in spray pyrolysis.

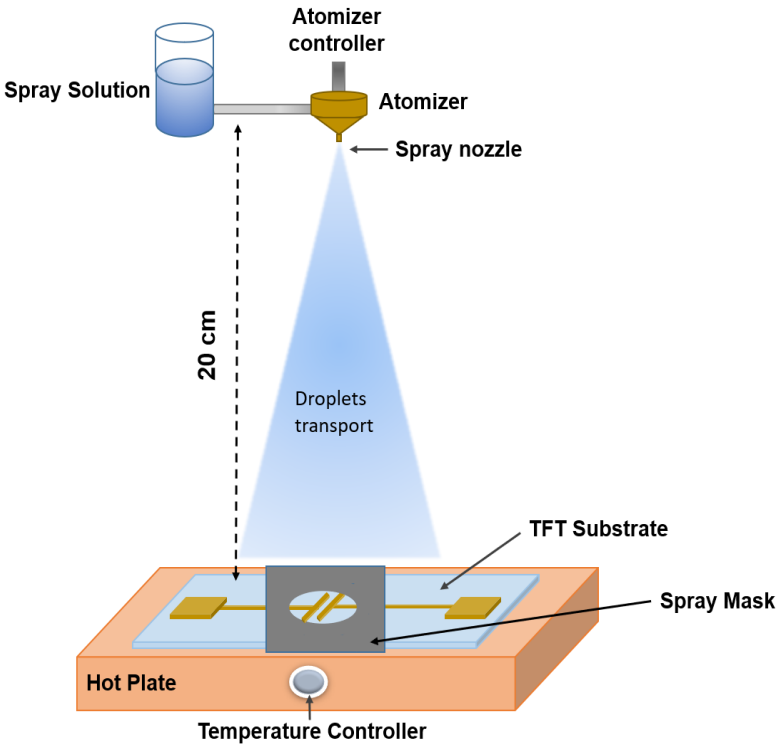

Figure 4.6: Schematic diagram of the spray pyrolysis process and equipment

To clarify the growth mechanism of a thin film made using the spray pyrolysis technique, four different processes occur to form a film from precursor droplets, as illustrated in figure 4.7.

These stages all depend on the substrate temperature (or on the droplet size at a constant temperature as in Figure 4.7.a). In stage (A) when the temperature is low, the droplet hits the substrate, solvent evaporates by forming a ring shape (coffee ring effect) and decomposition occurs. At intermediate temperature (higher than in stage A), the solvent in the droplet vaporizes to a dry precipitate which impacts the substrate and decomposes (process B). In process (C) the temperature is high, so as in (B) a dry precipitate is formed. These precipitates are vaporized near the substrate surface but do not decompose, instead they go through a CVD process. At even higher temperature than in (C), the dry precipitate in this case vaporizes and undergoes a chemical reaction in the vapor phase to form solid particles which deposit on the substrate surface (process D)[177,176,178.] Such processes can also occur at a constant temperature with different droplet sizes, as shown in figure 4.7.b.

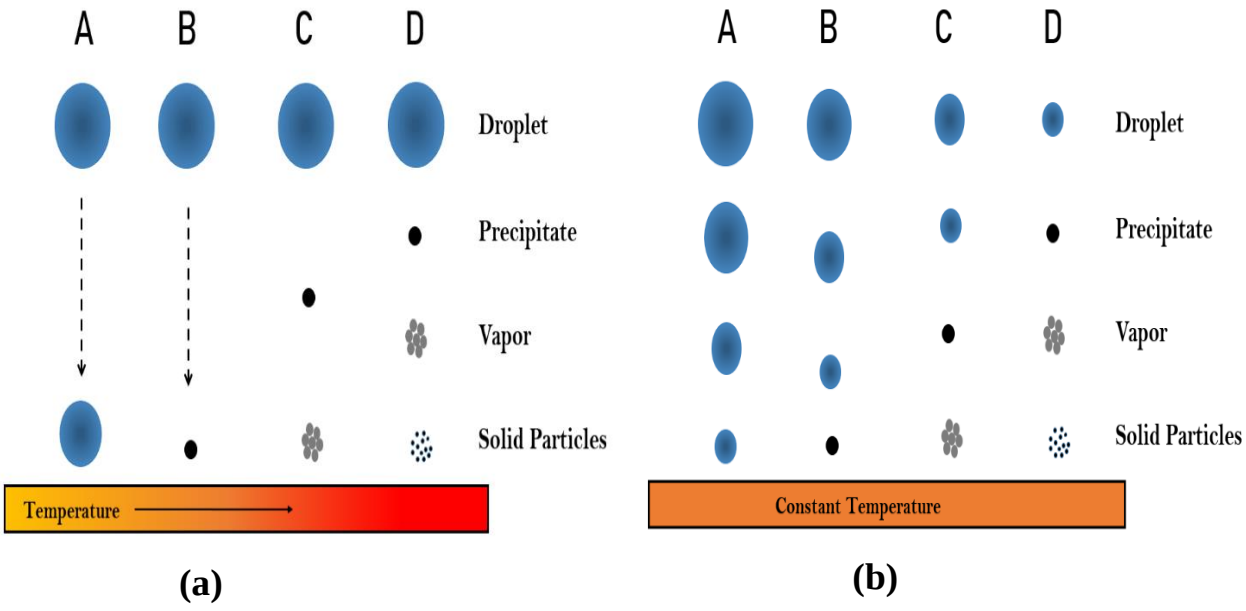

Figure 4.7: Diagram of the four deposition routes in spray pyrolysis process that occur when a droplet travels to a heated substrate. (a)The size of the initial droplet is constant, substrate temperature is variable. (b) The size of the initial droplet is variable, substrate temperature is constant.

As reported by Viguie and Spitz, films obtained from processes A and D are relatively rough. Films with excellent adhesion are formed by processes A and B. The deposition mechanism in D can also lead to films having a powdery appearance. The rare or not often seen process in sprayed deposited films is C, this is due to the low temperature to vaporize the precursor and also decompose the precursor before vaporization[176].

The process parameters have significant effects on the properties of the obtained films. The most important reported parameter is the growth temperature (substrate temperature). The influence of the substrate temperature seems to be apparent in the morphology, visible transmission, electrical properties, and crystallinity[176,179]. For example, ZnO films deposited from aqueous zinc acetate precursor at varied substrate temperature have some variation. By increasing the substrate

Figure 4.7: Diagram of the four deposition routes in spray pyrolysis process that occur when a droplet travels to a heated substrate. (a)The size of the initial droplet is constant, substrate temperature is variable. (b) The size of the initial droplet is variable, substrate temperature is constant.

temperature to 490 ℃, thinner films with a high level of light transmission were obtained[180]. In addition, at higher temperatures the films are more crystalline and homogeneous, and the grains are larger in size, leading to improved carrier mobility [181].

The final sprayed film properties can be altered by choice of the precursor solution. The main ways to do this are by altering the precursor salt used or the molar concentration of the precursor solution. A low concentration solution results in thinner, smoother and more transparent films in comparison with more concentrated solutions[182]. The most common ZnO precursors are Zinc chloride ($ZnCl_2$), Zinc acetate (ZnAc) and Zinc nitrate ($Zn(NO_3)_2$). When comparing between ZnO films from these different precursors with DI water as a solvent, a clear variation can be found in the crystallinity and transparency level, $ZnCl_2$ shows better crystallinity while ZnAc related films are more transparent[88]. The physical properties of each precursor solution listed above, specifically density (ρ), viscosity(μ), surface tension(σ), are found to clearly influence the properties of the final processed film[183]. Furthermore, for SnO_2 the use of films from pentahydrate tin chloride ($SnCl_4.5H_2O$) have lower resistivity than those from anhydrous tin chloride ($SnCl_4$)[184].

There are many other parameters such as solvent, air pressure and the addition of additives to the precursor solution. For example, films prepared from water have inferior optical transparency when compared to films sprayed from alcohol solvents[185]. Higher air pressure tends to give a smaller droplet size when spraying[176]. Additives and dopants influence the precursor solution too. For example, they can change the morphology of the film and other properties. For instance, a cracked film of TiO_2 can be changed to non-cracked by adding acetic acid to the precursor solution[176]. As acetic acid changes the precursor chemical properties and as a result the morphology of the obtained film changes[186]. In addition, the incorporation of Al in SnO_2 forms a smaller grain size and produces more resistive films[187].

In this work, SnO_2 and ZnO films were prepared by spray pyrolysis from chloride salt precursors ($SnCl_4.5H_2O$ for SnO_2 and $ZnCl_2$ for ZnO). An airbrush was used as a spraying tool with a 0.2 mm nozzle and an air pressure of approximately 1.5 bar. A hot plate was used as the heating source to heat the TFT substrates to a temperature of 400℃. A spray mask template was used, with film only deposited on the channel area of the TFT substrate. The spraying was performed in a number of puffs with intervals in between, afterward the substrates were left on the hot plate for 30 min allowing the film to fully decompose and convert chemically. All of these procedures were done in a fume cupboard using lab safety glasses, gloves and clean tweezers. The setup used is shown in figure 4.8 below.

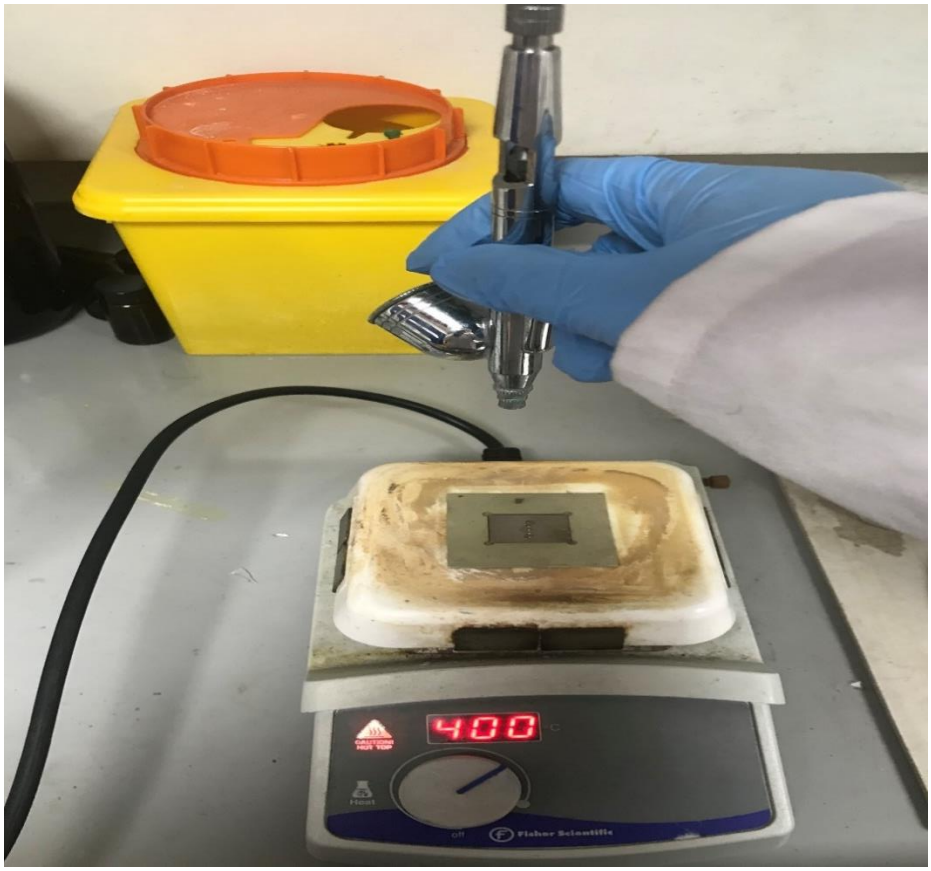

Figure 4.8: Photo of the setup used for spraying our TFT using solution precursors

Chlorides precursors were chosen here as they give the optimal film crystallinity, as reported[88] and widely used in sprayed films. The best molarity for the precursor solution when preparing SnO_2 for our application was 50 mM of $SnCl_4.5H_2O$, other higher molarity solution concentrations were tested. In the case of ZnO 100 mM molarity was used, as it very commonly used for the similar TFT applications[93],[188].

The decomposition of precursors to form the semiconductor film in both cases follows equation 4.3, 4.4 below[180,189]:

$$(ZnO) \qquad ZnCl_2 + H_2O \rightarrow ZnO + 2HCL \qquad 4.3$$

$$(SnO_2) \qquad SnCl_4 + 2H_2O \rightarrow SnO_2 + 4HCl \qquad 4.4$$

4.4 Two chambers design of WGTFT

The two chambers design consists of two units for the filling solutions. The lower compartment, which is in contact with the semiconductor film is filled with a reference solution and having a fixed concentration during the whole experiment. The upper compartment is filled with an analyte solution that can vary during the experiment. These two compartments are separated by a sensitizer-doped PVC membrane, as illustrated in figure 4.9. This design has been adopted in the potentiometric sensors field. Generally, such a design is implemented in the ion selective electrodes [131,132,130]. The paper by List-Kraatochvil et al. first demonstrated the two chamber design for WGTFTs [148], and they achieved remarkable results.

In this work, such a design was utilized in chapters 6, 7 and 8. Figure 4.9 shows a schematic of the design used. Two small pools each having a diameter of 5 mm and a depth of 5 mm were used. The lower pool was glued using epoxy to the TFT substrate over the channel area, then filled with the inner reference solution. The sensitised membrane was then glued to the lower side of the upper pool then both pools were held together in place. A small pressure is applied by hand to assure adhesion of the lower pool to the substrate, and also the membrane adhesion to the bottom of the upper pool after applying the epoxy. Note here, that the membrane thickness is very critical as thick membranes can block the gate voltage V_G communication with the semiconductor, this results in non-functioning devices, therefore the membrane thickness should be considered. Here a membrane of the thickness of 0.4 mm is used in chapter 6,7,8. The gate electrode, which is tungsten W in this work, was inserted in the upper pool, and a sample solution (with the analyte to be measured) was also filled in this pool.

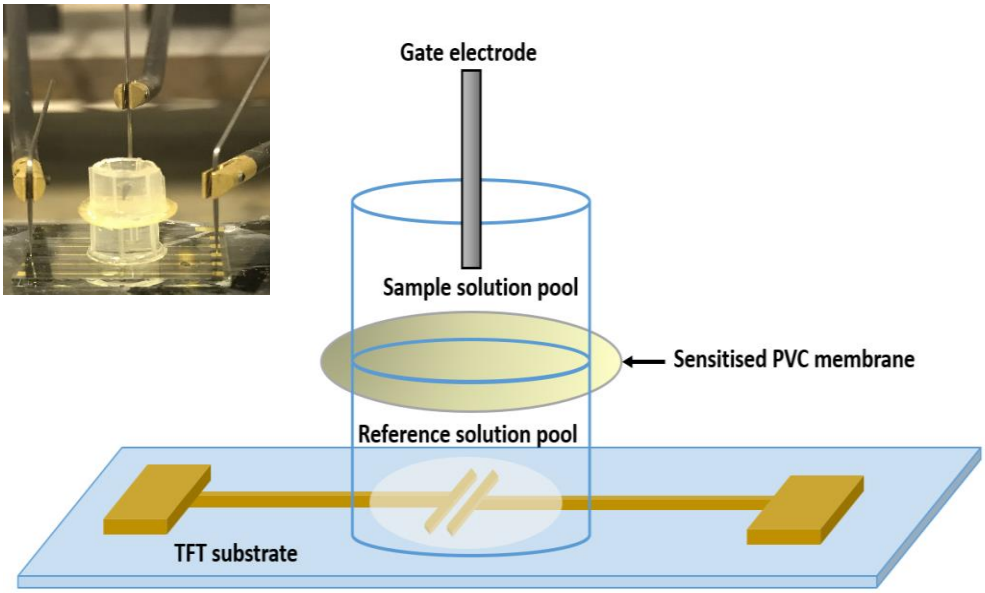

Figure 4.9: A schematic of the two-chamber design (on the left is a photo of the design used here).

This architecture has several advantages as it can be employed for sensing many different analytes and also using different types of sensitizer. In this design the semiconductor film does not contact the sample solution but is always in contact with a constant reference solution. In contrast to architectures of other WGTFTs sensors, where the sample solution is in contact with the semiconductor, a possible change could occur due to the interference of the analyte with the film [e.g[138]]. Accordingly, the two chamber design leads to high sensor stability. Another benefit of such a design which inspired us to adapt for our sensor is the capability to implant zeolites (as the sensitizer) in the WGTFT construction. After unsuccessful attempts to introduce such sensitizers onto the gate electrode [e.g.[93],[32]] or on the actual semiconducting film surface [e.g.[190]].

4.4.1 PVC membrane

The PVC (polyvinylchloride) membrane is the backbone component of the ion selective membrane matrix. It has been applied to both ISEs and WGTFTs sensors over the years. Ionophores can be immobilized within the PVC matrix. In particular, plasticised PVC membranes are used, these are permeable, and so allow ionophores to interact with analytes in the water, and they are

mechanically stable to be adopted in other sensors designs, for example here using the two-compartment architecture.

The plasticised PVC membrane mainly consists of an ionophore (sensitizer), PVC polymer, plasticiser, and an organic solvent. The plasticiser plays a role in the mechanical stability of the membrane by providing elasticity due to the brittle polymeric backbone. A suitable solvent to dissolve the PVC membrane mixture is tetrahydrofuran, THF. A standard membrane consists of 30-33% PVC by weight, and plasticiser around 66% by weight, the ionophore comprises about 1-3% of the overall weight in most organic sensitized membranes [191,192].

Generally, the following recipe was used in this work; 30 mg of polyvinylchloride (PVC), with 65 mg of 2-Nitrophenyl octyl ether (2NPOE) (as plasticiser) and ionophore in the range of 20-40 mg (generally this was zeolites sensitizers). The total mixture was than dissolved in 3 ml of tetrahydrofuran (THF).

To cast a thin flexible membrane from this solution, about 500 µL was pipetted into a small vial. This was left at room temperature overnight to dry till the solvent had completely evaporated. After that, the membrane was peeled from the glass using clean tweezers. As a general procedure the sensitised PVC membrane is left in a known concentration solution for a number of hours[93,149,131]. In our case we also left the membranes in the reference solution for a few hours. Membrane conditioning in a low analyte concentration has been reported to improve, and in some cases lower the sensor limit of detection (LoD)[193].

4.5 Morphology characterisation of the thin film in WGTFT

Before starting the electrical characterisation of WGTFTs, a set of characterisation techniques were performed to assess the quality of these devices. Different parts of the WGTFT including the TFT substrate with source/drain contacts, the channel area and the semiconducting film were studied. The characterisation methods throughout this PhD project were; optical microscopy,

surface profilometry, scanning electron microscopy (SEM), X-ray photoelectron spectroscopy, and will be explained in detail below.

4.5.1 Optical Microscopy

Optical microscopy was used regularly after depositing the contacts by thermal evaporation (see 4.2), to check for any shorts, cuts in the S/D contacts or misalignment or any connections in the channel area. A conventional Nikon optical microscope was used with a magnification of 100x. This microscope works in both modes transmission (illumination from below) and reflection (illumination from above). The aim of spotting such defects was to eliminate unwanted substrates before the semiconducting film was deposited. Figure 4.10 shows a picture of the Nikon optical microscope used.

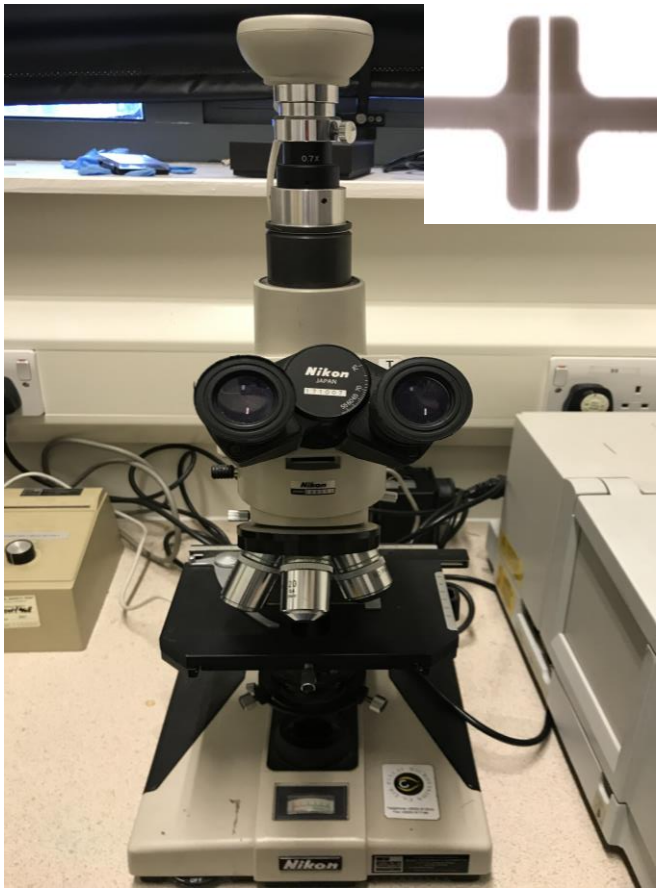

Figure 4.10: Picture of the Nikon optical microscope used. (Inset: image of the channel area under microscope)

4.5.2 Surface Profilometry

Surface profilometry is used to quantify the vertical profile of samples to determine film thickness and roughness. In this work, we used a Veeco Dektak 3ST surface profilometer, shown in figure 4.11 where the key components are illustrated. The main components of this profilometer include a diamond-tipped stylus, sample stage, sensor, illumination source and camera. The device operates electromechanically by lowering the stylus over the sample surface, with the scan parameters such as scan length, speed and stylus force programmed by the user. The sample surface profile is converted from an electrical signal to a digital format by a Linear Variable Differential Transformer (LVDT) which is linked to the stylus. In the case of measuring thicknesses for soft (organic) deposited films on hard substrates, the films should be scratched by a scalpel. The depth of the scratch (which is the thickness of the film) is measured by moving the stylus across the boundary between the film and the scratch. We used this Dektak profilometer to measure the thickness of the deposited semiconductor films (SnO_2 and ZnO).

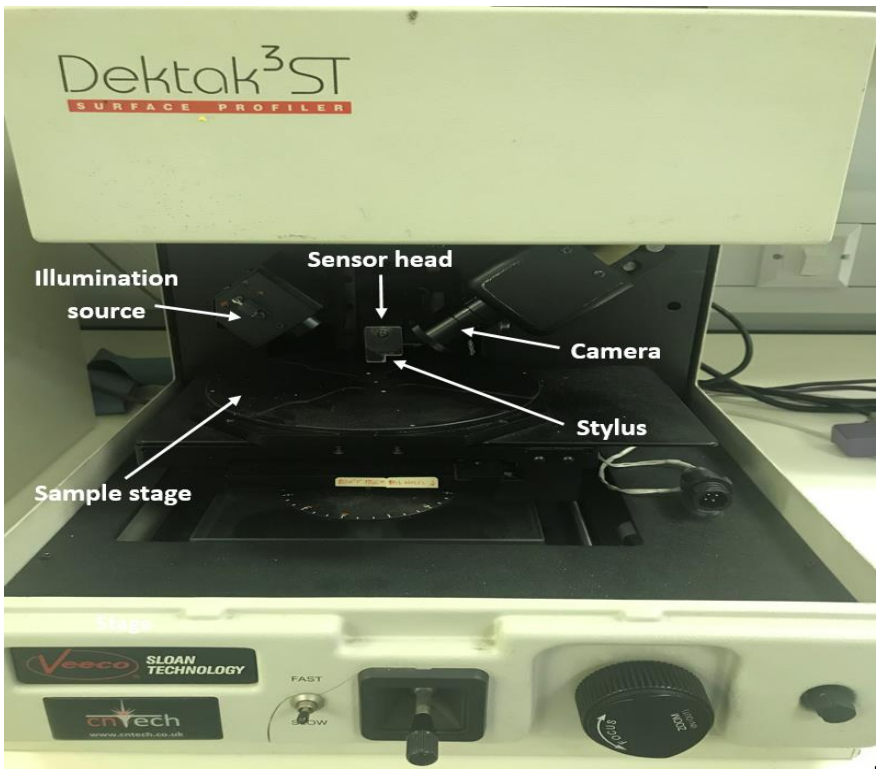

Figure 4.11: Photo of the Veeco Dektak 3ST model used in the work.

4.5.3 Scanning Electron Microscopy SEM

Scanning electron microscopy (SEM) is a widely used technique to produce micro-nanoscale images of surfaces with high magnification and resolution. SEM works by scanning a focused beam of electrons, focussed by electromagnetic lenses across the sample surface. As a result from the interaction between the electrons and the surface, secondary electrons are released and detected to form the SEM image[194]. Figure 4.12 below illustrates the configuration of the SEM. This technique requires some degree of conductivity, so for non-conducive samples, where electrons build up as charges instead of penetrating the surface, a thin layer of conductive material (e.g. Au) should be applied. A high vacuum environment is essential in SEM operation, in order to prevent deflection with air molecules.

In this thesis, SEM images for both SnO_2 and ZnO are presented in chapter 5. These SEM measurements were carried out by a colleague Hadi Alqahtani in King Abdulaziz City for Science and Technology, Riyadh Saudi Arabia.

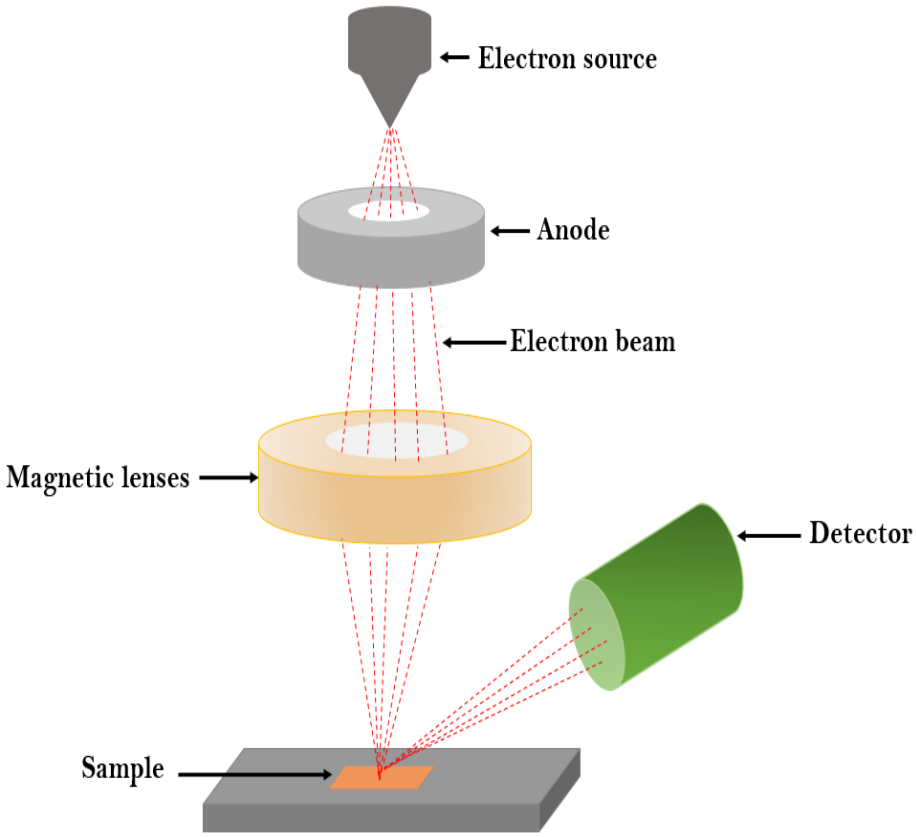

Figure 4.12: Scanning electron microscope diagram, showing the important elements.

4.5.4 X-ray photoelectron spectroscopy XPS

The X-ray photoelectron spectroscopy (XPS) technique is used to identify the chemical composition of materials and the chemical bonds between these elements. It also called Electron Spectroscopy for Chemical Analysis (ECSA). The working principle of this technique starts by the emission of an X-ray with a sufficient energy for core electron excitation and ejection from the top surface of the material (1-10 nm depth).

Then by measuring the kinetic energy of the emitted electron, the binding energy of the core electronic level can be determined (figure 4.13). The escaped core electrons kinetic energy E_K is given by equation 4.5:

$$E_K = E_x - E_b - \varphi \qquad (4.5)$$

Wherein E_x is the exciting energy of the X-ray, E_b the binding energy of the electron, the φ workfunction of the detector. The calculated E_b is then compared with known reference standard E_b values to find the specific element[195],[196].

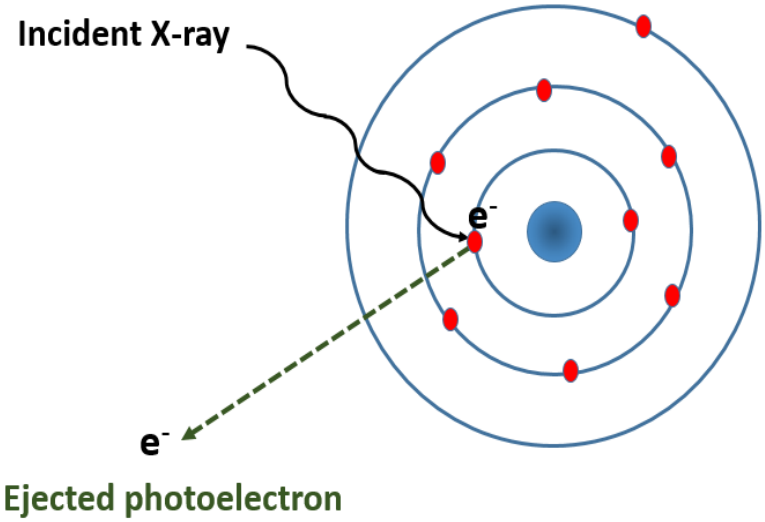

Figure 4.13: The principle of X-ray photoelectron spectroscopy (XPS).

We used XPS analysis to confirm the conversion of the sprayed Sn chloride precursors films to the semiconducting film of SnO_2. These XPS studies were performed at the Sheffield Surface Analysis Centre in the Sheffield Chemistry department by Dr Debbie Hammond.

4.6 Electric Characterisation of Thin Film Transistors

This section shows the electrical characterisation of the TFTs which were manufactured in many stages (detailed in sections 4.1- 4.3) and explained in (2.1-2.3). Prior to characterisation, the TFTs are gated by water as an electrolyte as shown in figure 4.1. Here both output and transfer characterisations are described. Also the extraction and the calculation of TFTs parameters are

explained including the threshold voltage and threshold voltage shift (V_{th} and ΔV_{th}), the charge carrier mobility μ, on/off current ratio and subthreshold swing S.S.

4.6.1 TFT Characterisation with Source Measure Units

Within this study two Keithley 2400 source measure units (figure 4.14.a) were used to characterise the TFTs, the measurement was automated using bespoke LabView software. With these source measure units, the voltage can be sourced, whilst the current is measured and vice versa. Such programming modes are named voltage source-current meter and current source-voltage meter. In our work we used the voltage source-current meter option, wherein the voltage is applied to the gate and drain electrodes and the drain current is measured (as the gate current should be negligible). Coaxial cables are used to electrically connect the TFT to the units via probe heads with fixed contact needles. A gate needle touches the gating medium (water) across the channel area, so connecting to the gate unit, while another needle connects the drain to the other unit, while the source is connected to electrical ground by the third needle (this is shown in figure 4.14.b).

Figure 4.14 (a): A photo of the two Keithley source measure units.

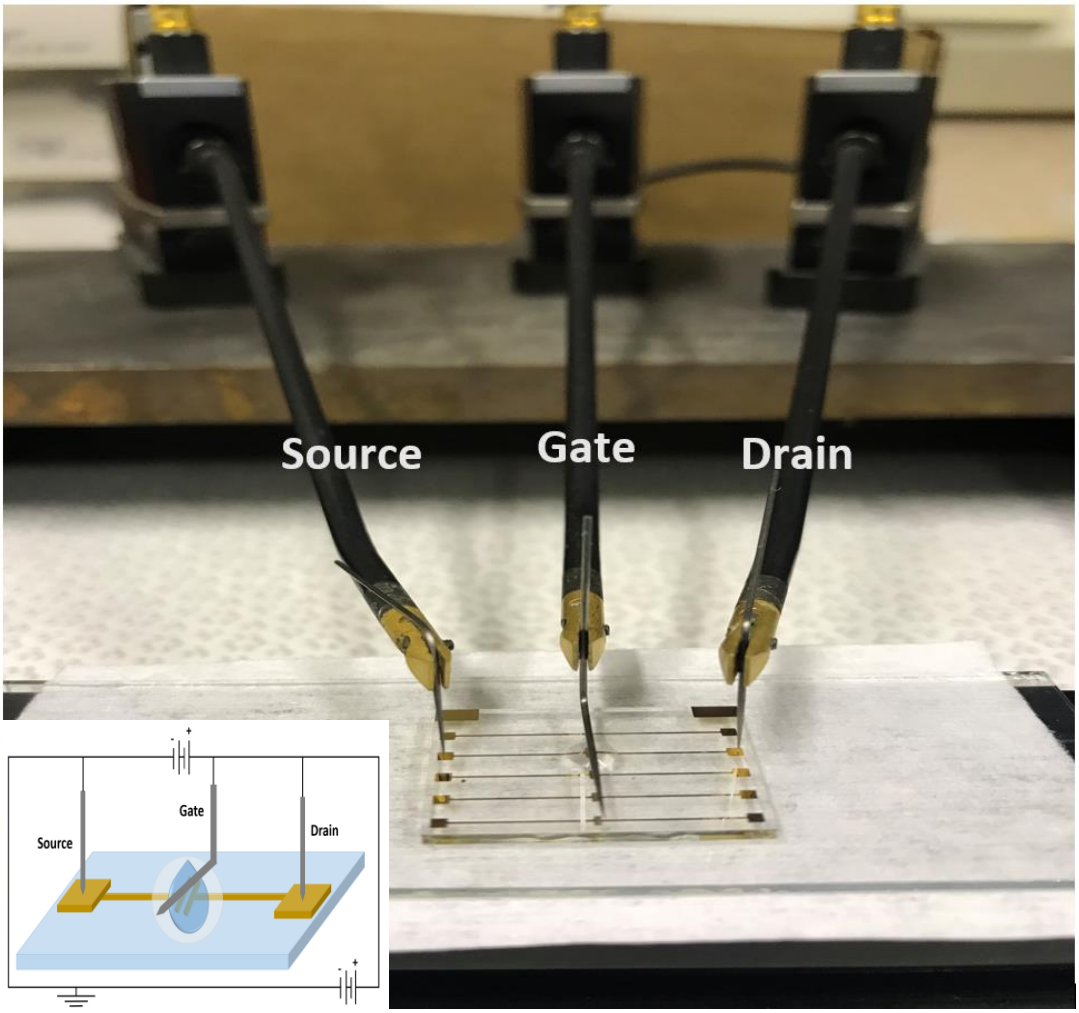

Figure 4.14 (b): A photo of the probe-heads where the needles are connected to the source, drain electrodes and overlap the water drop on the channel area. (inset: schematic shows the connection of different electrodes gate, source and drain)

The Keithley 2400 instruments were connected to a PC running bespoke LabView software by GPIB-PCI cables to record the TFTs characteristics. Both output and transfer characteristics can be performed by this software as it differentiates between them by using different modes of measurements. In addition, this software enables manipulation of the measurement parameters to optimise the final result. Some of these parameters are the voltage range, number of sweeps, step size, and delay time between these steps. Figure 4.15 shows screenshots of the Labview software when setting to record output (a) and transfer (b) characteristics.

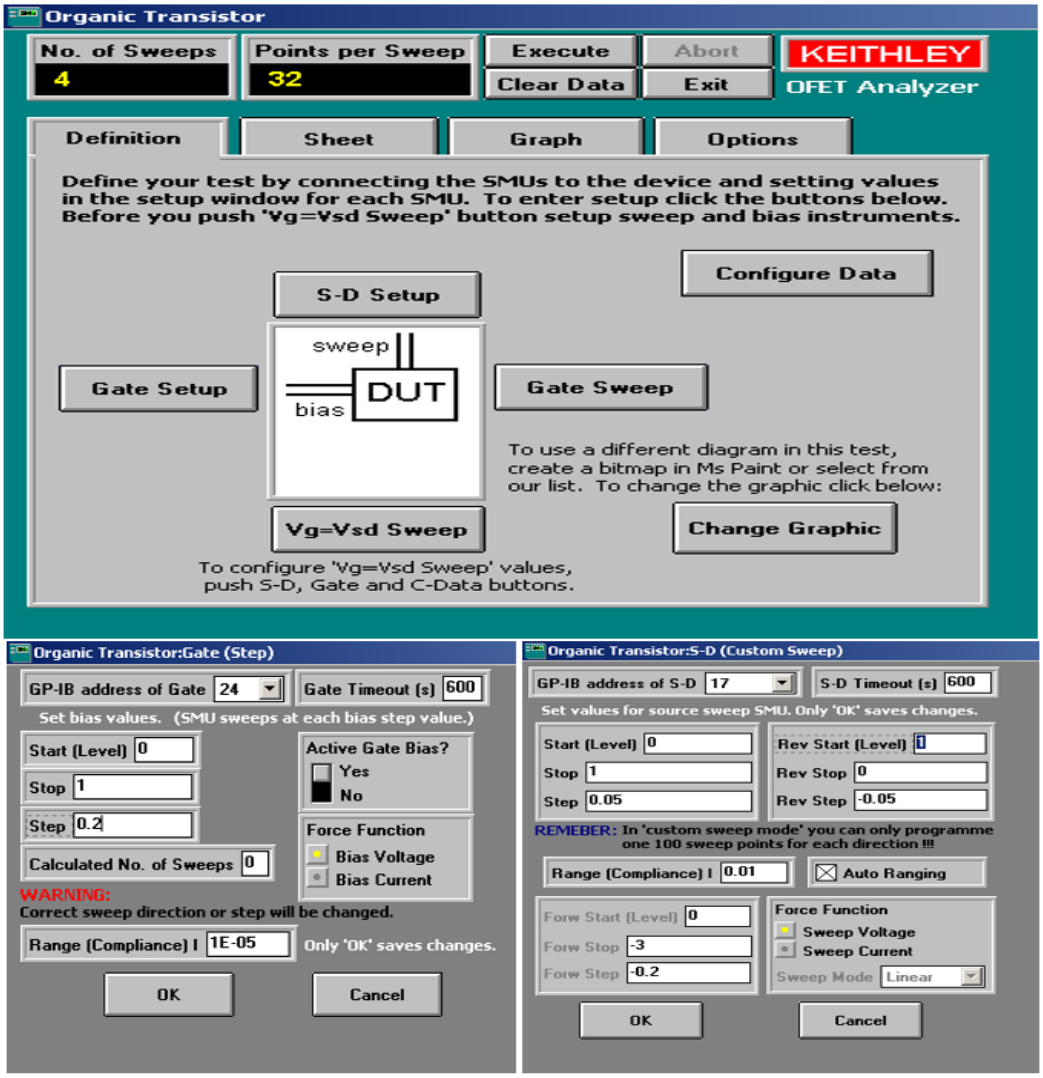

Figure 4.15 (a): A screenshot of the Labview software when set to record the output characteristics.

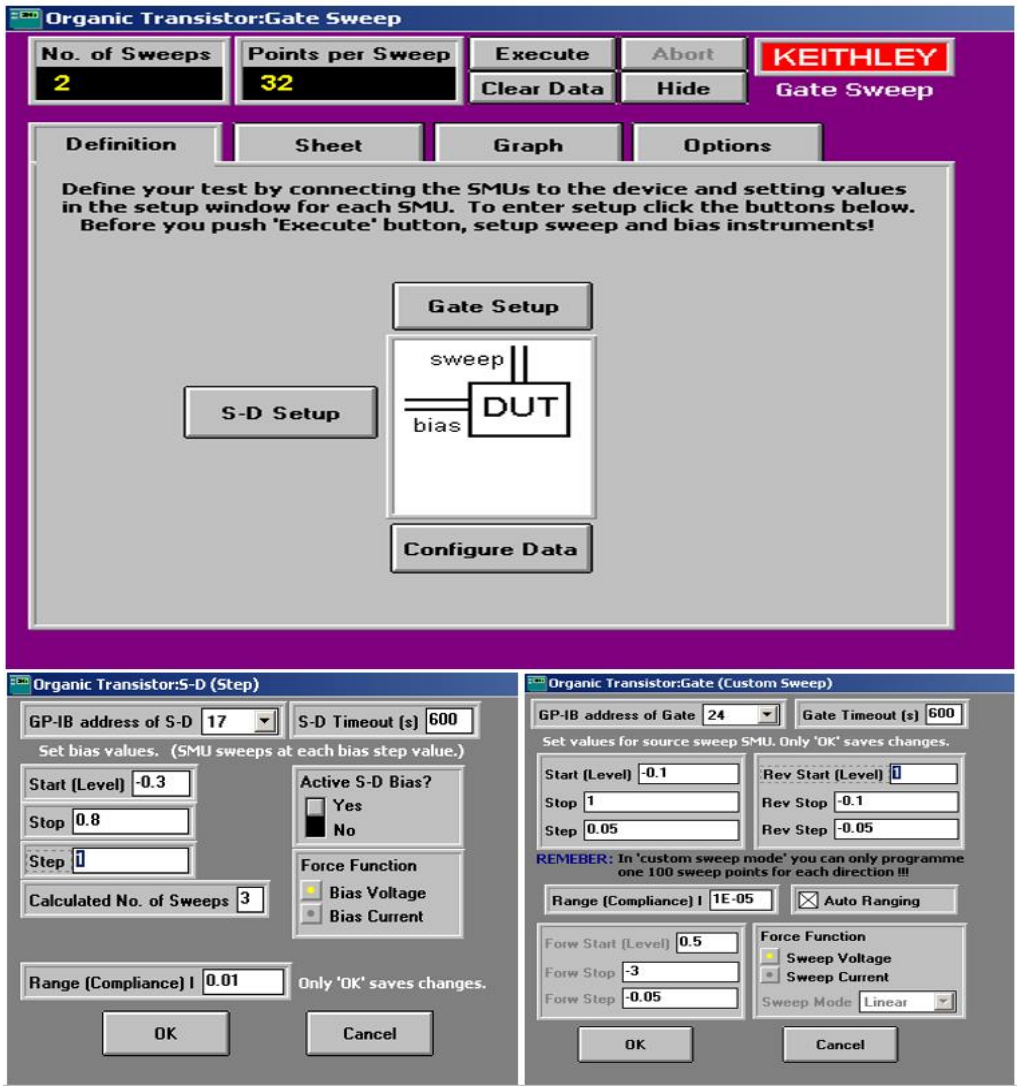

Figure 4.15 (b): Screenshot of the labview software when set to record the transfer characteristics.

4.6.1.1 Output Characteristics

In field effect transistors, the relation between the drain current I_D and the drain voltage V_D at constant values of the gate voltage V_G is called the output characteristics. The polarity of the applied V_G and V_D have to be the opposite of the semiconductor polarity. The value of V_G should not exceed the electrochemical window of the electrolyte in the case of electrolyte-gated TFTs. So, in our WGTFTs the limit of the applied V_G is 1.23 V, which is within the electrochemical window for water. When sweeping V_D we started from zero to maximum modulus in small steps,

in this work up to 1 volt, then returning to zero. In the low value of V_D, the relation between V_D and I_D is liner where it saturates at high values of V_D (no change of I_D with V_D) section (2.3).

Quantifying the output characteristics helps to identify the quality of the transistor and discover any faults / problems. Near-ideal transistor output characteristics are given in figure (4.16). For example, at high V_D, when I_D still increases with V_D this reveals the level of doping in the semiconductor film used in the TFT (figure 4.16 (b) orange). Also, sublinear behaviour instead of linear behaviour (at low V_D) indicates a contact problem (figure 4.16 (b) green). Undesirable effects, when the current leaks across the gate medium, can be clear if the output curves do not intersect the origin point (zero I_D and V_D), (figure 4.16 (b) blue). Because of the impurities in the semiconductor film or at the semiconductor and insulator interface, hysteresis can be shown in the output characteristics as displacement in I_D values, when scanning V_D from zero and toward zero.

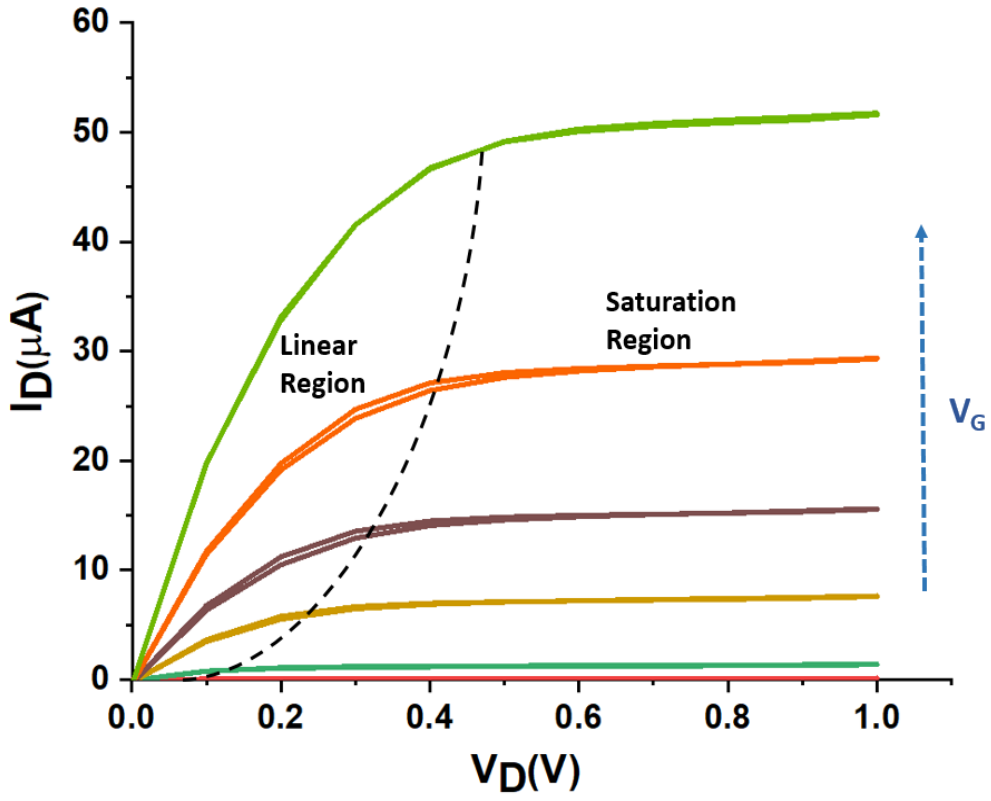

Figure 4.16 (a): An example of near-ideal transistor output characteristics.

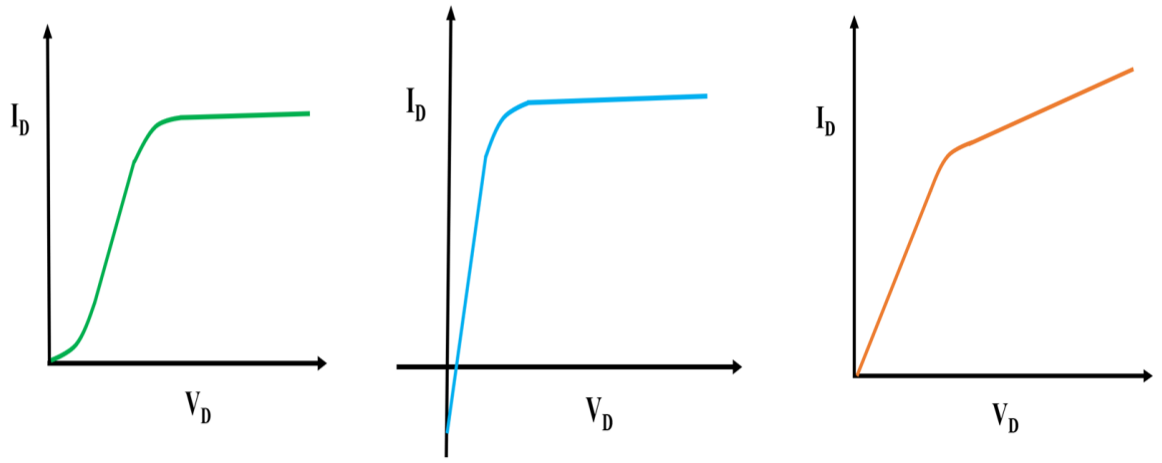

Figure 4.16 (b): Schematic of some examples of output characteristics indicating undesirable behaviors.

4.6.1.2 Transfer Characteristics

The transfer characteristics show the relation between the V_G and I_D at a fixed value of V_D. As described in section 2.3, there are two modes to the transfer characteristics, linear and saturated. At very low V_D ($V_D << V_G$), the characteristics are linear, whereas they saturate at high applied V_D ($V_D > V_G$). Figure 4.17 (a,b) illustrates both the linear and saturated characteristics. The latter plotted (4.17b) on two different scales of the I_D according to equation 2.9 in section (2.3).

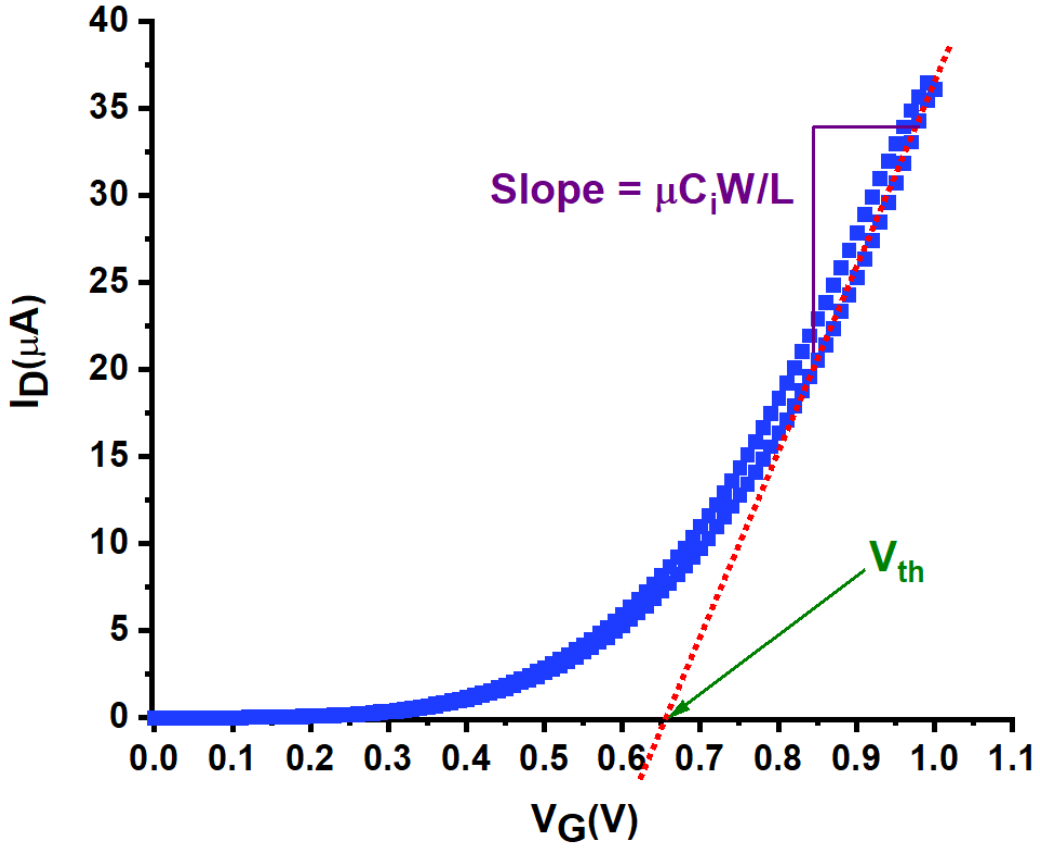

Figure 4.17 (a): An example of linear transfer characteristics. Where the threshold voltage and the slope are indicated.

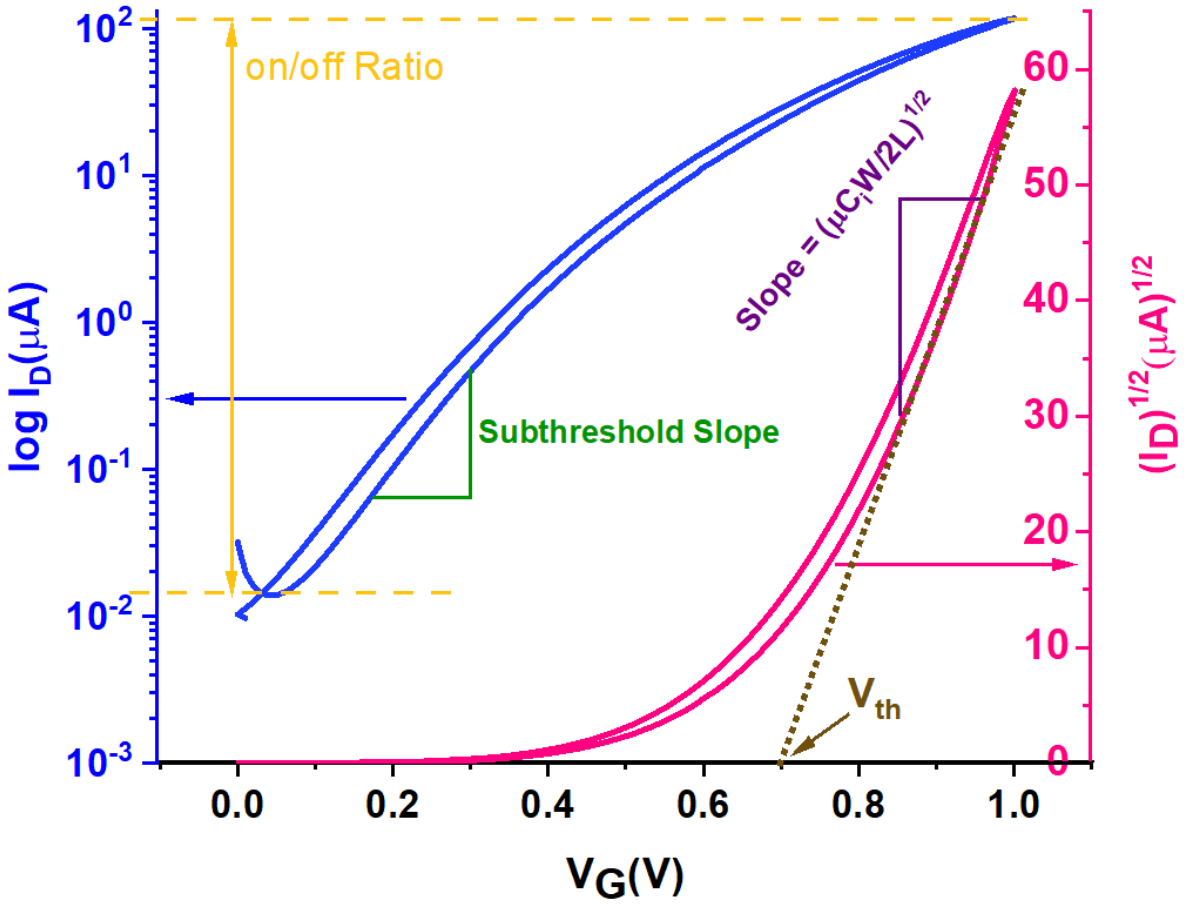

Figure 4.17 (b): Saturated transfer characteristics for a WGTFT, plotted on two different current scales, logarithmic and square root.

4.6.1.3 TFT Parameter Extraction

Transfer characteristics are very important to quantitatively evaluate a TFT, where essential parameters can be extracted (4.6.1.3 below). Here we show the calculation of important TFT parameter characteristics, including the threshold voltage and threshold voltage shift (V_{th} and ΔV_{th}), the charge carrier mobility μ, the on/off current ratio and subthreshold swing SS.

In this work we mainly use the linear transfer characteristics to study the response of our WGTFTs sensors.

Threshold voltage V_{th}:

The threshold voltage V_{th} is the most important parameter in this work. It can be extracted from both linear and saturated transfer characteristics. In the linear transfer region, the V_{th} value is extracted by fitting a straight line to the V_G-I_D plot at high V_G values, as illustrated in figure 4.17 a, the value on the V_G axis when this line intercepts the axis is V_{th}. The same fitting procedure is used for the saturated characteristics but this time it is a plot of V_G and $\sqrt{I_D}$, as illustrated in figure 4.17 b.

Mobility:

Charge carrier mobility when an electric field is applied, can be defined as the speed of carrier movement within the semiconductor with the common units of (cm^2/V.s). Mobility is a property of the semiconductor rather than the TFT, different semiconductors materials have different mobility values [46].

As for threshold voltage V_{th}, carrier mobility can be extracted from both linear and saturated transfer characteristics of a TFT. In the linear regime mobility can be obtained by equation 4.6:

$$\mu_{lin} = \frac{L}{WC_iV_D}\left(\frac{\partial I_D}{\partial V_G}\right) \qquad 4.6$$

$$\mu_{lin} = \frac{L}{WC_iV_D}(Slope) \qquad 4.7$$

Where C_i here is the specific capacitance of the gating medium, L and W represent the channel length and width respectively. The ratio of $(\frac{\partial I_D}{\partial V_G})$ is basically the slope of the dashed red line, fitted in figure 4.17.(a), so a value for the linear mobility μ_{lin}, can be calculated by extracting the slope and use this value along with the C_i, L, W constant values, as shown in eq.4.7.

Mobility in the saturated regime is given by equation 4.8:

$$\mu_{sat} = \frac{2L}{WC_i}\left(\frac{\partial\sqrt{I_D}}{\partial V_G}\right)^2 \qquad 4.8$$

From figure 4.17.(b) $\frac{\partial\sqrt{I_D}}{\partial V_G}$ is the slope of the brown dashed line, which is fitted to find the V_{th} value. As we know the values of C_i, L, W, the μ_{sat} can be simply calculated from equation 4.9 below:

$$\mu_{sat} = \frac{2L}{WC_i}(Slope)^2 \qquad 4.9$$

It is important to note here, that as we use water as the gating medium, the value of C_i is not exactly known, as it strongly depends on the frequency and to some extent on the salt concentration in the gating water. C_i is usually in the range 1-10 µF as reported in the literature[148,34]. So, it is recommended here as an extra caution to use the metric μC_i as a figure of merit instead of just the mobility, especially when relating to values in the literature.

On/off current Ratio:

I_{on} / I_{off} is the ratio between the highest I_D value (at the maximum V_G value), and the lowest I_D value (at V_G = zero Volt) in the saturation regime. It can be easily found from the log I_D axis in figure 4.17 b (shown as a dashed yellow line).

Subthreshold swing S.S:

The inverse of the subthreshold slope is called the subthreshold swing (S.S) and is described in detail in section (2.3). It can be extracted by reversing the slope of the plot of V_G with log I_D in the subthreshold voltage regime of the saturated transfer characteristic, as shown in figure 4.17 b in green color. The S.S unit is mV/decade as it indicates how many mV of V_G is needed to increase the drain current tenfold.

Threshold voltage shift ΔV_{th}:

To find the change in the threshold voltage V_{th} values ΔV_{th}, between two different linear (or saturated) transfer characteristics of the same transistor, two different methods are used. For the first one, the threshold voltage V_{th} is extracted for each characteristic then the difference between the two V_{th} is calculated ($\Delta V_{th} = V_{th(1)} - V_{th(2)}$). Another method, used within this thesis, is relatively simple and does not rely on fitting, calculation or theoretical models. In this method, linear transfer characteristics for both measurement (1) and (2) are plotted, where the scales used in both axes are the same. Then both plots are brought together, and we try to overlap the two plots, to evaluate the shift in the gate voltage V_G needed for both characteristics to exactly match. In this approach the only varying parameter between the two characteristics is the threshold voltage V_{th}, mobility should be the same as a different slope of the linear part of the plot (at high V_G) would cause a mismatch in the two curves. To clarify this method, the figure below explains in steps how to find the threshold voltage shift $\Delta V_{th.}$ From left to right in figure 4.18, at the beginning both characteristics A and B are in the same plot, then B was shifted along the gate voltage V_G axis toward A. In this case we found ΔV_{th} equal to 220 mV, to produce the resulting curve in 4.18 (third to the right) that is called the master curve. We utilised this method to find the ΔV_{th} between different analytes concentrations in our WGTFTs sensors, this has been used extensively in this field[93,138,32] .

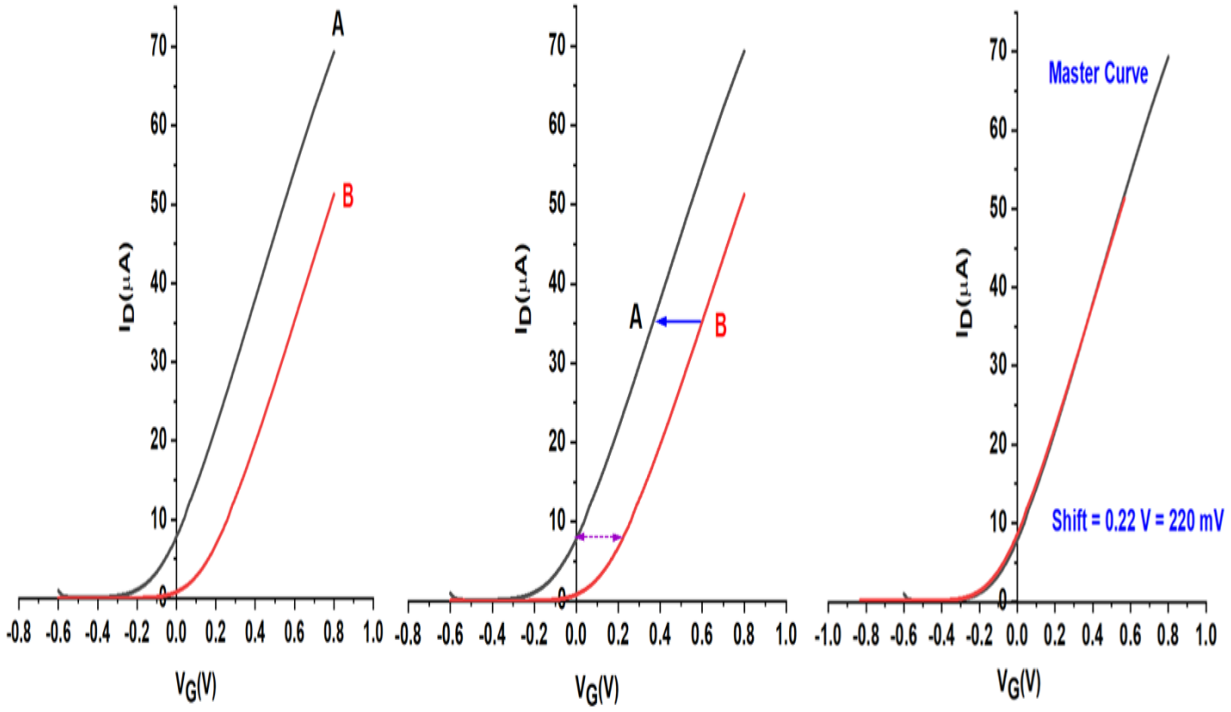

Figure 4.18: Illustration of how to determine the threshold voltage shift ΔV_{th} via a parameter-free shift procedure. A threshold voltage shift of 220 mV between A and B was found.

Hysteresis:

Hysteresis is one of the very common phenomena to occur in TFTs, particularly in electrolyte gated TFTs. Hysteresis is clearly shown in figure 4.19, when the measured values of I_D in scanning the gate voltage V_G from off to on (e.g. 0 to 1 V) are lower or higher than I_D values in a backward scan from on to off. In other words, the falling flank does not match with rising flank (see figure 4.19). The main reason for hysteresis is charge traps, found on the semiconductor insulator interface or in the semiconducting films [197,198,199]. There are two directions for hysteresis; clockwise and anticlockwise, these rotations are dependent on the type of semiconductor, n-type gives anticlockwise whilst p-type is clockwise[200]. In our work, we dealt with hysteresis in WGTFTs transfer characteristics by considering the raising flank according to IEEE standards in organic transistors[201]. In most of our work the transistor transfer characteristics suffer from high

levels of hysteresis, and as these characteristics are the tool to find the sensing responses ‘threshold voltage shift’, we consider using the rising side (off to on) of the whole curve. The falling side (on to off) generally show an imperfect master curve.

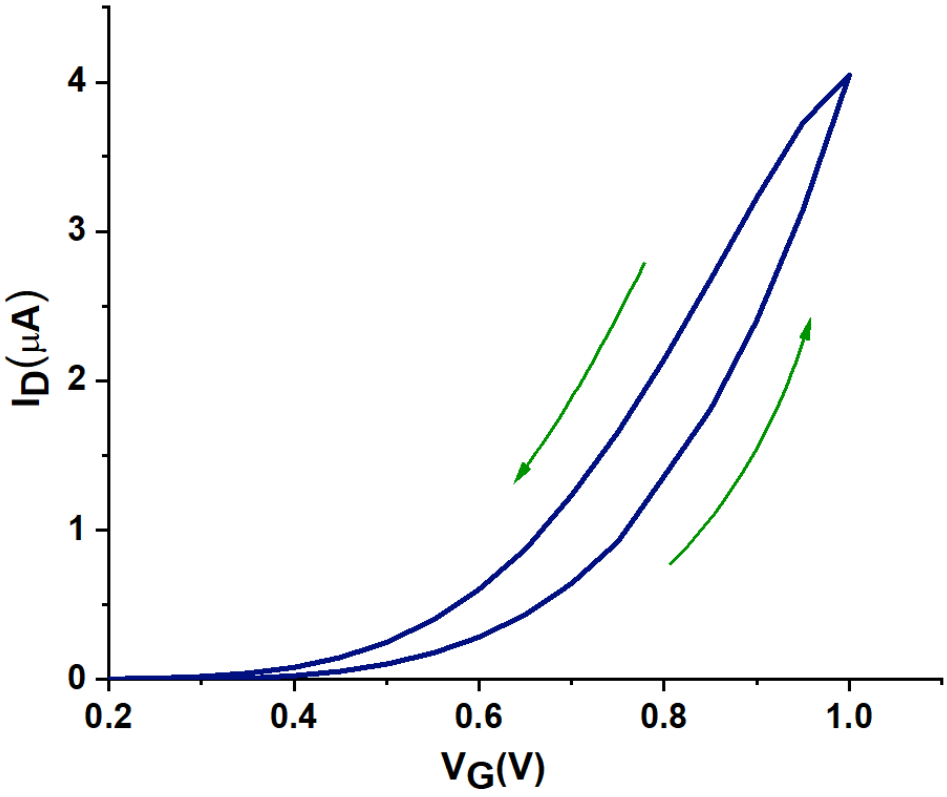

Figure 4.19: An example of hysteresis in the liner transfer characteristics of a WGTFT.

Chapter 5: Characterizations of SnO_2 TFTs

5.1 Introduction to the work

In water gated thin film transistors various semiconductors can be utilized, both organic and inorganic. Each particular type of semiconducting film has its own advantages and disadvantages especially when linking to a specific application. For example, water-soluble semiconductors would be favourable in biodegradable electronics applications[202,203] but not for water monitoring applications, as the stability of the sensor is a priority. The most commonly used films in WGTFTs are polymers and metal oxide semiconductors[148,138,93,204]. The long term stability of semiconducting polymers is not optimal[27], as they might degrade at high voltage (> 0.7 volt) [148], and they may also become electrochemically doped at higher concentrations of the gate media[125]. In addition, they need special care and handling as they can be affected under normal atmospheric conditions and even under illumination (especially UV)[205]. Metal oxide semiconductors (e.g. ZnO, IGZO,InO_3)[92,204,206,29] possess better stability compared with polymers in WGTFTs. The nature of the bonding in these semiconductors is partly ionic due to the high electronegativity of oxygen, which leads to solubility in ionic and polar solutions[207]. Accordingly, a highly stable metal oxide semiconductor is required in WGTFTs. From the nature of SnO_2 and by comparing it with other metal oxides in this field, we see SnO_2 to be promising as its bond nature is less ionic, being closer to covalent[95,208]. In this chapter, the use of SnO_2 as a semiconductor film in a WGTFT device will be studied for the first time.

5.2 Preparation of sprayed pyrolysis SnO_2

As we aimed to use solution processing methods to prepare the SnO_2 film, several precursor approaches and methods were tried. For example, spin coating from a tin chloride precursor and SnO_2 nanoparticles[209] and spray pyrolysis from an aqueous precursor of $SnCl_4.5H_2O$[70], but these approaches did not produce appropriate transistors films. The film used in this work was prepared by spray pyrolysis from tin chloride pentahydrate ($SnCl_4.5H_2O$) dissolved in isopropanol, as this gives the best semiconducting film for our transistors and applications [209,69,210]. The molar concentration for the precursor solution controls the unintentional doping of SnO_2, for this reason,

we used 50 mM[211]. The spray deposition parameters are included in table (5.1) (ZnO is also included as it will be used in section 5.4).

Table 5.1: Spray deposition parameters for SnO2, ZnO semiconducting films

Parameters	SnO_2	ZnO
Precursor material	$SnCl_4.5H_2O$	$ZnCl_2$(anhydrous)
Molar Concentration (M)	0.05	0.1
Solvent	isopropanol	DI water
Substrate temperature	400 ºC	400 ºC
Substrate to nozzle distance	20 cm	20 cm
Spraying duration On:Off	2-3 sec:1 min	1-2 sec:20 sec
Number of sprays	4	5

The thickness of SnO_2 film is = 45 ± 14 nm. Scan electron microscope (SEM) images of the film are shown in figure (5.1) and the X-ray photoelectron spectroscopy XPS test of the SnO_2 in figure (5.2) below.

SEM was used to evaluate the surface morphology of sprayed pyrolyzed SnO_2 films cast from $SnCl_4.5H_2O$ in isopropanol as a solvent. The energy of the incident electrons was set at 4.4 keV, providing magnification from (1,000 to 30,000) and 100 nm resolution. Figure 5.1 show the morphology of SnO_2 film at three different scales, it is evident from the SEM characteristics that this procedure forms a very homogeneous film.

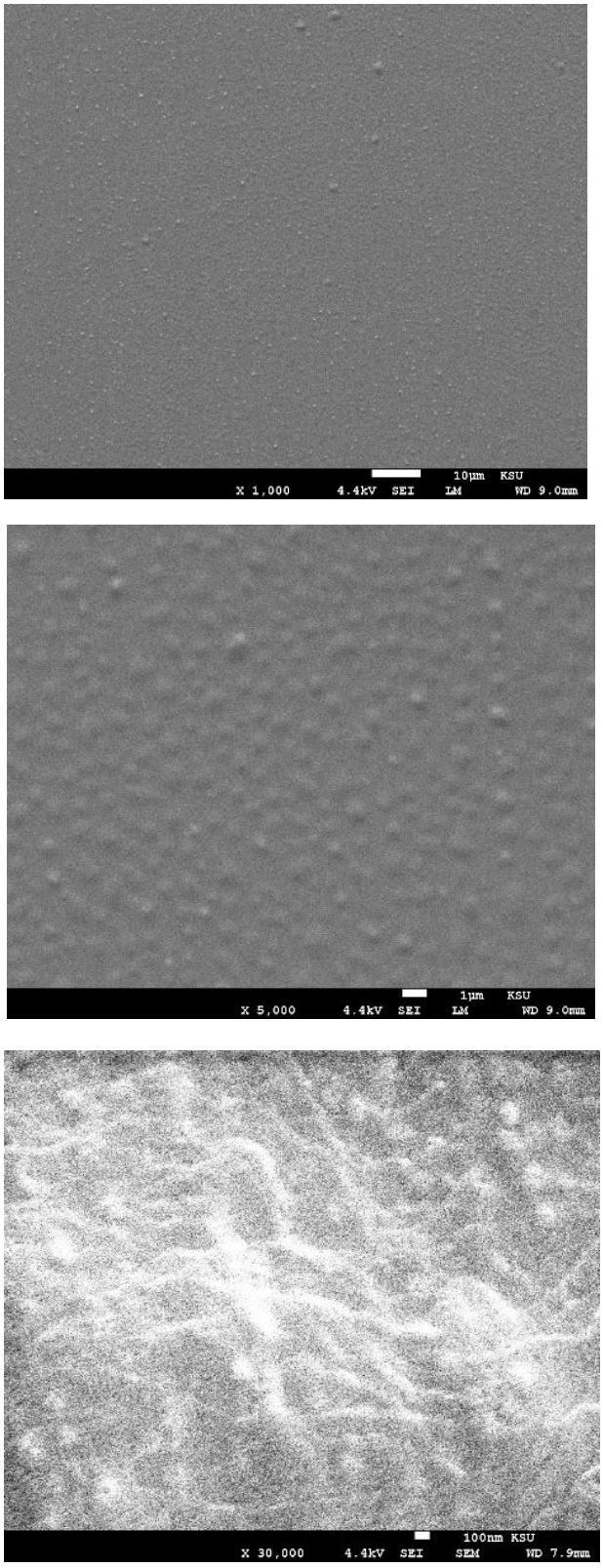

Figure 5.1: SEM images of SnO_2 film at three different magnification scales.

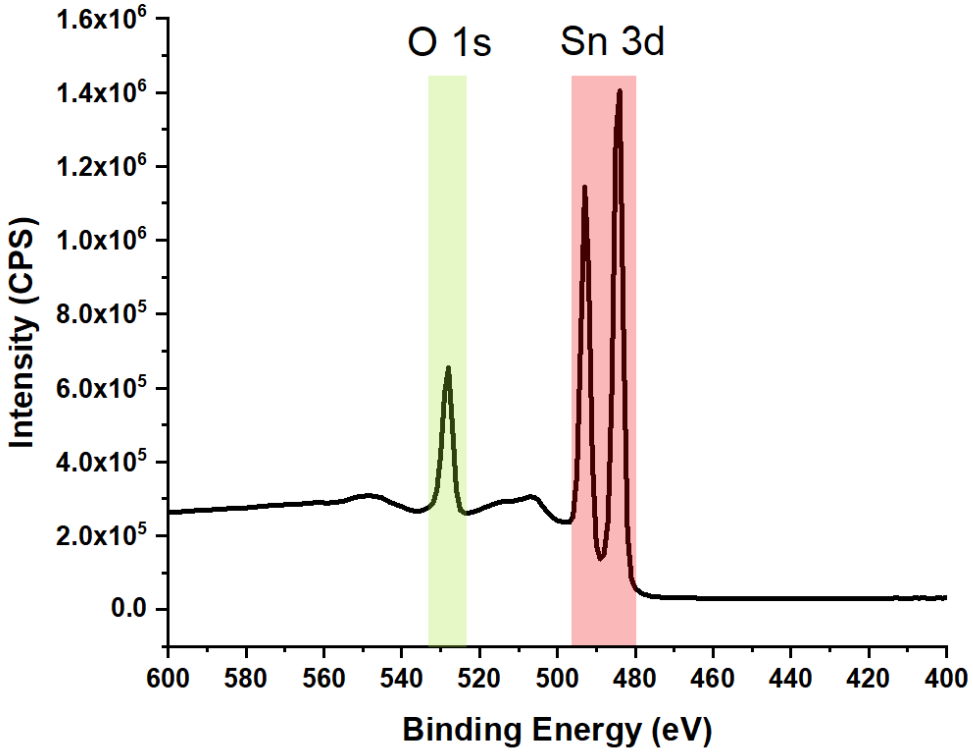

Figure 5.2: XPS spectra of O 1s and Sn 3d for SnO_2 prepared by the thermal conversion of the $SnCl_4$ precursor.

To further investigate that the sprayed pyrolyzed $SnCl_4.5H_2O$ precursor forms a SnO_2 film, XPS characterization was performed. The samples were analyzed using a Kratos Ultra XPS spectrometer. Monochromated Aluminium radiation was used to collect XPS survey scans (wide scans) with a 160 eV pass energy and 1 eV intervals. High-resolution XPS spectra at 20 eV pass energy, and 0.1 eV intervals were collected over the O 1s, Sn 3d, C 1s peaks and over the Sn valence band region. The surface composition was determined using the high-resolution scans collected for tin, carbon and oxygen. Sn and O accounted for the largest components whereas C accounted for less than 10%, which is considered as contamination. It is noticeable that the O:Sn ratio is substantially less than the value of 2 expected. This could be due to there being a mix of SnO and SnO_2, or could be due to the oxygen signal being more depressed than the tin signal due to an overlayer of carbonaceous contamination. However, the carbon concentration is low.

5.3 The Electrical characteristics of SnO_2 TFTs

To measure the transistor characteristics, for both output and transfer, a droplet of DI water was mounted on the channel area of the transistor and the drain current was recorded. For the output measurements the gate voltage scan range was from 0 to 1 volt, in steps of 0.2 volt, the drain voltage was scanned from 0 to 1 volt in 50 millivolt steps. For the linear transfer characteristics, we recorded the drain current at 0.1 volt in the gate voltage range from -0.5 to 1 volt in step of 20 millivolt.

To examine the performance of SnO_2 in WGTFTs, two devices were studied, A and B, figure 5.3 (a, b) shows the output characteristics for both devices. Both devices are prepared by the same procedures onto different substrates to ensure reproducibility of the used method in the deposition of the SnO_2 film. We find SnO_2 WGTFT operates as a typical electron transporting field effect transistor and it **is** normally on, i.e., slightly above the threshold voltage, even at zero gate voltage.

SnO_2 WGTFTs also show some doping which is seen as a positive slope in the saturated regime (similar to figure 4.16 (b) third characteristics to the right).

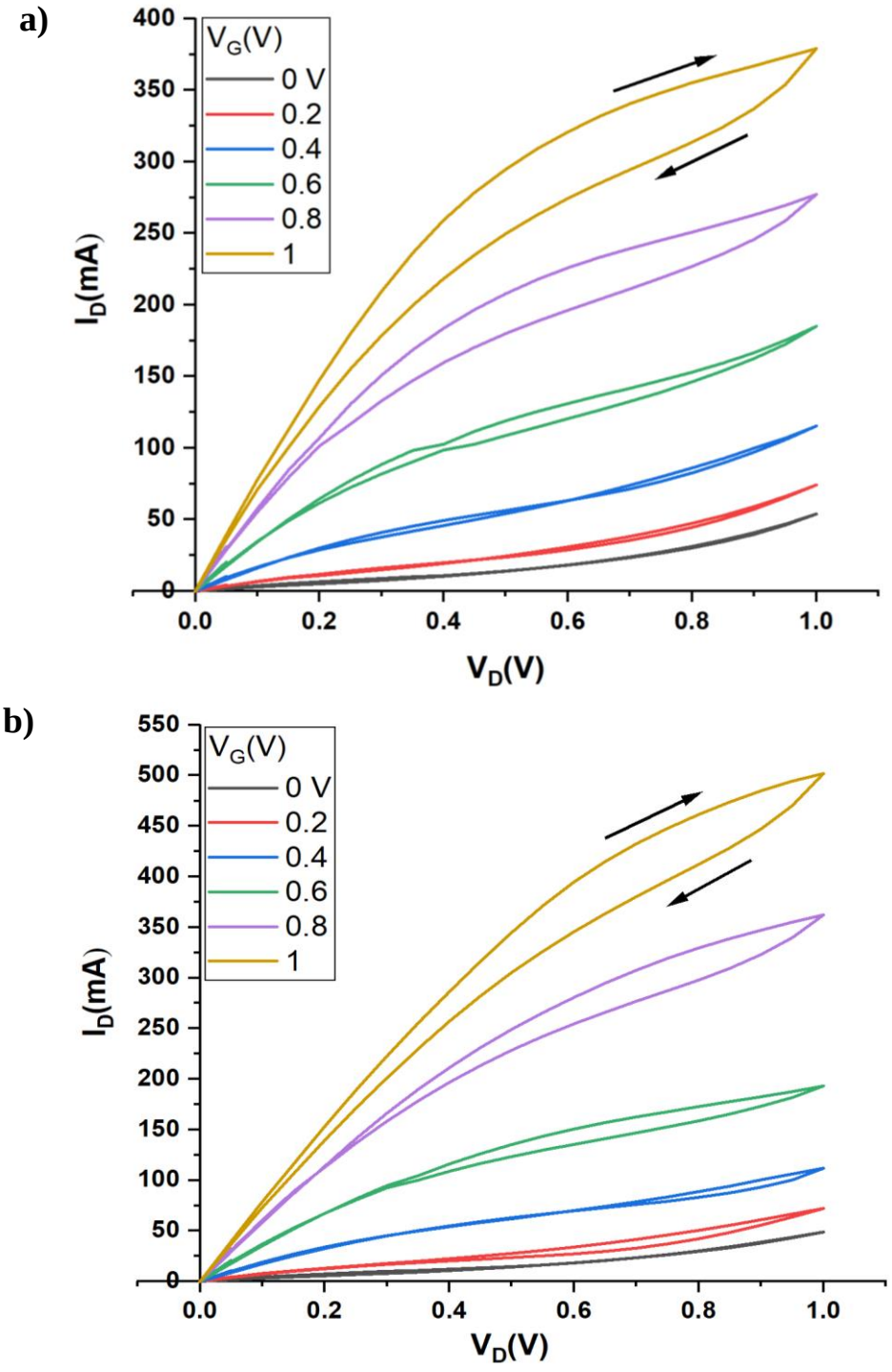

Figure 5.3: The output characteristics of SnO_2 WGTFTs, a) device A. b) device B.

Despite the larger bandgap, SnO_2 (3.6 eV), the output characteristics show no evidence of contact limited behavior.

The linear transfer characteristics for SnO_2 WGTFTs are displayed in the figure 5.4 (a, b) below, with the saturation transfer characteristics shown as the inset.

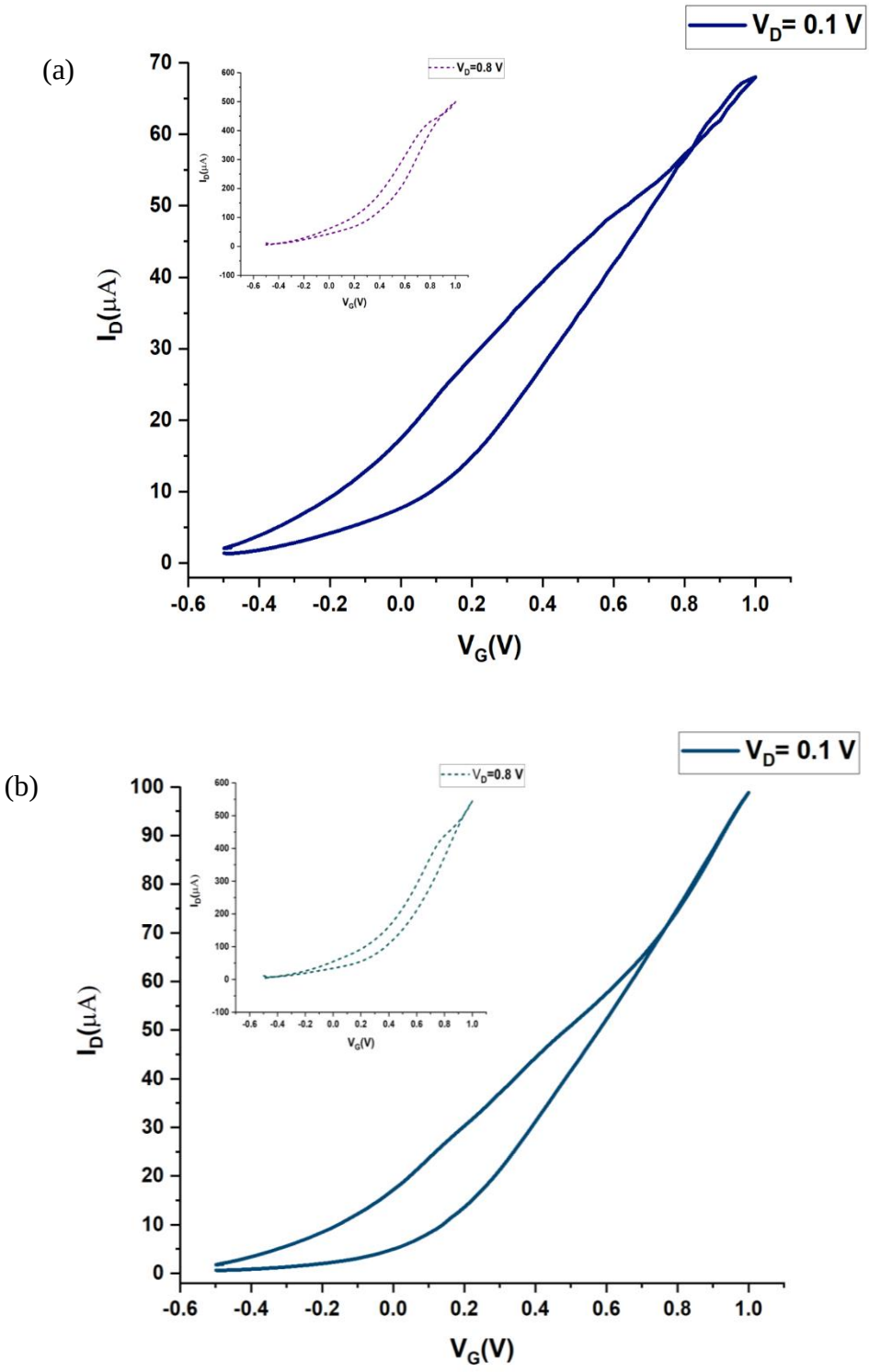

Figure 5.4: Liner transfer characteristics of SnO_2 WGTFT (inset saturation transfer characteristics). a) device A. b) device B.

A quantitative study of the performance parameters of SnO_2 WGTFTs are illustrated in table (5.2) below.

Table 5.2: SnO_2 and ZnO WGTFTs extracted parameters from transfer characteristics

Parameter	Device A	Device B	ZnO
Threshold Voltage [V]	-0.02	0.06	0.5
Mobility (linear) [$cm^2/V.S$]	7.3	11	9.3
I_{on}/I_{off} Ratio	56.3	69	5063
Subthreshold Swing [mV/decade]	650	549	200

From table (2), we find that SnO_2 gives a very low threshold voltage of nearly zero, the electric field mobility is fairly good for solution processed film (compared to values reported in the literature [212,213,72]). Due to the SnO_2 films having a high level of unintentional doping, the switching ratio (high I_{off}), the I_{on}/I_{off} ratio is low. The subthreshold swing (the inverse of the subthreshold slope) is high which is undesirable and unrealistic because of the doping.

To evaluate the performance of SnO_2 WGTFTs in our application (sensing analyte in water), we compare it with another spray-processed electron transporting films of ZnO in WGTFTs. The material ZnO (E_g=3.37eV) is commonly used for it valuable properties (including direct and wide band gap, high thermal conductivities, and radiation hardness)[207,76] and it has already been reported in WGTFTs sensors[93,37,214].

We sprayed ZnO WGTFT as in 5.2, the thickness of the sprayed ZnO film is ≈ 180 nm. The output and linear transfer characteristics are shown in figure 5.5 (a, b), (the extracted parameters shown as an inset).

Note here that the measured films of SnO_2 and ZnO have different thicknesses, which is probably due to the different precursor concentration. For both semiconductors SnO_2 and ZnO, different molarities of the precursor solution were tested. For SnO_2, higher molarity precursors give a high level of doping, at 50 mM precursor concentration of $SnCl_4$ the best performance was achieved for the WGTFT. In the case of ZnO, a lower concentration of 50 mM results in a lower current (few µA). So for more reasonable comparison, I selected these devices due to the similarity in the performance despite the variation in their thickness and precursors molar concentrations.

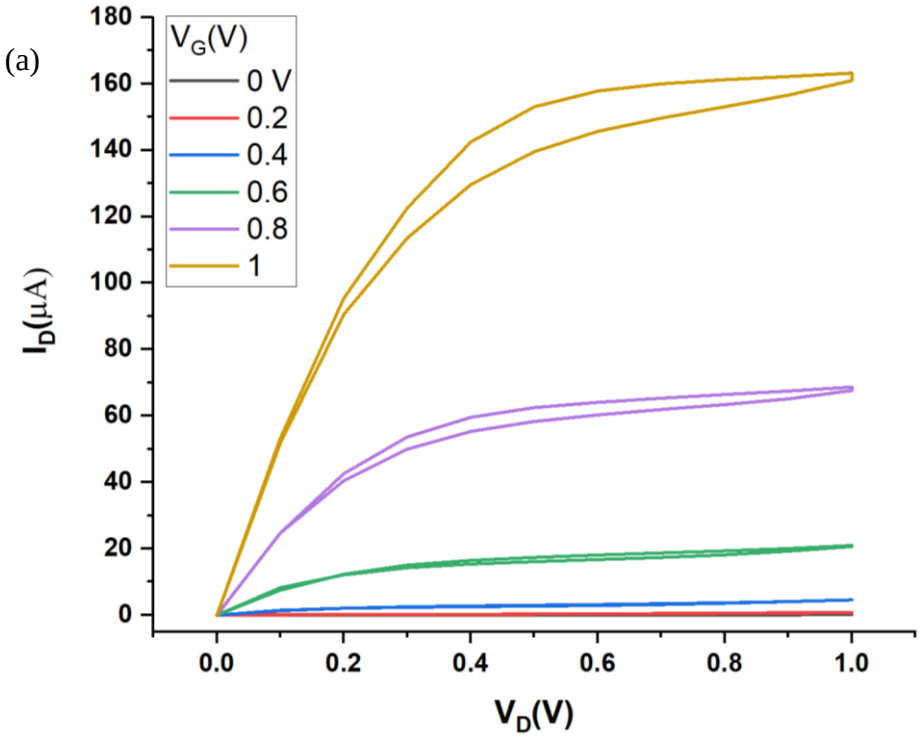

Figure 5.5 (a): Output characteristics of sprayed ZnO WGTFT

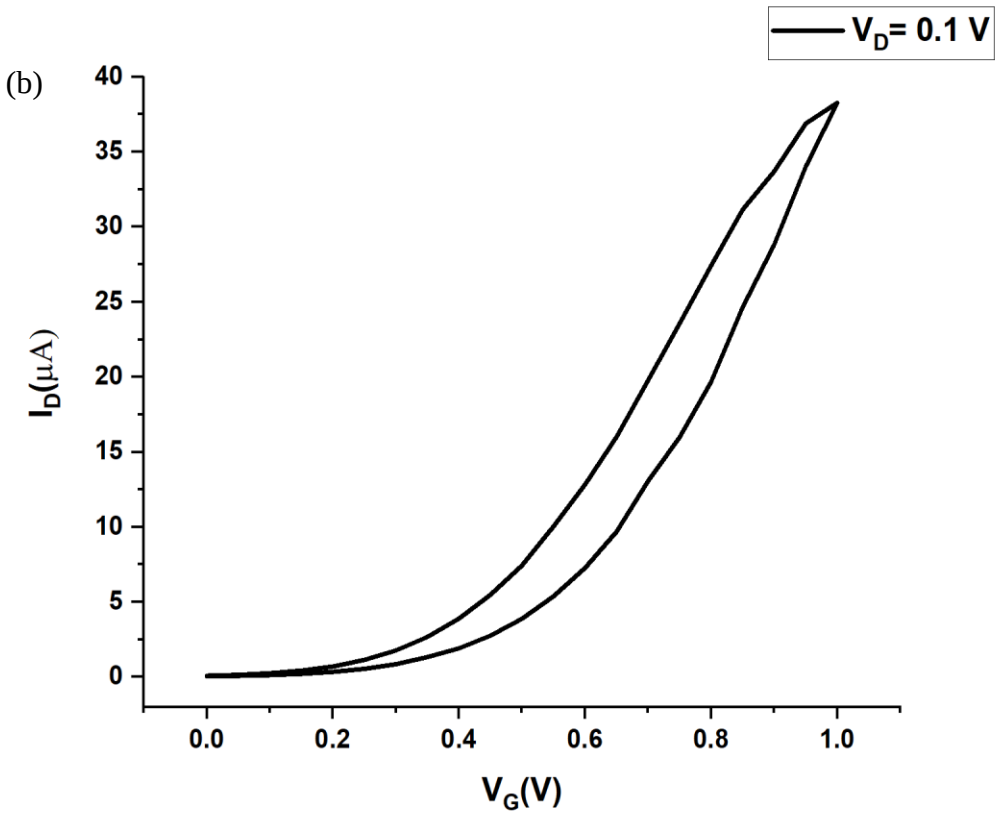

Figure 5.5 (b): Linear transfer characteristics of sprayed ZnO WGTFT (the extracted parameters are shown in table 5.2).

When comparing between SnO_2 and ZnO WGTFTs, there are clear differences in most of the parameters. The SnO_2 devices have a significantly lower threshold voltage and such characteristics are preferred in our sensing application. Due to the fundamental limitation of the water electrochemical window (which cannot be exceeded 1.23 volt), the low threshold voltage in SnO_2 allows for a larger accessible voltage range in the positive gate voltage axis in the case of a threshold voltage shift scheme. The I_{on}/I_{off} ratio in ZnO is two orders of magnitude higher than for SnO_2, such a high value is crucial in other TFTs applications (e.g. switches), but it should not be an obstacle in our sensing applications as the main parameter we monitor is threshold voltage. Subthreshold swing S.S also appears better for ZnO and again this does not compromise SnO_2 for the potential sensing application in this project. Electric field mobility is nearly in the same range, which could be due to similar levels of crystallinity and the same deposition method for both films.

5.4 SnO_2 long term stability compared with ZnO under water gating

In order to study and compare the stability of both SnO_2 and ZnO thin film transistors under water gating for a long period of time we used fresh samples of SnO_2 and ZnO. After initial characterization of these samples (output characteristics here as a qualitative measure), the transistor substrates were then stored in a container filled with 20 mL of PBS buffer solution (pH = 7.4) for extended periods of time and were occasionally retrieved from storage containers and characterized again. The PBS buffer was used here instead of water as it has higher ionic strength than water, thus representing a slightly 'harsher' environment for stability testing. The measured maximum saturated drain current $I_{D,max}$ was recorded against a logarithmic storage time scale (figure 5.6). $I_{D,max}$ can be defined as the I_D at the highest values of V_G and V_D, in this case at $V_G = V_D = 1$.

It is evident that ZnO transistors fail after only a few days of storage in PBS buffer. However, SnO_2 films still give viable transistors after more than 20 weeks (≈ 5 months) of storage under PBS. The zinc- to- oxygen bond in ZnO has partly ionic character [207] which leads to gradual dissolution of ZnO in water, severely limiting its practical use as water gated sensor transistors. The tin-oxygen bond in SnO_2 has largely covalent character which makes it considerably less soluble in water than ZnO.

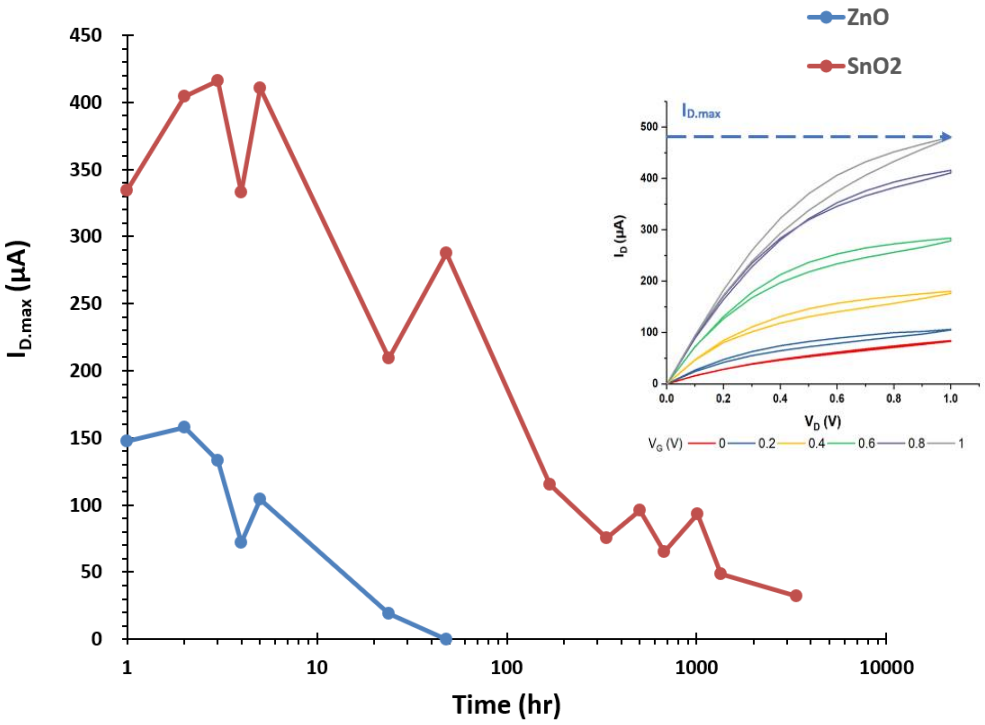

Figure 5.6: Comparison between the stability of SnO_2 and ZnO in PBS buffer for about 5 months. (inset: how to find $I_{D.max}$).

From figure 5.6, it is clear that after a specific time (here, after nearly 10 hours), the performance of SnO_2 transistors start to change (reduction in $I_{D,max}$). As they are used as sensors, I would prefer to highlight here that recalibration of the sensor is required at that stage to guarantee the accuracy of our device.

5.5 Conclusion

We studied the performance of spray pyrolyzed SnO_2 WGTFTs and especially its use in sensing analytes in the gating water. Overall, the good long term stability of SnO_2 under water, and the low threshold voltage of SnO_2 WGTFTs give advantages of SnO_2 WGTFTS. Despite the high off current, due to doping, we should not be concerned about using SnO_2 in WGTFTs sensors. So, the utilization of spray pyrolyzed SnO_2 rather than ZnO for practical WGTFT applications was decided.

Chapter 6: Sub-nanomolar detection of cesium with water-gated transistor

6.1 Zeolite as sensitizer in WGTFTs

Before showing how zeolites act as a sensitizer in WGTFTs sensors, I will start this chapter by giving an introduction about zeolites and their properties and applications, and what lead us to the idea of zeolite sensitized membrane in WGTFTs.

Zeolites are minerals that naturally form after volcanic activity. The structure of zeolite is composed of an aluminosilicate framework of SiO_4 and AlO_4 tetrahedra. These tetrahedra form the primary building units abbreviated to PBUs. By sharing oxygens between adjacent PBUs the obtained alignment is called secondary building units SBUs. SBUs can be arranged in different ways to form a number of units in a variety of shapes (for example a ring shape) which results in cages and channels in zeolites (see figure 6.1). These cavities in zeolites frameworks are usually occupied by H_2O molecules and commonly exchangeable cations (e.g. Na^+, K^+, Ca^{2+}). Some Al^{3+} ions replace Si^{4+} ions which leads to negative charges in the framework due to the valency difference between $(AlO_4)^{5-}$and $(SiO_4)^{4-}$ tetrahedrons. On the external surface of the zeolite, this negative net charge in the aluminosilicate structure is balanced by bonding with counter ions (cations). Generally, such bonds are weak electrostatic bonds which allows for the exchange of ions[215,216,217,218].

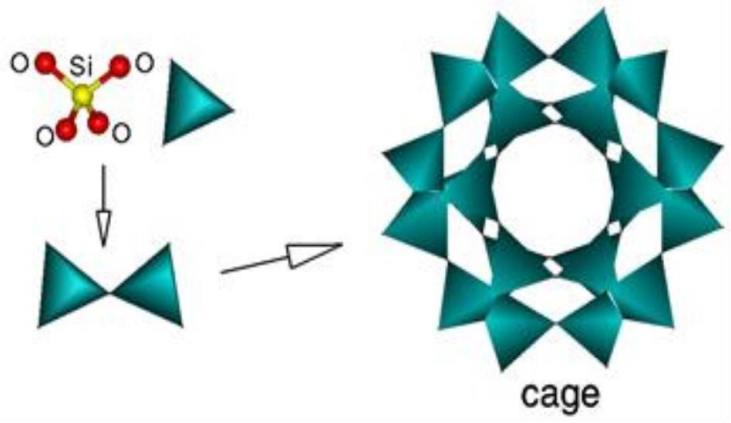

Figure. 6.1: Combination of SiO_4 PBUs to form a larger SBUs arrangement, which results in a cage[215].

Zeolites are exploited in various applications due to their valuable properties. Mainly as ion exchanging materials, molecular sieves and their absorption properties, which make them useful in important applications such as in water treatment, environmental monitoring , medical uses and catalysis[215,219,220]. Ion exchange occurs if the loosely bound ion on the zeolite surface is replaced with another ion from the surrounding environment[215,216]. The released ions (e.g. Na^+, K^+, Ca^{2+}) after ion exchange are usually harmless to the environment. Zeolites are also used as molecular sieves due to the different sizes of the cages and pores, only molecules and ions with the same size of these pores or smaller can pass and larger ones cannot pass through at all[215,216]. Therefore, zeolites are known as highly selective sorbents. Also, zeolites possess other advantages including mechanical and thermal stability, large surface area, availability and low cost[215,219]. In addition to natural zeolites and in order to obtain molecular sieve materials with specific properties and pores sizes, synthetic zeolites were developed. There are about 40 types of natural zeolite and 200 types of synthetic zeolites[221].

The use of zeolites in water treatment is very important and the most relevant application to this thesis. There is increasing demand for clean and safe water not only for drinking, also there is the problem of contaminated wastewater which is released into the ecosystem. Due to the high absorption, size selectivity and ion exchange quality of zeolites, they are utilized widely in this field. Many pollutants including organic, inorganic compounds, heavy metal and radionuclides have been removed from aqueous medium by different types of zeolites[215, 221]. Ammonium for example was removed from greywater and wastewater using natural zeolites[218,222]. In addition, zeolites have been reported to purify water containing a number of heavy metal cations[223,224,225,226] such as Cu^{2+}, Zn^{2+}, Cd^{2+}, Pb^{2+}, Hg^{2+} and Mn^{2+}. Organic compounds and inorganic anions (e.g. F^-, NO^-_3, ClO^-_4) can be adsorbed by surface modified zeolites. That is because of the negatively charged zeolite surface which requires surfactant modification to adsorb anions and hydrophobic organic contaminants[224,227,228]. Examples of organic contamination, include petroleum and phenolic compounds which are usually released to the environment from industrial processes[224,229,230]. Another important role for zeolites in water treatment is the removal of radioactive ions caused by nuclear incidents, for example Cs^+, Sr^{2+} as reported in [231,232]. Different types of zeolite show high affinity toward certain ions or molecules. Clinoptilolite for example,

the most abundant natural zeolite, absorbs heavy metals well[223,233]. Zeolites with high Silicon content (high Si/Al ratio) such as ZSM-5 (a synthetic zeolite) exhibit good ability to remove phenol from water[230,234].

Zeolites have emerged in the field of potentiometric sensors due to their excellent selectivity and ion-exchanging capacity which make them promising candidates for preparing selective sensitized membranes[133]. It has been reported in ion-selective electrodes (ISE) when zeolite was exploited as a sensitizer. For instance, in pH sensitive electrode[221], perchlorate and Cs^+ sensors[228,235]. Also, in ion selective field effect transistor (ISFET) biosensors the zeolites were exploited and shown to increase the sensitivity[31],[236]. The use of zeolite sensitizers in newer sensor families deserves to be evaluated and assessed. Therefore, in this chapter, we will demonstrate the implantation of Cs selective zeolite (mordenite) in a WGTFT.

The results included in this chapter are reproduced from [Alghamdi, N., Alqahtani, Z., & Grell, M. (2019). Sub-nanomolar detection of cesium with water-gated transistor. *Journal of Applied Physics*, *126*(6), 064502.], with the permission of AIP Publishing". All the experimental work in this publication was done by myself (Nawal Alghamdi) in collaboration with Zahrah Alqahtani and under Dr Martin Grell's supervision.

6.2 Introduction

The report by Kergoat *et al*[34] that thin film transistors can be gated across water as the electrolytic gate medium (water-gated thin film transistors, WGTFTs) has paved the way for a new sensor technology for waterborne analytes. When a WGTFT is sensitized with a suitable receptor, an analyte borne in the gating water may bind to the sensitizer. This binding is transduced into a change of the WGTFT characteristics, usually this is a shift in threshold voltage, V_{th}. The V_{th} is the gate voltage required for an accumulation layer to form in the transistor channel and is evident from the increase in drain current with gate voltage once V_G exceeds V_{th}. A number of examples for such sensors have been reported, *e.g.* for dopamine and other analytes[32,150,190]. An important sub-genre of WGTFTs are the ion- selective WGTFTs, first introduced by List-Kratochvil [148]. So far, the sensitizer in such devices has always been an organic 'ionophore', for example a crown

ether[93], calixarene[237,138], or valinomycin [149]. Typical 'target' ions are K^+, Na^+, Li^+, Ca^{2+}, Mg^{2+} [238]. The ionophore is often introduced into the WGTFT within a plasticised PVC membrane, for example in a 2- chamber design [148]similar to the classical electrochemical potentiometry [239,240,] or by direct application of the membrane onto the gate contact [93], or the semiconducting channel [149], of the WGTFT. Also, membrane-free ion sensitive WGTFTs have been demonstrated [138] where the ionophore is incorporated into the semiconducting channel. WGTFT sensors are typically formed using solution-processed semiconductors, *e.g.* semiconducting polymers [150,93,138], precursor- route metal oxides [93], or carbon nanotubes [149]. Selective binding of waterborne ions in the gating water to the ionophore leads to a membrane potential, V_M, and consequentially a shift in V_{th}. Quantitatively, the threshold shift $\Delta V_{th}(c)$ follows a Nikolsky- Eisenman law [93],[241], *i.e.* Nernstian (linear on a logarithmic concentration scale) at high ion concentrations ($c >> c_{st}$), but flatlining below a concentration c_{st}, hence giving a limit-of-detection (LoD) $\approx c_{st}$:

$$V_M(c) = \Delta V_{th}(c) = 58\ mV/z \log [(c + c_{st}) / c_{ref}] \qquad 6.1$$

Wherein z is the valency of the cation (z = 1 for alkaline metals), and $c_{ref} >> c_{st}$ is the ion concentration in a reference solution. The c_{st} depends on the ion and ionophore, but typically is in the range 100 nM to 1µM [93, 30, 137]. Strictly speaking equation 6.1 should be formulated in terms of ion activities rather than concentrations but we neglect this difference here, as response characteristics are usually linear on a log concentration scale without correction for activities. The Nikolsky- Eisenman characteristic is distinct and different from the Langmuir adsorption isotherm which quantifies fractional surface coverage $\theta(c)$ ($0 < \theta(c) < 1$) of an adsorbate on a surface providing adsorption sites. Mathematically, Langmuir gives $\theta(c)$ by equation. 6.2:

$$\theta(c) = Kc / (Kc + 1) \qquad 6.2$$

Wherein K is the stability constant for the adsorbate / adsorption site binding; $1/K = c_{1/2}$ with $c_{1/2}$ defined as $\theta(c_{1/2}) = ½$. Response characteristics logically equivalent to equation 6.2 are usually

found for optical sensors, known as the 'Hildebrand- Benesi' law for sensors based on optical absorption, or 'Stern- Vollmer law' for sensors based on fluorescence [*e.g.* [26]]. A potentiometric sensor following equation 6.2 would be characterised by a threshold shift $\Delta V_{th}(c) = \Delta V_{th}(sat)\ \theta$ (c), wherein $\Delta V_{th}(sat)$ is a saturation value in the limit $c >> c_{1/2}$ as $\theta\ (c >> c_{1/2}) \rightarrow 1$.

Here, we introduce an inorganic ionophore, namely a zeolite, into a WGTFT architecture. Zeolites are microporous hydrated aluminosilicates with tetrahedral primary building blocks made of a central silicon or aluminum atoms surrounded by four atoms of oxygen at the corners of the tetrahedron, forming regularly arranged nanocavities or 'channels' [220, 221]. Substitution of Si^{4+} by Al^{3+} introduces negative charges into the zeolite framework. These are balanced by counter-cations such as Na^{+} or H^{+} inside the cavities. When zeolites come into contact with aqueous media that carry other ions, their original counter-cations can be exchanged for cations drawn from the surrounding media. As the channels have a clearly defined diameter, this ion exchange is often highly selective for cations with a favorable radius [221].

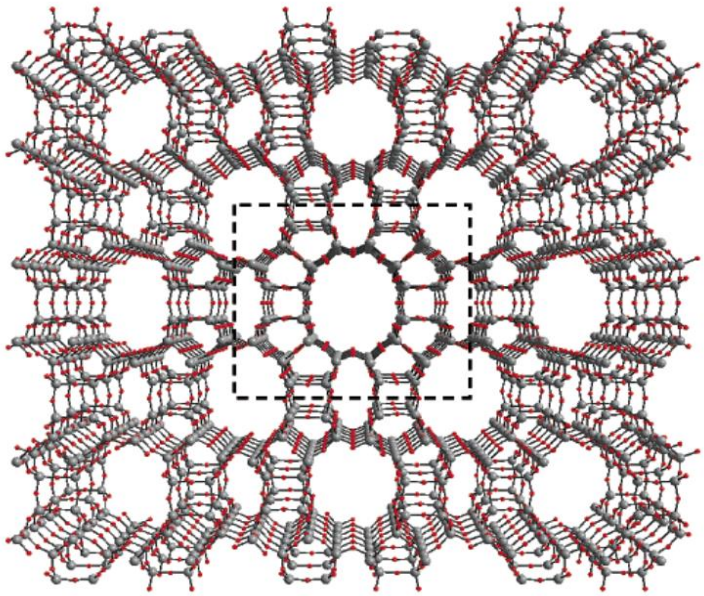

Figure 6.2: The structure of mordenite zeolite[302] .

Here, we used the natural zeolite known as 'mordenite' figure 6.2, which has main channels with a cross-section of 0.65 nm x 0.70 nm and smaller channels of 0.26 nm x 0.57 nm [242, 243, 244]. Mordenite exhibits good selectivity towards the alkaline metal cation, Cs^+ (hydration radius 0.33 nm) , which it extracts from aqueous media even when these contain a vast excess of Na^+ and K^+ [231, 12]. This qualifies mordenite as sensitiser for the selective detection of waterborne Cs^+, as well as for its specific removal. While Cs^+ is rare in nature, the β^- active radioisotope ^{137}Cs is released into the environment *e.g.* in nuclear accidents[245, 246]. Detection of Cs^+ in drinking water (and removal from it) is therefore relevant for the detection of such incidents, which may be concealed, and the protection of humans and animals from drinking contaminated water. Prior work on detecting Cs^+ ions with mordenite used atomic absorption spectroscopy (AAS) [231] applied to mordenite after contact with Cs^+ contaminated water. However, the WGTFT transducer has a much lighter experimental footprint than AAS. As the semiconductor we used spray pyrolysed SnO_2. In response to increasing Cs^+ concentration in water, we find a WGTFT threshold shift that follows the Langmuir adsorption isotherm (equation 6.2) rather than the Nikolsky- Eisenman law, equation 6.1. We find a large stability constant of K = (3.9 +/- 0.4) x 10^9 L/mole and a LoD of 33 pM, 4 orders-of-magnitude below potentiometric Cs^+ detection with organic ionophores[137,247]. Our device is therefore well suited to assay water for the potability limit of 7.5 nM Cs^+ as recommended by the Agency for Toxic Substances and Disease Registry [248].

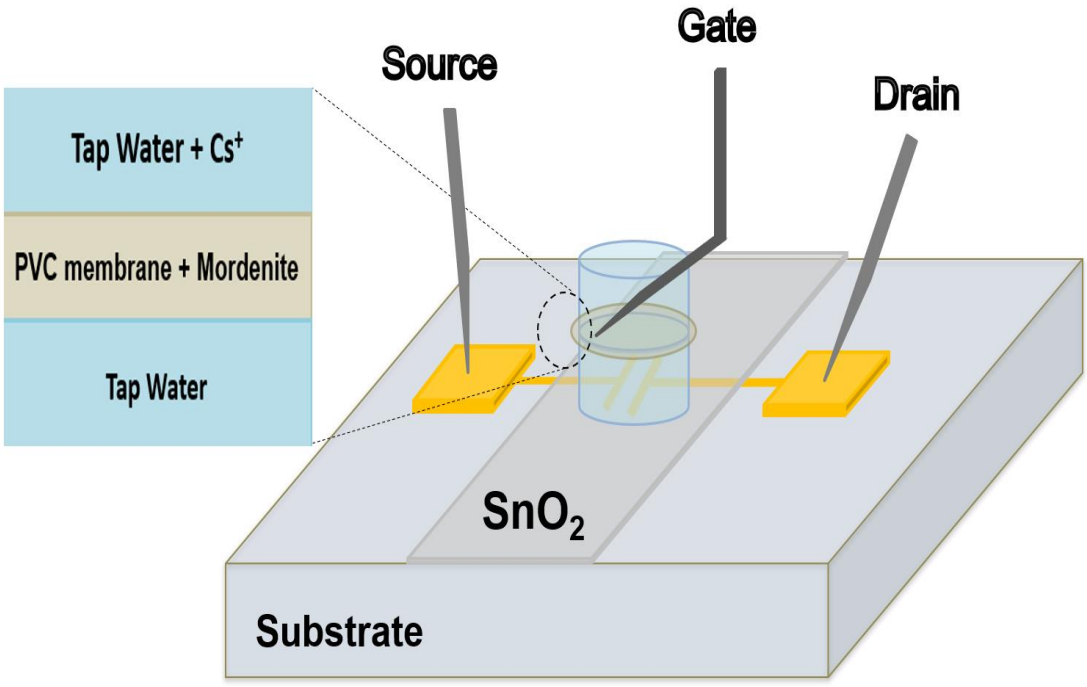

Figure. 6.3: Design of a Cs^+- sensitive water gated field effect transistor.

6.3 Material and methods

6.3.1 Preparation of SnO_2 transistor substrates by spray pyrolysis

Transistor contact substrates were prepared by thermal evaporation of Au(100 nm) with Cr (10 nm) as an adhesion layer onto clean quartz- coated glass substrates sourced from Ossila Ltd (order code S151) by a shadow mask. Each substrate contains 5 pairs of electrodes separated by a channel with a length L = 30 µm and width W = 1000 µm (W/L = 33.3). Onto the contact substrates, a SnO_2 film was prepared by spray pyrolysis. Spraying was performed using an airbrush from 20 cm distance onto contact substrates preheated to 400 ^oC. SnO_2 was sprayed from 0.05 M $SnCl_4.5H_2O$ dissolved in isopropanol by four similar sprays with 1 min intervals [249, 209, 210]. Afterward substrates were left on a hot plate for 30 min for full decomposition of the SnO_2 precursor. We measured SnO_2 film thickness of ~ 45 nm with a Dektak surface profilometer. The literature value for the bandgap of SnO_2 is 3.6 eV [210].

6.3.2 Preparation of ion- selective PVC membranes

Poly(vinyl chloride) (PVC), 2-Nitrophenyl octyl ether (2NPOE), and tetrahydrofuran (THF) were purchased from Sigma Aldrich while the zeolite mordenite was sourced as a fine powder from Fisher scientific. Caesium chloride (CsCl) and Sodium chloride (NaCl) were sourced from Atom Scientific and APC Pure, respectively. The PVC membranes were prepared based on the procedure described in [133]. We dissolved (30 mg) of PVC, (65 mg) of plasticiser 2NPOE, and (20...40) mg of mordenite in (3 mL) of THF. 500 µL of the solution was poured into a small vial and left overnight at room temperature to allow evaporation of THF. The resulting membranes were ~ 0.4 mm thick and they were then conditioned for one day in tap water. Finally, the membrane was glued in between two plastic pools with epoxy, see Figure. 6.1. A microphotograph of a conditioned membrane is shown as inset to figure. 6.4a, which illustrates the dispersion of powdered sub- micrometer mordenite particles within the plasticised PVC matrix.

6.3.3 Preparation of test solutions

To simulate realistic conditions for practical use of our sensor, we did not work with deionised water but drew water samples from drinking water taps at our lab at the University of Sheffield. The most common cations in tap water are calcium, magnesium, sodium, and potassium [250] . For the assessment of water quality in the UK, the Drinking Water Inspectorate (DWI) releases an annual summary report [251] where it reports its monitoring of many chemicals in water, but this does not include Cs^+ as it is usually negligible from drinking water. We hence work with water that contains a 'cocktail' of common ions, but initially, no considerable amount of Cs^+ (Appendix table 6A.1&2). We then prepared a Cs^+ stock solution by dissolving CsCl in tap water at 1 µM concentration. We then get the desired (lower) concentrations used in experiments by diluting with more tap water to (500, 300, 100, 50, 10, 1, 0.5, 0.4, 0.3, 0.2, and 0.1) nM Cs^+. For control experiments, Na^+ solutions were prepared similarly from NaCl.

6.3.4 Two- chamber gating setup

To test the response of membrane- sensitized WGTFTs to Cs^+, we used a 2- chamber design, similar to some previous workers [235,148], which is derived from the design of traditional

potentiometric ion sensors [239]. The SnO_2 transistor substrate was in contact with tap water held in an 'inner' reference pool that is separated by the sensitized PVC membrane from a second, 'outer' sample pool. The outer pool is initially also filled with tap water, but this is then subsequently replaced with ion solutions of increasing concentrations, while the inner pool remains filled with tap water as an analyte- free reference. The transistor is gated by a tungsten (W) contact needle that is in contact with the solution in the outer pool. As with all electrolyte- gated transistors, the potential applied to the gate contact is communicated to the semiconductor surface via interfacial electric double layers (EDLs). The potential that is applied at the semiconductor surface is different from the potential applied to the gate needle by any potential that builds across the membrane, V_M, in response to different ion concentrations in the outer *vs.* inner solution. The setup is illustrated in figure. 6.3.

6.3.5 WGTFT characterisation and analysis

As V_M adds to the applied gate voltage it can be measured as a shift in the WGTFT's threshold voltage, ΔV_{th}. We therefore recorded linear transfer characteristics using a standard transistor characterisation setup reported earlier [93,138]. After 30 seconds of exposure each time a new electrolyte was filled into the outer pool as described in 2.4, we scanned V_G from - 0.2 V to + 0.7 V in steps of 20 mV at constant drain voltage V_D = 0.1 V ('off → on' sweep), and back from + 0.7 V to - 0.2 V ('on → off' sweep). Waiting longer than 30 sec did not result in different characteristics, we thus conclude the membrane had equilibrated within the initial 30 sec incubation in the respective new (increased) analyte concentration. To determine membrane potential $V_M = \Delta V_{th}$, we compensate for it by shifting recorded linear transfer characteristics for each Cs^+ concentration along the gate voltage (V_G) axis. We identify ΔV_{th} as the gate voltage shift required to achieve best overlap with the characteristic under tap water without any added Cs^+. This method does not rely on any particular mathematical model of the linear transfer characteristics and is therefore robust even when transistors do not strictly follow theoretical TFT equations. This same analysis has been used previously in other WGTFT sensors work, *e.g.* [32,93,138]. Finally, data were presented in appropriate plots (Inset figure.6.5a, figure.6.5b) and straight lines were fitted using the linear regression routine available in Origin.

6.4 Results and discussion

6.4.1. Cs^+ ion sensing

Figure. 6.4.a shows the linear transfer characteristics of a SnO_2 TFT substrate gated as shown in figure. 6.3 under increasing Cs^+ concentrations in the outer pool. Note we only show the transfer characteristics' 'rising' flank (gate sweep from 'off → on'), as these closely match the theoretical expectation for TFT linear transfer characteristics. Full characteristics do display hysteresis, *i.e.* the 'on → off' sweep does not exactly replicate the rising flank. 'On → off' sweeps are omitted in figure. 6.4a for clarity, but full hysteresis loops are provided in appendix, figure. A6.1.

We find that all characteristic' 'rising flanks' are similar to each other but with increasing threshold voltages, V_{th} under increasing Cs^+ concentration, with a significant threshold shift even under 100 pM Cs^+, which compares favourably to the recommended potability limit of 7.5 nM [248]. This is despite the simultaneous presence of other alkaline and alkaline earth ions (Na^+, K^+, Ca^{2+}, Mg^{2+},...) in common tap water at significantly higher concentrations than 500 nM [252,253]. At higher Cs^+ concentrations, ~ 50 nM and more, threshold shift saturates, *i.e.* it no longer increases with increasing Cs^+ concentration. This saturation happens probably due to that all the binding sites in the mordenite are occupied by Cs^+, so higher concentrations of Cs^+ do not result in any further shift. The known selectivity of mordenite for Cs^+ over other cations [231] does translate to the WGTFT transducer. In figure. 6.4b we show the characteristics from figure. 6.4a after shifting them along the gate voltage axis for best overlap with the characteristic at c = 0. We find that all curves overlap well into a single 'master curve', confirming that threshold shift is the only impact of increasing Cs^+ concentration in the outer pool on the WGTFT characteristics. If for instance carrier mobility would also be affected, no master curve could be achieved. This allows the interpretation of the required shift along the gate voltage axis as membrane potential, $V_M(c) = \Delta V_{th}(c)$.

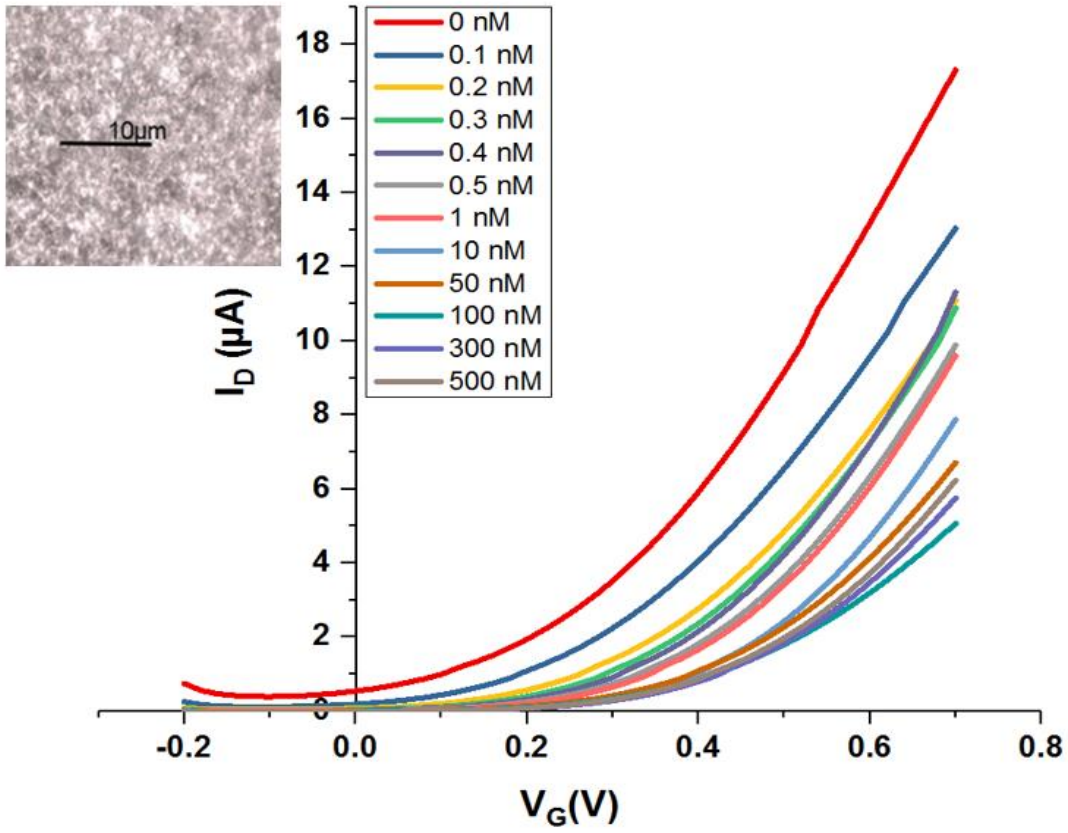

Figure. 6.4a: Transfer characteristics of mordenite- sensitized SnO_2 WGTFT gated as shown in figure. 6.1 under increasing Cs^+ concentrations in the outer pool. Inset: Optical microscope photograph of a mordenite- loaded PVC membrane. Mordenite loading in the membrane was 3.3 mg.

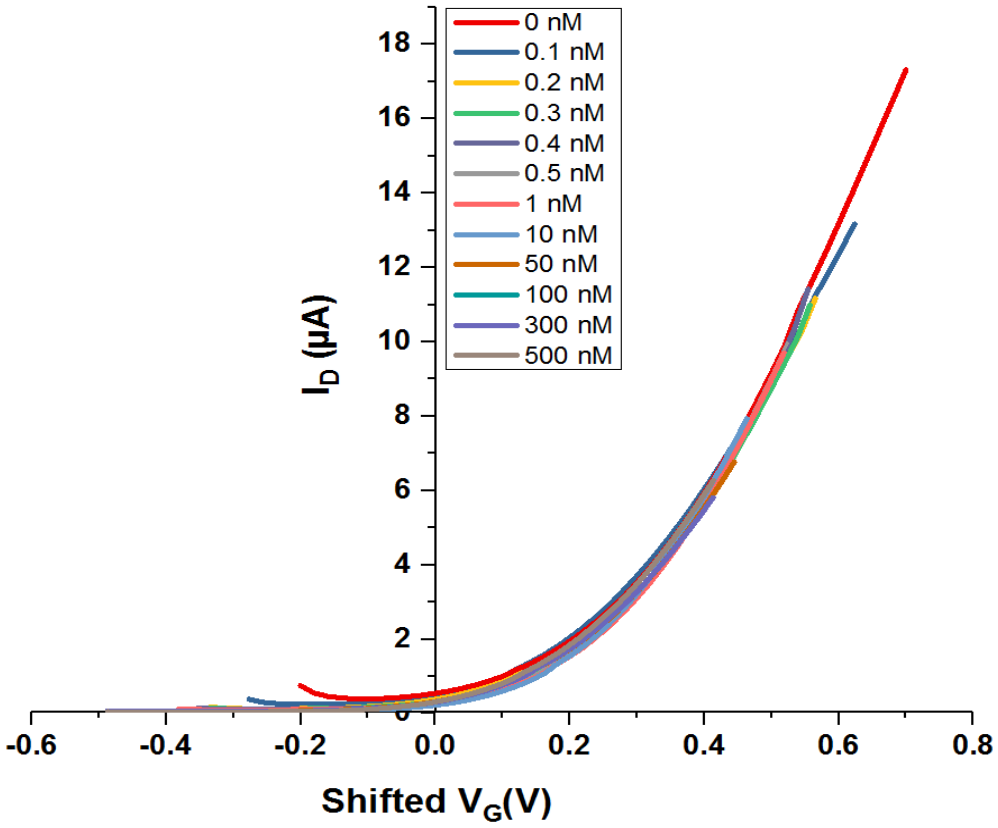

Figure. 6.4b: The same measured transfer characteristics as in figure. 6.4a but shifted along the V_G axis to overlap with zero Cs^+ characteristics and create a master curve.

The shift- and- match procedure that leads from figure. 6.4a to figure. 6.4b gives us $\Delta V_{th}(c)$ quantitatively. $\Delta V_{th}(c)$ is tabulated in table 6.1 and presented on a linear concentration scale in figure. 6.5a. The $\Delta V_{th}(c)$ rises rapidly (approximately linearly) for low concentrations ($c << 50$ nM), but saturates at $c > 50$ nM. To ascertain reproducibility, we have prepared two more SnO_2 substrates and mordenite membranes nominally identically to the device used for figure. 6.4 and exposed them to a Cs^+ concentration of 1 nM. Table 6.1 also shows the observed threshold shift under 1 nM for all 3 devices; we find a similar threshold shift every time, demonstrating good reproducibility of these devices.

Table 6.1: Threshold shift, as determined by the procedure leading from figure. 6.4a → 6.4b, vs. Cs+ concentration in the outer pool. The measurement under 1nM Cs+ has been repeated on 2 more devices to demonstrate consistency.

c [nM]	$\Delta V_{th}(c)$ [mV]
0.1	80
0.2	130
0.3	160
0.4	170
0.5	200
1	220
1 (2^{nd} device)	205
1 (3^{rd} device)	210
10	260
50	270
100	310
300	300
500	300

However, the threshold shift *vs.* concentration characteristic in figure. 6.5a is clearly different from the Nikolsky- Eisenman law, equation 6.1, which is linear on a logarithmic concentration scale for high concentrations, with no saturation at high c, but flatlines at low concentrations ($c < c_{st}$). Instead, the $\Delta V_{th}(c)$ characteristics resemble a Langmuir adsorption isotherm, equation 6.2.

The Langmuir-like form of the response characteristic is confirmed by the good straight line fit to the corresponding Hildebrand-Benesi plot, $1/\Delta V_{th}(c)$ *vs* 1/c, shown as inset to figure. 6.5a.

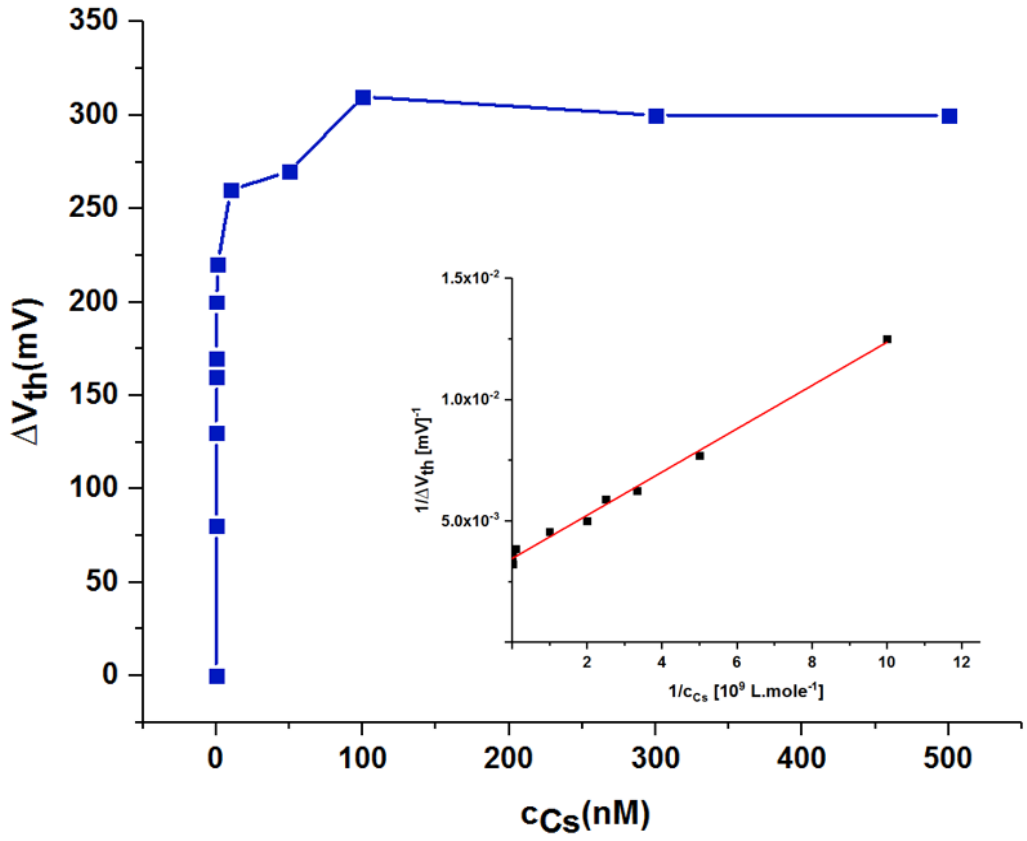

Figure. 6.5a: The threshold shift ΔV_{th} *vs* concentration of Cs^+, c_{Cs}. Inset: Hildebrand- Benesi plot with a straight line fit.

The Hildebrand- Benesi plot (inset figure. 6.5a) allows the extraction of the parameters $\Delta V_{th}(sat)$ from the intercept with $1/\Delta V_{th}$ axis, and K from the ratio of intercept to slope. The linear regression

routine in Origin gives $\Delta V_{th}(sat)$ = (290 +/-7) mV, and K = (3.9 +/- 0.4) x 10^9 L/mole, corresponding to $c_{1/2}$ = (258 +/- 26) pM. Optical sensors using organic ionophores usually show significantly smaller K, e.g. K = 5 x 10^4 L/mole [254], or 10^5 L/mole[247]. We believe this is due to the channel- like nanocavities in zeolite structures wherein cations absorb more strongly than in the rather point- like 'holes' in ring- shaped organic cation sensitiser molecules, e.g. crown ethers [247]. As a caveat, we note that the observed threshold shift results from the extraction of Cs^+ by mordenite from the sample, which will reduce Cs^+ concentration in the sample. The Cs^+ concentrations we here quote are the concentrations we have initially introduced and do not account for depletion due to partial extraction. The degree of depletion will depend on the relative proportions of mordenite loaded into the membrane and the sample volume. Other workers using different membrane compositions and areas, and/or different pool volume, should recalibrate their sensor. The very high K also explains our observation that sensors do not recover when the solution in the outer pool is replaced by Cs^+- free water after it was once exposed to 500 nM Cs^+ solution: The binding of Cs^+ to mordenite is so strong that it cannot easily be reversed. Recovery may be possible by washing membranes in running Cs^+- free water, but we recommend using a fresh membrane after a sensor has once detected Cs^+ in water, which should practically be a rare event, due to its scarcity in the environment.

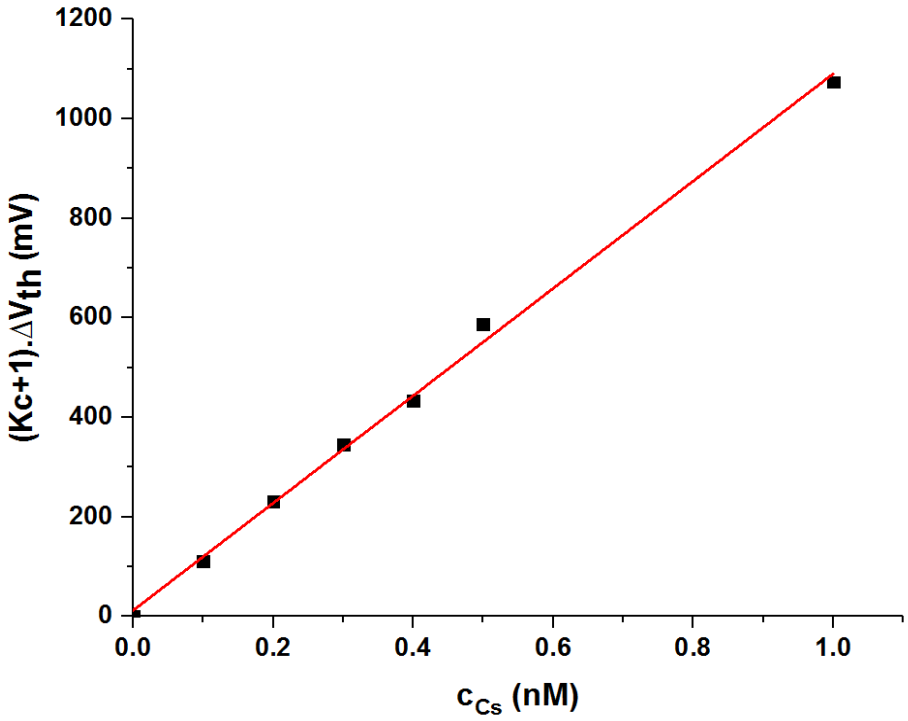

Figure. 6.5b: Linearised plot of the response characteristics from Figure. 6.5a, $(Kc + 1)\Delta V_{th}(c)$ *vs* c in the limit of small c.

It is this large K that allows the detection of Cs^+ with very low limit-of-detection (LoD). To determine LoD, we have plotted the response characteristics in linearised form, $(Kc + 1)\Delta V_{th}(c)$ *vs* c for small c in figure 6.5b, which according to equation 6.2 should result in a straight line with slope m and a near-zero intercept b +/- Δb with $\Delta b \gtrsim b$. We here find a good straight line fit, as expected, with m = 1078 mV/nM and b = (12.8 +/- 11.8) mV, which we use to determine LoD with the conventional '3 errors' criterion, equation 6.3 [26]:

$$LoD = 3\Delta b / m \qquad 6.3$$

We here find LoD = 33 pM, this is more than 3 orders- of- magnitude lower than typical LoD $\approx c_{st}$ for K^+- selective WGTFTs sensitised with organic ionophores [93,30], and 4 orders- of- magnitude

below prior potentiometric Cs^+ sensors using organic ionophores [137,255].

To investigate the unusual Langmuir- like response characteristic in more detail, we prepared PVC membranes containing different amounts of mordenite. The response characteristics were similar to those in figure. 6.5a, however they saturated at different $\Delta V_{th}(sat)$ under Cs^+ concentration c >> 1/K, see figure. A6.4 in the appendix section. The $\Delta V_{th}(sat)$ increased with sensitizer concentration but complex stability constants K were found having the same order- of- magnitude, see table A6.3. This is another difference to Nikolsky- Eisenman behaviour where response depends only on analyte concentration but is independent of the amount of sensitiser in the membrane, *cf.* equation 6.1. Further, when we reverse the application of analyte to the WGTFT by introducing it into the inner rather than the outer pool, the threshold shift retains its positive sign but its magnitude is much reduced, *cf.* figure. A6.4. In a sensor following Nikolsky- Eisenman characteristics, threshold shift for $c >> c_{st}$ would reverse its sign but retain its magnitude under reversal of sample *vs* reference compartment. These comparisons show that response characteristics of zeolite-sensitised membranes are clearly different from Nikolsky- Eisenman behaviour. We also tried to use another semiconductor of p-type (P3HT) to see if a membrane potential and a threshold shift in the same direction can be obtained. Figure A6.5 in the appendix shows that we do get shift from the membrane potential in the same direction (toward positive axis) if P3HT WGTFT is used.

It is important to note here that by comparing K and $c_{1/2}$ for mordenite extracting Cs^+ in our method, the threshold voltage shift (membrane potential) with mass extraction[154] method, $c_{1/2}$ was very much smaller for membrane potential than for mass extraction. In the later method, the value of $c_{1/2}$ = 50 mg/L = 0.365 mM (>> 258 pM). Another point to raise here is that the different characteristics we get here could be related to a different Cs^+ extraction mechanism. In the case of mordenite ion exchanging with Cs perhaps occurs, while in other sensitizers the mechanism maybe different. This is only a hypothesis and needs further study.

6.5 Conclusions

When plasticised PVC membranes are sensitised with organic ionophores, these achieve limit-of-detection (LoD) values in the order (100 nM - 1µM) in the potentiometric detection of common

waterborne cations such as Na^+, K^+, Ca^{2+}, (*e.g.* [235,148, 93, 138, 149, 239, 137, 255]). This is adequate for detection at their relevant concentrations in the (micro…milli) molar range. However, the detection of radioactive or toxic elements (*e.g.* $^{137}Cs^+$, Sr^{2+}, Pb^{2+}, Cd^{2+}) demands LoD in the order nanomolar (nM) or below, which organic ionophores do not currently achieve.

Here we demonstrate sub-nanomolar membrane-based potentiometric WGTFT ion sensors using the highly relevant analyte Cs^+. Cs^+ is rare in nature, but traces of the β^- active radioisotope ^{137}Cs are often found in drinking water in the wake of nuclear accidents. We sensitized a PVC membrane with an inorganic zeolite, 'mordenite', instead of using an organic ionophore, and introduced this membrane into a WGTFT architecture using a spray- pyrolysed semiconductor, SnO_2. We find Langmuir- like response characteristics with a high stability constant, K = (3.9 +/- 0.4) x 10^9 L/mole, (~ 4 - 5) orders of magnitude larger than typical K's for the complexation of cations to organic chromoionophores [254,247]. This leads to an extremely low LoD of 33 pM against a realistic 'interferant cocktail' of common cations, as we worked with tap water drawn in our lab rather than DI water. The dynamic range of our sensor spans 3 orders from LoD = 33 pM to saturation at ~ 50 nM Cs^+, overlapping well with the practically relevant potability limit of 7.5 nM Cs^+ [248]. For comparison, potentiometric transduction of Cs^+ with organic (crown ether) sensitised membranes showed Nikolsky- Eisenman characteristics with LoD 380 nM and 240 nM, respectively [137, 255], 4 orders- of- magnitude larger than our LoD, and significantly above the safe Cs^+ potability limit.

With regard to observing Langmuir- like membrane potential characteristics here, rather than the Nikolsky- Eisenman law, we note a key difference between the common experimental protocol for potentiometric ion sensors, and our work: Conventionally, the inner reference pool contains analyte ions at a concentration $c_{ref} >> c_{st}$, and membranes are pre-conditioned in analyte solution at the same or similar concentration as c_{ref}, cf. e.g. [239,240,137]. We rejected such conditioning because typical c_{ref} is in the range of mM, many orders larger than the Cs^+ potability limit. A membrane conditioned in mM Cs^+ could potentially contaminate samples to and beyond 7.5 nM when they come in contact, giving false positives. Instead we used common tap water as the reference- and membrane conditioning medium. This will contain a realistic interferant 'cocktail' of common cations (Na^+, Ca^{2+}, K^+, Mg^{2+},...), but no Cs^+ analyte, *i.e.* $c_{ref} = 0$. Note the Nikolsky- Eisenman law,

equation 6.1, fails for $c_{ref} \rightarrow 0$. While the exact reason for the unusual Langmuir membrane potential characteristics warrants further investigation, we here pragmatically use it to push the LoD to the extremely low levels needed to assay drinking water for traces of potentially harmful Cs^+ ions.

Chapter 7: Monitoring the lead- and- copper rule with a water- gated field effect transistor

7.1. Introduction

The discovery in 2010 by Kergoat et al. [34] that water can work as electrolyte gate media in thin film transistor (WGTFTs) opened a new category of water-borne analytes sensors. When these WGTFTs are sensitized with suitable receptors (sensitizers), the binding between the analyte and the sensitizer will be transduced into an electrical signal that can be measured by the WGTFT. Since this finding WGTFTs have been exploited for the sensing of different water-borne analytes such as ions, mainly using PVC membranes loaded (doped) with organic ionphores[32,150,148,138,93].

We have recently incorporated an inorganic ionophore, a zeolite mineral called 'mordenite', into a WGTFT [256](chapter 6). Mordenite is known to selectively extract Cs^+ ions from water [231,12]. This is useful for assessing water contaminated with the radioisotope $^{137}Cs^+$ [257]. We found a strong WGTFT threshold voltage shift at very low Cs^+ concentrations (~ picomolar) with response characteristics given by the Langmuir adsorption isotherm, equation 7.1, rather than equation 6.1 (Nikolsky- Eisenman equation):

$$\Delta V_{th}(c) = \Delta V_{th}(sat)\, Kc / (Kc + 1) \qquad 7.1$$

Wherein K is the stability constant for the analyte / sensitiser binding and $\Delta V_{th}(sat)$ the saturated value of threshold shift in the limit $c >> c_{1/2} = 1/K$, with $c_{1/2}$ defined as $\Delta V_{th}(c_{1/2}) = ½\, \Delta V_{th}(sat)$. We found a very large K, $K = 3.9 \times 10^9$ L/mole, and very low LoD value of 33 pM, well below the 'potability' limit of 7.5 nM for Cs^+.

Two common low-level toxic pollutants in drinking water are the heavy metal cations lead (Pb^{2+}) and copper (Cu^{2+}), *e.g.* lead leaches from historic water pipes, copper from 'low tech' water sterilisation[258,259]. Lead and copper are subject to governmental regulation, for example, the US Environmental Protection Agency's (EPA) 'lead- and- copper rule' [260] sets 'action levels' of 0.015 mg/L = 72 nM for lead and 1.3 mg/L = 20.5 μM for copper in the domestic water supply.

In drinking water treatment, another zeolite, 'Clinoptilolite', is used to extract Pb^{2+} and Cu^{2+} from water[261]. Clinoptilolite forms naturally by volcanic ash alternation in water[262] and is mined from natural deposits[223]. Here we show that WGTFTs sensitised with a clinoptilolite- filled membrane provide a simple potentiometric sensor with very low limit- of- detection that is suitable for monitoring the lead- and- copper rule. The response characteristic is described by a generalisation of equation 7.1, known as the 'Langmuir- Freundlich' (LF) isotherm,

$$\Delta V_{th}(c) = \Delta V_{th}(sat)\ (Kc)^{\beta} / ((Kc)^{\beta} + 1) \qquad 7.2$$

The additional parameter $\beta < 1$ describes inhomogeneity in the analyte / ionophore binding sites [263]. The relation $c_{1/2} = 1/K$ remains true regardless of the value of β. The ratio of K's for a target analyte *vs.* an interferant (or the inverse ratio of $c_{1/2}$'s) quantifies the selectivity, S, of a sensitiser, for analyte *vs.* interferant.

The results included in this chapter have been published as Z. Alqahtani, N. Alghamdi, and M. Grell, J. Water Health 18, 159 (2020). All the experimental work in this publication is done in collaboration between myself (Nawal Alghamdi) with Zahrah Alqahtani and under Dr Martin Grell's supervision.

7.2. Experimental section

7.2.1. Preparation of SnO_2 transistor substrates by spray pyrolysis:

Transistor contact substrates and SnO_2 films were prepared exactly as in 6.3.1. We have shown previously in chapter 5 that SnO_2 leads to WGTFTs with very low threshold voltage and sufficient carrier mobility whilst also having good stability under water. These transistors can operate well up to two weeks, where calibration is needed for each experiment.

7.2.2. Preparation of ion- selective PVC membranes

Poly(vinyl chloride) (PVC), 2-Nitrophenyl octyl ether (2NPOE), and tetrahydrofuran (THF) were purchased from Sigma Aldrich. The zeolite clinoptilolite was sourced from DC Minerals' eBay shop (https://www.ebay.co.uk/str/DC-Minerals?_trksid=p2047675.l2568) as a fine powder, grain size < 40 µm. It is a natural product mined in bulk from mineral deposits and may be a mixture of different but similar compounds, which the supplier does not fully characterise. An approximate overall composition is given as $[(Ca, Fe, K, Mg, Na)_{(3\ to\ 6)}Si_{30}Al_6O_{72}].24H_2O$. PVC membranes were prepared based on the procedure described in[256,133]. We dissolved 30 mg of PVC, 65 mg of plasticiser 2NPOE, and 42 mg of clinoptilolite in 3 mL of THF. 500 µL of the solution was poured into a small vial and left overnight at room temperature to allow evaporation of THF. The resulting membranes were then conditioned for four hours in tap water which did not contain any deliberately added ions. Finally, the membrane was glued in place between two plastic pools with epoxy, see figure. 7.1.

7.2.3. Preparation of test solutions

To simulate realistic conditions for practical use of our sensor, we did not work with deionised water but drew water samples from drinking water taps at the University of Sheffield in March/April 2019.The local supplier 'Yorkshire Water' provides a list of ion concentrations in Sheffield tap water [117]. A 1mM Cu^{2+} stock solution was prepared by dissolving copper nitrate, $Cu(NO_3)_2$, in tap water, we then got the desired (low) concentrations used in our experiments by diluting with more tap water to (300, 200, 100, 50, 10, 1, 0.5) µM Cu^{2+}. For Pb^{2+}, we prepared a 1µM stock solution of lead nitrate, $Pb(NO_3)_2$, dissolved in tap water and then diluted to lower concentrations (0.5, 1, 5, 10, 25, 50, 100, 250) nM.

7.2.4. Twin- pool gating setup

To test the response of membrane- sensitised WGTFTs to Cu^{2+} / Pb^{2+}, we used a 2- chamber design (as in 6.3.4), and similar to previous studies[256,148,235] which is derived from the design of traditional potentiometric ion sensors[239]. The SnO_2 transistor substrate was in contact with tap water held in an inner (reference) pool that is separated from an outer (sample) pool by the

sensitised PVC membrane. The water in the reference pool was tap water as drawn, with no deliberately added ions. For sensor calibration, the outer pool is initially also filled with tap water, but this is then subsequently replaced with solutions of known and increasing concentrations of lead or copper, prepared as described in 7.2.3, while the inner pool remains filled with tap water as a reference. For practical use, rather than calibration, of the WGTFT as a lead and copper sensor, the sample pool would be filled with potentially contaminated water. The transistor is gated by a tungsten (W) contact needle that is submerged in the outer pool. As with all electrolyte- gated transistors, a potential applied to the gate contact will be communicated to the semiconductor surface via interfacial electric double layers (EDLs). However, the potential at the semiconductor surface will be different from the potential applied to the gate needle by any membrane potential, $V_M(c)$ in response to different ion concentrations, *c*, in the outer (sample) *vs.* inner (reference) pool. The setup is illustrated in figure. 7.1.

7.2.5. WGTFT characterisation and analysis

As $V_M(c)$ adds to the applied gate potential it can be measured as a shift in the WGTFT's threshold voltage, ΔV_{th}. We therefore recorded linear transfer characteristics using a standard transistor characterisation setup, reported earlier [256,93,138] Each time a new sample was filled into the outer pool, we allowed 2 minutes to equilibrate. We then scanned V_G from - 0.4 V to 0.7 V in steps of 20 mV at constant drain voltage V_D = 0.1 V. To determine membrane potential $V_M = \Delta V_{th}$, we compensate for it by shifting the recorded linear transfer characteristics along the gate voltage (V_G) axis to achieve best overlap with the characteristic recorded under pure tap water in the sample pool. We identify the gate voltage shift required for best overlap with the pure tap water characteristic as threshold shift ΔV_{th}. This method is also used in chapter 6 above and does not rely on any particular mathematical model of the linear transfer characteristics. It gives $V_M = \Delta V_{th}$ even when transistors do not exactly follow theoretical TFT equations, and is independent of channel geometry and the semiconductor's carrier mobility. The ame analysis has been used previously in other WGTFT sensors work, *e.g.*[256,32,93,138] . Results were fitted against a quantitative model (equation 7.2) using the nonlinear fitting routine in Origin 2018 software.

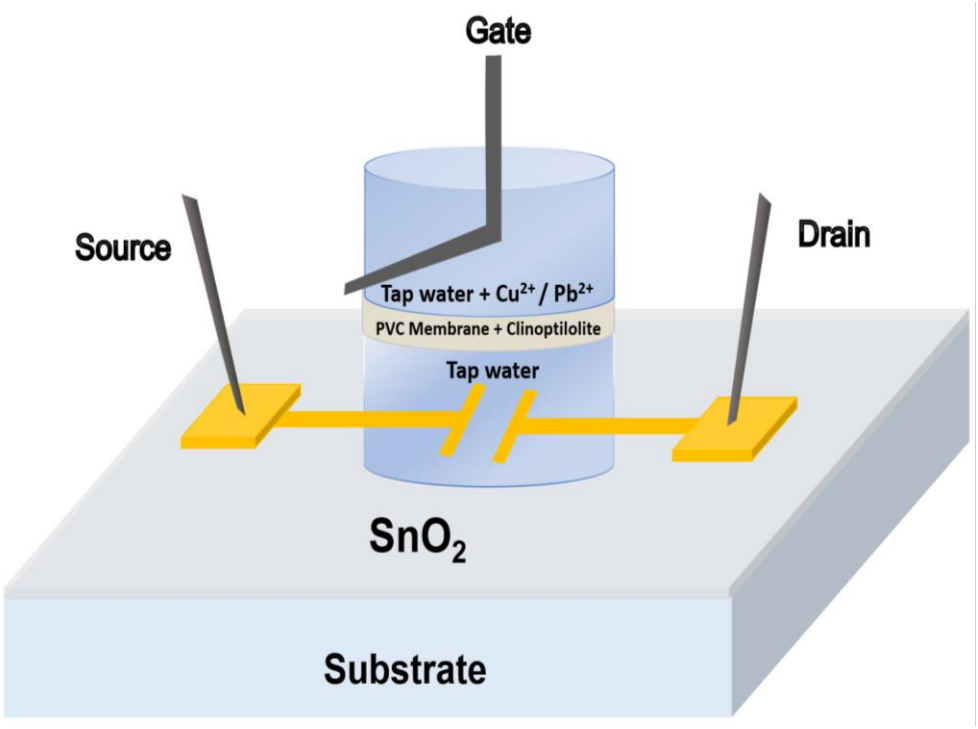

Figure. 7.1: Design of water gated field effect transistor sensor. The inner 'tap water' pool acts as reference against the outer 'sample' pool. The gate voltage is applied to the 'sample' pool via a tungsten needle.

7.3 Results and Discussion

7.3.1. Lead and Copper sensing results

In figure 7.2.a, we show the linear transfer characteristics of SnO_2 WGTFT transistors sensitised with a clinoptilolite membrane. The reference (inner) pool was filled with tap water, and the sample (outer) pool with tap water with increasing concentrations of Pb^{2+} up to 250 nM. Transfer characteristics clearly shift to more negative threshold voltages (toward the positive voltage axis, larger values to V_{th}) with increasing lead concentration, which indicates a lead concentration dependent membrane potential. For quantitative analysis, we have shifted all transfer

characteristics under water containing lead ($c_{Pb} > 0$) to match the $c = 0$ characteristic, as described in 7.2.5. The resulting 'master' transfer characteristic is shown in figure. 7.2.b.

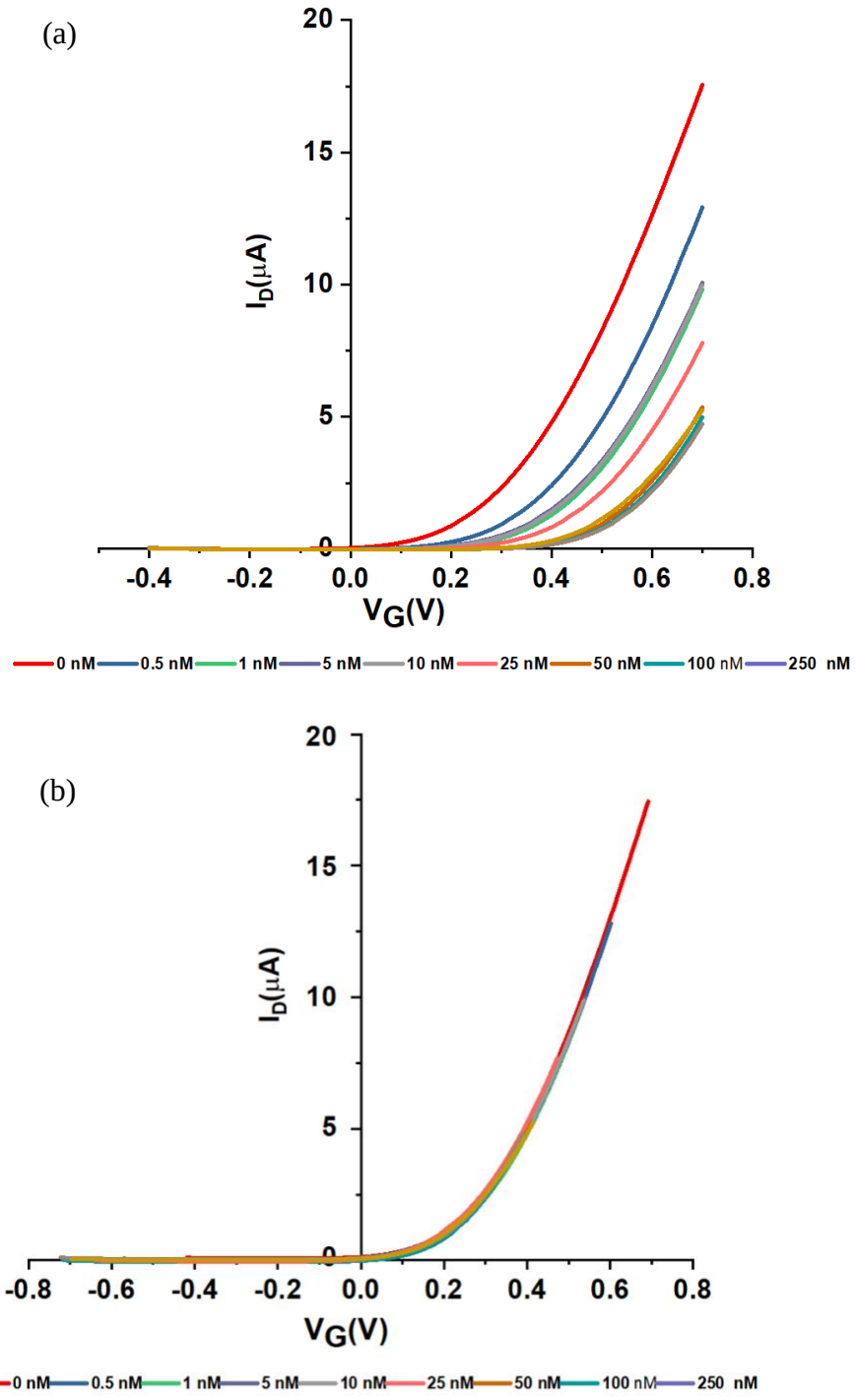

Figure. 7.2.a: Transfer characteristics of clinoptilolite- sensitised SnO_2 WGTFT gated under increasing Pb^{2+} concentrations in the outer pool. b: The 'Master' transfer characteristic after shifting transfers from figure. 7.2a along the V_G axis for optimum overlap.

Figure. 7.2.b shows excellent overlap of all transfer characteristics into a single 'master' characteristic plot. This confirms that increasing lead concentration in the sample pool only impacts the threshold voltage, and not any other WGTFT performance parameter. We identify the gate voltage shift required for best overlap as the WGTFT's threshold voltage shift under increasing lead concentration, $\Delta V_{th}(c_{Pb})$. These are shown and analysed in section 7.3.2 below.

We have then repeated the above experiment using nominally identical transistors, but adding increasing concentrations of copper (Cu^{2+}) up to 300 μM rather than lead to the outer pool. Note the ~ 1000 times higher concentrations of Cu^{2+} *vs* Pb^{2+}. Corresponding results are shown in figure. 7.3.

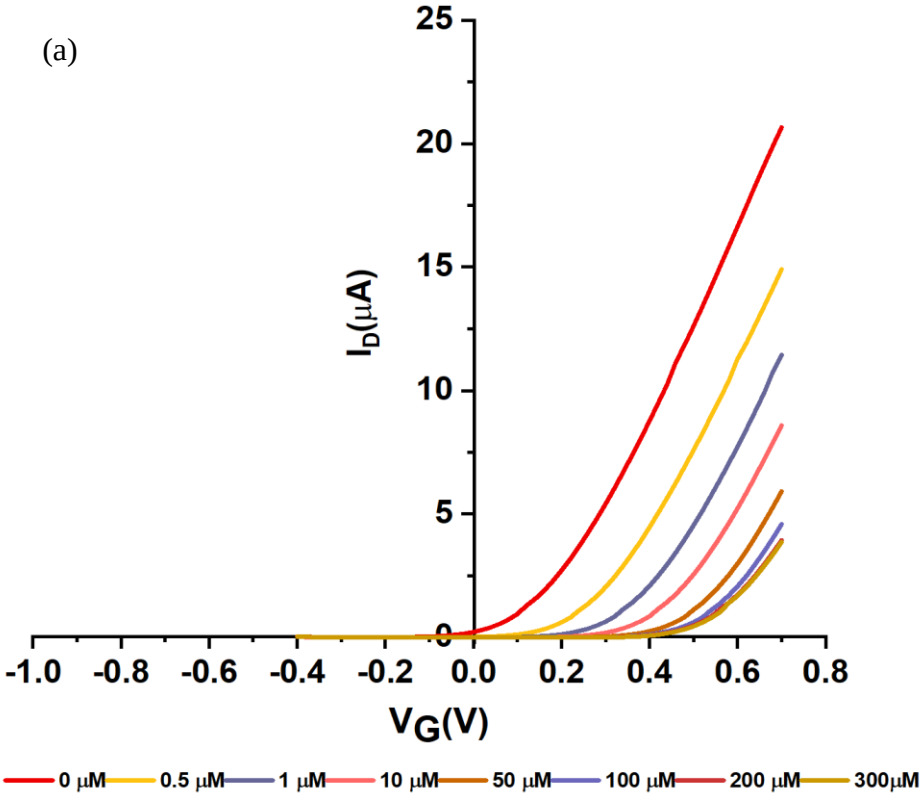

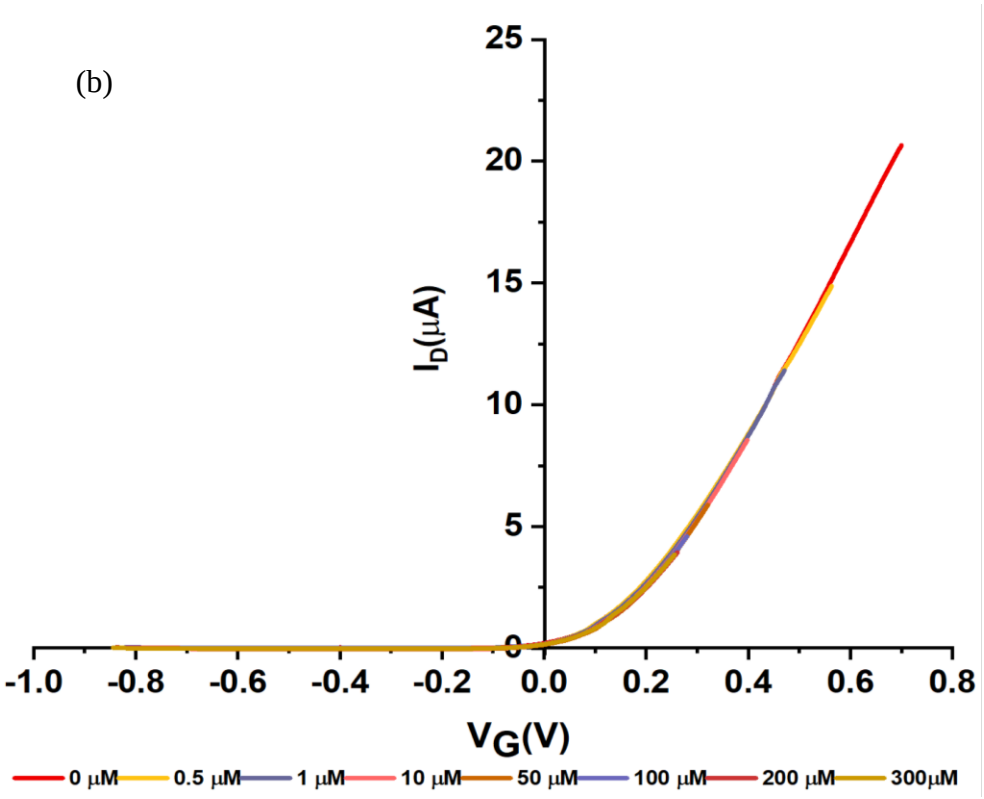

Figure. 7.3.a: Transfer characteristics of clinoptilolite- sensitised SnO_2 WGTFT gated under increasing Cu^{2+} concentrations in the outer pool. b: 'Master' transfer characteristic after shifting transfers from figure. 7.3.a along the V_G axis for optimum overlap.

Figure. 7.3.b again shows excellent overlap of all transfer characteristics into a single 'master' transfer characteristic. Threshold shifts $\Delta V_{th}(c_{Cu})$ are shown and analysed in section 7.3.2.

7.3.2. Quantitative analysis of Pb and Cu sensing

Figure. 7.4 shows $\Delta V_{th}(c_{Pb})$ and $\Delta V_{th}(c_{Cu})$, as evaluated from the shift of transfer characteristics along the V_G axis to construct 'master' characteristics.

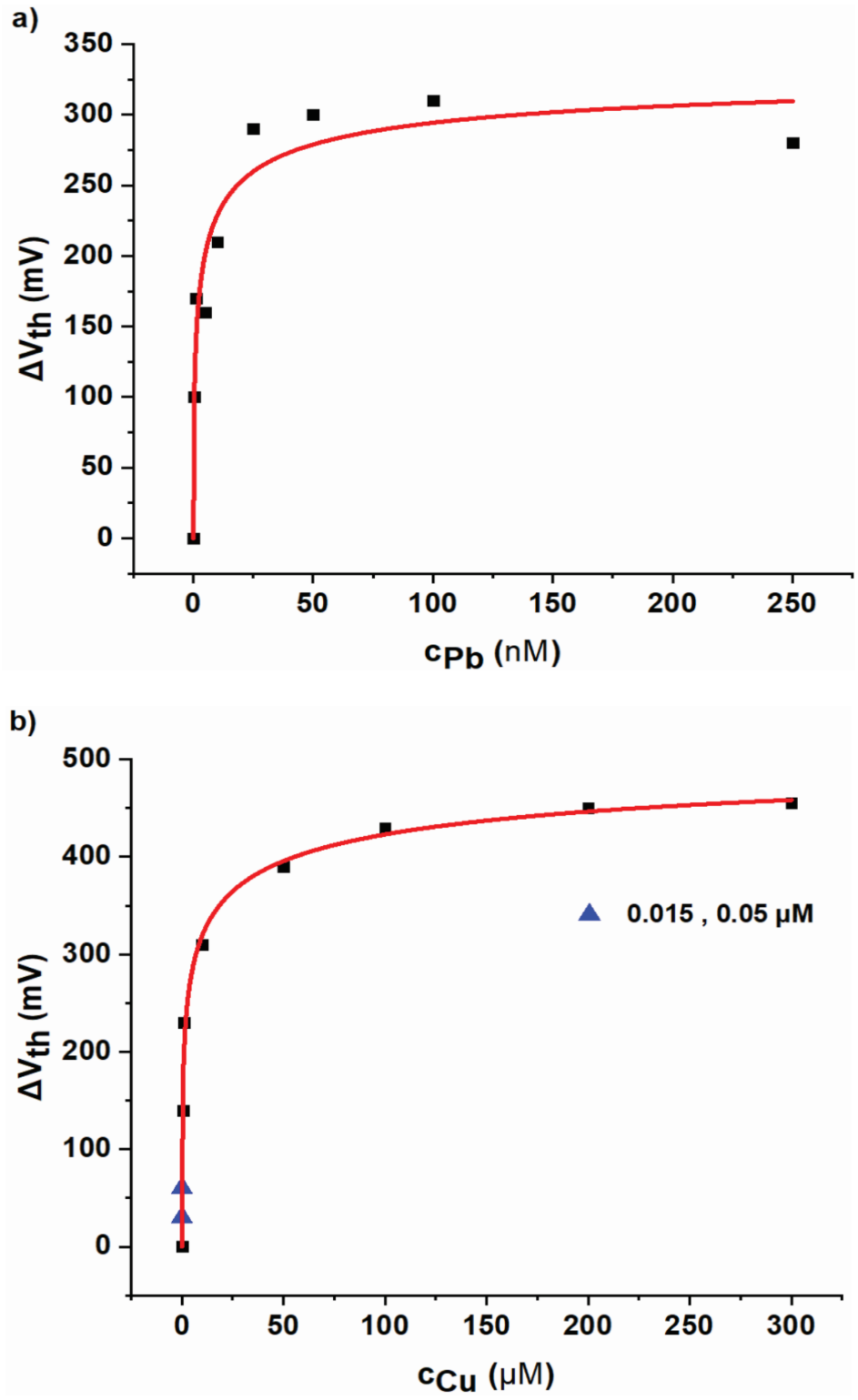

Figure. 7.4.a: Squares: Threshold shift ΔV_{th} *vs* concentration of Pb^{2+}, c_{Pb}, as evaluated from figure. 7.2. b: Squares: Threshold shift ΔV_{th} *vs* concentration of Cu^{2+}, c_{Cu}, as evaluated from figure. 7.3. Blue triangles: Data from similar experiment at 15 nM and 50 nM. Solid red lines are fits to equation 7.2.

We find that the threshold shifts observed in WGTFTs with increasing concentration of Pb^{2+} and Cu^{2+} increase rapidly for low concentrations and approach saturation $\Delta V_{th}(sat)$ of several 100 mV at high concentration. This is different from the Nikolsky- Eisenman law equation 6.1 but similar to our previous results with zeolite mordenite[256] albeit we required the LF isotherm, equation 7.2, rather than the simpler equation 7.1, for the fits shown in figure 7.4. Homogenous adsorption sites are required for a Langmuir isotherm, to deal with non-homogeneous surface sites, another isotherm (LF) is applied which was based of Langmuir isotherms. So, from the fit results fit we assume that clinoptilolite zeolite has heterogenous surface adsorption sites[157,264]. We find a satisfactory match for Pb^{2+} and a very good match for Cu^{2+}. The values for the fit parameters *K*, *β*, and $\Delta V_{th}(sat)$ from equation 7.2 for both Pb^{2+} and Cu^{2+} sensing are summarized in table 7.1.

Table 7.1: Fit parameters for the best fit of equation 7.2 to the data in figure. 7.4

Parameter ↓ / cation →	Pb^{2+}	Cu^{2+}
K [L /mol]	(4.3 +/- 0.4) x 10^8	(2.5 +/- 0.2) x 10^5
$c_{1/2}$ = 1/K	(2.3 +/- 0.2) nM	(4 +/- 0.3) μM
β	0.5 +/- 0.2	0.4 +/- 0.1
$\Delta V_{th}(sat)$ [mV]	341 +/- 68	542 +/- 74

The 3- orders- of- magnitude larger K for lead *vs.* copper indicates the stronger extraction of lead over copper by clinoptilolite, which is already evident from the concentration series used in figure 7.2 (nM) *vs.* figure. 7.3 (μM). To determine values for the limit- of- detection (LoD), we replot the data in figure 7.4 in its linearised form, $\Delta V_{th}(c)((Kc)^{\beta}+1)$ *vs.* $(Kc)^{\beta}$ (figure 7.5), using *K* and *β* for Pb and Cu, respectively, from table 7.1. We then fit straight lines of the form $y = mx + b$; resulting parameters *m* (slope) and *b* (intercept) with their respective errors are listed in table 7.2.

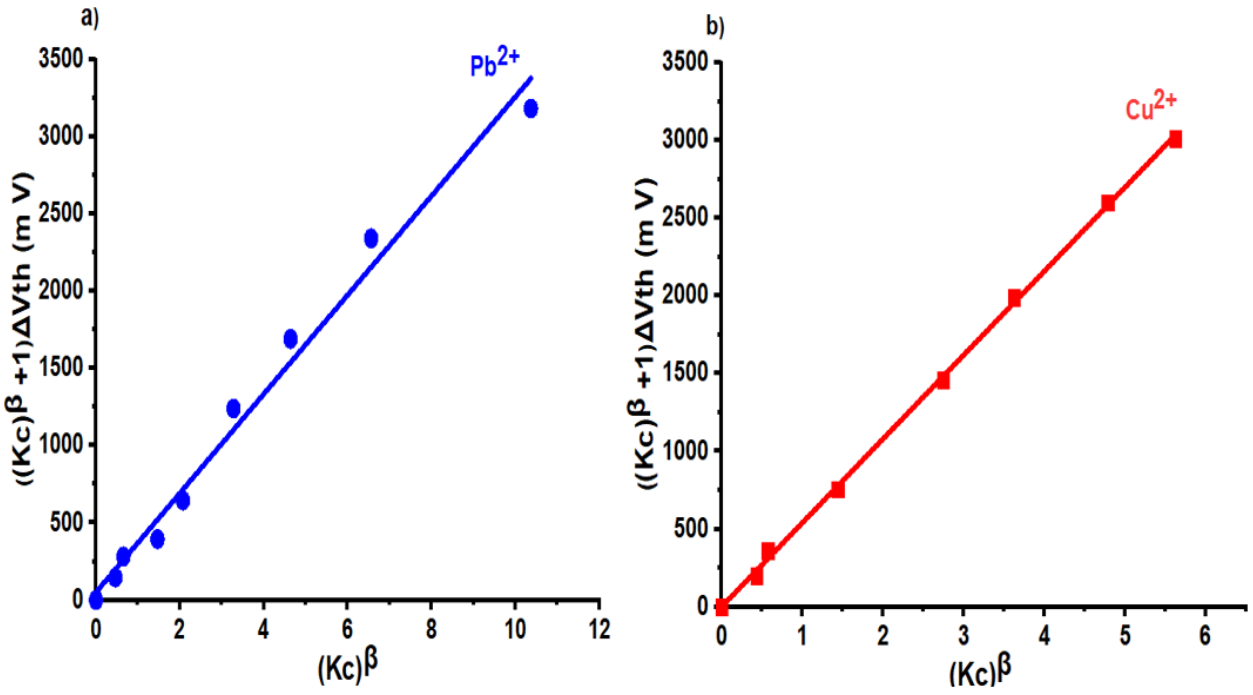

Figure. 7.5.a: Linearised plot for clinoptilolite- sensitised WGTFT threshold shifts, $\Delta V_{th}(c)[(Kc)^{\beta}+1]$ *vs.* $(Kc)^{\beta}$, under Pb^{2+}. b: same plot for Cu^{2+}. Respective parameters *K* and β taken from table 7.1.

Table 7.2: Fitted slope (*m*) and intercept (*b*), with errors, for the linearised threshold shift plots, figure. 7.5.

Parameter	Pb^{2+}	Cu^{2+}
m +/- Δm	321 +/- 15	540 +/- 6
b +/- Δb	50 +/- 68	0.53 +/-18.6
LoD	0.9 nM	14 nM

As expected from equation 7.2, b overlaps with zero within its error Δb. The concentration corresponding to LoD can be determined with the common '3 errors' criterion, equation 7.3:

$$(Kc_{LoD})^{\beta} = 3\Delta b/m \qquad 7.3$$

Using this we find a LoD (Pb^{2+}) = 0.9 nM and LoD (Cu^{2+}) = 14 nM, which are already included in table 7.2. To make sure Cu^{2+} LoD is realistic rather than an artifact of mathematical analysis, we have repeated the experiment shown in figure 7.3b with very small Cu^{2+} concentrations (15 and 50 nM), resulting threshold shifts are shown as blue triangles in figure 7.4.b. Note that the triangles agree well with the fit (red line), and 15 nM is very close to the evaluated LoD and does lead to a recognizable threshold shift ($\approx$ 30 mV), hence the calculated LoDs for Cu^{2+} are confirmed as realistic. The LoD for lead is quite a lot lower than for copper when compared to *1/K*, which reflects the larger scatter (poorer fit to the model equation 7.2) in the original data, particularly at higher concentrations. Visually, the lead LoD formally evaluated by equation 7.3 seems an overestimate when inspecting figure 7.2a, which shows a clear threshold shift under LoD = 0.9 nM lead. Nevertheless, formally evaluated LoDs for both lead and copper are significantly smaller than the action levels of the lead- and- copper rule, which qualifies our sensors for use in monitoring them.

7.3.3. Sensor performance in acidic conditions

While the tap water drawn in our lab has near neutral pH (pH = 7.2, measured using a pH meter (CyberScan PH 300), generally drinking water may vary in pH, the permitted range for drinking water (in the EU) is pH (6.5 - 9.5)[4]. Practically, water samples could be tested for pH with a pH meter and adjusted to pH 7 by adding small amounts of strong base (or acid) prior to lead- and-copper testing. Contamination with e.g. Na^{+} from NaOH will in itself not lead to significant threshold shift, as we show below in 7.3.5. However, we show here that the impact of pH on sensing of lead and copper is small. We added a drop of acetic acid to our tap water to deliberately make it mildly acidic, pH 5.2 as measured with same pH meter. We then tested clinoptilolite- based WGTFTs to sense lead and copper in acidified tap water. Threshold shifts at one representative heavy metal concentration for as- drawn (pH 7.2) vs acidified (pH 5.2) tap water are compared in

table 7.3. Concentrations of lead were chosen to be near- saturated threshold shift regime as seen in figure. 7.4.

Table 7.3: Threshold shifts at selected lead- and copper concentrations at pH 5.2 vs. pH 7.2

Concentration	ΔV_{th}(mV) at pH = 7.2	ΔV_{th}(mV) at pH = 5.2
100 nM Pb^{2+}	310	255
300 µM Cu^{2+}	455	415

Heavy metal induced threshold shifts under acidic conditions are slightly smaller than under near-neutral pH. However, shifts are still significant at pH 5.2, which is more than one pH unit below the permitted pH range for drinking water. Clinoptilolite membranes are therefore suitable to detect lead and copper within the permitted pH range of drinking water. For accurate quantitative determination at significantly non- neutral pH, we advise calibration (as in figures 7.2 and 7.3) at several pH's, or prior neutralisation of acidic samples with small amounts of strong base, e.g. NaOH.

7.3.4. Lead and copper extraction with clinoptilolite

As the usual application of clinoptilolite is to extract lead and copper pollution from the drinking water supply[261,223], we have here used clinoptilolite membrane sensitised WGTFTs to test extraction performance. We 'spiked' 15 mL of tap water with 1 µM lead and copper, respectively (we used the same concentration to allow direct comparison of extraction), and then attempted to extract the heavy metal again. For this, we added 100 mg of clinoptilolite to spiked water, agitated, and left to settle for 2 hrs. We then tested water samples resulting from this spiking / extraction procedure in a WGTFT transistor sensitised with clinoptilolite membrane in the same way as in

section 7.3.1. The resulting transfer characteristics are shown in figure 7.6, which for comparison also includes the transfer characteristic for as- drawn tap water that has not been spiked / extracted.

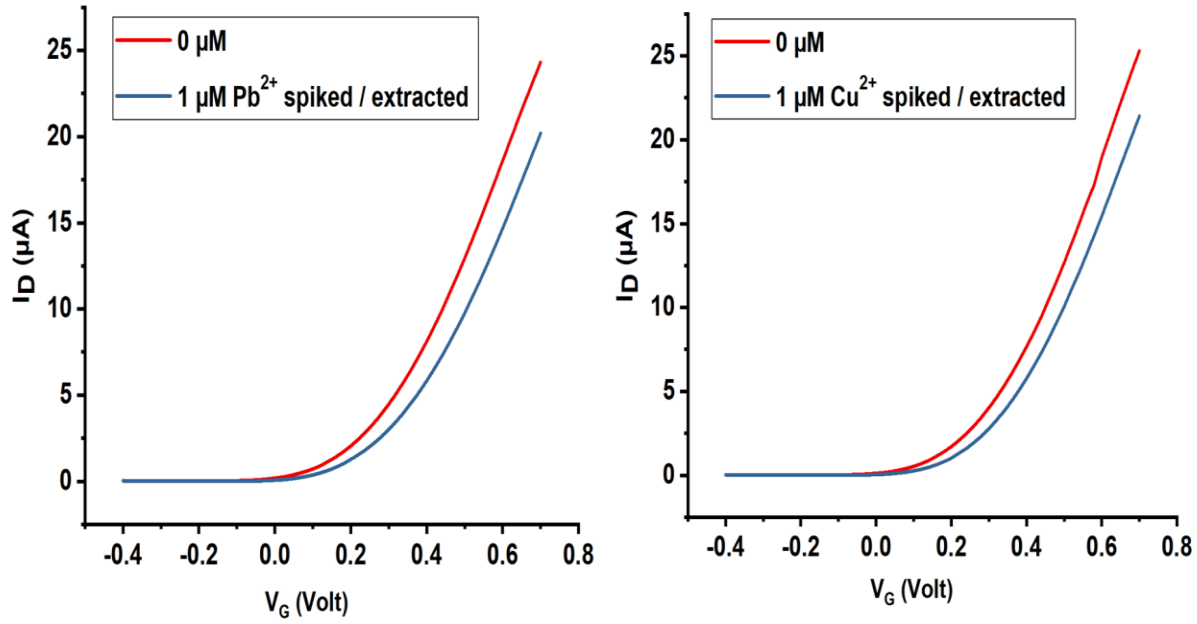

Figure. 7.6: Transfer characteristics for clinoptilolite membrane sensitised WGTFT gated by (1 µM heavy metal spiked / extracted) tap water sample *vs*. tap water as drawn. a: Cu^{2+} spiked / extracted, b: Pb^{2+} spiked / extracted, red : tap water as drawn.

We find that characteristics for both spiked/extracted samples do display a small threshold shift compared to a tap water sample that has never been spiked. However, the shift is significantly smaller than what we found in section 7.3.1. This suggests that the extraction procedure has significantly reduced the initial 1 µM heavy metal concentration, albeit a small amount of pollution remains. Results are summarised in table 7.4, which also shows the heavy metal concentration remaining after extraction. These are calculated with equation 7.2 from the measured threshold shifts after extraction, using the parameters listed in table 7.1.

Table 7.4: Threshold shift under 1 µM lead and copper *vs.* threshold shift after extraction with clinoptilolite. Remaining Cu/Pb concentration in solution calculated from threshold shift after extraction with equation 7.3 and the parameters from table 7.1.

Tap water spiked with...	ΔV_{th} (mV) before extraction	ΔV_{th} (mV) after extraction	Remaining concentration
1 µM Pb^{2+}	340	60	106 pM
1 µM Cu^{2+}	230	50	13 nM

Table 7.4 shows that clinoptilolite is indeed effective in extracting lead and copper from drinking water. The remaining heavy metal pollution after extraction is far below the action level. The larger K for lead *vs*. copper established previously is reflected again in the much reduced concentration of lead after extraction. The higher sensitivity of Pb over Cu might be caused by the better match of the ion hydrated radius with clinoptilolite pore size. The clinoptilolite selectivity toward Pb has previously been reported to be higher than Cu in water cleaning as in[233,265].

7.3.5. Interference from common co- cations

Drinking water naturally contains common cations of alkaline and alkaline earth metals (e.g. Na, Ca, Mg) in concentrations typically ranging in the order (100 µM - 1mM), for example our lab's water supplier Yorkshire Water quotes a typical 'cocktail' of 200 µM Ca^{2+}, 99 µM Mg^{2+}, and 783 µM Na^{+} [117]. These concentrations are significantly larger than the 'action levels' for heavy metals under the lead- copper rule but alkaline and alkaline earth metal co- cations at these levels are not harmful and should not lead to 'false positives'. As described in 7.2.3, we account for the common tap water interference 'cocktail' by preparing calibration solutions, and testing our WGTFTs, using tap water rather than DI water. We have nevertheless studied the interference from co- cations on our WGTFT heavy metal sensor. Figure. 7.7 shows the transfer characteristics of a SnO_2 WGTFT transistor sensitised with a clinoptilolite membrane when using tap water with deliberately added

sodium (Na^+) ions (from NaCl) or calcium (Ca^{2+}) ions (from $CaCl_2$) in the sample pool *vs.* tap water as drawn in the reference pool.

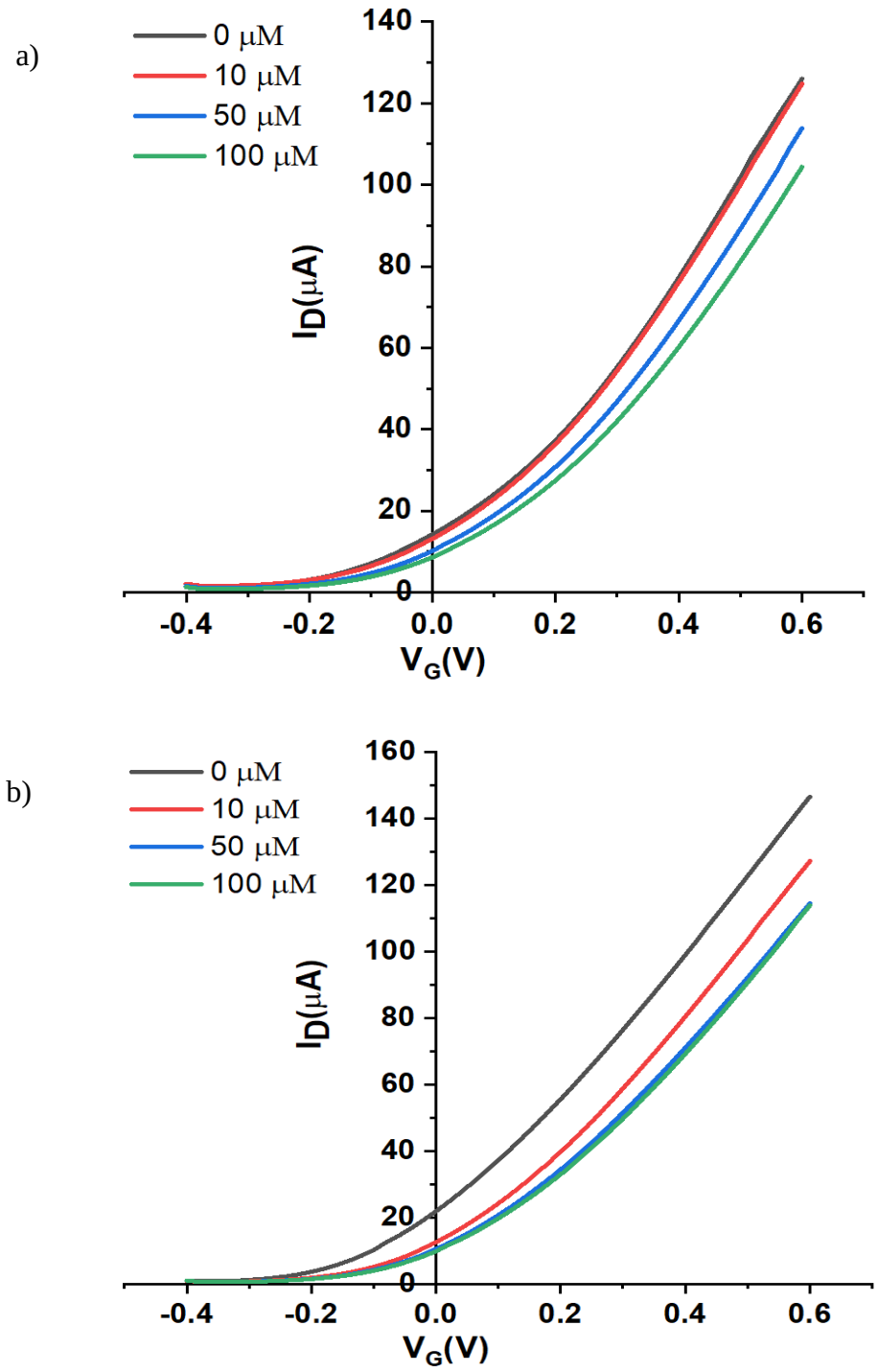

Figure. 7.7.(a): Transfer characteristics of clinoptilolite- sensitised SnO_2 WGTFT under samples of tap water with deliberately added Na^+ in concentrations (10, 50, and 100) μM. (b) Same for Ca^{2+} in concentrations (10, 50, and 100) μM.

There are measurable shifts in threshold voltage with the addition of co- cations, as summarised in table 7.5.

Table 7.5: Threshold shifts under high concentrations of the interferants Na^+ and Ca^{2+}.

Concentration (μM)	ΔV_{th} (mV) (Na^+)	ΔV_{th} (mV) (Ca^{2+})
10	15	75
50	65	120
100	85	120

We find that the highest threshold shifts due to Na^+ and Ca^{2+} is significantly smaller than ΔV_{th}(sat) under Pb^{2+} or Cu^{2+}. At 100 μM, we find a shift of 85 mV for Na^+ and 120 mV for Ca^{2+} while ΔV_{th}(100 μM) > 400 mV for Cu^{2+}. According to equation 7.3 with the parameters listed in table 7.1, the action levels of 72 nM for lead and 20.5 μM for copper would lead to threshold shifts of 289 mV (lead) or 356 mV (copper), both significantly larger than 100 mV, so at least qualitatively we can still decide potability with respect to lead and copper despite co-cation interference. To quantify selectivity, we observe from figure 7.7.a that $c_{1/2} \approx 30$ μM for Na^+, hence selectivity S for lead over sodium is S (Pb^{2+} *vs.* Na^+) = K(Pb) / K(Na) = $c_{1/2}$(Na) / $c_{1/2}$(Pb) ≈ 13,000; log S ≈ 4.5.

7.3.6 Interferant matching by extraction

For the sensor calibration in 7.3.1, co- cation (*i.e.*, interferant) concentration in sample and reference were matched by calibrating sensors with sample solutions we have prepared from the same tap water as we use for reference, *cf.* 7.2.3. Clinoptilolite selects nanomolar lead from a ~ millimolar interferant cocktail when the reference pool carries a matched cocktail. In 7.3.5 we

study the practically unrealistic scenario of adding interferants to the sample solution without matching in the reference, and find that such a mismatch would still allow lead and copper sensing, at least qualitatively. A more realistic interference 'loophole' arises not because we would deliberately add interferants to a sample, but because test samples taken in the environment would carry an *a* priori unknown interferant cocktail that will be different from our tap water. If we nevertheless use our tap water in the reference pool, interferants in reference and sample would not be matched.

To address this 'interference loophole', we propose a procedure based on extraction as described in 7.3.4 to generate interferant (and pH) matched reference solutions. When obtaining a sample of unknown lead and/or copper content, we would first split it in two, and then generate an interferant-matched reference solution from one of the two by extracting lead and copper with clinoptilolite. We then first fill both reference- and sample pool with extracted (*i.e.*, self- generated reference) solution and record a reference transfer characteristic, corresponding to the '0 nM / μM' curves in figures 7.2 and 7.3. Then we replace the extracted solution in the sample pool with non- extracted (*i.e.*, actual) sample and test for threshold shift. We tested this procedure by applying it to a control, and a sample contaminated with lead, i.e. on the potability limit (72 nM), figure. 7.8.

Figure. 7.8 a provides a control experiment, applying the above extraction procedure to Sheffield tap water (drawn on a different day as previously) without (deliberately) added lead. The two transfers in 7.8.a were both taken with extracted 'reference' in the reference pool, but we compare extracted 'reference' and non- extracted 'sample' in the sample pool. The two curves are virtually identical, reflecting that the 'sample' was in fact tap water with no added lead, like the reference. This control experiment shows that the extraction procedure itself does not introduce false positives, e.g. by the unintended extraction of interferants. In figure. 7.8.b, we have then applied the same procedure to a sample which we prepared by adding 72 nM lead (potability limit) from lead nitrate to tap water drawn on a different day, so not necessarily identical to the water used for the experiments in figure. 7.2 and 7.3. We then split this 'spiked' sample and generated an interferant matched reference by extraction. The reference pool was filled with extracted sample (*i.e.,* interferant matched reference). The sample pool was first filled with the same extracted sample to record a reference transfer characteristic, and was then replaced by untreated 72 nM lead- spiked sample to record the transfer characteristic under sample exposure.

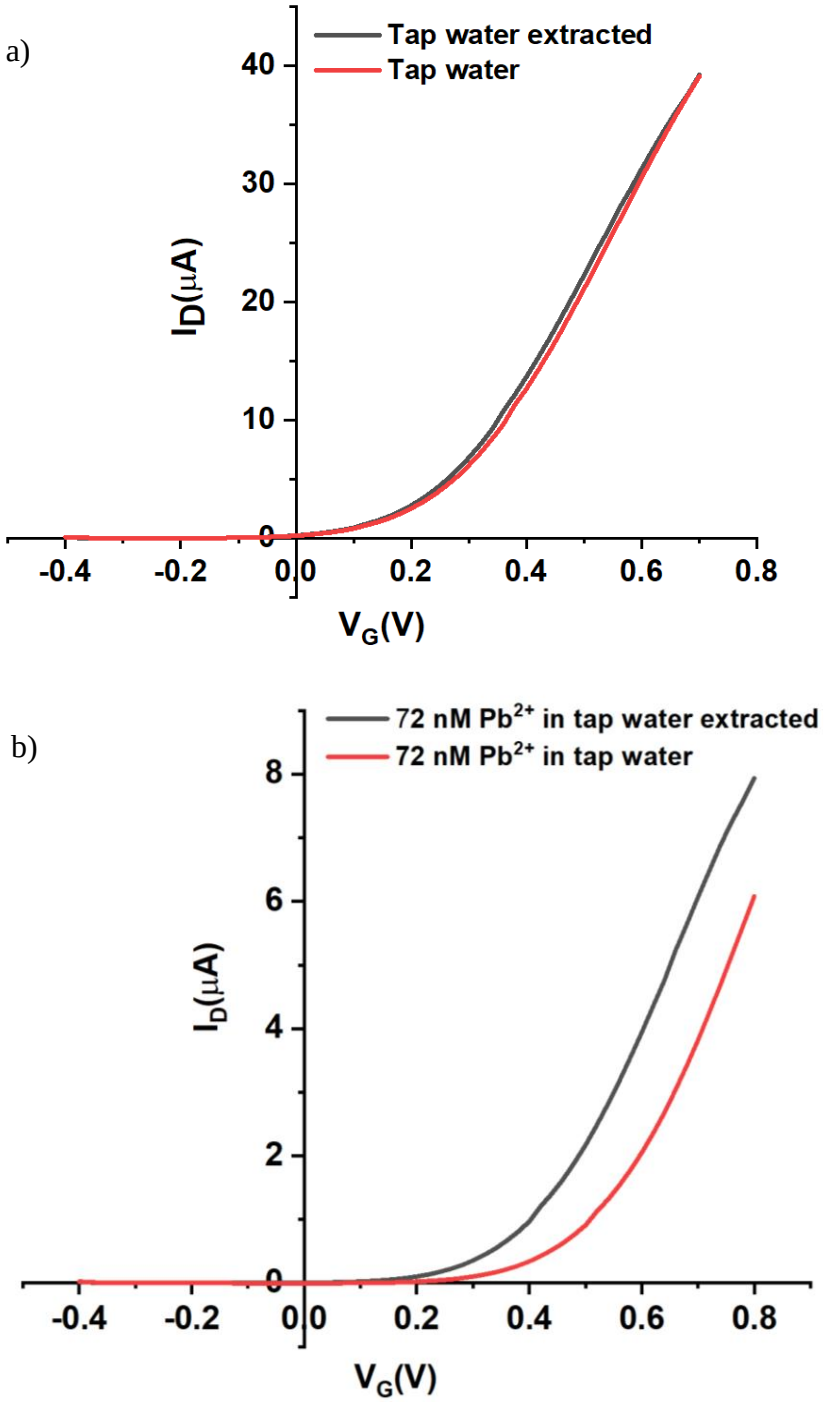

Figure. 7.8.a: Transfer characteristics with tap water *vs.* 'extracted' tap water in the sample pool, with 'extracted' tap water in reference pool. b: Transfer characteristics with 72 nm lead- spiked tap water *vs.* extracted spiked tap water in the sample pool, with extracted spiked tap water in the reference pool.

Now we observe a significant threshold shift $\Delta V_{th} \approx 110$ mV between 'reference' (extracted sample) and actual sample in the sample pool. With the extraction procedure, we unambiguously detect lead at potability limit, relying only on clinoptilolite and the sample itself. The unknown interferant cocktail in the sample is accounted for by referencing to an extracted sample with matching (albeit unknown) interferants.

7.4. Conclusions

The cheap and naturally abundant zeolite clinoptilolite is not only useful for removal of the toxic heavy metals copper and lead from contaminated water, but also for their sensing and monitoring of the lead- and- copper rule. When we embed powdered clinoptilolite into a plasticised PVC membrane that we use to separate a sample- and a reference pool in a water- gated SnO_2 thin film transistor, we find a membrane potential that leads to transistor threshold shift in response to the presence of either Pb or Cu in the sample pool. Threshold shift follows a Langmuir- Freundlich (LF) characteristic, equation 7.2. This contrasts to Nikolsky- Eisenman (NE) characteristics, equation 6.1, which are usually found for potentiometric membranes sensitized with organic ionophores, *e.g.*[148,93,138,149,239,240], but also in prior reports on zeolite- sensitized membranes, *e.g.*[235]. The NE characteristic flatlines at concentrations $c < c_{st}$, hence LoD $\approx c_{st}$, which is typically in the order (100 nM to 1 µM). The LF characteristic lacks such a lower cut- off and in fact shows the steepest slope of membrane potential with c in the limit $c \rightarrow 0$, opening a window to much lower LoDs. We here determine limits- of- detection (LoDs) which for both Pb^{2+} and Cu^{2+} are significantly smaller than the 'action levels' stipulated by the lead- and- copper rule[260], Pb^{2+}: LoD 0.9 nM *vs* 72 nM action level, Cu^{2+}: LoD 14 nM *vs* 20.5 µM action level. Threshold shift saturates for high ion concentrations, namely at 341 mV (Pb^{2+}) and 542 mV (Cu^{2+}), which is large within the 1.23 V electrochemical window of water. These sensors are also pH tolerant and work even in mildly acidic conditions. This qualifies clinoptilolite- sensitized WGTFTs as a low footprint sensor technology for monitoring the lead- and- copper rule, and to confirm the efficacy of clinoptilolite to extract lead and copper from water. For the practical use of such sensors, potential interference from common co- cations such as Na^{+}, Ca^{2+}, and Mg^{2+} is a more serious challenge than LoD. However, we provide and verify a routine for generating interferant- matched reference solutions by using clinoptilolite as extractant as well as sensitizer, closing the interference 'loophole'.

The reason for the unusual but useful LF response characteristic warrants further study. We note an important difference between conventional macrocycle- sensitized potentiometric sensors, and zeolite based sensors: Namely, macrocycles capture the target ion and hence charge the membrane. Zeolites are ion exchangers, so acquire no net charge under target ion exposure.

Chapter 8: Sensing aromatic pollutants in water using catalyst- sensitised water-gated transistors

8.1 Introduction

The water-gated thin film transistor (WGTFT)[34] has emerged as a device to transduce the binding of a waterborne analyte to a sensitizer into a potentiometric signal, *i.e.* a voltage[32]. For this purpose, sensitizers can be introduced into the WGTFT architecture in several ways. A number of ion-selective WGTFTs have been demonstrated that incorporated a phase transfer membrane carrying selective 'ionophores' - typically, organic macrocycles - into a WGTFT architecture [148,93,149,138]. Macrocycle size-selectively captures ions in their central cavity, leading to an ion concentration dependent membrane potential, $V_M(c)$, given by a Nikolsky-Eisenman (modified Nernstian) characteristic. WGTFTs transduce membrane potential into a shift in the threshold voltage, $\Delta V_{th}(c)$. Recently, we have instead introduced an ion exchanging (rather than ion capturing) ionophore into WGTFT membranes, the caesium-selective zeolite mineral 'mordenite' [256] that is already used to extract caesium from drinking water [154], *e.g.* when water is polluted with radioisotope $^{137}Cs^+$. The heavy metals Pb^{2+} and Cu^{2+} were also detected by clinoptilolite zeolite sensitized WGTFT, where clinoptilolite is known for adsorption of heavy metals from water. In both cases the ion-exchanging zeolite sensitizer response characteristics follow Langmuir and Langmuir-Freundlich isotherms. Although ion exchange does not build up a net charge on the sensitizer, we find ion exchangers can lead to high membrane potentials (several 100 mV) and sensors with very low limit-of-detection (LoD) as in the results presented in chapter 6 and 7. The membrane potential $V_M(c)$ followed a Langmuir isotherm, which is a special case of the Langmuir-Freundlich (LF) adsorption isotherm, equation 8.1:

$$V_M(c) = \Delta V_{th}(c) = \Delta V_{th}(\text{sat})\ (Kc)^{\beta} / [(Kc)^{\beta} + 1] \qquad 8.1$$

The Langmuir isotherm is a special case where $\beta = 1$. Here K quantifies the strength of the interaction between a sorption site and the sorbate, $\beta \leq 1$ quantifies inhomogeneity between sorption sites ($\beta = 1$, K for all sorption sites is equal). For mordenite responding to Cs^+, we found $\beta = 1$ [256]. $\Delta V_{th}(\text{sat})$ is the saturation value for membrane potential /threshold shift under large c. A

characteristic concentration $c_{1/2}$ is given by $\Delta V_{th}(c_{1/2}) = ½\ \Delta V_{th}(sat)$; $c_{1/2} = 1/K$ independent of β. Note, for mordenite, mass uptake for Cs^+ ion extraction also follows equation 8.1, but $c_{1/2}$ for membrane potential ($c_{1/2} \approx 260$ pM [256]) was more than 6 orders of magnitude smaller than for mass uptake ($c_{1/2} \approx 365$ μM [154]). We therefore consider the membrane potential to be a surface phenomenon, while extraction is to the bulk.

In this context, the first step in heterogeneous catalysis is the adsorption of a 'substrate', *i.e.* a molecule that is meant to be catalysed, from solution onto the surface of a solid catalyst. Adsorption is often highly selective [266,267]. If the initial adsorption of substrate onto a catalyst surface can be transduced into a physical (*e.g.* electrical) signal, then a material known to be a catalyst for a particular substrate and could therefore also act as a selective receptor or 'sensitizer' in a sensor for this substrate, which then would be the sensor's 'analyte'. Such a sensor will be effective even below the temperature required for a catalyst to be active, because sensing relies on adsorption only.

Here, we selected candidate catalysts/sensitizers from families commonly applied in heterogeneous catalysis [266,267,268] these are powdered transition metal doped zeolites and similar frameworks, and are already in use *e.g.* for the treatment of water polluted with aromatic contaminants [269,270,271]. We first established catalytic activity on a few examples of aromatic water pollutants (toluene, phenol, benzyl alcohol). Then we prepared phase transfer membranes filled with these new candidate sensitizers. Using the WGTFT as a transducer, we find that some zeolite catalyst loaded membranes do indeed show potentiometric sensor response to benzyl alcohol, but not to toluene or phenol. We thus establish a new application for catalysts beyond catalysis itself, which we recommend for wider uptake. From our findings, we discuss the potentiometric sensing mechanism, establish criteria for which type of non-ionic aromatic pollutants can be sensed in this way, and discuss the relationship between catalytic activity, and sensing performance.

In this chapter, material from: N. Alghamdi et al. , Sensing aromatic pollutants in water with catalyst-sensitized water-gated transistor, chemical papers, published [2020],springer. All the experimental work related to the use of catalytic zeolites as sensitizers in WGTFTs sensors was done by me (Nawal Alghamdi) under Martin Grell's supervision. The experimental work related

to the catalytic zeolite preparation, doping, characterization and activities measurements, was done by our chemist collaborators Changyan Zhou, Naoko Sano, Marco Conte.

8.2. Material and methods

8.2.1 Selection and modification of Zeolites and related materials

Within this study, we investigated 10 candidate catalysts/sensitizers (from our collaborators in Sheffield University, Department of Chemistry) which were derived from a common zeolite and similar frameworks (ZSM-5, Zeolite type 13X, type Y, MCM-41, SBA-15) these are frequently used as support materials for catalysts. Note, MCM-41 and SBA-15 are not strictly zeolites but similar mesoporous silicate frameworks that lack the aluminium centres of zeolites with their associated Brønsted acid properties. However, due to their otherwise similar structure, we will refer to all frameworks as 'zeolites' rather than 'zeolite and related frameworks'. Materials were sourced commercially as fine powders [272,273,274,275,276] to represent a range of different pore sizes, aluminium content (including zero for MCM-41, SBA-15) and surface areas. These parameters affect the growth of metal nanoparticles [277] under the subsequent doping protocols (described in the appendix A8.1). Usually, the larger the surface area, the smaller and more isolated are the resultant dopant metal nanoparticles[278]. Surface area and pore size may also introduce diffusion effects which can influence their catalytic activity. The framework's molar Al : Si ratio affects the stability of the framework and its acidity (the higher the Al : Si ratio, the more acidic a zeolite is), which is a key characteristic for catalytic activity [279]. Zeolite frameworks were then modified by doping with 1 wt% of transition metals Cu, Fe, or Mn. These are able to catalyse the decomposition of organic pollutants like phenol to CO_2 and water in the presence of molecular oxygen or peroxides [280,281], or to oxidize alcohols to ketones. Transition metal doping was achieved by using different protocols: wet impregnation (WI); ion exchange (IE); and deposition precipitation (DP). WI [282] leads to relatively large clusters (> 20 nm) of CuO, this is mostly outside the pores of the zeolite. IE instead leads to smaller (usually < 5 nm) CuO clusters or to the exchange of the Al centres with Cu centres, or other metals [283]. DP can lead to the formation of mixed metal oxide CuO/Cu_2O species in the range of 10 nm or lower [284]. Details on the doping protocols employed here are in the appendix (A8.1). A numbered list of the materials used in this work is listed in table 8.1.

Table 8.1: The 10 zeolites and related frameworks studied here. ZSM-5, X, Y, MCM, and SBA denote the respective zeolite framework: ZSM-5, Zeolite Socony Mobil 5 [272], 13X, Y: Zeolite type 13X [273] / type Y [274], MCM-41: Mobil Composition of Matter [275], SBA-15: Santa Barbara Amorphous-15 [276]. All the zeolites are used in their acidic form, with the exception of No.4, where an ammonium zeolite precursor (NH4-ZSM) was used.

Zeolite No.	Composition (wt%) / Preparation	Si : Al molar ratio
1	1% Cu/ZSM-5-WI	46 : 1
2	1.5% Cu/ZSM-5-IE	46 : 1
3	1% Cu/ZSM-5-DP	46 : 1
4	1% Cu/NH4-ZSM-5-WI	46 : 1
5	1% Cu/13X-WI	1.2 : 1
6	1.5% Cu/Y-IE	11 : 1
7	1% Fe/ZSM-5-WI	46 : 1
8	1% Fe/MCM-41-WI	1 : 0
9	1% Fe/SBA-15-WI	1 : 0
10	1% Mn/ZSM-5-WI	46 : 1

8.2.2 Selection of analytes and solution preparation

Here, we tested sensing on dilute solutions of three example aromatic water pollutants selected to allow systematic comparisons: benzyl alcohol, phenol, and toluene, shown in figure. 8.1a, as

examples of water pollutants. All three candidate analytes consist of a rigid benzene ring with one substitution, hence adhesion should be similar for all with any difference to be ascribed to the only different functional group. On the other hand, due to the different substitutions, the three molecules show very different molecular dipoles. The magnitude of these dipole moments ranges from strong to weak: benzyl alcohol 1.7 Debye (D), phenol 1.5 D, and toluene 0.2 D, respectively [285],[286]. Further, benzyl alcohol has a dipole at the pendant -OH group that can rotate out of the plane of the benzene ring around the dihedral angle of the saturated carbon-carbon bond that links it to the benzene ring (figure 8.1.a, rotatable bond in red). Phenol also shows an -OH dipole but this is fixed in the plane of the ring as it is attached without 'spacer'. Toluene shows (almost) no dipole from the pendant non-polar methyl group. Test solutions of benzyl alcohol and phenol were prepared by diluting 1 mM stock solutions. For toluene, a saturated stock solution was prepared by mixing an excess of toluene with water, stirring for 24 hours then leaving for 2 days in a separating funnel to ensure separation, and drawing saturated solution of toluene in water from the funnel. According to Polak et al[287], at ambient temperature this corresponds to a concentration of 30 mM. This saturated toluene solution was then diluted to make test solutions.

8.2.3 Catalytic activity measurements

Before testing zeolites 1 to 10 as potential sensitizers in WGTFT sensors for the above three candidate analytes, we have established catalytic activity of zeolites for the oxidation of these same molecules when they are considered as substrates. The measurements of the catalytic activity for phenol and benzyl alcohol are illustrated in the appendix (A8.2). (this measurement was done in the chemistry department by one of my colleagues on this work)

8.2.4 Phase transfer membrane preparation

To prepare PVC membranes we dissolved 30 mg of PVC, 65 mg of plasticiser 2NPOE in 3 mL of THF, which is a good solvent for all ingredients. All chemicals were purchased from Sigma Aldrich. We then dispersed 7 mg of powdered zeolite as listed in table 8.1 in 500 μL of such solution in a small vial and left it overnight at room temperature to allow the evaporation of THF.

The resulting membranes were ~ 0.4 mm thick and were then conditioned for one hour in DI water. Finally, the membrane was glued in between two plastic pools with epoxy, see figure. 8.1b.

8.2.5 Water- gated transistor preparation, setup, and measurement protocol

Transistor source/drain contact substrates were prepared by thermal evaporation of Au (100 nm) with Cr (10 nm) as adhesion layer onto clean quartz- coated glass substrates sourced from Ossila Ltd (order code S151) by a shadow mask. Each substrate contains 5 pairs of electrodes separated by channel with a length L = 30 μm and width W = 1 mm (W/L = 33.3). We sprayed 4 sprays of 0.05 M $SnCl_4 \cdot 5H_2O$ dissolved in isopropanol using an airbrush from 20 cm distance onto contact substrates preheated to 400 ^oC. Afterwards, substrates were left on the hot plate for 30 min for full decomposition of tin chloride precursor into semiconducting SnO_2. We measure resulting film thickness of ~ 45 nm with a Dektak surface profilometer. To test the response of membrane-sensitised WGTFTs to aromatic substrates, we used a 2- chamber design, similar to previous workers [148],[256],[235], which is derived from the design of traditional potentiometric ion sensors, *e.g.* [239]. The SnO_2 transistor substrate was in contact with DI water held in an 'inner' reference pool that is separated by the sensitized PVC membrane from a second, 'outer' sample pool. The outer pool is initially also filled with DI water, this is then subsequently replaced with solutions of increasing analyte (substrate) concentrations, while the inner pool remains filled with DI water as an analyte- free reference. The transistor is gated by a tungsten contact needle that is in contact with the sample solution in the outer pool. The setup is illustrated in figure. 8.1b. As with all electrolyte- gated transistors, the potential applied to the gate contact is communicated to the semiconductor surface via interfacial electric double layers (EDLs). To record linear transfer characteristics, a small, constant positive voltage (+ 0.1 V) is applied to the drain contact while the source remains grounded. We then record the drain current I_D as a function of the voltage applied to gate (gate Voltage, V_G). V_G is ramped from –0.6V → +0.8V. Drain current is low for negative or small positive gate voltage but rises linearly with gate voltage when gate exceeds threshold, V_{th}. However, the potential that applies at the semiconductor surface is different from the potential applied to the gate needle by a membrane potential V_M in response to substrate solution in the sample pool. Hence, substrate- concentration membrane potential $V_M(c)$ is transduced into a threshold shift $\Delta V_{th}(c)$, and the transfer characteristic shifts along the gate voltage axis.

a)

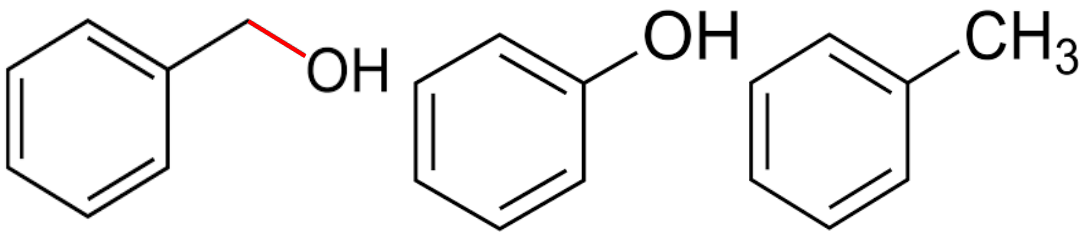

b)

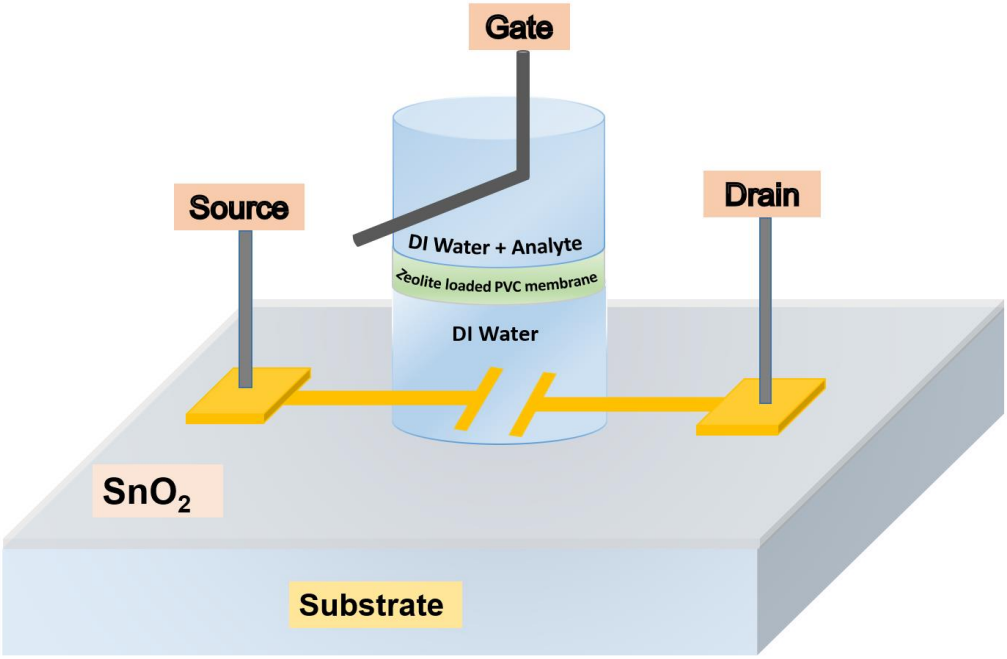

Figure. 8.1a: Chemical formulae of the three non- ionic aromatic analytes tested in this study, left to right: benzyl alcohol, phenol, and toluene. 1b: Schematic illustration of WGTFT sensor setup. SnO_2 is spray deposited from a pyrolysed tin chloride precursor over previously deposited Au / Cr adhesion layer source / drain contact pairs.

8.2.6 Data analysis

To determine threshold shift $\Delta V_{th}(c)$ quantitatively, we shifted recorded transfer characteristics at substrate concentration $c > 0$ along the V_G axis for best overlap with the $c = 0$ transfer characteristics. The required shift for best overlap was taken as $\Delta V_{th}(c)$. Resulting ΔV_{th} *vs* c response characteristics were fitted to the 'Langmuir-Freundlich' (LF) isotherm, equation 8. 1, using the Origin 2019 non-linear fitting routine. We found that fitting returned β values not significantly different from 1 within the margin of error. We therefore used $\beta = 1$ for determination of limit-of-detection (LoD), *i.e.* the lowest concentration of analyte (substrate) that can be detected with a particular zeolite in the WGTFT. Data were re- plotted in linearized form, $\Delta V_{th}(sat)$ (Kc +1) *vs.* Kc. A straight line of the form $\Delta V_{th}(sat)$ (Kc +1) = mKc + b was fitted, and linear fit parameters m and b +/– Δb evaluated using the linear fitting routine in Origin software. The coefficient b overlapped with zero within +/– Δb, as expected. The LoD was calculated from the common '3 errors' criterion,

$$Kc_{LoD} = 3\Delta b / m \qquad 8.2$$

LoD is a key measure of sensor performance.

8.3. Results and discussion

8.3.1 Catalytic activity

The catalytic activities of zeolites 1 to 10, as introduced in table 8.1, for the oxidation of aromatic water pollutants were determined following the protocol described in section 8.2.3 and A8.2. The resulting activities are summarized in table 8.2.

Table 8.2: Summary of catalytic activity of zeolites 1 to 10 on substrates phenol (P) benzyl alcohol (BA). 'No.', zeolite number from table 8.1; (a) conversion rate after 24h, reaction conditions: 80 °C atmospheric pressure, (b) conversion rate calculated as initial rate over a reaction period of 20 min (as after 4 h all catalysts lead to completion).

Zeolite No.	Composition / preparation	Benzyl alcohol conversion rate / $mM \cdot h^{-1}$ (a)	Phenol initial conversion rate / $mM \cdot h^{-1}$ (b)
1	1% Cu/ZSM-5-WI	0.09	0.65
2	1.5% Cu/ZSM-5-IE	0.12	1.43
3	1% Cu/ZSM-5-DP	0.16	0.43
4	1% Cu/NH4-ZSM-5-WI	0.01	0.38
5	1% Cu/13X-WI	0.20	1.59
6	1.5% Cu/Y-IE	0.17	1.59
7	1% Fe/ZSM-5-WI	0	0.34
8	1% Fe/MCM-41-WI	0	0.05
9	1% Fe/SBA-15-WI	0	1.54
10	1% Mn/ZSM-5-WI	0.24	< 0.01

Further explanations for the catalytic activities in table 8.2 are in the appendix (A8.3).

8.3.2 Sensing benzyl alcohol

First, all zeolites were tested for sensing of waterborne benzyl alcohol, an aromatic hydrocarbon with high solubility in water (> 277 mM). As a detailed example, we show results for WGTFTs for membranes sensitised with zeolite No. 3. Linear transfer characteristics under increasing benzyl alcohol concentration in the sample pool are shown in figure. 8.2a.

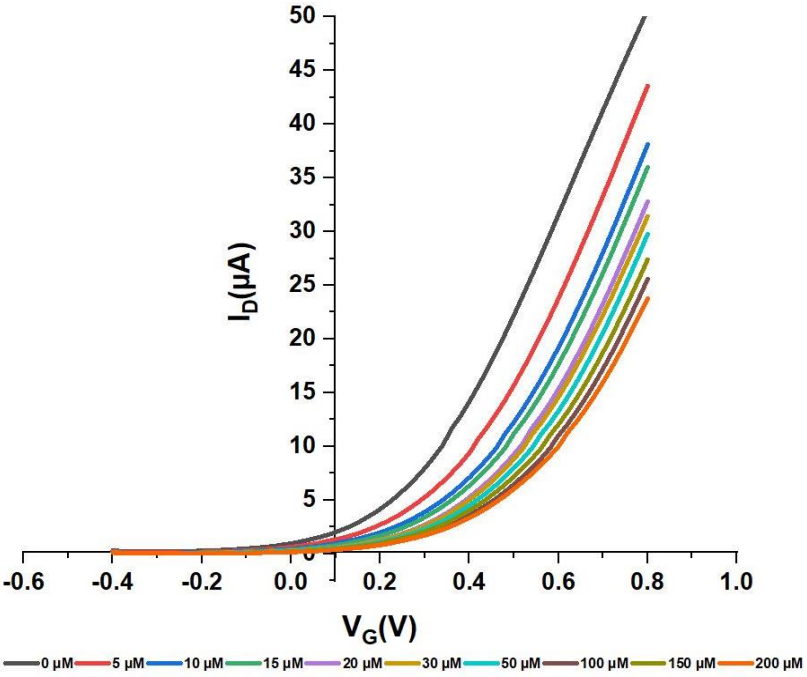

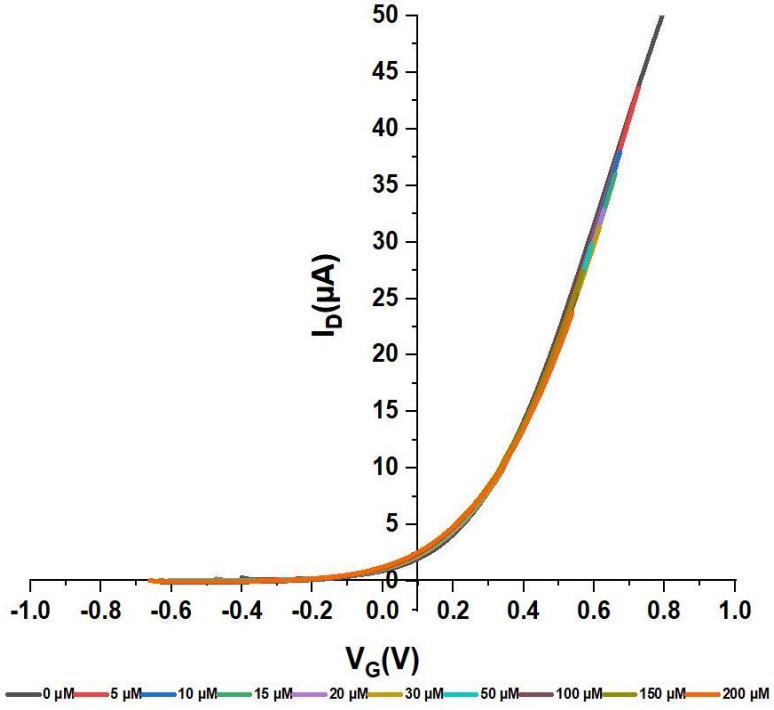

Figure 8.2 (a): (*top*) Linear transfer characteristics for SnO_2 WGTFTs sensitised with zeolite No. 3 filled plasticised PVC membrane under water with increasing benzyl alcohol concentration. 8.2 (b): (*bottom*) Resulting 'master curve' after shifting all transfers along the V_G axis for best overlap with $c = 0$.

All transfer characteristics are similar but shift along the gate voltage axis towards larger voltages in response to a few micromolar or higher benzyl alcohol concentration in water. Threshold shift $\Delta V_{th}(c)$ is due to an increase of PVC membrane potential, $V_M(c)$, with increasing concentration c of the analyte, benzyl alcohol, in the sample pool. We assign membrane potential to the adsorption of dipolar benzyl alcohol molecules onto the surface of zeolite grains in the phase transfer membrane. A zeolite that was developed as a catalyst for aromatic pollutants in water also acts as sensitizer for such a chemical at micromolar concentrations, even at ambient temperature where catalysis will not yet be occurring. To quantify threshold shift, all transfer characteristics are shifted along the gate voltage axis to match the $c = 0$ characteristics. The resulting 'master curve' is shown in figure. 8.2b. The good overlap into a single master curve confirms that the only impact of increasing analyte concentration in the sample pool is a membrane potential leading to a threshold shift, no other transistor parameter is affected.

We carried out similar tests for all compounds listed in table 8.1 under benzyl alcohol. We found that a number of them (No.s 1, 2, 4, 7, 8, 9) gave no response under benzyl alcohol concentrations up to 200 μM. However, candidates No.s 5, 6, 10 also succeeded in giving a threshold shift in response to benzyl alcohol, similar as for zeolite No.3. All response characteristics ΔV_{th} *vs.* c for the benzyl alcohol-sensing zeolites are shown in figure. 8.3:

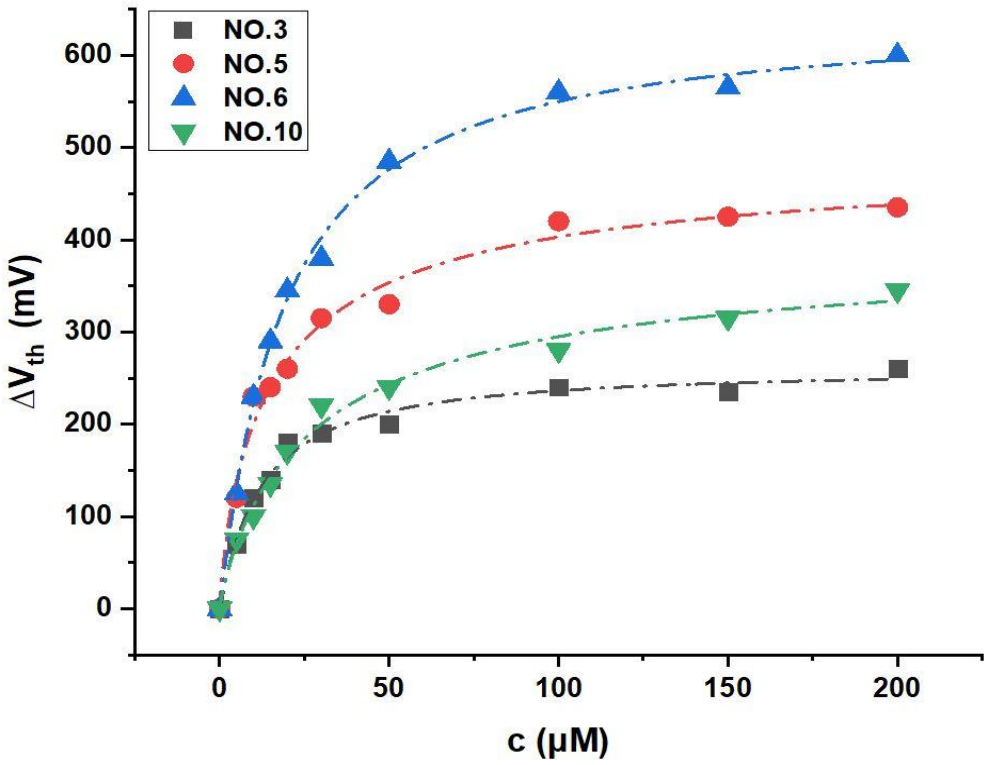

Figure. 8.3: Threshold shift ΔV_{th} *vs.* c in response to waterborne benzyl alcohol for WGTFTs sensitized with zeolites No.s 3, 5, 6, 10. The dashed lines are fits to equation 8.1.

It is obvious that the characteristics in figure 8.3 are not described by a Nikolsky-Eisenman law (linear shift on log *c* scale for high *c* / flat lining for low *c*), as it is observed for ion selective WGTFTs using ion 'capturing' organic ionophores [148 - 138]. Instead, the threshold shift increases steeply at low *c* but saturates at high *c*, as in (chapter 6)[256]. Dashed lines are therefore fit to a Langmuir- Freundlich (LF) adsorption isotherm, equation 8. 1, which provides a good match to the data. We found that the fitting returned β values close to 1 within the margin of error. We therefore used $\beta = 1$ for the determination of LoD. Resulting parameters and evaluated LoDs are listed in table 8.3:

Table 8.3: Characteristic parameters for fits of response characteristics, figure. 8.3a, to LF model, equation 8.1, for all zeolites that gave a threshold response to benzyl alcohol.

Zeolite No.	Substrate / Analyte	ΔV_{th}(sat) [mV]	K [10^4 L/mol]	β	LoD [μM]
3	Benzyl alcohol	262+/-13	8.3 +/- 1.0	1.05 +/- 0.16	4.6
5	Benzyl alcohol	484 +/- 34	6.7 +/- 1.3	0.86 +/- 0.14	2.4
6	Benzyl alcohol	635 +/- 19	5.7 +/- 0.4	1.09 +/- 0.08	2.1
10	Benzyl alcohol	396 +/- 37	3.4 +/- 0.9	0.87 +/- 0.13	4.3

Here all K's are similar in the order a few 10^4 L/mol, which is ~ 5 orders of magnitude smaller than the K values we find for Cs^+ ion exchange with zeolite mordenite [256]. All four successful zeolites lead to benzyl alcohol- sensitive WGTFTs with LoDs of a few μM, 5 orders- of- magnitude lower than the concentration of a saturated benzyl alcohol solution in water (~ 370 mM at 25 ^oC [288]), and below the 'potability limit' (the concentration that should not be exceeded in water for human consumption) of 19 μM [289]. The saturated threshold shift is large, particularly for zeolite No. 6 – compare this to 59 mV/decade for a Nernstian response law [148], and the electrochemical window of water, 1230 mV. ΔV_{th}(sat) is similar or larger than for Cs^+ ion exchange with mordenite [256]. We compare the surface areas of 'Zeolite Y', the support of catalyst No. 6, and 'ZSM-5', the support of catalysts No.s 3 and 10: Surface area of zeolite Y is given as 700 m^2 / g [290], whereas for zeolite ZSM5 it is only 400 m^2 / g [291]. The larger ΔV_{th}(sat) for catalyst No. 6 may , therefore, be due to larger surface area of Zeolite Y.

We can establish a clear correlation between catalytic activity, as shown in table 8.1, and activity as benzyl alcohol sensitizer: successful sensitizers 3, 5, 6 and 10 are also those with the highest catalytic conversion rates, above 0.15 mM/h. Zeolites with lower or no catalytic activity for benzyl

alcohol also do not act as benzyl alcohol sensitizers. We find that all protocols used to dope transition metal into the zeolite framework can lead to benzyl alcohol sensitivity - No. 3: DP; No.s 5, 10: WI; No. 6: IE all lead to benzyl alcohol sensitizers. Both Cu and Mn doped frameworks can lead to benzyl alcohol sensitizers, but not Fe doped frameworks which also summarily failed as catalysts, *cf.* section 8.3.1. Also, sensitizers are not limited to a specific Si : Al ratio, spanning 1.2 : 1 (No. 5) to 46 : 1 (No.s 3, 10). Frameworks MCM and SBA that lack Al altogether (No.s 8, 9) did not act as sensitizers, however this may be due to their doping with Fe only rather than a lack of Al.

8.3.3 Attempted sensing of phenol and toluene

Following successful sensing of waterborne benzyl alcohol with WGTFTs, we have attempted to replicate similar response for phenol. We selected a number of catalysts that we considered particularly promising: ZSM- 5 based zeolites show a high Si : Al ratio which is known to lead to strong adsorption of phenols [234,292], hence we tested No.s 2,3,7 and 10. The zeolite No. 2 is an active catalyst for phenol, No. 10 is almost inactive for phenol, *cf.* table 8.2. Further, we tested No. 6 for its good performance in benzyl alcohol sensors, albeit it having a low Si : Al ratio. However, while the catalytic activity for some of the zeolites selected here (*cf.* table 8.2) suggests good adhesion of phenol on their surface, we found very little or no threshold shift for WGTFTs sensitized with either of these catalysts. The most 'pronounced' response to phenol (figure.8.4) was for No. 2, which is also among the most active catalysts for phenol degradation (table 8.2), but the threshold shift was still less than 80 mV even under 200 μM phenol. As phenol concentration in potable water should not exceed 10 nM [293], none of the zeolites studied here can lead to practical phenol sensors.

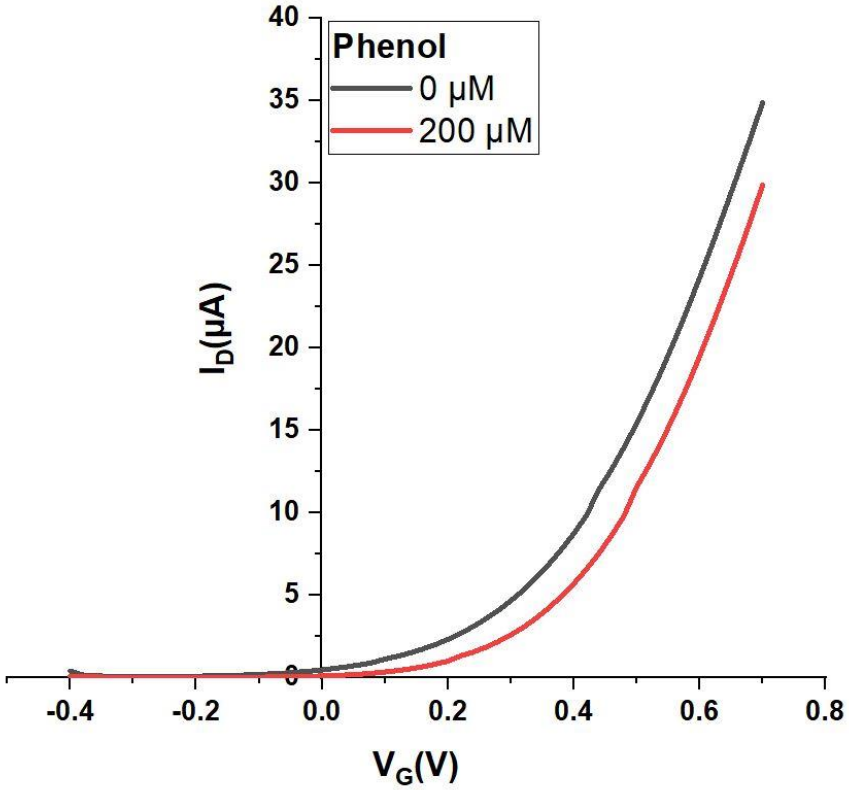

Figure. 8.4: Linear transfer characteristics for SnO_2 WGTFTs sensitised with zeolite No. 2 filled plasticised PVC membrane under pure water, and water with high concentration (200 µM) of phenol.

We suggest the lack of clear response to phenol comes from the different nature of its molecular dipole moment compared to benzyl alcohol: the dipole of phenol is locked in the plane of the aromatic ring as it is directly attached to it, while the dipole of benzyl alcohol is 'free', in a sense it is decoupled from the ring by a short saturated 'spacer' so it is not confined to the ring's plane. Even if phenol can adsorb well onto catalyst, if adsorption is 'face on' onto catalyst surface, the dipole will be lateral (in the surface plane), and dipoles will cancel over an ensemble of many adsorbed phenols as they will be randomly orientated in the adsorption plane. We have also tested WGTFT response to waterborne toluene on the example of catalysts No.s 5, 6, 10. These all showed response to benzyl alcohol, and they represent different zeolite 'families': No. 5, based on zeolite type X, 6: Based on zeolite type Y, No. 10, based on ZSM5.

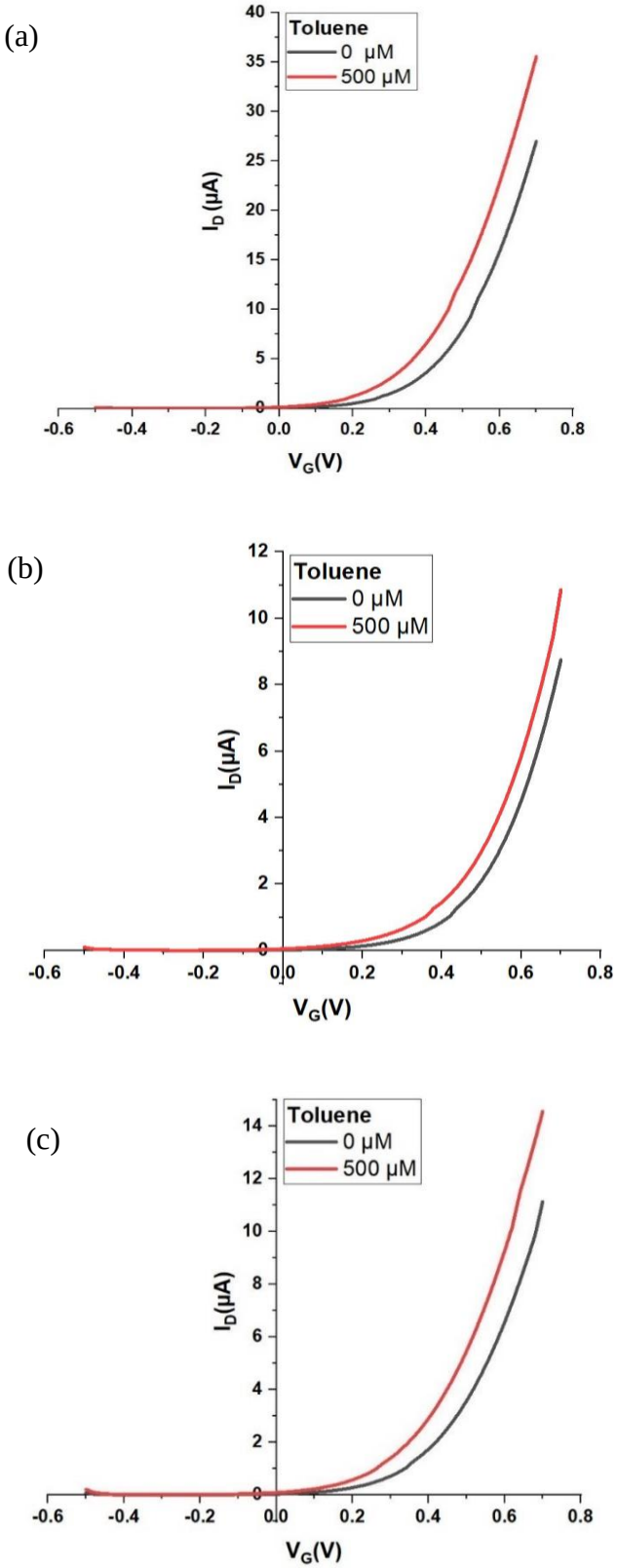

Figure. 8.5: Response of transfer characteristics of WGTFTs sensitised with zeolite 5 (a), 6 (b), and 10 (c), to 500μM toluene.

However, even under 500 μM of toluene, which is far above the potability limit of 11 μM [294], the threshold shift does not exceed 70 mV, *cf.* Figure. 8.5. Toluene shows almost no molecular dipole, so even if it adsorbs well to catalyst surface, only a very small surface potential will develop. Also, threshold shift is in the opposite direction than for benzyl alcohol, indicating reversed orientation of the (small) dipole moment or a screening effect of surface dipoles on the 'blank' zeolite sensitizer.

We examined another molecule 'acetophenone' which has similar dipole nature to benzyl alcohol with zeolite No.5. By increasing the acetophenone concentration the threshold voltage shifts in the same way as benzyl alcohol. The linear transfer characteristics and master curve are shown in figures A.8.1 in the appendix. This proves that the right type of molecule dipole (free dipole) allows for potentiometric sensing in WGTFTs.

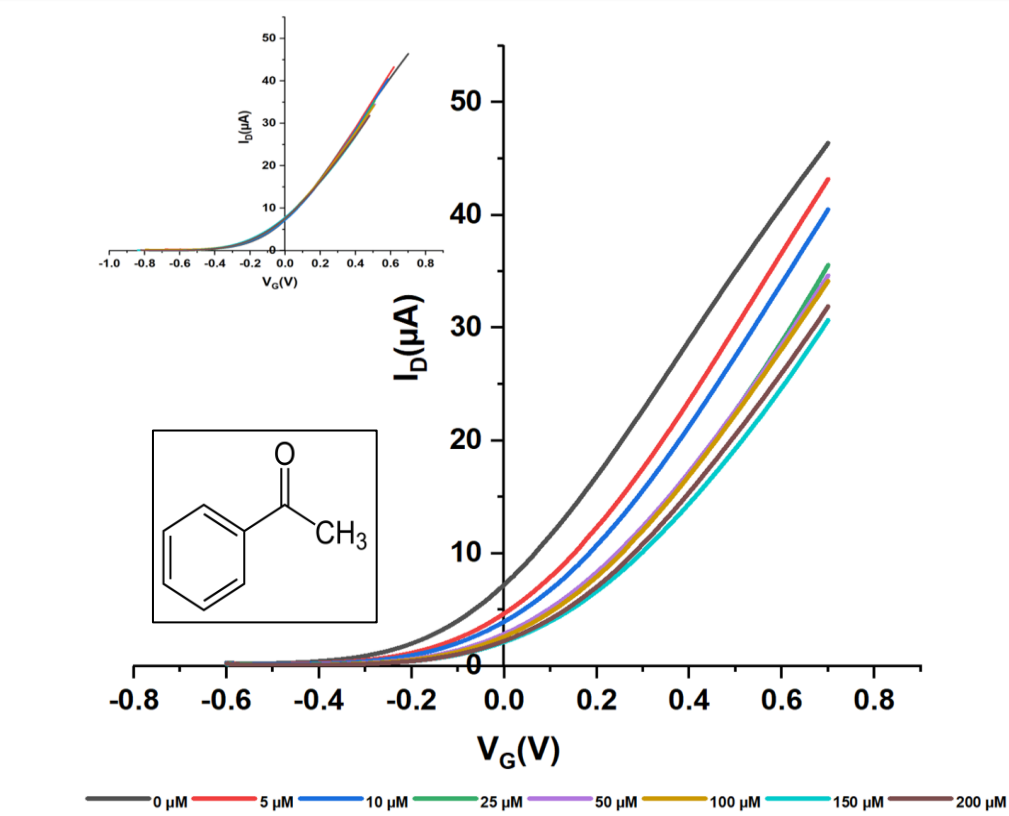

Figure 8.6: Linear transfer characteristics for SnO_2 WGTFTs sensitised with zeolite No. 5 filled plasticised PVC membrane under water with increasing acetophenone concentrations. (insets: resulting 'master curve' after shifting all transfers along the V_G axis for best overlap with c = 0, and acetophenone structure).

8.4. Conclusions

Sensitised phase transfer membranes are traditionally used for the sensing of waterborne ions with a variety of potentiometric transducers (electrochemical cells, the ISFET, and recently, the WGTFT [32-256]). Here, we show that when such membranes are appropriately sensitised, they can also give a potentiometric response to some non- ionic aromatic solutes, which we transduce with the WGTFT. This allows the sensing of the aromatic water pollutant, benzyl alcohol, with a limit-of- detection (LoD) below its potability limit. We believe the observed potentiometric response results from interfacial dipoles when an analyte with a 'free' molecular dipole (*i.e.* a dipole not locked in the molecular plain) adsorbs onto the surface of grains of powdered sensitizer. This is supported by the observed response characteristics that follow Langmuir surface adsorption isotherms rather than the Nikolsky-Eisenman characteristics for typical ion sensors [148-138]. The need for a 'free' molecular dipole limits the scope for potentiometric sensing of aromatic pollutants in water, but also imparts selectivity to the potentiometric sensor concept.

To identify sensitizers for aromatic water pollutants, we were guided by a common pre-requisite for both sensing, and heterogeneous catalysis: Both require adhesion of a 'target' pollutant molecule (*i.e.*, the analyte for sensing or the substrate for catalysis) on the surface of the sensitizer or catalyst. As candidate sensitizers, we have therefore tested a number of transition metal doped zeolites and related frameworks that are also considered as heterogeneous catalysts for the oxidation of the same pollutants. For benzyl alcohol, we establish a clear correlation between 'good' catalysts (those with relatively high conversion rates) and successful sensitizers, namely the four candidates successful as sensitizers were those which displayed the highest catalytic activity. Attempted sensing of phenol was always unsuccessful despite good catalytic activity for a number of the zeolites studied here on phenol as substrate. It was these negative sensing results despite having good catalytic activities that lead us to the 'free dipole' criterion.

The present work provides a first example for the use of a catalyst as a sensitizer in a phase transfer membrane for WGTFT potentiometric sensors. Hence, we introduce an application for catalysts beyond catalysis, a concept that we recommend for more general consideration. In future, we also propose to use the method established here 'in reverse', namely to use potentiometry with the WGTFT to screen for promising candidate catalysts as a 'shortcut' from the labour- intensive procedure described in 8.2.3. This will require detailed consideration of specific reactive pathways

though, note *e.g.* the breakdown of phenol is by peroxide decomposition while oxidation of alcohols like benzyl alcohol is via hydrogen abstraction[295]. Potentiometric response signals surface adsorption only, without distinguishing later reactive pathways, and can only be applied for substrates with a ‘free’ dipole.

Chapter 9: Conclusion and future work

9.1 Overall Conclusion

The main two achievements of this thesis and the involved experimental work are: first, the incorporation of a stable solution processed semiconductor of SnO_2 in WGTFTs. Secondly the integration of a new sensitizer family namely zeolites in WGTFTs sensors to detect harmful ions and non-ionic pollutants which result in desirable low LoDs.

Chapter 5 shows the SnO_2 WGTFTs and their capability as sensors for waterborne analytes. SnO_2 WGTFTs display a good performance including optimal stability under water, regardless of some drawbacks such as the high off current.

In chapter 6,7 and 8 different zeolites were used as sensitizers in sensitised phase transfer membranes in WGTFTs and low LoD were obtained below the potability limit of the target analytes. In chapter 6 a PVC membrane was sensitized with the zeolite mordenite and incorporated into SnO_2 WGTFT to detect Cs^+ ions in tap water. The response characteristics follow Langmuir characteristics with good sensing parameters. The binding constant K is in the order of 10^9 L/mole and the LoD is in the sub-nano molar range in a background of a cocktail of interfering ions. Similarly, in chapter 7, a clinoptilolite zeolite was used in the sensitized WGTFT architecture to sense heavy metal ions, specifically Pb^{2+} and Cu^{2+}. Also, a detection limit within the potability in drinking water was obtained with Langmuir- Freundlich (LF) characteristics. The unusual characteristics reported here in both chapters 6 and 7 differ from the generally reported characteristics in potentiometric ion sensors.

Chapter 8 shows that also non-ionic aromatic molecules can be detected in the same way by using catalytic zeolites sensitised WGTFTs. In addition, the specific type of aromatic hydrocarbons that can be detected are found to be the molecules with ‘free’ dipoles such as benzyl alcohol. It is found also that the good zeolites catalysts for benzyl alcohol give good sensitizers as well. As in chapter 6 Langmuir response characteristics were obtained with a reasonable LoD.

Two different response characteristics were obtained here in this work in the three sensing experiments, which are Langmuir and Langmuir-Freundlich isotherms. This difference is probably

associated with the nature of the zeolites and their binding sites. For example, for a homogenous surface of binding sites where a mono-layer is formed by the binding of analytes with these sites, and this follows Langmuir isotherm like in chapter 6 and 8. In the case where the homogeneity is reduced (heterogeneous surface) the characteristics are modified to Langmuir-Freundlich isotherms instead of Langmuir isotherms similar to the work in chapter 7 when clinoptilolite is used to detect heavy metals.

9.2 Outlook for future work

Some proposed future work is suggested here based on this thesis work and the overall conclusion, and are listed below:

1. Further experiments are recommended regarding the sensing mechanism and some unsolved issues related to this mechanism. For example, in such sensing via membrane potential, the mechanism was considered from chapters 6 and 8 to be a surface mechanism. This assumption for this reason was that a comparison between characteristics parameters (e.g. c1/2) of Cs extraction by mordenite[154] and what was measured in the experiments, and also from chapter 8 where the membrane of No.6 zeolite has the highest surface area and associated with larger recorded membrane potential. So further experiments to clarify that using different grinding degrees of the sensitizers would hopefully provide evidence of a surface mechanism. Another issue in chapter 6 is when reverse sample and reference pools, the threshold shift is very low and does not reverse if compared with the conventional potentiometric sensors with the same design of two compartments.

2. The obtained characteristics here with ions potentiometric sensors is Langmuir (and Langmuir- Freundlich) characteristics which is unusual especially when using organic macrocycles sensitizers. Such characteristics with zeolites sensitizers are not fully understood and worthy of further study. Some desirable findings are associated with the Langmuir like characteristics, such as the low LoD. More experiments could be conducted such as applying the same zeolites sensitized membrane into an ISE (another

potentiometric sensor) to see if the same characteristics are obtained, or flow the same protocol and procedures with organic macrocycles sensitized membranes as was used for the zeolites sensitized membrane in this work.

3. Trying to incorporate other families of adsorbents as sensitizers within WGTFTs sensors in the same way as zeolites were integrated. For examples clay [296], activated carbon[297], and Metal-organic frameworks' MOFs. The MOFs have large surface area and have been used to adsorb different ions and molecules [298].

4. From the work in chapter 8 we could also use different catalysts as sensitizers for the molecules that meant to catalyze if these molecules with a free dipole. In our work, benzyl alcohol was used and as a further example acetophenone (in appendix A8.4).

References:

[1] K.A. Sharp, Encycl. Life Sci. (2001).[online] Available at:http://crystal.med.upenn.edu/sharp-lab-pdfs/sharp_EncLifeSci.pdf [Accessed 9 Aug 2020].

[2] F.F. GORDALLA BC, MÜLLER MB, Desert Plants **40**, (2007).

[3] C.E. Boyd, *Water Quality: An Introduction.* (Springer Nature, 2019).

[4] Eur-lex.europa.eu. (2015). *Consolidated TEXT: 31998L0083 — EN — 27.10.2015*. [online] Available at: https://eur-lex.europa.eu/legal-content/EN/TXT/HTML/?uri=CELEX:01998L0083-20151027&from=EN [Accessed 9 Aug. 2020].

[5] M. Noda and H. Sakuta, Trends Neurosci. **36**, 661 (2013).

[6] K. Al-Akeel, "The pollution of water by Trace Elements Research Trends." Adv. Bioremediation Phytoremediation **10**, (2017).

[7] R.P. Schwarzenbach, T. Egli, T.B. Hofstetter, U. von Gunten, and B. Wehrli, Annu. Rev. Environ. Resour. **35**, 109 (2010).

[8] M. Jaishankar, T. Tseten, N. Anbalagan, B.B. Mathew, and K.N. Beeregowda, Interdiscip. Toxicol. **7**, 60 (2014).

[9] Nepis.epa.gov. (2008). *Lead and Copper Rule: A Quick Reference Guide*. [online] Available at: https://nepis.epa.gov/Exe/ZyPDF.cgi?Dockey=60001N8P.txt [Accessed 9 Aug. 2020].

[10] R.W. Herschy, Encycl. Earth Sci. Ser. 876 (2012).

[11] Virginia Alonso de Linaje, (2017). Soil and water pollution in Europe – A problem that concerns everyone. Available at: [online] https://metalaidblog.wordpress.com/2017/02/27/pollution-europe/. [Accessed 9 Aug 2020].

[12] E. Johan, T. Yamada, M.W. Munthali, P. Kabwadza-Corner, H. Aono, and N. Matsue, Procedia Environ. Sci. **28**, 52 (2015).

[13] M.R. Awual, S. Suzuki, T. Taguchi, H. Shiwaku, Y. Okamoto, and T. Yaita, Chem. Eng. J. **242**, 127 (2014).

[14] A.S. David and S.C. Wessely, J. Psychosom. Res. **39**, 1 (1995).

[15] the Guardian. (2015). *Benzene Found In Montana Water Supply After Yellowstone Oil Spill*. [online] Available at: <https://www.theguardian.com/environment/2015/jan/20/benzene-montana-water-supply-yellowstone-oil-spill> [Accessed 9 August 2020].

[16] Reuters. (2014). *China's Tap Water Cleared Of Benzene In Some Areas: Xinhua*. [online] Available at: <https://www.reuters.com/article/us-china-pollution/chinas-tap-water-cleared-of-benzene-in-some-areas-xinhua-idUSBREA3A0J120140413> [Accessed 9 August 2020].

[17] S. Li, Y. Zhang, Y. Wang, K. Xia, Z. Yin, H. Wang, M. Zhang, X. Liang, H. Lu, M. Zhu, H. Wang, X. Shen, and Y. Zhang, InfoMat **2**, 184 (2020).

[18] L. Dai, Y. Wang, X. Zou, Z. Chen, H. Liu, and Y. Ni, Small **16**, 1906567 (2020) (2020).

[19] X. Yan, H. Li, and X. Su, TrAC - Trends Anal. Chem. **103**, 1 (2018).

[20] A. Dey, Mater. Sci. Eng. B Solid-State Mater. Adv. Technol. **229**, 206 (2018).

[21] U. Choudhary, **8**, 386 (2019).

[22] G. Seo, G. Lee, M.J. Kim, S. Baek, M. Choi, K.B. Ku, C. Lee, S. Jun, D. Park, H.G. Kim, S. Kim, J. Lee, B.T. Kim, E.C. Park, and S. Il Kim, *ACS nano*, **14**(4):5135-5142 (2020).

[23] M. Chung, G. Fortunato, and N. Radacsi, J. R. Soc. Interface **16**, (2019).

[24] L. Torsi, M. Magliulo, K. Manoli, and G. Palazzo, Chem. Soc. Rev. **42**, 8612 (2013).

[25] E. Bakker and E. Pretsch, TrAC - Trends Anal. Chem. **24**, 199 (2005).

[26] K.A. Tuwei, N.H. Williams, and M. Grell, Sensors Actuators, B Chem. **237**, 1102 (2016).

[27] R.A. Picca, K. Manoli, E. Macchia, A. Tricase, C. Di Franco, G. Scamarcio, N. Cioffi, and L. Torsi, Front. Chem. **7**, 1 (2019).

[28] A.H. Alshammari, Z. Alqahtani, F.B. Mohd Suah, S.A. Nizar, A. Dunbar, and M. Grell, Anal. Chim. Acta **1105**, 1 (2020).

[29] G. Cai, L. Qiang, P. Yang, Z. Chen, Y. Zhuo, Y. Li, Y. Pei, and G. Wang, IEEE Electron Device Lett. **39**, 1409 (2018).

[30] T.M. Althagafi, S.A. Algarni, and M. Grell, Talanta **158**, 70 (2016).

[31] O.O. Soldatkin, M.K. Shelyakina, V.N. Arkhypova, E. Soy, S.K. Kirdeciler, B. Ozansoy Kasap, F. Lagarde, N. Jaffrezic-Renault, B. Akata Kurç, A.P. Soldatkin, and S. V. Dzyadevych, Nanoscale Res. Lett. **10**, (2015).

[32] S. Casalini, F. Leonardi, T. Cramer, and F. Biscarini, Org. Electron. Physics, Mater. Appl. **14**, 156 (2013).

[33] E. Zdrachek and E. Bakker, Anal. Chem. **91**, 2 (2019).

[34] L. Kergoat, L. Herlogsson, D. Braga, B. Piro, M.C. Pham, X. Crispin, M. Berggren, and G. Horowitz, Adv. Mater. **22**, 2565 (2010).

[35] B.K. Bansod, T. Kumar, R. Thakur, S. Rana, and I. Singh, Biosens. Bioelectron. **94**, 443 (2017).

[36] P. Kruse, J. Phys. D. Appl. Phys. **51**, (2018).

[37] M. Singh, G. Palazzo, G. Romanazzi, G.P. Suranna, N. Ditaranto, C. Di Franco, M.V. Santacroce, M.Y. Mulla, M. Magliulo, K. Manoli, and L. Torsi, Faraday Discuss. **174**, 383 (2014).

[38] J.E. Lilienfeld, 1745175 (1930).

[39] M. Kahng, D. and Atalla, (3,102) (1963).

[40] P.K. Weimer, 6 (1962).

[41] U. Zschieschang and H. Klauk, J. Mater. Chem. C **7**, 5522 (2019).

[42] A. Sharma, C. Madhu, and J. Singh, Int. J. Comput. Appl. **89**, 36 (2014).

[43] E. Fortunato, P. Barquinha, and R. Martins, Adv. Mater. **24**, 2945 (2012).

[44] C. Tanase, E.J. Meijer, P.W.M. Blom, and D.M. De Leeuw, Org. Electron. **4**, 33 (2003).

[45] J. P. Colinge and C.A. Colinge, *PHYSICS OF SEMICONDUCTOR DEVICES* (2005).

[46] H. Du, X. Lin, Z. Xu, and D. Chu, *Electric Double-Layer Transistors: A Review of Recent Progress* (Springer US, 2015).

[47] Z. Bao and J. Locklin, *Organic Field-Effect Transistors.* (2007).

[48] D.W. Chou, K.L. Chen, and S.F. Wang, Microelectron. Reliab. **91**, 323 (2018).

[49] J. Temme, T. Meyers, J. Reker, F.F. Vidor, J. Vollbrecht, H. Kitzerow, J. Paradies, and U. Hilleringmann, **1104314**, 14 (2019).

[50] Lingling Huang, D. Han, Y. Zhang, P. Shi, W. Yu, G. Cui, Y. Cong, J. Dong, S. Zhang, X. Zhang, and Y. Wang, Electron. Lett. **51**, 1595 (2015).

[51] Z. Chen, L. Lan, and J. Peng, RSC Adv. **9**, 27117 (2019).

[52] L. Zhang, W. Xu, W. Liu, P. Cao, S. Han, D. Zhu, and Y. Lu, J. Phys. D. Appl. Phys. **53**, (2020).

[53] H. Lee, S. Ha, J.H. Bae, I.M. Kang, K. Kim, W.Y. Lee, and J. Jang, Electron. **8**, 1 (2019).

[54] S.S.T. Transistor, W. Lee, H. Lee, S. Ha, C. Lee, J. Bae, I. Kang, K. Kim, and J. Jang, 1 (2020).

[55] H. Liu, J. Sun, Q. Tang, and Q. Wan, J. Phys. Chem. C **114**, 12316 (2010).

[56] C. Wei Shih, A. Chin, C. Fu Lu, and W. Fang Su, Sci. Rep. **6**, 2 (2016).

[57] K.H. Seol, S.J. Lee, K.G. Cho, K. Hong, and K.H. Lee, J. Mater. Chem. C **6**, 10987 (2018).

[58] B. Kumar, B.K. Kaushik, Y.S. Negi, P. Mittal, and A. Mandal, 2011 IEEE Recent Adv. Intell. Comput. Syst. RAICS 2011 706 (2011).

[59] S.D. Brotherton, Introd. to Thin Film Transistors (2013).

[60] S. Dimitrijev, *PRINCIPLES OF SEMICONDUCTOR DEVICES* (Oxford university press, New York, 2012).

[61] M. Lin, J. Huang, C. Ku, C. Lin, H. Lee, and J. Juang, J. Alloys Compd. **727**, 565 (2017).

[62] J. Li, W. Ou-yang, and M. Weis, J. Phys. D. Appl. Phys. *50*(3), 035101(2017).

[63] S.M. Sze, *Semiconductor Devices Physics and Technology*, 2nd ed. (John Wiley & Sons, Hsinchu, Taiuan, 2002).

[64] A. Tixier-Mita, S. Ihida, B.D. Ségard, G.A. Cathcart, T. Takahashi, H. Fujita, and H. Toshiyoshi, Jpn. J. Appl. Phys. **55**, (2016).

[65] C. Liu, X. Liu, T. Minari, M. Kanehara, and Y.Y. Noh, J. Inf. Disp. **19**, 71 (2018).

[66] J.Y. Choi and S.Y. Lee, J. Korean Phys. Soc. **71**, 516 (2017).

[67] H. Ray-Hua, Crystals **9**, 415(2019).

[68] Ü. Ozgur, D. Hofstetter, and H. Morkoç, Proc. IEEE **98**, 1255 (2010).

[69] S. F Oboudi, N.F. Habubi and S.S. Chiad, MSAIJ, 10(9), (2014).

[70] G.E. Patil, D.D. Kajale, V.B. Gaikwad, and G.H. Jain, ISRN Nanotechnol. **2012**, 1 (2012).

[71] H.Y. Liu, W.C. Hsu, J.H. Chen, P.H. Hsu, and C.S. Lee, IEEE Trans. Electron Devices **67**, 1009 (2020).

[72] K.K. Banger, Y. Yamashita, K. Mori, R.L. Peterson, T. Leedham, J. Rickard, and H. Sirringhaus, Nat. Mater. **10**, 45 (2011).

[73] L. Znaidi, Mater. Sci. Eng. B Solid-State Mater. Adv. Technol. **174**, 18 (2010).

[74] T.M. Althagafi, S.A. Algarni, A. Al Naim, J. Mazher, and M. Grell, Phys. Chem. Chem. Phys. **17**, 31247 (2015).

[75] M. Ganchev, A. Katerski, S. Stankova, J.S. Eensalu, P. Terziyska, R. Gergova, G. Popkirov, and P. Vitanov, J. Phys. Conf. Ser. **1186**, (2019).

[76] A. Janotti and C.G. Van de Walle, Rep Prog Phy **72**, 126501 (2009).

[77] O. Madelung, *Madelung SEMICONDUCTOR BASIC-DATA* (Springer Science & Business Media, 2012).

[78] T. Minami, H. Sonohara, S. Takata, and H. Sato, Jpn. J. Appl. Phys. **33**, L743 (1994).

[79] C. Coskun, D.C. Look, G.C. Farlow, and J.R. Sizelove, Semicond. Sci. Technol. **19**, 752 (2004).

[80] and H.M. Ü. Özgür, Ya. I. Alivov, C. Liu, A. Teke, M. A. Reshchikov, S. Doğan, V. Avrutin, S.-J. Cho, J. Appl. Phys. **98**, 1 (2005).

[81] S. Fajardo, García-Galvan, F. R., V. Barranco, J.C. Galvan, and S.F. Batlle, Intech **i**, 13 (2012).

[82] A. Kohan, G. Ceder, D. Morgan, and C. Van de Walle, Phys. Rev. B **61**, 15019 (2000).

[83] Z. Zhang, J. Huang, S. Chen, X. Pan, L. Chen, and Z. Ye, Superlattices Microstruct. **100**, 468 (2016).

[84] G.F. Boesen, J.E Jacobs, Proc. Inst. Electr. Electron. Eng. *Proceedings of the IEEE*, *56*(11),

pp.2094-2095. (1968).

[85] R.L. Hoffman, B.J. Norris, and J.F. Wager, Appl. Phys. Lett. **82**, 733 (2003).

[86] K. Nomura, H. Ohta, K. Ueda, T. Kamiya, M. Hirano, and H. Hosono, Science. **300**, (5623) 1269 (2003).

[87] B.S. Ong, C. Li, Y. Li, Y. Wu, and R. Loutfy, J. Am. Chem. Soc. **129**, 2750 (2007).

[88] N. Lehraki, M.S. Aida, S. Abed, N. Attaf, A. Attaf, and M. Poulain, Curr. Appl. Phys. **12**, 1283 (2012).

[89] B. Bayraktaroglu et al, IEEE Electron Device Lett. **29**, 1024 (2008).

[90] G. Adamopoulos, A. Bashir, S. Thomas, W.P. Gillin, S. Georgakopoulos, M. Shkunov, M.A. Baklar, N. Stingelin, R.C. Maher, L.F. Cohen, D.D.C. Bradley, and T.D. Anthopoulos, Adv. Mater. **22**, 4764 (2010).

[91] G. Adamopoulos, S. Thomas, P.H. Wöbkenberg, D.D.C. Bradley, M.A. McLachlan, and T.D. Anthopoulos, Adv. Mater. **23**, 1894 (2011).

[92] A. Al Naim and M. Grell, Appl. Phys. Lett. **101**, (2012).

[93] A.F. Al Baroot and M. Grell, Mater. Sci. Semicond. Process. **89**, 216 (2019).

[94] E. Bandiello, M. Sessolo, and H.J. Bolink, J. Mater. Chem. C **2**, 10277 (2014).

[95] S. Das and V. Jayaraman, Prog. Mater. Sci. **66**, 112 (2014).

[96] T. Serin, N. Serin, S. Karadeniz, H. Sari, N. Tuğluoğlu, and O. Pakma, J. Non. Cryst. Solids **352**, 209 (2006).

[97] Q. Jiang, X. Zhang, and J. You, Small **14**, 1 (2018).

[98] B. Cojocaru, D. Avram, V. Kessler, V. Parvulescu, G. Seisenbaeva, and C. Tiseanu, Sci. Rep. **7**, 4 (2017).

[99] H.A.K.H. KOELMANS, Solid State Electron. **7**, 701 (1964).

[100] C. Avis, Y.G. Kim, and J. Jang, Materials (Basel). **12**, (2019).

[101] Akira Aoki and Hiroshi Sasakura, Jpn. J. Appl. Phys. (1970).

[102] M.W.J. Prins, K.O. Grosse-Holz, G. Müller, J.F.M. Cillessen, J.B. Giesbers, R.P. Weening, and R.M. Wolf, Appl. Phys. Lett. **68**, 3650 (1996).

[103] R.E. Presley, C.L. Munsee, C.-H. Park, D. Hong, J.F. Wager, and D. a Keszler, J. Phys. D. Appl. Phys. **37**, 2810 (2004).

[104] K.C. Yeaju Jang, Hahoon Lee, AIP Adv. **10**, 035011 (2020).

[105] A. Chin, C.W. Shih, C.F. Lu, and W.F. Su, In *2016 23rd International Workshop on Active-Matrix Flatpanel Displays and Devices (AM-FPD)* (294-297). IEEE. 294 (2016)

[106] G. Huang, L. Duan, G. Dong, D. Zhang, and Y. Qiu, ACS Appl. Mater. Interfaces **6**, 20786 (2014).

[107] J. Sun, W. Huang, C. Qian, J. Yang, and Y. Gao, Phys. Chem. Chem. Phys. **16**, 1084 (2014).

[108] I. Valitova, M.M. Natile, F. Soavi, C. Santato, and F. Cicoira, ACS Appl. Mater. Interfaces **9**, 37013 (2017).

[109] C. Zou, J. Sun, G. Gou, L.A. Kong, C. Qian, G. Dai, J. Yang, and G. hua Guo, Appl. Phys. A Mater. Sci. Process. **123**, 1 (2017).

[110] J. Sun, A. Lu, L. Wang, R.E. Presley, C.L. Munsee, C. Park, B. Oh, Y. Kim, and H. Lee, (n.d.).

[111] Z.W. Zhang X, Zhai J, Yu X, Zhu R, J. Nanosci. Nanotechnol. **15**, (2015).

[112] N. Mohammadian. and L.A. Majewski, High Capacitance Dielectrics for Low Voltage Operated OFETs." *Organic Field-Effect Transistors*. IntechOpen, (2020)

[113] S.H. Kim, K. Hong, W. Xie, K.H. Lee, S. Zhang, T.P. Lodge, and C.D. Frisbie, ***5*** (14), 6580-6585 (2013).

[114] H. Wang and L. Pilon, Electrochim. Acta **63**, 55 (2012).

[115]Lenntech, Water Conduct.[online] Available at: https://www.lenntech.com/applications/ultrapure/conductivity/water-conductivity.htm [Accessed 29 Mar 2020).

[116] T.S. Light, B. Kingman, A.C. Bevilacqua. In *209th American Chemical Society National Meeting* (2-6) (1995).

[117] Yorkshirewater.com. *Hard Water, Water Hardness Map | Yorkshire Water*. [online] Available at: https://www.yorkshirewater.com/water-quality/check-your-water-hardness/ [Accessed 24 Nov. 2019].

[118] Y. Fujii, Y. Muramoto, and N. Shimizu, In *2010 Annual Report Conference on Electrical Insulation and Dielectic Phenomena* (1-4). IEEE. (2010).

[119] P. Yang, G. Cai, X. Wang, and Y. Pei, EEE Trans. ELECTRON DEVICES **66**, 3554 (2019).

[120] Y. Fang, D. Zhang, H. Cheng, N. Fu, X. Zhou, S. Fang, and Y. Lin, ACS Appl. Nano Mater **3**, 342−350 (2020).

[121] P. Nanofibers, S.W. Lee, H.J. Lee, J.H. Choi, W.G. Koh, J.M. Myoung, J.H. Hur, J.J. Park, J.H. Cho, and U. Jeong, Nano Lett. **10**, 347 (2010).

[122] A. F. Al Naim and M.Grell., J. Appl. Phys **112**, 114502 (2012).

[123] R. Liu, Q. Zhu, W. Wang, X. Hui, P. Liu, and Q. Wan, ***4***(33),7744-7750. (2016).

[124] L. Kergoat, B. Piro, and M. Berggren, Anal Bioanal Chem **402**, 1813 (2012).

[125] A. Al Baroot, A. Alshammari, and M. Grell, Thin Solid Films **669**, 665 (2019).

[126] N.R. Stradiotto, H. Yamanaka, and M.V.B. Zanoni, J. Braz. Chem. Soc. **14**, 159 (2003).

[127] A. Bratov, N. Abramova, and A. Ipatov, Anal. Chim. Acta **678**, 149 (2010).

[128] P. Vadgama, **50**, 141 (1990).

[129] N. Mihali, C. and Vaum**,** *Recent Advances in Plasticizers*, p.125 (2012).

[130] M.M. Ardakani, M.K. Kashani, M. Salavati-Niasari, and A.A. Ensafi, Sensors Actuators, B Chem. **107**, 438 (2005).

[131] M. Esmaelpourfarkhani, G.H. Rounaghi, and M.H. Arbab-Zavar, J. Braz. Chem. Soc. **26**, 963 (2015).

[132] F. Pouya, M. Arabi, and G. Absalan, Appl. Organomet. Chem. **32**, 1 (2018).

[133] S. Sohrabnejad, M.A. Zanjanchi, M. Arvand, and M.F. Mousavi, Electroanalysis **16**, 1033 (2004).

[134] M. Sharifi-Sistani, Int. J. Electrochem. Sci. **14**, 10681 (2019).

[135] F. Perret and A.W. Coleman, Chem. Commun. **47**, 7303 (2011).

[136] K. Sharma and P. Cragg, Chem. Sensors, **1**(9), pp.1-18. (2011).

[137] Y. Choi, H. Kim, J.K. Lee, S.H. Lee, H. Bin Lim, and J.S. Kim, Talanta **64**, 975 (2004).

[138] T.M. Althagafi, A.F. Al Baroot, S.A. Algarni, and M. Grell, Analyst **141**, 5571 (2016).

[139] H. Oh, E.M. Choi, H. Jeong, K.C. Nam, and S. Jeon, Talanta **53**, 535 (2000).

[140] W. Walkowiak and C.A. Kozlowski, Desalination **240**, 186 (2009).

[141] D. Lee and J.D.R. Thomas, Talanta **41**, 901 (1994).

[142] K. Suzuki, K. Sato, H. Hisamoto, D. Siswanta, K. Hayashi, N. Kasahara, K. Watanabe, N. Yamamoto, and H. Sasakura, Anal. Chem. **68**, 208 (1996).

[143] K.T. ERN0 PUNGOR, Analyst **95**, 625 (1970).

[144] A.H. Kaye and E.R. Laws, Analyst **119**, 1 (1994).

[145] P. Bergveld, IEEE Trans. Biomed. Eng. (1) 70 (1970).

[146] P. Bergveld, Sensors Actuators, B Chem. **88**, 1 (2003).

[147] C. Jimenez-Jorquera, J. Orozco, and A. Baldi, Sensors **10**, 61 (2010).

[148] K. Schmoltner, J. Kofler, A. Klug, and E.J.W. List-Kratochvil, Adv. Mater. **25**, 6895 (2013).

[149] K. Melzer, A.M. Münzer, E. Jaworska, K. Maksymiuk, A. Michalska, and G. Scarpa, Analyst **139**, 4947 (2014).

[150] S.A. Algarni, T.M. Althagafi, A. Al Naim, and M. Grell, Talanta **153**, 107 (2016).

[151] F.B.M. Suah and M. Ahmad, Anal. Chim. Acta **951**, 133 (2017).

[152] K.N. Mikhelson, *Ion-Selective Electrodes* (Springer Heidelberg, Berlin, 2013).

[153] F. Deyhimi, Talanta **50**, 1129 (1999).

[154] K.Y. Lee, M. Park, J. Kim, M. Oh, E.H. Lee, K.W. Kim, D.Y. Chung, and J.K. Moon,

Chemosphere **150**, 765 (2016).

[155] S.A. Al-Muhtaseb, M.H. El-Naas, and S. Abdallah, J. Hazard. Mater. **158**, 300 (2008).

[156] Y.S. Ho, J.F. Porter, and G. Mckay, Water, Air, Soil Pollut. **141**, 1 (2002).

[157] R.A. Latour, J. Biomed. Mater. Res. - Part A **103**, 949 (2015).

[158] D.G. Duff, S.M.C. Ross, and D.H. Vaughan, J. Chem. Educ. **65**, 815 (1988).

[159] S.M. Basheer, M. Muralisankar, T. V. Anjana, K.N. Aneesrahman, and A. Sreekanth, Spectrochim. Acta - Part A Mol. Biomol. Spectrosc. **182**, 95 (2017).

[160] Í.F.T. de Souza and D.F.S. Petri, J. Mol. Liq. **266**, 640 (2018).

[161] H.K. Chung, W.H. Kim, J. Park, J. Cho, T.Y. Jeong, and P.K. Park, J. Ind. Eng. Chem. **28**, 241 (2015).

[162] O. Dada, A.O, Olalekan, A.P, Olatunya, A.M., DADA, IOSR J. Appl. Chem. **3**, 38 (2012).

[163] G.P. Jeppu and T.P. Clement, J. Contam. Hydrol. **129**–**130**, 46 (2012).

[164] H. Yang, S. Nishitani, and T. Sakata, ECS J. Solid State Sci. Technol. **7**(7), Q3079 (2018).

[165] S. Wustoni, C. Combe, D. Ohayon, M.H. Akhtar, I. McCulloch, and S. Inal, Adv. Funct. Mater. **29**, 1 (2019).

[166] H.H. Gatzen, V. Saile, and J. Leuthold, Micro Nano Fabr. (2015).

[167] G.L. Weissler, R.W. Carlson, and R.W. Hoffman, Phys. Today **33**, 58 (1980).

[168] D. Johannsmann, Quartz Cryst. Microbalance Soft Matter Res. pp.191-204 (2015).

[169] M.A. Trunov, M. Schoenitz, and E.L. Dreizin, Combust. Theory Model. **10**, 603 (2006).

[170] J. Leng, Z. Wang, J. Wang, H.H. Wu, G. Yan, X. Li, H. Guo, Y. Liu, Q. Zhang, and Z. Guo, Chem. Soc. Rev. **48**, 3015 (2019).

[171] T.C. Pluym, S.W. Lyons, Q.H. Powell, A.S. Gurav, T.T. Kodas, L.M. Wang, and H.D. Glicksman, Mater. Res. Bull. **28**, 369 (1993).

[172] J.H. Kim, V.I. Babushok, T.A. Germer, G.W. Mulholland, and S.H. Ehrman, J. Mater. Res. **18**,

1614 (2003).

[173] R. Kumar, G. Kumar, O. Al-Dossary, and A. Umar, Mater. Express **5**, 3 (2015).

[174] I. Isakov, H. Faber, M. Grell, G. Wyatt-Moon, N. Pliatsikas, T. Kehagias, G.P. Dimitrakopulos, P.P. Patsalas, R. Li, and T.D. Anthopoulos, Adv. Funct. Mater. **27**, 1 (2017).

[175] L. Filipovic, S. Selberherr, G.C. Mutinati, E. Brunet, S. Steinhauer, A. Kock, J. Teva, J. Kraft, J. Siegert, F. Schrank, C. Gspan, and W. Grogger, IEEE Trans. Semicond. Manuf. **27**, 269 (2014).

[176] D. Perednis and L.J. Gauckler, *14*(2),103 (2005).

[177] L. Filipovic, S. Selberherr, G.C. Mutinati, E. Brunet, S. Steinhauer, K. Anton, J. Teva, J. Kraft, and F. Schrank, Proc. World Congr. Eng. **II**, *27*(2) 269 (2013).

[178] C. Falcony, M.A. Aguilar-Frutis, and M. García-Hipólito, Micromachines **9**, 1 (2018).

[179] S.W. Oh, H.J. Bang, Y.C. Bae, and Y.K. Sun, J. Power Sources **173**, 502 (2007).

[180] U.S.T. As, A.G. Stephen, and K. Novel, **2**, 3 (1991).

[181] T.P. Rao, M.C.S. Kumar, A. Safarulla, V. Ganesan, S.R. Barman, and C. Sanjeeviraja, Phys. B Phys. Condens. Matter **405**, 2226 (2010).

[182] A.I. Hassan, A.J. Addie, and J. Admon, Mater. Res. Express **6**, (2019).

[183] M. Khammar, S. Guitouni, N. Attaf, M.S. Aida, and A. Attaf, **43**(13), 9919(2017).

[184] V. Vasu and A. Subrahmanyam, Thin Solid Films, **973,** 193–194 (1990).

[185] J.F. Guillemoles, D. Lincot, P. Cowache, and J. Vedel, Tenth E.C. Photovolt. Sol. Energy Conf. SE - 156 609 (1991).

[186] C.H. Chen, E.M. Kelder, and J. Schoonman, J. Eur. Ceram. Soc. **18**, 1439 (1998).

[187] G.K. Deyu, D. Muñoz-Rojas, L. Rapenne, J.L. Deschanvres, A. Klein, C. Jiménez, and D. Bellet, Molecules **24**, 1 (2019).

[188] R. Maller, Y. Porte, H.N. Alshareef, and M.A. McLachlan, J. Mater. Chem. C **97**, 14 (2016).

[189] N. Memarian, S.M. Rozati, E. Elamurugu, and E. Fortunato, Phys. Status Solidi Curr. Top. Solid State Phys. **7**, 2277 (2010).

[190] M. Singh, M.Y. Mulla, K. Manoli, M. Magliulo, N. Ditaranto, N. Cioffi, G. Palazzo, L. Torsi, M. V. Santacroce, C. Di'Franco, and G. Scamarcio, Proc. - 2015 6th IEEE Int. Work. Adv. Sensors Interfaces, IWASI 2015, 261 (2015).

[191] I.A. Pechenkina and K.N. Mikhelson, Russ. J. Electrochem. **51**, 93 (2015).

[192] R.D. Armstrong and G. Horvai, Electrochim. Acta **35**, 1 (1990).

[193] A. Ceresa, E. Bakker, B. Hattendorf, D. Günther, and E. Pretsch, Anal. Chem. **73**, 343 (2001).

[194] J.A. Seyforth, Exp. Experimental Techniques In Condensed Matter Physics. (2015).

[195] A. Knop-Gericke, X-Ray Photoelectron Spectroscopy. An Introduction to Principles and Practices. By Paul van Der Heide. *Angewandte Chemie International Edition*, **51**(37), pp.9218-9218. (2012).

[196] G. Greczynski and L. Hultman, Prog. Mater. Sci. **107**, 100591 (2020).

[197] A. Di Bartolomeo, L. Genovese, F. Giubileo, L. Iemmo, G. Luongo, T. Foller, and M. Schleberger, 2D Mater. **5**, (2018).

[198] R.S. Park, G. Hills, J. Sohn, S. Mitra, M.M. Shulaker, and H.S.P. Wong, ACS Nano **11**, 4785 (2017).

[199] S.Y. Park, M. Park, and H.H. Lee, Appl. Phys. Lett. **85**, 2283 (2004).

[200] M. Egginger, S. Bauer, R. Schwödiauer, H. Neugebauer, and N.S. Sariciftci, Monatshefte Fur Chemie **140**, 735 (2009).

[201] O. Transistors, IEEE Spectr. **10**, 106 (2004).

[202] M. Irimia-Vladu, Chem. Soc. Rev. **43**, 588 (2014).

[203] R. Li, L. Wang, and L. Yin, Materials (Basel). **11**, (2018).

[204] M. Singh, M.Y. Mulla, M.V. Santacroce, M. Magliulo, C. Di Franco, K. Manoli, D. Altamura, C. Giannini, N. Cioffi, G. Palazzo, G. Scamarcio, L. Torsi. Orgiu E, J. Phys. D. Appl. Phys. **49**, 275101 (2016).

[205] T. Tromholt, M. Manceau, M. Helgesen, J.E. Carlé, and F.C. Krebs, Sol. Energy Mater. Sol.

Cells **95**, 1308 (2011).

[206] N. Kumar, J. Kumar, and S. Panda, IEEE Electron Device Lett. **37**, 500 (2016).

[207] C.F. Klingshirn, B.K. Meyer, A. Waag, A. Hoffmann, and J. Geurts, EBooks **120**, (2010).

[208] E. Çetinörgü and S. Goldsmith, J. Phys. D. Appl. Phys. **40**, 5220 (2007).

[209] E.H. Anaraki, A. Kermanpur, L. Steier, K. Domanski, T. Matsui, W. Tress, M. Saliba, A. Abate, M. Grätzel, A. Hagfeldt, and J.P. Correa-Baena, Energy Environ. Sci. **9**, 3128 (2016).

[210] C. Sankar, V. Ponnuswamy, M. Manickam, R. Mariappan, and R. Suresh, Appl. Surf. Sci. **349**, 931 (2015).

[211] A.R. Babar, S.S. Shinde, A. V. Moholkar, C.H. Bhosale, J.H. Kim, and K.Y. Rajpure, J. Alloys Compd. **509**, 3108 (2011).

[212] Y.H. Lin, H. Faber, J.G. Labram, E. Stratakis, L. Sygellou, E. Kymakis, N.A. Hastas, R. Li, K. Zhao, A. Amassian, N.D. Treat, M. McLachlan, and T.D. Anthopoulos, Adv. Sci. **2**, 1 (2015).

[213] Y.S. Rim, H. Chen, X. Kou, H.S. Duan, H. Zhou, M. Cai, H.J. Kim, and Y. Yang, Adv. Mater. **26**, 4273 (2014).

[214] E. Bandiello, M. Sessolo, and H.J. Bolink, J. Mater. Chem. C **2**, 10277 (2014).

[215] M. Moshoeshoe, M.S. Nadiye-Tabbiruka, and V. Obuseng, Am. J. Mater. Sci. **7**, 191 (2017).

[216] R.M. Barrer, Zeolites and Clay Minerals as Sorbents and Molecular Sieves (Academic Press, London, 1978).

[217] D.S. Coombs, A. Alberti, T. Armbruster, G. Artioli, C. Colella, E. Galli, J.D. Grice, F. Liebau, J.A. Mandarino, H. Minato, E.H. Nickel, E. Passaglia, D.R. Peacor, S. Quartieri, R. Rinaldi, M. Ross, R.A. Sheppard, E. Tillmanns, and G. Vezzalini, Can. Mineral. **35**, 1571 (1997).

[218] N. Widiastuti, H. Wu, H.M. Ang, and D. Zhang, Desalination **277**, 15 (2011).

[219] P. Misaelides, Microporous Mesoporous Mater. **144**, 15 (2011).

[220] C. Perego, R. Bagatin, M. Tagliabue, and R. Vignola, Microporous Mesoporous Mater. **166**, 37 (2013).

[221] M.G. Valdés, A.I. Pérez-Cordoves, and M.E. Díaz-García, TrAC - Trends Anal. Chem. **25**, 24 (2006).

[222] Z.Y. Ji, J.S. Yuan, and X.G. Li, J. Hazard. Mater. **141**, 483 (2007).

[223] E. Erdem, N. Karapinar, and R. Donat, J. Colloid Interface Sci. **280**, 309 (2004).

[224] S. Wang and Y. Peng, Chem. Eng. J. **156**, 11 (2010).

[225] S.A. Al-Saydeh, M.H. El-Naas, and S.J. Zaidi, J. Ind. Eng. Chem. **56**, 35 (2017).

[226] S.R. Taffarel and J. Rubio, Miner. Eng. **22**, 336 (2009).

[227] S. Samatya, Ü. Yüksel, M. Yüksel, and N. Kabay, Sep. Sci. Technol. **42**, 2033 (2007).

[228] A. Nezamzadeh-Ejhieh and A. Badri, J. Electroanal. Chem. **71**, 660 (2011).

[229] J. Xie, W. Meng, D. Wu, Z. Zhang, and H. Kong, J. Hazard. Mater. **57**, 231–232 (2012).

[230] N. Jiang, R. Shang, S.G.J. Heijman, and L.C. Rietveld, Water Res. **144**, 145 (2018).

[231] M.W. Munthali, E. Johan, H. Aono, and N. Matsue, J. Asian Ceram. Soc. **3**, 245 (2015).

[232] H. Mimura and K. Akiba, J. Nucl. Sci. Technol. **30**, 436 (1993).

[233] M.A. Stylianou, M.P. Hadjiconstantinou, V.J. Inglezakis, K.G. Moustakas, and M.D. Loizidou, J. Hazard. Mater. **143**, 575 (2007).

[234] L. Damjanović, V. Rakić, V. Rac, D. Stošić, and A. Auroux, J. Hazard. Mater. **184**, 477 (2010).

[235] M. Arvand-Barmchi, M.F. Mousavi, M.A. Zanjanchi, and M. Shamsipur, Sensors Actuators, B Chem. **96**, 560 (2003).

[236] M.K. Shelyakina, O.O. Soldatkin, V.M. Arkhypova, B.O. Kasap, B. Akata, and S. V. Dzyadevych, Nanoscale Res. Lett. **9**, 1 (2014).

[237] V. Arora, H.M. Chawla, and S.P. Singh, Arkivoc. **2**, 172 (2007).

[238] D. Ammann, D. Erne, H.-B. Jenny, F. Lanter, and W. Simon, Prog. Enzym. Ion-Selective Electrodes, Springer, Berlin, Heidelberg. 9-14 (1981).

[239] S.K. Menon, N.R. Modi, B. Patel, and M.B. Patel, Talanta **83**, 1329 (2011).

[240] A. Cadogan, Z. Gao, A. Lewenstam, A. Ivaska, D. Diamond, A. Lewenstam, and Z. Gao, Anal. Chem. **64**, 2496 (1992).

[241] A. Tarasov, M. Wipf, R.L. Stoop, K. Bedner, W. Fu, V.A. Guzenko, O. Knopfmacher, M. Calame, and C. Schönenberger, ACS Nano **6**, 9291 (2012).

[242] L.B. McCusker, D.H. Olson, and C. Baerlocher, *Atlas of zeolite framework types*. Elsevier (2007).

[243] L.F. GILLIS JOHANSSON, LARS RISINGER, Anal. Chim. Acta **119**, 25 (1980).

[244] X.F. Li, R. Prins, and J.A. van Bokhoven, J. Catal. **262**, 257 (2009).

[245] T. Tsurumura, Y. Tsumori, H. Qiu, M. Oda, J. Sakurai, M. Nagahama, and H. Tsuge, Proc. Natl. Acad. Sci. U. S. A. **110**, 7524 (2013).

[246] M.C. Honda, T. Aono, M. Aoyama, Y. Hamajima, H. Kawakami, M. Kitamura, Y. Masumoto, Y. Miyazawa, M. Takigawa, and T. Saino, Geochem. J. **46**, 1 (2012).

[247] B.J. Müller, S.M. Borisov, and I. Klimant, Adv. Funct. Mater. **26**, 7697 (2016).

[248]Atsdr.cdc.gov. (2019). *ATSDR - Public Health Statement: Cesium*. [online] Available at: https://www.atsdr.cdc.gov/phs/phs.asp?id=575&tid=107 [Accessed 6 Nov. 2019].

[249] A.S. V. VASU, Thin Solid Film. **202**(2), 283 (1991).

[250] www.nwl.co.uk, *What's in your tap water?* [online] Available at: https://www.nwl.co.uk/_assets/documents/3124_Web_PDF_-_Whats_in_your_tap_water.pdf [Accessed 20 June 2019].

[251] Dwi.defra.gov.uk, [online] Available at: http://www.dwi.defra.gov.uk/about/annual-report/2017/Summary_CIR_2017_England.pdf for "Drinking Water 2017: Chief Inspector's Report for Drinking Water in England," accessed 10 August 2020.

[252] K.Y. Patterson, P.R. Pehrsson, and C.R. Perry, J. Food Compos. Anal. **31**, 46 (2013).

[253] S. Collinson et al., [online] Available at: https://www.open.edu/openlearn/ocw/mod/oucontent/view.php?printable=1&id=20880 for "What Chemical Compounds Might be Present in Drinking Water," [Accessed 10 Augest 2020].

[254] A.K. Tuwei, N.H. Williams, M.Y. Mulla, C. Di Natale, R. Paolesse, and M. Grell, Talanta **164**, 228 (2017).

[255] H.T. and T.S. KEIICHI KIMURA and Department, J. Electroanal. Chem. **105**, 335 (1979).

[256] N. Alghamdi, Z. Alqahtani, and M. Grell, J. Appl. Phys. **126**, 064502 (2019).

[257] I. Sato, H. Kudo, and S. Tsuda, J. Toxicol. Sci. **36**, 829 (2011).

[258] V. Masindi, and K.L. Muedi, 2018. Environmental contamination by heavy metals. *Heavy metals*, *10*, 115.

[259] V.B.P. Sudha, S. Ganesan, G.P. Pazhani, T. Ramamurthy, G.B. Nair, and P. Venkatasubramanian, J. Heal. Popul. Nutr. **30**, 17 (2012).

[260] Nepis.epa.gov. (2008). *Lead and Copper Rule: A Quick Reference Guide*. [online] Available at: https://nepis.epa.gov/Exe/ZyPDF.cgi?Dockey=60001N8P.txt [Accessed 9 Aug. 2020].

[261] J. Perić, M. Trgo, and N. Vukojević Medvidović, Water Res. **38**, 1893 (2004).

[262] F.A. Mumpton, Proc. Natl. Acad. Sci. U. S. A. **96**, 3463 (1999).

[263] E. Turiel, C. Perez-Conde, and A. Martin-Esteban, Analyst **128**, 137 (2003).

[264] A. Kilincarslan and S. Akyil, J. Radioanal. Nucl. Chem. **264**, 541 (2005).

[265] O. Oter and H. Akcay, Water Environ. Res. **79**, 329 (2007).

[266] W. Hölderich, M. Hesse, and F. Näumann, Angew. Chemie Int. Ed. English **27**, 226 (1988).

[267] A.J. Medford, A. Vojvodic, J.S. Hummelshøj, J. Voss, F. Abild-Pedersen, F. Studt, T. Bligaard, A. Nilsson, and J.K. Nørskov, J. Catal. **328**, 36 (2015).

[268] J. Čejka, R.E. Morris, and D.P. Serrano, Catal. Sci. Technol. **6**, 2465 (2016).

[269] K.M. Valkaj, A. Katović, and S. Zrnčević, Ind. Eng. Chem. Res. **50**, 4390 (2011).

[270] N.S. Inchaurrondo, P. Massa, R. Fenoglio, J. Font, and P. Haure, Chem. Eng. J. 198–199, **426**

(2012).

[271] M.M. Rahman, B.M. Abu-Zied, and A.M. Asiri, J. Ind. Eng. Chem. **61**, 304 (2018).

[272] ThermoFisher Scientific (2019). 45879 zeolite ZSM-5 ammonuium. [online] Available at: https://www.alfa.com/en/catalog/045879/ . [Accessed 9 December 2019].

[273] ThermoFisher Scientific.(2019). A10378 Molecular sieves, 13X, powder. [online] Available at: https://www.alfa.com/en/prodspec/A10378 [Accessed 9 December 2019].

[274] ThermoFisher Scientific. (2019). 45866 Zeolite Y, hydrogen. [online] Available at:

https://www.alfa.com/en/catalog/045866/ [Accessed 9 December 2019].

[275] Sigma-Aldrich. Silica,mesostructured MCM-41 type (hexagonal). [Online] Available at: https://www.sigmaaldrich.com/catalog/product/aldrich/643645?lang=en&region=GB [Accessed 9 December 2019].

[276] Sigma-Aldrich. Silica,mesostructured SBA-15, 99% trace metals basis. [Online] Available at: https://www.sigmaaldrich.com/catalog/product/aldrich/777242?lang=en&region=GB [Accessed 9 December 2019].

[277] H. Zhao, T.M. Nenoff, G. Jennings, P.J. Chupas, and K.W. Chapman, J. Phys. Chem. Lett. **2**, 2742 (2011).

[278] C.A. Wilde, Y. Ryabenkova, I.M. Firth, L. Pratt, J. Railton, M. Bravo-sanchez, N. Sano, P.J. Cumpson, P.D. Coates, X. Liu and M. Conte, *Applied Catalysis A: General* 570: 271-282. (2019)

[279] B. Xu, S. Bordiga, R. Prins, and J.A. van Bokhoven, Appl. Catal. A Gen. **333**, 245 (2007).

[280] K.M. Valkaj, A. Katovic, and S. Zrnčević, J. Hazard. Mater. **144**, 663 (2007).

[281] Y. Meng, H.C. Genuino, C.H. Kuo, H. Huang, S.Y. Chen, L. Zhang, A. Rossi, and S.L. Suib, J. Am. Chem. Soc. **135**, 8594 (2013).

[282] M. Conte, J.A. Lopez-Sanchez, Q. He, D.J. Morgan, Y. Ryabenkova, J.K. Bartley, A.F. Carley, S.H. Taylor, C.J. Kiely, K. Khalid, and G.J. Hutchings, Catal. Sci. Technol. **2**, 105 (2012).

[283] R.M. Barrer and R.P. Townsend, J. Chem. Soc. Faraday Trans. 1 Phys. Chem. Condens. Phases **72**, 661 (1976).

[284] A. Gurbani, J.L. Ayastuy, M.P. González-Marcos, J.E. Herrero, J.M. Guil, and M.A. Gutiérrez-Ortiz, Int. J. Hydrogen Energy **34**, 547 (2009).

[285] T. Schaefer, R. Sebastian, J. Peeling, G.H. Penner, and K. Koh, Can. J. Chem. **67**, 1015 (1989).

[286] J.A. Pople and M. Gordon, J. Am. Chem. Soc. **89**, 4253 (1967).

[287] J. Polak and B.C.-Y. Lu, Can. J. Chem. **51**, 4018 (1973).

[288] H.W. Lin, C.H. Yen, and C.S. Tan, Green Chem. **14**, 682 (2012).

[289] Toxnet.nlm.nih.gov. (2018) BENZYL ALCOHOL—National Library of Medicine HSDB Database, [online] Available at: https://toxnet.nlm.nih.gov/cpdb/chempages/BENZYL%20ALCOHOL.html. [Accessed 8 Dec 2019]

[290] L.B. Bortolatto, R.A.A. Boca Santa, J.C. Moreira, D.B. Machado, M.A.P.M. Martins, M.A. Fiori, N.C. Kuhnen, and H.G. Riella, Microporous Mesoporous Mater. **248**, 214 (2017).

[291] M. Tortorelli, G. Landi, L. Lisi, and G. Russo, Microporous Mesoporous Mater. **200**, 216 (2014).

[292] M. Khalid, G. Joly, A. Renaud, and P. Magnoux, Ind. Eng. Chem. Res. **43**, 5275 (2004).

[293] H. Babich and D.L. Davis, Regul. Toxicol. Pharmacol. **1**, 90 (1981).

[294] Agency for Toxic Substances and Disease Registry. (2017). Toxicological Profile for Toluene, 4770 Buford Hwy NE, Atlanta, GA 30341. [Online] Available at: https://www.atsdr.cdc.gov/ToxProfiles/tp.asp?id=161&tid=29 [Accessed 10 August 2020].

[295] J.O. Weston, H. Miyamura, T. Yasukawa, D. Sutarma, C.A. Baker, P.K. Singh, M. Bravo-Sanchez, N. Sano, P.J. Cumpson, Y. Ryabenkova, S. Kobayashi, and M. Conte, Catal. Sci. Technol. **7**, 3985 (2017).

[296] S. Sen Gupta and K.G. Bhattacharyya, Phys. Chem. Chem. Phys. **14**, 6698 (2012).

[297] S. Wong, N. Ngadi, I.M. Inuwa, and O. Hassan, J. Clean. Prod. **175**, 361 (2018).

[298] A. Amini, S. Kazemi, and V. Safarifard, Polyhedron **177**, 114260 (2020).

[299] H.E. Gottlieb, V. Kotlyar, and A. Nudelman, J. Org. Chem. **62**, 7512 (1997).

[300] S. Ma, J. Liu, S. Li, B. Chen, J. Cheng, J. Kuang, Y. Liu, B. Wan, Y. Wang, J. Ye, Q. Yu, W. Yuan, and S. Yu, Adv. Synth. Catal. **353**, 1005 (2011).

[301] K. Brezinsky, T.A. Litzinger, and I. Glassman, Int. J. Chem. Kinet. **16**, 1053 (1984).

[302] G. Maurin, R.G. Bell, S. Devautour, F. Henn, and J.C. Giuntini, J. Phys. Chem. B **108**, 3739 (2004).

Appendix:

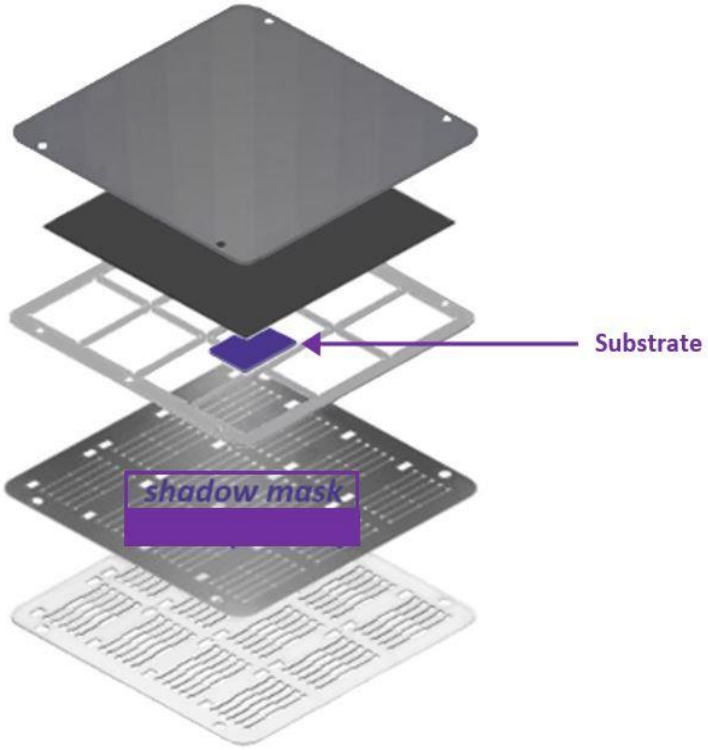

Figure A4.1: The components used in the evaporation stack including the shadow mask (from Ossila.com).

Table A6.1: 10 ml of tap water from our lab analyzed by the method of Inductively coupled plasma electrospray mass spectrometry (ICP)

Ba	Ca	Cu	K	Mg	Na	Ni	P	Pb	S	Si	Zn	Cs*
0.011	3.47	0.067	0.617	2.54	19.9	0.020	0.911	< 0.008	13.9	2.37	0.146	0.011

All results mg/l

* results µg/l

Table A6.2: cations related to this thesis work Molarity unit:

Cation	Molarity
Cu^{2+}	1 µM
Pb^{2+}	< 38 nM
Cs^{+}	80 pM

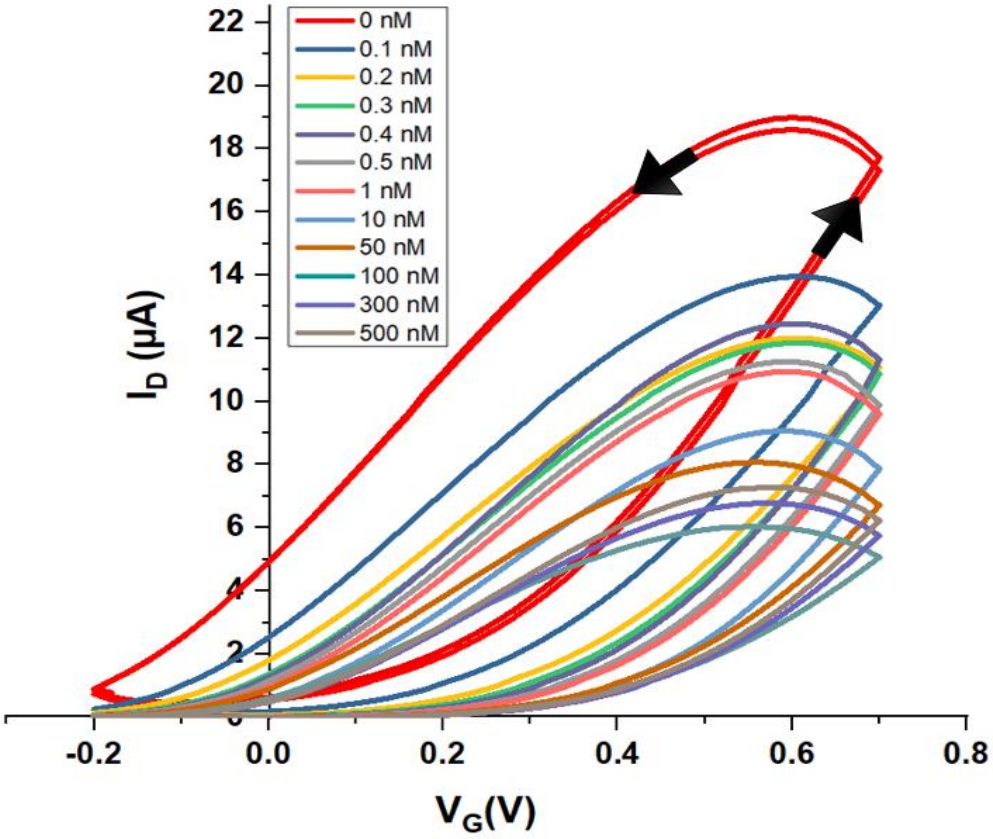

Figure. A6.1: An extended version of figure. 6.3a, showing full linear transfer hysteresis loops for a membrane-sensitised SnO_2 WGTFT under the full gate voltage sweep cycle (-0.2 V ⇌ +0.7 V), under increasing Cs^{+} concentration in the outer pool. Arrows indicate the sweep direction.

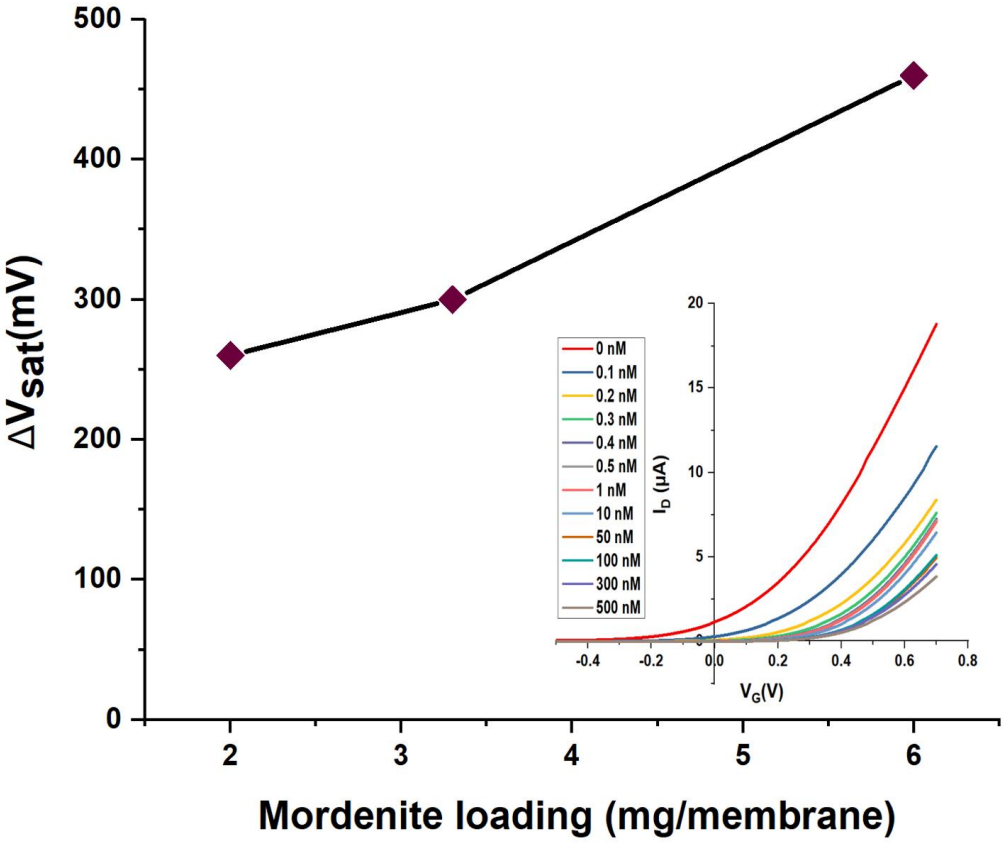

Figure. A6.2: ΔV(sat) *vs.* mordenite loading in membrane (2, 3.3, 6 mg / membrane): Inset: Family of transfer characteristics under increasing Cs^+ as in figure. 6.3a, but membrane loaded with 6 mg mordenite.

Table A6.3: Stability constant K, evaluated as described in 6.4, for membranes with different mordenite loading. Note K differs by orders- of- magnitude between different sensitisers, *e.g.*[247,254,255] and is often reported on a log K scale, the variation of K here is within the usual 'scatter' between different reports for the same sensitiser [*e.g.*[237]].

Mordenite loading [mg]	K [10^9 L/mol]
2.2	3.1 +/- 0.2
3.3 (from figure 6. 3a)	3.9 +/- 0.4
6	7.1 +/- 0.8

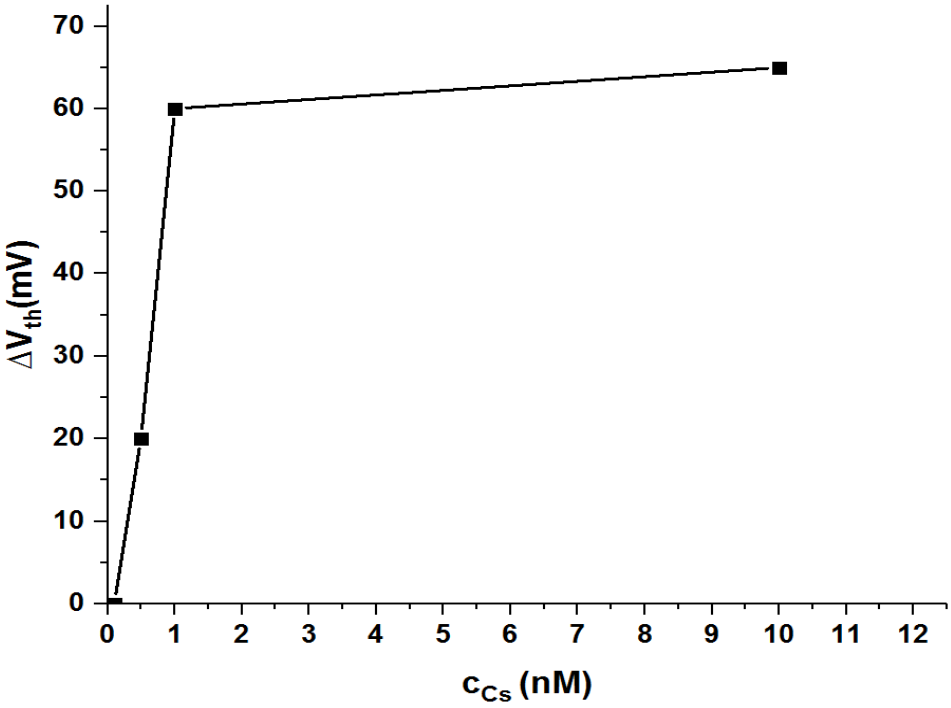

Figure. A6.3 Threshold shift ΔV_{th} vs concentration of Cs^+ when the sample/ reference pool is reversed with respect to Fig. 6.3a, now a tap water reference was used in the outer pool and Cs^+ samples are in the inner pool. The inner pool is defined as the one that contacts the semiconductor.

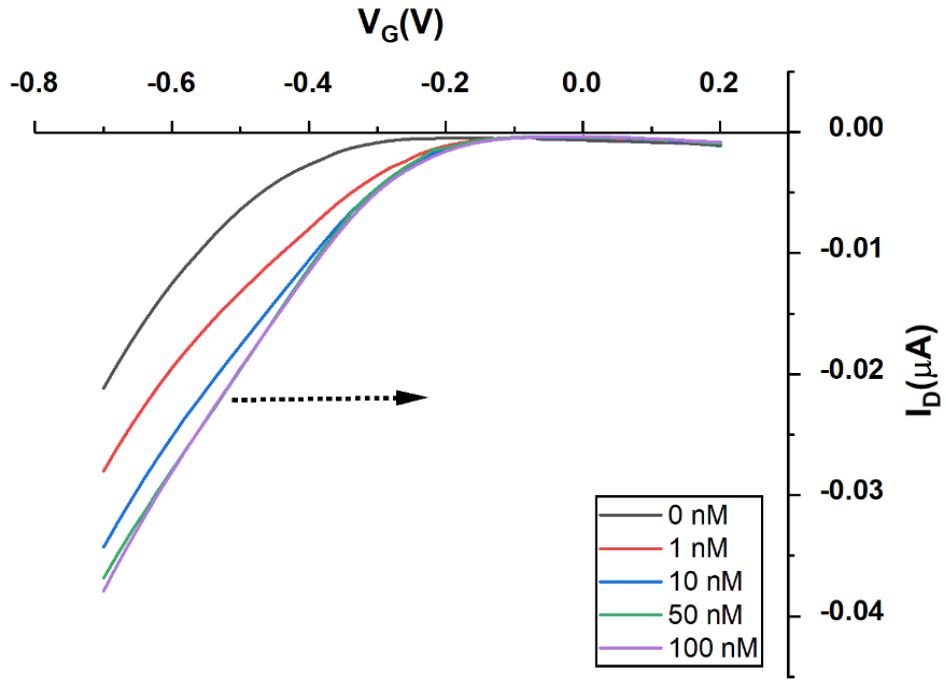

Fig. A6.4: Transfer characteristics of mordenite- sensitised P3HT WGTFT gated under increasing Cs^+ concentrations in the outer pool

A8.1 Transition metal doping protocols

a. Wet impregnation (WI)

The WI protocol to dope ZSM-5 with Copper, Iron and Manganese was as follows: impregnation with aqueous solutions of metal precursors $Cu(NO_3)\cdot 2.5H_2O$ (Acros, 98+%), $Fe(NO_3)_3\cdot 9H2O$ (Acros, 98+%) and $Mn(NO_3)2\cdot 4H_2O$ (Sigma Aldrich, ≧97%) respectively. Zeolite Y (Zeolyst International CBV720, Si: Al = 11: 1) was used in its acidic form, here denoted as HY. In order to obtain a final metal loading of 1% wt, the desired amount of metal precursor was dissolved in water (25 mL) and mixed with 2 g of zeolite support (ammonia ZSM-5, HZSM-5, 13X, HY, MCM-41 or SBA-15) under vigorous stirring. Before preparation, the ammonia ZSM-5 was calcined at 550 ºC in air for 4 h with temperature ramping of 20 °C min^{-1} to get the hydrogen ZSM-5. The amount of zeolite was adjusted to compensate the metal assay for each precursor. The resulting slurry was heated up slowly to 80 °C and evaporated to dryness. Each catalyst was dried at 120 °C for 16 h, and calcined at 550 °C for 4 h in static air (temperature ramp 20 °C min^{-1}) for Cu and Fe catalysts while 500 ºC was used for Mn catalysts.

b. Ion exchange (IE)

For IE, 2 g of zeolites (ZSM5, Y) was added to an aqueous metal nitrate solution (25 mL) of appropriate concentration (typically 1 M) to achieve a final metal loading of 1-2 wt%. The resulting slurry was heated and stirred in a container at 95 ºC (using an oil bath) for 24 h using a setup equipped with a condenser. After cooling, the slurry was filtered and the solid washed with deionized water (1 L per 2 grams of solid). The resulting powder was dried at 120 ºC for 16 h and then calcined at 550 ºC (temperature ramp of 20 ºC/min) for 4 h.

c. Deposition-precipitation (DP)

The zeolite support (hydrogen ZSM-5, 2 g) was stirred in distilled water (25 mL), and $Cu(NO_3)_2$ solution (25 mL) was added dropwise over 10 min, to produce a final Cu loading of 1 wt%. The slurry was then heated to 80 ºC, and the pH was adjusted by adding a saturated Na_2CO_3 solution

to reach pH 10 under continuous stirring. After stirring for another 1 h and cooling, the slurry was filtered and washed in approximately 4 L of distilled water. The solid was then dried at 120 ^{o}C for 16 h, followed by calcination at 550 ^{o}C for 4 h.

A8.2 Catalytic activity measurements

Catalytic tests for phenol oxidation were carried out by dispersing the solid catalyst in an aqueous solution containing 10.6 mM of phenol and by adjusting catalyst amount or reactant in order to maintain a constant molar metal to substrate ratio (M : S) of 1:100. In a typical experiment approximately 30 mg of catalyst and 50 mL of aqueous phenol solution were used. All catalytic tests were carried out in custom made glass 100 mL flasks equipped with a Young's valve - to be used as a batch reactor - at a constant reaction temperature of 80 ^{o}C. 0.76 mL of H_2O_2 (30%, VWR International) was added to the phenol solution as an oxidant when the temperature reached 80 ^{o}C to start the reaction. The flask containing the reaction mixture was inserted into a pre- heated temperature calibrated aluminium block for the desired reaction time, under stirring at 500 rpm. The reaction was quenched into an ice-water bath after 4 h. Analysis of the reaction mixture was carried out via HPLC using the following analysis condition: XBridge C18 column, acetonitrile / 0.1% orthophosphoric acid solution with ratio of 30%/70% (V/V) as mobile phase with a flow rate of 1 mL·min^{-1}. For catalytic activity tests on benzyl alcohol as substrate, the catalyst was dispersed in 5 mL of 277 mM of benzyl alcohol (Acros, 99%) solution adjusting the amount of substrate to a molar metal to substrate ratio of 1: 100 for each catalyst with respect to the total amount of active metal. The reaction mixture was heated using a reflux condenser at 80 ^{o}C for 24 hours with a magnetic stirrer operating at 300 rpm at atmospheric pressure. Analysis of the reaction mixture to determine product selectivity and conversion was obtained via ^{1}H-NMR using a Bruker Avance IIIHD 400 spectrometer operating at 400 MHz. NMR spectra were collected using $CDCl_3$ as solvent. Before NMR analysis, the reaction mixture was extracted with $CDCl_3$ for 1 h under stirring. After that, the substance was collected and analysed. Chemical shifts were reported in parts per million (ppm) from tetramethylsilane. [299].

A8.3 Catalytic activity result

From table 8.2 conversion rates for phenol are considerably higher than those of benzyl alcohol. The reason of this behaviour is two-fold: (i) the oxidation of phenol is assisted by hydrogen peroxide, whereas the oxidation of benzyl alcohol is assisted by molecular oxygen, and (ii) the doping metals that we have selected for the zeolites are inherently more efficient at hydrogen peroxide activation rather than molecular oxygen activation under our experimental conditions. Materials that are active for phenol oxidation may not be active for alcohol oxidation and vice-versa, because reaction mechanisms are different. An example of this is the Fe containing catalysts, which fail to catalyse benzyl alcohol oxidation. In fact, Fe-doped frameworks are known to be a poor oxidizers for alcohols unless nitroxide species are added [300], and as such served as a control here. In fact, Fe-doped frameworks (No 7, and 8) also fail to catalyse phenol decomposition, but No. 9 is very active for phenol. We note though that sensing relies in the first step of catalysis only, namely adsorption to the catalyst surface, which nevertheless may be strong for benzyl alcohol despite of the lack of subsequent oxidation of adsorbed substrate.

All candidates were also tested for catalytic activity on toluene but there was no measurable catalysis of toluene at the conditions (atmospheric pressure and 100 ^{o}C) It is known that catalytic breakdown of toluene usually requires autoclave conditions [301].